INVESTIGATIONS INTO THE ROLE OF SILVER ON THE MAGNETIC BEHAVIOR OF IG PROCESSED BULK YBCO/Ag COMPOSITE SUPERCONDUCTORS

A thesis submitted to

University of Hyderabad

In Partial Fulfillment of the Requirements for the Degree of

Doctor of Philosophy

By

R. PARTHASARATHY
06PHPH03

School of Physics

University of Hyderabad

Hyderabad – 500046
July 2012

DEDICATED

TO

THE SPIRIT OF DOING SCIENCE

DECLARATION

I hereby declare that the work presented in this thesis has been carried out by me under the supervision of Prof. V. Seshubai, School of Physics, University of Hyderabad, Hyderabad, India. I also declare that the said work has not been, in part or the whole thereof, submitted to any other University/ institution for the award of any other degree/diploma.

                                                            R. PARTHASARATHY

Date:

Place: Hyderabad.

CERTIFICATE

This is to certify that the research work compiled and presented in the thesis titled "**Investigations into the role of silver on the magnetic behavior of IG processed bulk YBCO/Ag composite superconductors**" has been carried out by **Mr. R. Parthasarathy** under my supervision and the same has not been submitted for the award of degree by any other University.

Dr. V. SESHUBAI

RESEARCH SUPERVISOR
Professor, School of Physics
University of Hyderabad

Date:

Place: Hyderabad

DEAN

SCHOOL OF PHYSICS

CHAPTERS IN THE THESIS

<u>CONTENTS</u>

CHAPTER 1

INTRODUCTION

CHAPTER 2

EXPERIMENTAL TECHNIQUES

CHAPTER 3

FABRICATION OF YBCO/AG COMPOSITE SUPERCONDUCTORS BY INFILTRATION GROWTH PROCESSING TECHNIQUE – ROLE OF SILVER ADDITION

CHAPTER 4

LEVITATION AND SUSPENSION FORCES OF YBCO/Ag SUPERCONDUCTORS, SAMPLE GEOMETRY DEPENDENCE OF THESE FORCES, RELAXATION BEHAVIOR OF LEVITATION AND SUSPENSION FORCES

CHAPTER 5

RAPID INFILTRATION GROWTH PROCESSING TECHNIQUE FOR FABRICATION OF YBCO AND YBCO/Ag SUPERCONDUCTING COMPOSITES

CHAPTER 6

MAGNETIC FIELD AND TEMPERATURE DEPENDENCE OF CRITICAL CURRENT DENSITY AND PINNING FORCE DENSITY OF YBCO AND YBCO/Ag SUPERCONDUCTORS FABRICATED BY INFILTRATION GROWTH PROCESSING AND RAPID INFILTRATION GROWTH PROCESSING TECHNIQUES

CHAPTER 7

CHAPTER 1

INTRODUCTION

1.1 Superconductivity

The discovery of the phenomenon of superconductivity in 1911 by K. H. Onnes [1-3] has its origins in constant efforts by low temperature physicists those days in several laboratories around the world to compete with each other to do compression and liquefaction of gases and to achieve cryogenic temperatures through these efforts [4-11]. The foremost experiments involved using the cryogens to measure the resistance of metals. One such fortuitous moment led to the discovery of complete loss of resistance in mercury cooled to liquid helium temperatures [12-13]. The phenomenal observation of zero resistance in mercury led to discovery of superconductivity in several other elements [12]. Twenty two years after the discovery of superconductivity, W. Meissner and R. Ochsenfeld discovered [14], what is now commonly referred to as, Meissner effect whereby the complete expulsion of magnetic flux by a superconductor occurs on cooling under a magnetic field. The twin properties of zero resistance and magnetic flux expulsion defined the state of superconductivity until A. A. Abrikosov [15], based

on the phenomenological theory of V. L. Ginzburg and L.D. Landau [16], predicted the possibility of existence of a mixed state where zero resistance and magnetic flux penetration both could co-exist, though experimentally L.V Shubnikov and his co-workers had observed the mixed state in some alloys twenty years earlier in 1937 [17]. This led to the classification of the materials possessing the vortex or mixed state between a lower and an upper critical magnetic field as type-II superconductors compared to the materials with a single critical magnetic field as type-I wherein the magnetic field causes the material to cease being a superconductor. The type-II superconductors, initially considered exotic, have become the most common type of superconductors with most of the materials found to be superconducting in the last five decades belonging to this category. The type-II superconductors consists of several families of materials such as metallic alloys, high T_c cuprates, fullerenes, organic systems, Chevrel phases, borides including MgB_2, iron oxypnictides, heavy fermionic systems [18] etc.

1.2 Zero resistance

The term superconductivity essentially implies this aspect of the material whereby below a certain material-dependent temperature

called the transition temperature, T_c, the specimen loses all its resistance or attains infinite conductance. The material effectively transforms from a normal state to a superconducting state. Above the transition temperature, the material can show resistance to current, the magnitude of which depends on the normal state of the material such as metallic, insulating or semi-conducting. The resistivity-temperature curve starts to show a sudden drop as the material starts to lose its resistance drastically. The temperature at which the transition starts is called the transition onset temperature. The difference in temperature between the transition onset and the zero-resistance temperature is the transition
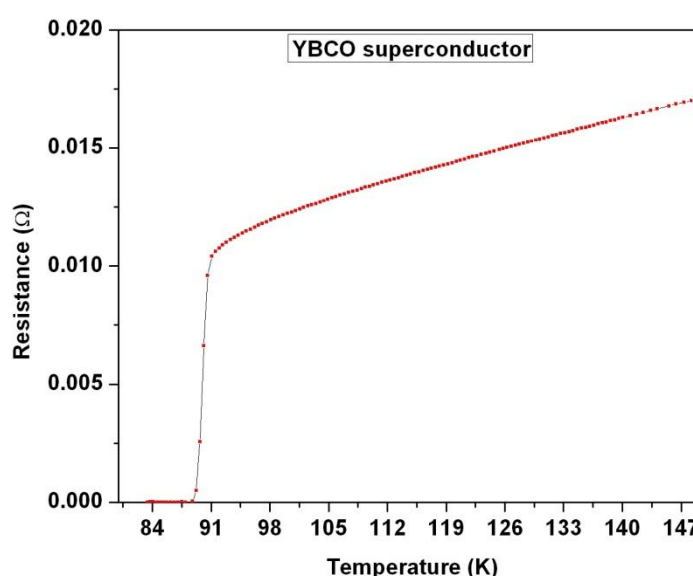
Figure 1.1 A typical resistance versus temperature plot of a superconductor showing its transition from normal state to the superconducting state. Here, the sample studied was an YBCO superconductor.

width of the material. In the transition width regime, the material is neither in a completely superconducting state nor in a normal state. Figure 1.1 shows the resistance versus temperature plot of a high T_c superconductor YBCO sample in the temperature range 80 K to 150 K. The resistivity in normal metals at room temperature is attributed to collisions between free electrons and ions in the lattice, scattering by defects and other impurities [19] etc. The electrons lose their kinetic energy during such collisions causing dissipation of energy carried by the current. This appears as electrical resistance in the material. Normal metals, when cooled to very low temperatures, lose much of their resistance due to thermal effects but retain a residual resistivity which depends mainly on the impurity levels. Superconductors on the other hand lose all their resistance when cooled to temperatures below the transition temperature. Hence, the current conduction mechanism in superconductors is entirely different from that in normal metals which we shall discuss in a later section.

1.3 Meissner effect

German physicists Walther Meissner and Robert Ochsenfeld observed that lead and tin superconducting samples, in addition to showing zero resistance, also expelled magnetic flux in their vicinity on being cooled

to temperatures below their T$_c$'s in the presence of a magnetic field [14]. This strange occurrence could not be explained based on any classical theories available then. Assuming a superconductor to be the same as a perfect conductor, when cooled to sufficiently low temperatures, can oppose any change in magnetic field in its vicinity by producing eddy currents that oppose the change. But, such perfect conductors are not expected to expel flux from inside on being field-cooled. This is what separates superconductors from such normal materials.
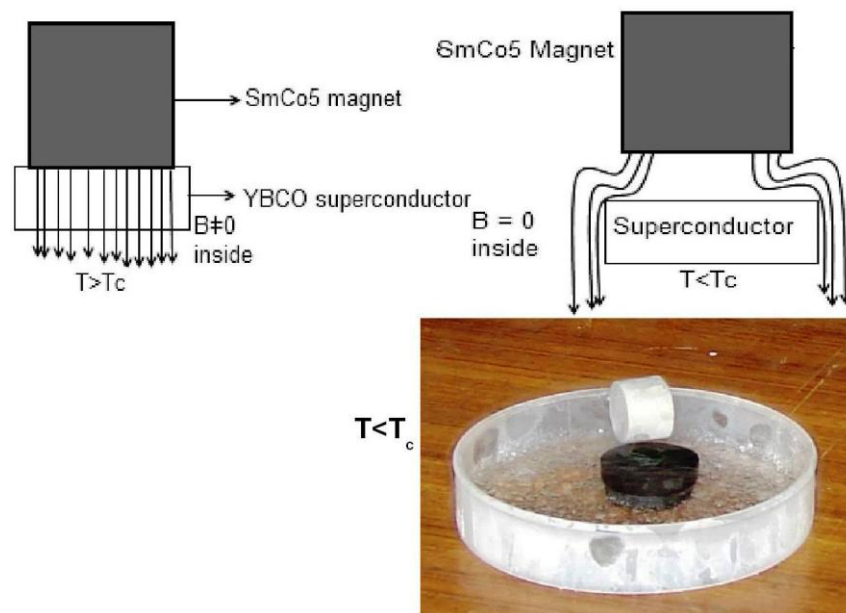
Figure 1.2 A schematic representation of Meissner effect and levitation of a SmCo$_5$ permanent magnet over an YBCO superconductor revealing an aspect of the Meissner effect.

The Meissner effect is a result of perfect diamagnetism in the material. Levitation of permanent magnets by superconductors or vice-versa is an experimental signature of Meissner effect, which is shown in figure 1.2. The theoretical explanation for Meissner effect could be obtained based on London equations [20] which describe the superconductivity in simplest terms. Based on intuitive logic, the London brothers, Fritz and Heinz, wrote the equations for electric and magnetic fields in the superconductor in the following forms.

$$\frac{\partial j_s}{\partial t} = \frac{n_s e^2}{m}\, \mathbf{E} \qquad (1.1); \qquad \nabla \times \mathbf{j_s} = -\frac{n_s e^2}{mc}\, \mathbf{B} \qquad (1.2)$$

$\mathbf{j_s}$ is the superconducting current density E and B are the electric and magnetic fields respectively, n_s is the number density of superconducting electrons, m and c are the mass electron mass and velocity of light respectively in cgs units.

According to Ampère's law,

$$\nabla \times \mathbf{B} = \frac{4\pi\, \mathbf{j}}{c} \qquad (1.3)$$

Taking curl of equation (1.2) and applying eqn. 1.3, one can arrive at

$$\nabla^2 \mathbf{B} = \frac{1}{\lambda^2} \mathbf{B}^2 \qquad (1.4)$$

Where λ is called the London penetration depth expressed as

$$\sqrt{\frac{mc^2}{4\pi n_s e^2}} \qquad (1.5)$$

The solution of the London's eqn. 1.4 is of the form

$$B_z(x) = B_0 e^{-x/\lambda} \tag{1.6}$$

Thus the London penetration depth, λ can be defined as a characteristic length scale over which the applied magnetic field vanishes exponentially to zero inside the superconductor [21].

The electrons were assumed to be under a uniform electric field and the Lorentz force on the electrons is given as

$$\mathbf{F} = e\mathbf{E} \times \frac{e}{c} (\mathbf{v} \times \mathbf{B}) \tag{1.7}$$

Thus the electrons are under a uniform force and undergo a uniform acceleration which is described by the first of the two London equations, namely eqn. (1.1).

According to Faraday's law,

$$\nabla \times \mathbf{E} = -\frac{1}{c} \frac{\partial \mathbf{B}}{\partial t} \tag{1.8}$$

Taking curl of the first London eqn. (1.1) and applying eqn. (1.8), one gets (1.2).

The using Faraday's law, one can obtain

$$\frac{\partial}{\partial t} \left(\nabla \times \mathbf{j_s} + \frac{n_s e^2}{mc} \mathbf{B} \right) = 0 \tag{1.9}$$

The eqn. 1.9 implies both constant and zero solutions for the terms in the parenthesis. Since a non-zero constant solution is unphysical, the term must be equal to zero implying the second London equation. This indicates that the change in magnetic field inside the superconductor is zero and hence the magnetic field itself is zero inside the superconductor thereby achieving complete flux expulsion, i.e., Meissner effect.

1.4 Type-I and Type- II superconductors

The superconductors can be classified broadly into type-I and type-II based on their basic behavior to applied magnetic fields [22-25]. Type- I superconductors are those materials which when cooled below their transition temperature retain superconductivity in zero magnetic field or up to an applied magnetic field, called critical magnetic field H_c. The type-I materials are in perfect diamagnetic state or Meissner state up to an applied field H_c. When the applied field exceeds the critical field, the material loses all its superconductivity and reverts to normal state even if kept below the transition temperature T_c. The transition to normal state occurs via a first-order phase transition. A phase separation within the type-II superconductor into regions of macroscopic superconducting and non-superconducting domains is possible, as proposed by Lev

Landau [26], depending on the demagnetization factor. Most of the pure metals are type-I superconductors.

Type-II superconductors, on the other hand, show an entirely different behavior under applied magnetic fields. These materials have two critical magnetic fields, the lower critical magnetic field H_{c1}, below which the material is in perfect diamagnetic state and an upper critical magnetic field H_{c2} above which the material loses all its superconductivity and becomes normal. In between these two critical fields, the material is said to be in a mixed state or vortex state as magnetic field penetrates the material in the form of flux bundles and supercurrent vortices are generated around the flux bundles [27]. Thus, in the vortex state the total current density of the material is a combination of the Meissner shielding currents and the vortex supercurrents.

The superconducting coherence length, ξ is the characteristic exponent of the variations in density of the superconducting component. The ratio of London penetration depth to the coherence length, λ/ξ is known as the Ginzburg-Landau parameter [21]. The G-L parameter is lesser than $1/\sqrt{2}$ for type-I superconductors and greater than $1/\sqrt{2}$ for type-II materials. Most of the alloys and compounds belong to the type-II. The

figure 1.3 below gives the behavior of the two types of superconductors under an applied magnetic field.
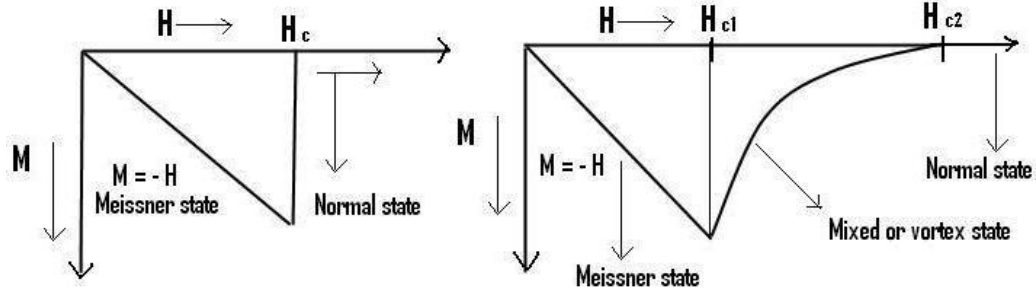
Figure 1.3 M-H phase diagram of type-I and type-II showing Meissner and mixed states.

1.5 Ginzburg-Landau theory of superconductivity

The Ginzburg-Landau theory (G-L theory), in its original form, could explain the phenomenon of superconductivity without probing the microscopic aspects of superconductors [16]. It was based on Landau's theory of second order phase transitions. According to this theory, the free energy, F of a superconductor, near its transition, can be expressed in terms of a complex order parameter field, Ψ which vanishes above the superconducting transition temperature, T_c. Accordingly the free energy is expressed as

$$F = F_n + \alpha|\Psi|^2 + \frac{\beta}{2}|\Psi|^4 + \frac{1}{2m}|(-ih\nabla - 2e\mathbf{A})\Psi|^2 + \frac{|\mathbf{B}|^2}{2\mu_0} \quad (1.10)$$

where F_n is the free energy of the normal phase, α and β were originally treated as phenomenological parameters, m is the effective mass of the carriers, **A** is the magnetic vector potential linked to the magnetic field **B**, μ_0 is the permeability of free space or vacuum.

By doing minimization of the free energy with respect to the fluctuations in the order parameter Ψ and the magnetic vector potential **A**, one can obtain the Ginzburg-Landau equations.

$$\alpha\Psi + \beta|\Psi|^2\,\Psi + \frac{1}{2m}\,(-ih\boldsymbol{\nabla} - 2e\mathbf{A})^2\Psi = 0 \qquad (1.11)$$

$$\mathbf{j} = \frac{2e}{m}\,\mathrm{Re}\{\Psi^*(-ih\boldsymbol{\nabla} - 2e\mathbf{A})\Psi\} \qquad (1.12)$$

Here, **j** represents the dissipation-free electric current density in the material.

The existence of two characteristic length scales namely, the London penetration depth λ and the coherence length ξ were predicted by the G-L theory and expressed as

$$\lambda = \sqrt{\frac{m}{4\mu_0\,e^2\Psi_0^2}} \qquad\qquad \xi = \sqrt{\frac{h^2}{2m|\alpha|}} \qquad (1.13)$$

Here Ψ_0 is the equilibrium value of density of superconducting electrons.

1.6 BCS theory of superconductivity

In 1957, J. Bardeen, L. N. Cooper and J. R. Schrieffer proposed the first microscopic theory of superconductivity [28]. The theory expresses superconductivity as a microscopic process of condensation of fermionic electrons into pairs, called cooper pairs, thereby becoming bosons. According to theory, the electronic pairing can occur at sufficiently low temperatures against the coulomb repulsion in the presence of even a weak attractive potential. In the type-I superconductors, the attraction between electrons is supposed to be mediated by lattice vibrations called phonons. This occurs when an electron moving through a crystal lattice attracts the positive ions of the crystal. The positive ions in turn would attract another electron with opposite spin. The two electrons thus become correlated indirectly and become a bound cooper pair. The collective behavior of majority of such electrons to form pairs those constitute the condensate necessary for superconductivity.

The BCS formalism is based on the reduced potential for the attraction of electrons. The behavior of electrons in a superconductor can be explained using many body theories and the BCS provides a good approximation for the many-body state of the system. The BCS theory has been one of the most successful theories of superconductivity.

Several of the predictions made by BCS theory have been observed in experiments.

The superconducting energy gap, E_g which is the energy to be supplied to break the cooper pairs is predicted to be

$$E_g = 3.53\, k_B T_c \sqrt{1 - (T/T_c)} \qquad\qquad (1.14)$$

Thus the superconducting energy gap E_g depends on the temperature and the transition temperature as given by eqn. 1.14. The energy gap in superconductors can be seen as a result of electronic correlation following the Pauli's exclusion principle in forming pairs.

The specific heat just below the transition temperature has been found to be more than that in the normal state and their ratio is found to be 2.5 in all the conventional superconductors [21]. At temperatures much below the transition temperature, the heat capacity, however, falls off exponentially.

BCS theory correctly predicts the Meissner effect, i.e., the expulsion of flux from the interior of the superconductor and the temperature variation of penetration depth λ (T). The transition temperatures of many of the superconductors can be accurately predicted by the BCS theory as given by the equation 1.15 below.

$$k_B T_c = 1.14 \, E_D \, e^{-1/N(0)V} \tag{1.15}$$

where V is the electron-phonon coupling potential, $N(0)$ is the electronic density at the Fermi energy and E_D is the Debye cutoff energy. The isotope effect, which is the observation of T_c of a given material being inversely proportional to the mass of the isotope being used in the material, is another of the successful predictions by the BCS theory.

1.7 High temperature superconductivity

The prediction of an upper limit for T_c around 30 K for superconductors by the BCS theory was proved incorrect with the discovery of superconductivity in Lanthanum based cuprate superconductor with T_c~ 35 K by J. G. Bednorz and K. A. Müller in 1986 [29]. On replacing Yttrium for Lanthanum in the original compound, the transition temperature could be pushed up to around 92 K in $Y_1Ba_2Cu_3O_{7-\delta}$, which is above the boiling point of liquid nitrogen [30]. This discovery kicked off a hectic search for materials with higher transition temperatures and with better superconducting properties, which continues till date [31]. A family of cuprate based high T_c materials has been discovered to have temperatures above 77 K up to a maximum of 138 K in mercury based [32-34] $HgBa_2Ca_2Cu_3O_{8+\delta}$.

The recent addition of iron-based oxypnictide superconductors in 2008 to the high T_c family has given a tremendous fillip to the high T_c superconductivity research [35]. The oxypnictides have T_c up to 55 K as of today.

1.8 REBCO family of superconductors

The discovery of superconductivity in YBCO in 1987 by two groups working at University of Houston and University of Alabama at Huntsville headed by C. W. Chu and Maw-Kuen Wu [30] respectively is a landmark achievement in superconductivity and materials science. This discovery triggered intense research in the area due to a very high transition temperature of around 92 K possessed by this family of materials which is above the boiling point of abundant and economical cryogen, liquid nitrogen. The search for materials with higher transition yielded a few more families of materials with higher transition temperatures based on other compounds such as BSCCO [32], TBCCO [33] and HBCCO [34] etc.,. Many of the general properties studied and predicted for YBCO are applicable to the larger family of cuprate superconductors to which all the above compounds belong to.

The earliest YBCO compounds were synthesized from metal carbonates of the respective elements whereas the later methods started employing

corresponding oxides and nitrates [36]. The replacement of Y atom with any other rare-earth elements among Gd, Sm, Nd, Eu, Dy etc yields a whole new family of compounds called (RE)BCO superconductors [37].

Much of the research activity on YBCO based superconductors today aims at fabricating superconductors suitable for applications [38]. The samples are made in bulk, thin film, tape or wire forms depending on the application aimed at. The present thesis consists of work on bulk YBCO based composite superconductors as described in later sections. The recent development of coated conductors based on YBCO materials employs coating the material on substrates using ion beam assisted deposition (iBAD) [39-41]. The substrates used in coated conductors are fabricated using a technique called Rolling Assisted Biaxially Textured Subsrates (RABiTS). The current carrying capabilities in these coated conductors have reached the industry requirements of 1 $MAcm^{-2}$ over lengths long enough for their practical applications.

Bulk YBCO superconductors, on the other hand, have not yet found full-fledged usage in commercial applications due to several inherent problems associated with bulk ceramic materials. But many of the problems have been solved over the years and some of them are being solved. For example, the sintered YBCO samples in the earlier days used to have lot of microstructural issues and even problems such as

macroscopic defects, porosity, reduced density, deformation of shape etc. The processing techniques developed over the last twenty five years have helped in addressing many of these issues positively. Now, samples with excellent microstructural properties and minimum defects [42-44], in any shape and size could be fabricated with available techniques [45-47]. We shall discuss later some of the processing techniques that have been successful in this area of research.

1.8.1 Structure of YBCO superconductor

The YBCO material belongs to the class of layered cuprates all of which have a defect perovskite structure. The geometry of the structure is orthorhombic but can be tetragonal depending on the oxygen content [48]. The structure consists of square planar CuO_2 planes with four oxygen atoms at the vertices of the square and the Cu atom at the centre. The CuO_4 ribbons are perpendicular to the CuO_2 planes sharing two vertices. The copper oxide planes can also be slightly puckered [49]. The Yttrium atoms are present between two copper oxide planes whereas the Barium atoms lie between the CuO_4 ribbons and CuO_2 planes. The term YBCO generally indicates the superconducting compound $Y_1Ba_2Cu_3O_7$ although several non-stoichiometric compounds form if there are fewer than seven oxygen atoms per unit cell. The general chemical formula corresponding to the non-stoichiometric compound is

$Y_1Ba_2Cu_3O_{7-\delta}$. The structure of YBCO is shown in figure 1.4 below. [Adapted from *http://en.wikipedia.org/wiki/Yttrium_barium_copper_oxide*]
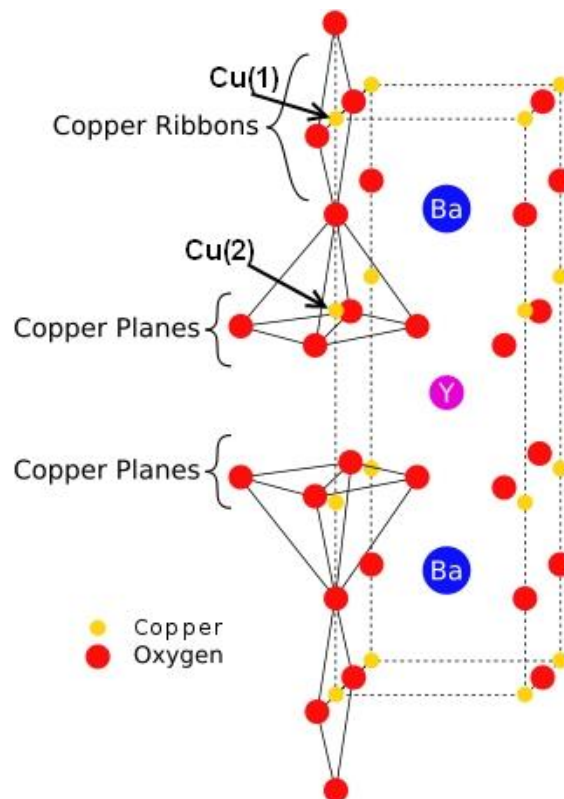
Figure 1.4 The structure of YBCO compound is shown here with the two different copper sites Cu(1) and Cu(2) identified.

The properties of the compound are very sensitive to the value of δ. When δ = 1, O(1) sites in the CuO_2 planes become vacant and the structure is tetragonal. The corresponding compound $Y_1Ba_2Cu_3O_6$ is non-superconducting and an insulator. As the oxygen content is

increased (or δ goes down in value from 1 towards zero) more and more O(1) sites are filled. The Cu-O chain formation occurs only when δ<0.65, along the b-axis of the crystal. This causes elongation of the b-axis thereby changing the structure from tetragonal to orthorhombic [50]. In orthorhombic phase, the lattice parameters are typically a = 3.82 Å, b = 3.89 Å and c = 11.68 Å. When the value of δ=0.07, there would be 6.93 oxygen atoms per unit cell and optimum properties of the compound are achieved with the T_c being the highest at 95 K. In YBCO, the conduction occurs in the CuO planes whereas the CuO chains act as charge reservoirs transferring the carriers to the planes [51-52]. This model does not however explain superconductivity in the homologue compound Pr-123 where praseodymium replaces the yttrium atom in Y-123. Because of the conduction being restricted to the CuO planes alone, the material is highly anisotropic with respect to many of the properties. For example, the normal conductivity is an order of magnitude higher along the a-b plane as compared to that along the c-axis. The anisotropy extends to even the superconducting length scale parameters such as the penetration depth and the coherence length [53]. The coherence length of the material, a parameter signifying the extent of cooper-pairing is of the order of 2 nm and 0.4 nm along the a-b plane and c-axis making the material more susceptible to small local disruptions at the interface level or defects on the order of unit cell dimensions.

1.8.2 YBCO preparation techniques
1.8.2.1 Sintering techniques

The first YBCO samples were prepared using common ceramic sintering methods [54-55]. Sintered bulk samples are typically prepared via solid state reaction by mixing the chemicals and grinding in an agate mortar or by ball milling. The powders are then sintered at appropriate temperatures before being pressed into pellets. The pressed pellets may be heat treated again and then annealed in oxygen atmosphere at lower temperatures compared to those used for heat treatments. The samples prepared by such sintering techniques typically have low density, high porosity, large macroscopic defect density, grain boundaries that are large enough to weaken the current flow across the grains [56] etc. Hence, the sintered methods needed to be improved a lot before producing samples of decent quality. The best sintered samples produced self-field currents of the order of 500 Acm^{-2} at 77 K. The low current densities offered by sintered samples did not make them suitable for any of the applications. One of the first priorities was to improve the density of the material. Melt-based growth techniques were developed to overcome many of the problems with sintering techniques [57-58].

1.8.2.2 Melt-Growth Processing techniques

Melt Growth Processing (MGP) of ceramic superconductors is one of the pioneering techniques used to grow large bulk samples of REBCO superconductors [59]. Conventional ceramic sintering techniques that were employed in the earlier days to fabricate bulk superconductor samples of YBCO were ridden with a lot of inherent problems such as disoriented grains, large grain boundaries acting as weak-links for current flow and other macroscopic defects that are inherent to the sintering techniques thus defeating the very purpose of use of these materials, that is, to carry large currents required by some of the potential practical applications that were foreseen earlier. The melt growth technique, on the other hand, allowed for a textured growth of grains along a particular axis [60]. The microstructure consisted of platelets within each grain stacked on one another with their normal parallel to the c-axis. The melt growth techniques, thus, enabled larger current densities to be carried by the material as the problem of misalignment of grains and the weak-links across grain boundaries was mostly solved [61].

 Melt Growth Processing (MGP) technique in its original form was developed by Jin et al. [62] based on a similar technique used in metallurgy for formation of metallic alloys. The technique, in its original

form, was first used to fabricate a bulk YBCO sample of size up to 1 mm x 2 mm x 30 mm. The first melt textured samples were significantly improved in their capacity to carry large currents on the order of 10^4 A/cm^2 at zero field and retained these values up to 1 T applied magnetic field. This was in sharp contrast to the low J_c values obtained by their sintered counterparts, the current at zero field for sintered samples being on the order of 500 A/cm^2 which rapidly fell to 1 A/cm^2 for fields as low as 1 T. So, their efforts to achieve a combination of densification, texturing and cleaner grain boundaries without "weak links" resulted in the melt growth technique.

The Melt textured growth of oxide material, a process thought out from an earlier "molten oxide processing" technique which had resulted in densification of YBCO wire, consists of heating the precursor material to above its melting temperature, growing and aligning the crystals from the supercooled melt. Additional heat treatments were required for homogenization, stress relief or enhancement of oxygen stoichiometry. The significant improvement in mechanical, electrical and magnetic properties of these melt textured samples triggered an increased attention towards improving and modifying the fabrication techniques resulting in the development of several other processing techniques, such as Quench Powder Melt growth [63], Melt powder melt growth

[64], Powder melting process [65], oxygen controlled melt growth processing [66], Top seeded melt growth [67], etc.

Over the years, a lot of improvements have taken place in melt growth processing of ceramic oxide superconductors. The significant feature of these materials is the microstructural aspects and our ability to tune and improve the superconducting properties from a study of these microstructural features. The ability of these materials to carry large currents in the presence of large magnetic fields lies in the appropriateness of their microstructure. It is this aspect of modifying, controlling and tuning the microstructure to get the desired mechanical, electrical and magnetic properties, that makes this class of materials an interesting one for study. The melt grown samples also have a distinct microstructure as compared to the sintered samples [68]. The microstructure of melt grown samples consists of well grown grains with parallel platelets of varying widths and platelet gaps within each grain along with a distribution of the non-superconducting secondary phase Y-211 particles in Y-123 matrix [69-70].

Before going into a discussion on melt growth process, it is worthwhile to understand the YBCO phase diagram as the texturing processes depend on the phase diagram of the material. A typical melt growth process involves heating the Y-123 phase to above its peritectic

transformation temperature, which is typically around 1010 ^0C for the YBCO system, to dissociate Y-123 into Y-211 and liquid phases. The slow cooling of this mixture results in growth of aligned grains of Y-213 [71]. The peritectic reaction of the YBCO system can be written as

$$Y_2Ba_1Cu_1O_5 + 3BaCuO_2 + 2\,CuO \rightleftharpoons 2\,Y_1Ba_2Cu_3O_{7-\delta} \qquad \textbf{(1.16)}$$
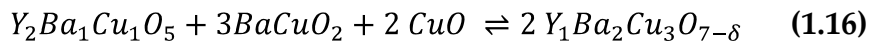
The growth of the platelets after this reaction on slow cooling depends on the rate of cooling as well. The decomposition of the secondary Y-211 phase does not occur till the system reaches to temperatures above 1250 ^0C [72], where the following secondary peritectic reaction occurs as

$$Y_2O_3 + (BaO + CuO) \rightarrow Y_2Ba_1Cu_1O_5 \qquad \textbf{(1.17)}$$
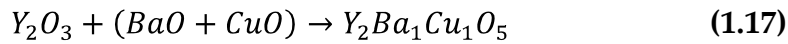
In the above reaction Y_2O_3 reacts peritectically with the liquid phases comprising BaO and CuO to yield solid $Y_2Ba_1Cu_1O_5$, which is a pro-peritectic phase for the formation of Y-123.

The pseudo-binary phase diagram of the YBCO system is given below in figure 1.5. The peritectic reactions are of great interest in metallurgy. Generally, in a peritectic system, three processes take place. The first is a reaction between pro-peritectic phase (α) and the liquid (L) at or below the peritectic transformation temperature T_P to form the peritectic phase β.
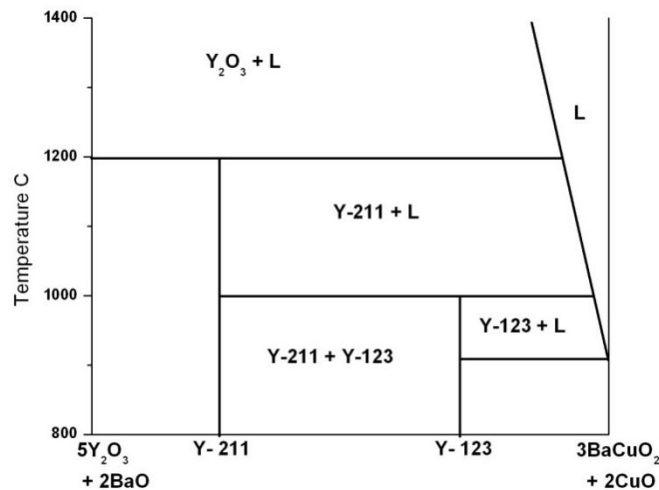
Figure 1.5 A pseudo-binary phase diagram for the Y-Ba-Cu-O system given here shows the various phases and their corresponding temperatures.

This can be represented as $\alpha + L \rightarrow \beta$. This reaction causes the formation of the phase β on the surface of the pro-peritectic phase α. The reaction continues only as long as the α-phase surface is open to the liquid. Once the α-phase surface is completely coated with β-phase and is no longer accessible to the liquid, the peritectic reaction ceases and further progress will be through diffusion of ions through the solid β-layer [73]. This diffusion reaction is called peritectic transformation. The third process is the direct crystallization of the β-phase from the supersaturated liquid. If this occurs without a matching dissolution of the pro-peritectic phase in the liquid due to large undercooling or

because the pro-peritectic phases is not any more exposed to the liquid, the process becomes a non-equilibrium one.

Texturing in melt grown samples is achieved through seeding the material suitably. The seed crystal used for this purpose should have a higher melting point compared to the material grown and the seed crystal is so chosen such that it has the same crystal structure as the material grown and it is chemically inert toward the material during the growth stage. The seed crystal helps in initiating and guiding the epitaxial nucleation to originate at the seed position thereby multiple nucleations throughout the sample are prevented. The grain misalignment problem that causes the current densities to rapidly fall at the boundaries is largely overcome using seeded melt grown techniques Among the several versions of this technique, the top seeded melt growth technique (TSMG) has been found to be very productive [74-76]. Single-grain bulk samples have been grown using this technique [77]. Multiple seeding techniques have been developed and tried by several researchers. Most of the multiple seeding techniques, however, have been found to be adverse to the superconducting properties of the material [78]. The single grain bulk samples are capable of carrying large currents and the deterioration of currents at the grain boundaries does not occur in these samples. From the applications view-point, the ability of these materials to trap large magnetic fields has been exploited to a

great extent [79-81]. In spite of the tremendous improvements in quality of the samples processed by melt growth techniques, melt grown samples have certain basic problems with respect to macroscopic defects mainly in the form of voids, pores and cracks as well as shrinkage of the sample from its original size during melt processing [82]. Also, the microstructure of the melt grown samples with respect to the secondary Y-211 phase particles contained non-uniform distribution of these particles in varied sizes and morphology. The pinning capabilities could be improved if problems such as macroscopic defect density, shrinkage and non-uniform distribution of acicular Y-211 phase particles could be avoided. Thus further improvements to the melt growth technique were required. Infiltration Growth Processing (IGP) technique has been developed to overcome many of the problems with the conventional melt growth techniques [83-96]. We discuss the Infiltration Growth Processing technique in a separate section next as the thesis studies the samples made by this technique only.

1.8.3 Infiltration Growth Processing technique for fabrication of YBCO and YBCO/Ag superconductors

Infiltration Growth processing (IGP), based on the melt growth technique, was developed to overcome the difficulties associated with the melt growth processing technique [83-85]. It has several advantages

over the rival MGP technique such as near-net shape fabrication of the end-product, better uniformity in Y-211 distribution and reduction in its size and improvement in morphology, considerable reduction in shrinkage and macroscopic defects, better control over melting etc.,. Infiltration Growth processing technique is a more suitable technique for the REBCO systems compared to any other technique because the melting of the liquid phases occurs separately in the source pellet whereas the peritectic reaction and growth occurs after infiltration in the target pellet. This is an ideal choice for such systems as one can have better control over the heat treatments and other process parameters. Figure below depicts schematically the sample processing configuration of the IGP technique.

In the conventional IGP technique, the target pellet, made of Y-211 precursor powders, is placed on top over the liquid source pellet made of either $Ba_3Cu_5O_8$ liquid phase powder or Y-123 powder which can supply the liquid phase after decomposition according to the peritectic process as shown in figure 1.6. The infiltration occurs via capillary action from the source pellet to the target pellet [83, 88, 90]. Various support layers made of Yttria, Yttria Stabilized Zirconia (YSZ) and Alumina powders are used to prevent liquid phases from overflowing during melting and the contamination of the source pellet during the processing.
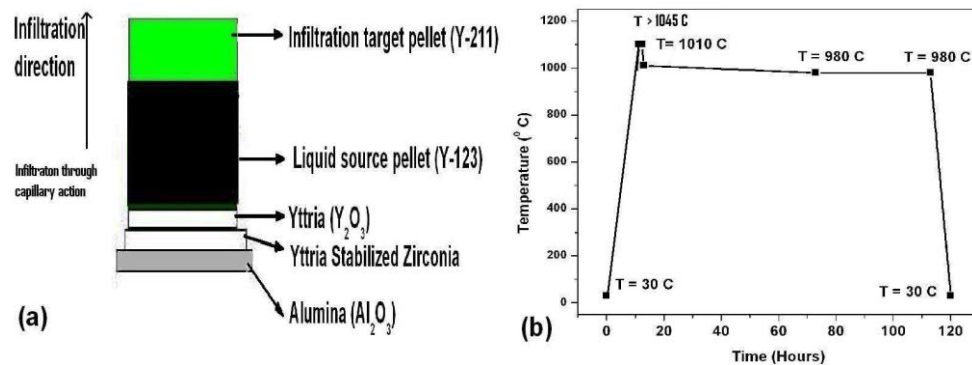
Figure 1.6 Sample processing configuration of the conventional IGP technique

The peritectic reaction for the IGP technique is the same as that given in eqn. 1.16. In IGP, the liquid phase infiltrates into the target pellet through the pores or gaps between the Y-211 particles and on slow cooling from above the peritectic transformation temperature of 1010 ^{0}C to about 980 ^{0}C at about 0.5 ^{0}C hr^{-1}, the liquid phases react with the Y-211 particles slowly to form Y-123 again. This leaves behind the unreacted or incompletely reacted Y-211 particles in Y-123 matrix in the target pellet. The Y-211 particles in samples made by IGP technique have uniformity in Y-211 distribution throughout the sample volume and have Y-211 particles of finer sizes and spherical morphology.

The processing configuration of the IGP technique has been varied by several researchers to optimize and improve this processing method. The variants to the original technique include performing the infiltration by having the source pellet on top of the Y-211 target pellet where

infiltration is achieved through gravity [96], by sandwiching the target pellet between two liquid source pellets on top and bottom [89] or on either side etc.,. It has not been clearly brought out in any of these works whether the liquid source on top or at the bottom gives better results. But, having the liquid source pellet on top or at the bottom can have significant impact on the final product since the reaction dynamics changes as the liquid phases melt. Depending on the viscosity of the liquid phase, the capillary or gravity force could give better results. But it has not been conclusively established as to which configuration is more suitable for sample processing using IGP technique. The samples studied in the thesis uses the latter configuration as discussed in chapter 3. In the next section, we discuss about a major development to the IGP technique directly adapted from the MGP technique, i.e., seeding.

1.8.3.1 Seeded Infiltration Growth Processing technique (SIGP)

Seeded Infiltration Growth Processing technique (SIGP) is IGP technique wherein additionally a single crystal or single grain seed is used to assist in grain growth and texturing or grain alignment [90-95]. This technique is a direct adaptation of the MGP based seeding technique Top-Seeded Melt Growth (TSMG). In the TSMG technique, typically an MgO crystal could be used on top of the sample before

processing. But in order to avoid contamination of the sample, the MgO single crystal seeds were replaced by Sm-123 or Nd-123 based seeds [97]. The preparation of any of the rare-earth (REBCO) based seeds is necessary as it is important to avoid seed melting during processing. The Nd-123 system has the highest melting point among the REBCO systems and hence was found more suitable for use as seeds [98]. Large grain or single grain samples could be grown using TSMG technique.

Seeded Infiltration Growth Processing technique (SIGP), on the other hand, requires the seed to be positioned appropriately for proper growth of the bulk sample. The size, orientation and position of the seed with respect to the target pellet are the important parameters that need to be taken care of before seeding. Nd-123 seeds or Sm-123 seeds have been found to be suitable to grow large or single grain YBCO samples. Typically, the seed crystals are cleaved along the ab-plane from a bulk large grain or multi-grain REBCO (here RE = Nd or Sm) samples grown on MgO substrates. The seed surface to be in contact with the sample is polished for better contact with the sample to be grown. The properties of SIGP samples vary drastically depending on, among several other parameters, the seeding parameters mentioned above. Multiple seeding has also been tried by several research groups in an effort to improve the homogeneity of the samples grown as well as to improve the current density and field-trapping capability [99]. But, the multiple-seed

techniques have not been found to be especially useful in improving the properties any further than single seeding techniques are.

1.8.3.2 Silver addition to YBCO to make YBCO/Ag composites

Silver has been added to YBCO system to make ceramic-metal YBCO/Ag composite system especially to improve the mechanical properties [100-103]. There are several advantages to prefer Ag over other elements. It is known to play a positive role in improvement of mechanical strength without drastically affecting the superconducting properties [104-105]. Several groups have worked on this problem and reported improvement in mechanical stiffness, hardness and elastic modulus of the samples with Ag addition. Silver was added initially to the sintered samples to improve the grain coupling and to seal the grain boundary gaps and to solve other defect related problems [106]. Improvements were reported on many of these issues with Ag addition [107]. Silver has been added in elemental metallic form or in several of its compound forms such as Ag_2O, $AgNO_3$ etc [108,100]. These works brought out largely the advantages of using silver to improve the mechanical strength of the material. A few of these works have also focused on the improvement or deterioration of superconducting properties with Ag addition particularly with respect to the current

carrying capabilities as the grain boundaries are reported to have been strengthened with Ag addition. This solved the weak-link problem to a large extent as inter-grain coupling seemed to have improved with Ag addition. It was reported that silver also helped in reducing the porosity and thereby improving the density of the material [100-108]. Apart from the improvement in mechanical properties, some of the earlier works focused on the role played by silver chemically by substitution into the Y-123 unit cell [50]. Intentional substitution of Ag for Cu in the YBCO unit cell was carried out in some of these works and it was reported that there is a concentration threshold, called concentration quenching [109], for Ag doping in Cu site beyond which no further doping occurs. By and large, these works reported improvement in superconducting properties such as current density with Ag addition. These works also revealed that there was a threshold value of Ag addition beyond which the superconducting properties started to deteriorate. The possibility of Ag getting substituted for any other atom other than copper was ruled out [109]. Among the two available Cu sites in the YBCO lattice, it has been reported that the Ag atom prefers to substitute for Cu(2) site in the Cu-O plane of the YBCO unit cell but when the lattice parameter 'a' varies with Ag content, it is possible that the copper atom in Cu(1) site also gets replaced by Ag [109]. Aside from the intentional doping of Ag in Cu sites, studies on silver substitution for copper in YBCO unit cell

due to physical mixing of Ag to YBCO to make composites were scarce. These studies were carried out in samples processed by either sintering techniques or through melt growth processing technique.

In samples processed via IGP technique to make YBCO/Ag composite superconductors, there aren't many reports focusing on Ag substitution in Cu sites. This is an important issue on three counts:

1) It is interesting to probe whether Ag substitutes for Cu in YBCO lattice and

2) If Ag does substitute for Cu, what is the concentration threshold value of Ag addition for which concentration quenching occurs?

3) What is the effective role of Ag if such a substitution occurs?

The crucial part of the thesis addresses these issues. We have tried to focus on this aspect of making YBCO/Ag composites through the IGP technique. The implications of such a study would include bringing to light the effective role Ag plays if it substitutes for Cu. The issues at hand also involve the effect of Ag addition on the processing conditions and parameters [110]. For example, the possibility of Ag modifying the melting temperatures and viscosity of the liquid phase $Ba_3Cu_5O_8$ with Ag addition is an important issue. Keeping the processing conditions the same, it would be interesting to probe what direct and indirect roles

silver addition plays in this system. It would also be interesting to study how the variation of Ag content in the YBCO/Ag composites affect various properties such as structural, mechanical, microstructural, magnetic and superconducting properties. Thus, the issues dealt in the work are relevant to both technological applications of these materials as well as to understanding the physics of these materials better.

1.9 Organization of the thesis into chapters

The thesis has been organized into seven chapters including the present one, chapter 1. The details of the contents of each of these seven chapters are discussed below.

Chapter 1 introduces the field of superconductivity and high T_c superconductivity giving an overall perspective of the field. The chapter gradually brings in the relevant issues in literature related to the present work and briefly discusses these issues. It gives a brief essay on important processing methods relevant to the thesis including the one used in the thesis work, the IGP method. It then discusses various problems related to the YBCO/Ag composite system studied in the thesis. It also briefly touches upon the problems at hand and the expected solutions to the problems.

Chapter 2 discusses various experimental techniques used to characterize and study the properties of the samples used in this work. The techniques include temperature variation of ac susceptibility, x-ray diffraction, levitation and suspension force measurement, nano-indentation, field-emission microscopy and magnetization loops as a function of field at different temperatures. The chapter addresses the relevance of these techniques to the present work and discusses briefly each of these techniques.

Chapter 3 deals with the preparation of YBCO/Ag composites superconductors through IGP technique. It studies the effect of addition of metallic silver on the structural, mechanical, microstructural, magnetic and superconducting properties of the system. The chapter discusses the various results and the possibility of Ag substitution on Cu sites in the YBCO lattice through some of these results. The possible direct and indirect roles played by silver on the system are discussed. The concentration quenching of Ag and the optimum value of Ag addition for obtaining samples of better quality are discussed. Finally, the effect of compaction pressure combined with Ag addition is discussed.

Chapter 4 The bulk applications of YBCO/Ag superconductors include their use in maglev based systems, as trapped field magnets, in motors

and generators, as frictionless bearings in flywheel based devices etc. One of the important properties in this context is the levitation and forces of the bulk samples. This chapter presents the results of studies on levitation and suspension forces of the YBCO/Ag samples and discusses the optimum amount of Ag addition with respect to best values of these forces. Also, the variation of these forces with sample size and geometry is an important factor for practical design and applications of these samples. Hence, we present our studies on the dependence of levitation force on sample size and geometry. Finally, relaxation studies on levitation forces in this system is interesting from both applications view-point as well as to better understanding the magnetic behavior through such measurements as this is one-of-a-kind of measurement that brings an aspect of magnetic relaxation in these materials as well. We present our results and observation of a near-oscillatory relaxation behavior of levitation force. We also briefly discuss the bistable equilibrium model proposed by us for the current structure in the material [111]. As supporting evidence to our model, we present results on our observation, for the first time, of counter-magnetization of the $SmCo_5$ permanent magnet in the presence of the bulk YBCO/Ag superconductor.

Chapter 5 describes a novel processing technique developed in the present work, called Rapid Infiltration Growth Processing (RIGP)

technique to fabricate bulk YBCO and YBCO/Ag composite superconductors in shorter time durations compared to conventional IGP technique. The characterization and physical properties of the samples prepared by this technique are discussed and compared with those of the samples made by conventional IGP technique.

Chapter 6 focuses results on the magnetization measurements at low temperatures up to 20 K and strong applied fields up to 9 T on the YBCO and YBCO/Ag samples prepared by both IGP and RIGP. It presents results on the current density and pinning force behavior of these samples. The chapter discusses the behavior of self-field critical current density as a function of temperature and the generalization of the property for various samples. Then, the effect of magnetic field on the critical current density as a function of temperature is brought out through generalized equations. The equations governing the critical current density and pinning force density behavior as a function of temperature both in the presence as well as absence of magnetic field in YBCO and YBCO/Ag samples are obtained and the various parameters and the possible physical meaning of these parameters are discussed.

Chapter 7 summarizes the work done in the thesis and draws relevant conclusions from the results obtained through this work. It discusses various issues in the interpretations of the results and the way

conclusions have been arrived at. The chapter ends with a brief essay on the importance of the present work and the possibility of future scope of the work.

References

[1] H. K. Onnes, *Commun. Phys. Lab. Univ. Leiden* **119b**, (1911).

[2] H. K. Onnes, *Commun. Phys. Lab. Univ. Leiden* **120b**, (1911).

[3] H. K. Onnes, *Commun. Phys. Lab. Univ. Leiden* **123a**, (1911).

[4] C. V. Linde, *Patent No. CH10704, Machine for the liquefaction of gas (in German)*, (1896).

[5] C. V. Linde, *Patent No. CH189512528, Process and Apparatus for Liquefying Gases or Gaseous Mixtures, and for Producing Cold, more particularly applicable for Separating Oxygen from Atmospheric Air –* UK (1896).

[6] C. V. Linde, *Patent No. US727 ,650, Linde Oxygen Process -*USA, (1903).

[7] R. P. Pictet, *Oxygen Liquefaction-Telegraphic communication* (1877).

[8] L. P. Cailletet, Science **6** (128), (1885).

[9] Z. F. Wróblewski, *Acad. Sci. Paris, Comptes rendus*, **94**, pp. 212–213 (1882).

[10] G. D. Living and J. Dewar, *Collected papers on spectroscopy*, CUP (1915).

[11] K. H. Onnes, *Haarlem Arch. Neerl.* **30**, (1896).

[12] K. H. Onnes, *Research Notebooks* **56, 57**, K. H. Onnes Archive, Boerhaave Museum, Leiden, the Netherlands.

[13] H. K. Onnes, *Investigations into the properties of substances at low temperatures, which have led, amongst other things, to the preparation of liquid helium,* Nobel Lecture (1913)*.*

[14] W. Meissner and R. Ochsenfeld, *Naturwiss.* **21**, 787 (1933).

[15] A. A. Abrikosov, *Soviet Physics JETP* **5**, 1174 (1957).

[16] V. L. Ginzburg and L. D. Landau, *Zh. Eksp. Teor. Fiz.* **20**, 1064 (1950).

[17] L. W. Shubnikov, W. I. Khotke-vich, J. D. Shepelev, and J. N. Riabinin, *Zh. Eksper. Teor. Fiz.* (USSR), **7**, 221 (1937).

[18] A. A. Abrikosov, *Type-II superconductors and the vortex lattice,* Nobel Lecture (2003).

[19] C. Kittel, *Introduction to Solid State Physics - 7th Ed.,* John-Wiley & Sons, Singapore (1995).

[20] F. London and H. London, *Proc. Roy. Soc. (London)* **A149**, 71 (1935).

[21] M. Tinkham, *Introduction to Superconductivity - 2nd Ed.,* Dover Publications Inc., US (1996).

[22] C. J. Gorter, *Physica* **2**, 449 (1935).

[23] H. London, *Proc. Roy. Soc.* (London) **A152,** 650 (1935).

[24] A. B. Pippard, *Proc. Roy. Soc.* (London) **A216**, 547 (1958).

[25] K. Mendelssohn, *Rev. Mod. Phys.* **36**, 50–51 (1964).

[26] L. D. Landau, *Phys. Z. der Sowjet Union*, **11**, 26 (1937).

[27] A. A. Abrikosov, *Doklady Akademii Nauk SSSR* **86**, 489 (1952).

[28] J. Bardeen, L. N. Cooper and J. R. Schrieffer, *Phys. Rev.* **108**, 1175 (1957).

[29] J. G. Bednorz, and K. A. Mueller, *Zeitschrift für Physik B* **64** (2), 189–193 (1986).

[30] M. K. Wu, J. R. Ashburn, C. J. Torng, P. H. Hor, R. L. Meng, L. Gao, Z. J. Huang, Y. Q. Wang, and C. W. Chu, *Phys. Rev. Lett.* **58**, 908-910 (1987).

[31] J. Timmer, *Arstechnica*, http://arstechnica.com/science/2011/04 (2011).

[32] H. Maeda, Y. Tanaka, M. Fukutumi, and T. Asano, *Jap. J. App. Phys.* **27**, L209–L210 (1988).

[33] Z. Z. Sheng, and A. M. Hermann, *Nature* **332**, (6160), 138–139 (1988).

[34] C. W. Chu, L. Gao, F. Chen, Z. J. Huagn, R. L. Meng, and Y. Y. Xue, *Nature* **365** (6444), 323 (1993).

[35] Y. Kamihara, T. Watanabe, M. Hirano, and H. Hosono, J. *Am. Chem. Soc.* **130** (11), 3296–3297 (2008).

[36] N. N. Greenwood, and A. Earnshaw, *Chemistry of the Elements -2nd Ed.*, Butterworth–Heinemann (1997).

[37] X. Yao and Y. Shiohara, *Supercond. Sci. Technol.* **10,** 249 (1997).

[38] F. N. Werfel, U. Floegel-Delor, R. Rothfeld, T. Riedel, B. Goebel, D. Wippich and P. Schirrmeister, *Supercond. Sci. Technol.* **25**, 014007 (2012).

[39] L. Fernández, B. Holzapfel, F. Schindler, B. de Boer, A. Attenberger, J. Hänisch, and L. Schultz, *Phys. Rev. B* **67**, 052503 (2003).

[40] J. Eickemeyer, R. Hühne, A. Güth, C. Rodig, H. Klauß, and B. Holzapfel, *Supercond. Sci. Technol.* **21,** 105012 (2008).

[41] K. Knoth, R. Hühne, S. Oswald, L. Schultz, and B. Holzapfel, *Supercond. Sci. Technol.* **18,** 334-339 (2005).

[42] M. Murakami, M. Morita, K. Doi and K. Miyamoto, *Jpn. J. Appl. Phys*. **28**, 1189-1194 (1989).

[43] Z. Lian, Z. Pingxiang, J. Ping, W. Keguang, W. Jingrong and W. Xiaozu, *Supercond. Sci. Technol.* **3**, 490 (1990).

[44] H.T. Ren, L. Xiao, Y.L. Jiao, and M.H. Zheng, *Physica C: Superconductivity*, **412-414**, 597-601 (2004).

[45] V. Ganesan, R. Srinivasan, S. Aswathy, K. D. Chandrasekaran, B. Srinivas, U. V. Varada Raju, G. V. Subba Rao, R. Gopalan, T. Rajasekaran, *Bull. Mater. Sci.* **7** (1), 87-93 (1994).

[46] K. Matsunaga, M. Tomita, N. Yamachi, K. Iida, J. Yoshioka and M. Murakami, *Supercond. Sci. Technol.* **15**, 842 (2002).

[47] E. S. Reddy, N. H. Babu, Y. Shi, D. A. Cardwell and G. J. Schmitz, *Supercond. Sci. Technol.* **16**, L40 (2003).

[48] P. Benzi, E. Bottizzo, and N. Rizzi, *J. Cryst. Growth* **269**, 635-629 (2004).

[49] G. Alecu, *Rom. Rep. in Phys.* **56** (3), 404-412 (2004).

[50] C. H. Kao, Y. S. Shiue, S. R. Sheen, and M. K. Wu, *Physica C* **205**, 186-190 (1993).

[51] J. T. Kucera and J. C. Bravman, *Phys. Rev. B* **51**, 8582–8590 (1995).

[52] R. Hayn, V. Yu. Yushankhai, *Phys. Stat. solidi (b)* **166** (2), 415-422 (1991).

[53] J. M. Tipper, *M Sc Thesis dissertation*, Univ. of Lethbridge, Canada (2007).

[54] F. Celani, A. Saggese, V. Calzona, M. Putti, L. Liberatori, S. Pace, B. Polichetti, and R. Scafuro, *Physica C* **162–164 (**2), 903–904 (1989).

[55] Y. Yamada, T. Donishi, T. Kuwahara, and S. Kubo, *J. of Phys.: Conf. Series* **43**, 425-428 (2006).

[56] S. E. Babcock and J. L. Vargas, *Annu. Rev. Mater. Sci.* **25,** 193-222 (1995).

[57] In-Gann Chen, G. Jamn, Jen-Chou Hsu, and M. K. Wu, *J. Appl. Phys.* **81**, 4947 (1997).

[58] K. Salama, V. Selvamanickam, L. Gao, and K. Sun, *Appl. Phys. Lett.* **54**, 2352 (1989).

[59] S. Jin and J. E. Graebner, *Mater. Sci. Engg. B* **7** (4), 243–260 (1991).

[60] P. Diko, *Supercond. Sci. Technol.* **13**, 1202 (2000).

[61] S. Jin, T. H. Tiefel, R. C. Sherwood, M. E. Davis, R. B. van Dover, G. W. Kammlott, R. A. Fastnacht, and H. D. Keith, *Appl. Phys. Lett.* **52**, 2074 (1988).

[62] S. Jin, T. H. Tiefel, R. C. Sherwood, R. B. van Dover, M. E. Davis, G. W. Kammlott, and R. A. Fastnacht, *Phys. Rev. B* **37**, 7850–7853 (1988).

[63] M. Morita, S. Takebayashi, M. Tanaka, K. Kimura, K. Miyamoto, K. Sawano, *Advances in Superconductivity III (ISS '90)*, 733-736 (1991).

[64] M. Murakami, T. Oyama, H. Fujimoto, S. Gotoh, K. Yamaguchi, *IEEE Trans. Magnetics*, **27** (2) 1479 (1991).

[65] Z. Lian, Z. Pingxiang, J. Ping, W. Keguang, W. Jingrong, and W. Xiaozu, *Supercond. Sci. Technol.* **3**, 490 (1990).

[66] T. Goto, T. Miura, and T. Hayashi, *Jpn. J. Appl. Phys.* **36**, L909-L911 (1997).

[67] Y. Yamada and Y. Shiohara, *Physica C* **217** (1–2), 182-188 (1993).

[68] K. Kakimoto and Y. Shiohara, *Appl. Supercond.* **4** (10-11), 519-533 (1996).

[69] T. Rajasekharan, R. Gopalan, T. Roy, C. Rangarajan, N. Hari Babu, *Physica C: Superconductivity*, **244**, 106-114 (1995).

[70] M. Murakami, N. Sakai, T. Higuchi, and S. I. Yoo, *Supercond. Sci. Technol.* **9**, 1015–1032 (1996).

[71] C. Leblond, I. Monot, J. Provost, and G. Desgardin, *Physica C: Superconductivity*, **311**, 211-222 (1999)

[72] E. S. Reddy, *Mater. Lett.* **56** , 161 – 166 (2002).

[73] E. S. Reddy, *PhD Thesis*, Univ. of Hyderabad (1997).

[74] V. Belruss, J. Kalnajs, and A. Linz, *Mater. Res. Bull.* **6** (10), 899-905 (1971).

[75] K. Polgár, Á. Péter, L. Kovács, G. Corradi, and Zs. Szaller, *J. Cryst. Growth* **177** (3-4), 211-216 (1997).

[76] Y. A. Jee, C.-J. Kim, T.-H. Sung, and G.-W. Hong, *Supercond. Sci. Technol.* **13**, 195 (2000).

[77] D. A. Cardwell, Y.-H. Shi, N. H. Babu, S. K. Pathak, A. R. Dennis, and K. Iida, *Supercond. Sci. Technol.* **23**, 034008 (2010).

[78] P Schätzle, G Krabbes, G Stöver, G Fuchs and D Schläfer, *Supercond. Sci. Technol.* 12 69 (1999).

[79] Y. Ren, R. Weinstein, J. Liu, R. P. Sawh, and C. Foster, *Physica C: Superconductivity* **251** (1-2), 15-26 (1995).

[80] K. Nagashima, T. Higuchi, J. Sok, S. I. Yoo, H. Fujimoto, and M. Murakami, *Cryogenics* **37** (10), 577-581 (1997).

[81] S. Bræck, D. V. Shantsev, T. H. Johansen, and Y. M. Galperin, *J. Appl. Phys.* **92** (10) 6235 (2002).

[82] M. Murakami, *Melt Processed High-Temperature Superconductors*, World Scientific, Singapore (1992).

[83] I. K. Jeong, D. Y. Kim, Y. K. Park, K. W. Lee, and J. C. Park, *Physica C* **185-189**, 2393-2394 (1991).

[84] E. S. Reddy and T. Rajasekharan, *J. Mater. Res.* **13** (9), 2472 (1998).

[85] E. S. Reddy and T. Rajasekharan, *Supercond. Sci. Technol*. **11**, 523 (1998).

[86] H. Fang, K. Ravi-Chandar, *Physica C* **340**, 261-268 (2000).

[87] K. Iida, N. H. Babu, Y. Shi, and D. A. Cardwell, *Supercond. Sci. Technol*. **18, 1**421–1427 (2005).

[88] N. H. Babu and T. Rajasekharan, *J. Am. Ceram. Soc*. **82** (11) 2978–84 (1999).

[89] H. Fang, Y. X. Zhou, K. Ravi-Chandar and K. Salama, *Supercond. Sci. Technol.* **17**, 269-273 (2004).

[90] N. H. Babu, Y.-H. Shi, A. R. Dennis, S. K. Pathak, and D. A. Cardwell, *IEEE Trans. on Appl. Supercond*. **21** (3), 2698 (2011).

[91] K. Iida, N. H. Babu, Y. Shi, and D. A. Cardwell, *Supercond. Sci. Technol*. **18**, 1421–1427 (2005).

[92] N. V. N. Viswanath, T. Rajasekharan, N. H. Kumar, L. Menon and S. K. Malik, *Supercond. Sci. Technol*. **11**, 420–425 (1998).

[93] H. Cao, X. Chaud, J. G. Noudem, C. Zhang, R. Hu, J. Li, and L. Zhou, *Cerm. Inter*. **36**, 1383–1388 (2010).

[94] S.-Y. Chen, Y.-S. Hsiao, C.-L. Chen, D.-C. Yan, I.-G. Chen, and M.-K. Wu, *Mater. Sci. Engg*. B **151,** 31–35 (2008).

[95] S. Umakoshi, Y. Ikeda, A. Wongsatanawarid, C.-J. Kim, and M. Murakami, *Physica C* **471**, 843–845 (2011).

[96] N. D. Kumar, T. Rajasekharan, and V. Seshubai, *Supercond. Sci. Technol.* **24** 085005 (2011).

[97] S. Meslin, K. Iida,N. H. Babu, D. A. Cardwell, and J. G. Noudem, *Supercond. Sci. Technol.* **19,** 711–718 (2006).

[98] N. H. Babu, K. Iida, Y. Shi, and D. A. Cardwell, *Appl. Phys. Lett*. **87**, 202506 (2005).

[99] M. Sawamura, M. Morita, and H. Hirano, *Physica C* **378–381**, 617–621 (2002).

[100] J. Joo, J.-G. Kim, and W. Nah, *Supercond. Sci. Technol.* **11**, 645 (1998).

[101] A. Leenders, M. Ullrich and H. C. Freyhardt, *IEEE Trans. on Appl. Supercond.* **9** (2), 2074 (1999).

[102] P. Schatzle, G. Krabbes, S . GruB, and G. Fuchs, *IEEE Trans. on Appl. Supercond.* **9** (2), 2022 (1999).

[103] T. Nishio, Y. Itoh, F. Ogasawara, M. Suganuma, Y. Yamada, and U. Mizutani, *J. Mater. Sci*. **24**, 3228-3234 (1989).

[104] G. Plesch, I. Van Driessche, A. Cigaň, J. Maňka, S. Hoste, J. Kliment, *Meas. Rev. Sci*. **1** (1), 33 (2001).

[105] K. Iida, N. H. Babu, Y. Shi, T. Miyazaki, N. Sakai, M. Murakami, D. A. Cardwell, *J. Phys.: Conf.* **97** (1), 012105 (2008).

[106] A. Matsumuro, K. Kasumi, U. Mizutani, and M. Senoo, *J. Mater. Sci*. **26** (3), 737-742 (1991).

[107] E. Mendoza, T. Puig, E. Varesi, A.E. Carrillo, J. Plain, and X. Obradors, *Physica C* **334**, 7–14 (2000).

[108] P. Diko, V. Antal, M. Kaňuchová, M. Jirsa, and K. Jurek, *Physica C* **470,** 155–158 (2010).

[109] Ch. Zhang, A. Kulpa, and A. C. D. Chaklader, *Physica C* **252**, 67-78 (1995).

[110] U. Wiesner, G. Krabbes, M. Ueltzen, C. Magerkurth, J. Plewa, and H. Altenburg, *Physica C* **294**, 17–22 (1998).

[111] R. Parthasarathy, M. M. Lakshmi, and V. Seshubai, *Physica C* **471** (13-14), 395-399 (2011).

CHAPTER 2

EXPERIMENTAL TECHNIQUES

2.1 Introduction

In this chapter, we discuss the various experimental techniques used in the thesis in detail. We shall introduce each of the techniques, its importance in the present work, the theory and principle of the said technique and the instruments used to carry out the experiment. There are several techniques available to characterize bulk samples of oxide superconductors in order to extract information on the physical properties of these materials. Some of these techniques give direct information on these properties, i.e., a direct measurement for a physical quantity. Other techniques might involve obtaining the desired properties as derivatives or through analysis from a measured property. In the following few lines we list out the sequence of sample preparation steps and the characterization techniques used in the present work.

1) Sample preparation by Infiltration Growth Processing technique [1-3] and Rapid Infiltration Growth Processing technique including preparation of precursor powders by citrate chemical synthesis route, sintering the precursor powders, compaction of the powders into pellets, heat treatment of the samples and oxygenation of the samples.

2) Specimen preparation for various measurements involving precisely cutting the samples using a diamond precision saw and polishing the specimen for microstructure studies under the electron microscope.

3) Studies on levitation and suspension force of the samples using a homemade force measuring setup

4) Studying the structural changes with variation in Ag content using x-ray diffraction

5) Studying the variations in mechanical properties with varying Ag content

6) Studying the temperature dependence of ac susceptibility using a homemade ac susceptometer setup

6) Studying the microstructures of the samples using a Field-Emission Scanning Electron Microscope

7) Studying the magnetization behavior of the samples using a Physical Property Measurement System (QD-PPMS) based on the vibrating sample magnetometer (VSM).

Now, elaborate details about each of the above seven points is given below.

2.2 Sample preparation procedure

2.2.1 Preparation of Precursor powders by Citrate chemical synthesis route

The first step in the sample preparation procedure involves making the requisite precursor powders. The precursor powders in the present work are mainly Y-123 and Y-211 powders. Metal oxides of yttrium, copper namely Y_2O_3 and CuO and carbonate of barium ($BaCO_3$) are dissolved in appropriate amounts of conc. HNO_3 acid solution while stirring continuously. To the nitrate mixture, chelating agents citric acid and ethylene glycol are added. The pH of the solution is adjusted to 8 using ammonia solution [4-5].

Figure 2.1 A combined picture of preparation of precursor powders during combustion stage

After sufficient stirring and cooling, the gel-like solution is kept for combustion on a hot plate at 250 C for 3 hours. The figure 2.1 shows a combined picture of the sample preparation during combustion process. The solution mounted on the hot plate is heated to ignite the combustion reaction and the combustion reaction produces the end product in a honeycomb-like structure. The powders thus prepared are collected, mixed and ground well in an agate mortar before being transferred into alumina crucibles for sintering.

Figure 2.2 The picture shows the furnace used for heat treatment of the samples

The as-made powders of Y-123 and Y-211 are sintered at 900 ^{0}Cand 950 ^{0}C for 24 and 12 hours respectively. Figure 2.2 shows the furnace used

for sintering of the powders and heat treatment of the bulk samples. The sintered powders were thoroughly mixed and ground well in an agate mortar. The sintered powders were pelletized using a hydraulic press to obtain bulk samples. The hydraulic press used in the work for pelletizing the powders and the sample pellets made are shown in figure 2.3 below.
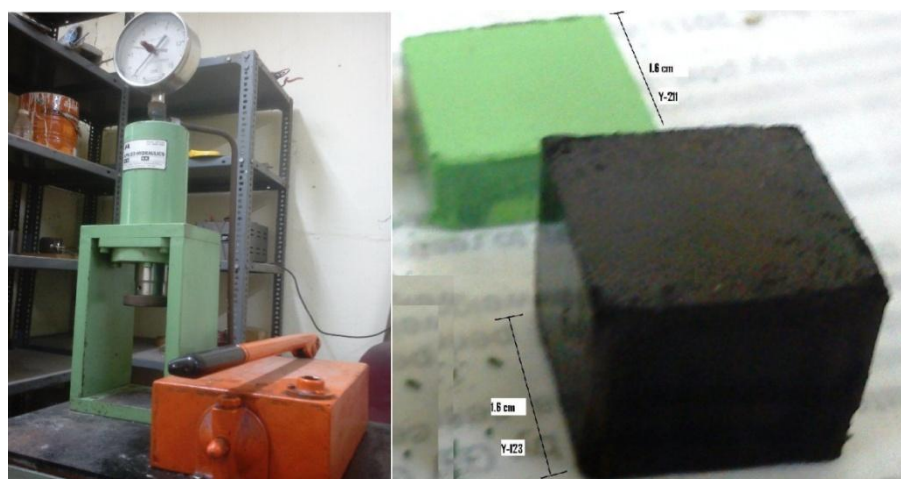
Figure 2.3 Hydraulic press used in the present work and the sample pellets made are shown

2.2.2 Infiltration Growth Processing of the YBCO and YBCO/Ag samples

The samples made with two different compaction pressures, both YBCO and YBCO/Ag composites with varying Ag content have been studied in the present work. The heat treatment schedules and other processing

conditions will be discussed at the appropriate places in the thesis with specific details. Figure 2.4 shows the schematic diagram of the furnace used for the heat treatment of samples by IG processing technique.
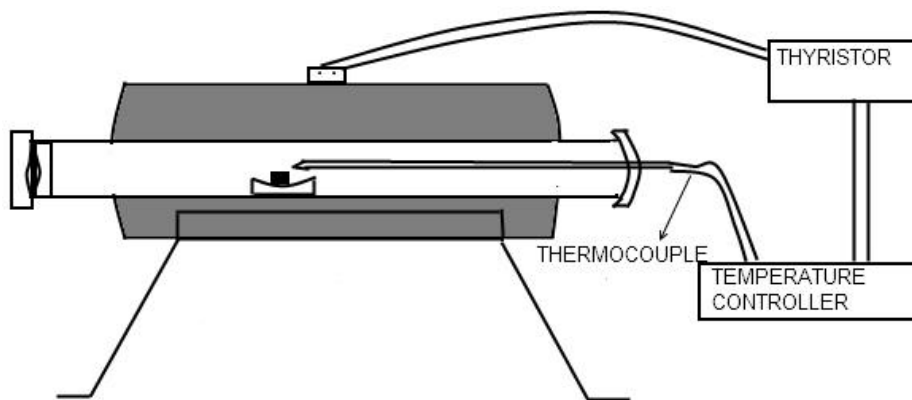
Figure 2.4 Schematic diagram of the furnace used for the heat treatment of the samples

The sample mounting configuration details are discussed in the relevant sections in corresponding chapters. The samples on supporting pellets were placed in an alumina crucible filled with alumina powder for uniform heat conduction. The crucible containing the samples was placed at the center of hot zone of the muffle furnace. The temperature of the furnace was controlled by temperature controller (*Eurotherm make - model 2404*) and thyristors (*model TE10A*). After heat treatment as per the schedule, the samples are oxygenated in a specially designed

furnace for 120 hours at 460 ^{0}C [6]. The picture of the specially designed furnace for oxygenation of the samples is shown in figure 2.5 below.

Figure 2.5 Picture of the specially designed oxygenation furnace for oxygenation of the samples

2.2.3 Specimen preparation for various measurements

Specimens were cut from the bulk samples for various measurements as per the requirements using a diamond precision saw (*Buehler make*). For microstructural studies using FESEM, the cut samples were mounted on bakelite mounts specially made for the purpose using hot-pressing technique. Figure 2.6 below shows the diamond saw and the polishing machine used in the present work.

Figure 2.6 Diamond saw used for cutting specimens from bulk samples and the polishing machine used for polishing the specimens along with the specimens mounted on Bakelite mounts for microstructural studies are shown

The specimens for various measurements are cut as per the required dimensions from the bulk samples. The bulk samples, after processing, retain their shapes to near-net shape and do not suffer from shrinkage to any considerable levels [7]. The sample (target pellet in IGP) is separated form the source pellet after processing before oxygenation using the diamond saw. The processed samples have an area of 1.6 cm x 1.6 cm and a thickness of 8-9 mm. The specimens for temperature dependence of ac susceptibility [8] and magnetization measurements using PPMS are precisely cut using the diamond saw into parallelepipeds of length 4-5 mm along the c-axis of the sample and area 1.5 to 2 mm by 1.5 mm to 2 mm along the *ab*-plane, from the edges of the bulk samples. A thin

slice of 1.5 to 2 mm thickness and area of nearly 1.6 x 1.6 cm^2 is cut for microstructural characterization, select pieces from which are hot-pressed into Bakelite mounts. The samples on Bakelite mounts are polished first on emery papers of grades 600, 800, 1000 and 1200. Subsequent fine-polishing is done using diamond-particle based pastes of grades 2 μm, 1 μm, 0.5 μm and finally down to 0.25 μm on polishing cloths with kerosene as the lubricating medium. The polishing time for each of the stages ranges from 0.5 hour to 1 hour for the lower grade sizes. The well-polished samples were used for both microstructural as well as nanoindentation studies as described in corresponding sections later in this chapter.

2.3 Structural variations in YBCO/Ag composites with variation in Ag content using x-ray diffraction

X-ray diffraction technique has been used to study the variation of structural parameters with varying Ag content in our samples. This is an important tool to establish the role of silver in YBCO/Ag composites as to find out whether the physical mixing of Ag to the system does not affect the YBCO unit cell parameters [9]. X-ray is a technique which would tell us whether Ag gets into the Y-123 unit cell in Cu sites as Ag substitution to any other sites are highly unlikely [10]. Thus, any systematic variation to the lattice parameters of the samples with

varying Ag content would indicate a substitution of Ag for Cu sites in Y-123 lattice. A Bruker make D90 Advance model of x-ray diffraction system has been used in the present work to study the structural variations. The system used in the present work is shown in figure 2.7 below.
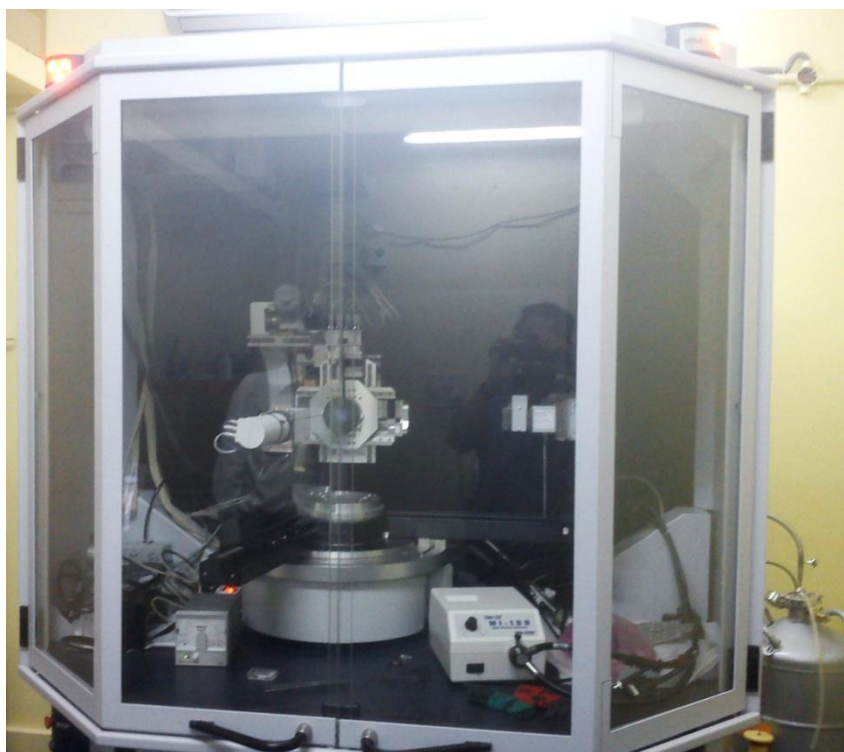
Figure 2.7   The x-ray diffraction system used in the present work (*Bruker make - model D90 Advance*)

Specimens from randomly chosen regions of the bulk sample were powdered and these powders were used to get the x-ray diffraction pattern. The angle range for diffraction was kept between 0 and 90 degrees.

2.3.1 Principle of x-ray diffraction

X-rays generated from the source are monochromatized and made incident on the specimen. The wavelength of the x-rays is typically in the range of 1-2 Å. In the present case, the copper K_α radiation emanating from a cooper target is focused onto the sample specimen in powder form. The powder contains crystallites of different sizes and orientations. The layers of atoms in the crystallites act as diffraction gratings and reflection occurs only from those planes that satisfy the Bragg's condition [11] for diffraction at a particular angle namely

$$2\ dsin\theta = n\lambda \qquad\qquad (2.1)$$

Here λ = 1.5414 Å is the wavelength of the copper K_α radiation, θ is the angle of diffraction i.e., the angle between the incident x-ray beam and the normal to the family of parallel planes causing diffraction, n is the order of diffraction and d is the inter-planar spacing for a particular family of planes that causes the reflection by satisfying the Bragg condition. Thus the angle θ can be expressed as

$$\theta = 2\,sin^{-1}(\frac{\lambda}{d_{hkl}}) \qquad\qquad (2.2)$$

Here d_{hkl} is the inter-planar spacing for a particular family of parallel planes with Miller indices (hkl) [11]. For a given source of x-ray wavelength, the diffraction pattern is unique for a given material. From the x-ray diffraction pattern, using the 2θ angle values, the hkl values are identified for each of the diffraction peak. In the present work, powderx software has been used for analysis. The unit cell parameters a, b and c of the orthorhombic structure and the cell volume are calculated from the known data. Thus, the structural variations could be studied using the x-ray diffraction technique.

2.4 Study of Mechanical properties using nanoindentation

The study of mechanical properties of YBCO/Ag composites with varying silver content was motivated by an intention to verify whether Ag added to the system really improved the mechanical properties since Ag undergoes concentration quenching [10] beyond a certain limit and starts to agglomerate as precipitates in the matrix. The concentration quenching of silver beyond its threshold value of addition to the Y-123 matrix could cause either saturation in the mechanical properties or an increase in the strength of the materials for a corresponding increase in the Ag content. Nanoindentation mechanical studies probe the system at

the sub-micro level thereby bringing out the relevant mechanical properties such as nanohardness [12] etc. The properties studied include stiffness, hardness, elastic modulus and Young's modulus. A nano-indenter (*Hysitron make –Tribodent model*) has been used for the purpose. Figure 2.8 below shows the picture of the instrument used in the present work.

Figure 2.8 The mechanical properties of YBCO/Ag composites were studied using the nano-indenter (*Hysitron make-Triboindent model*) shown in the picture

The nanoindenter consists of a diamond tip called Berkovich tip used for making indents on the samples. Generally, well polished surfaces are chosen. The surface roughness can cause inhomogeneities in the data being recorded. Typically, two different modes of operation for the present system are possible. The first mode involves applying a constant

load and recording the corresponding depth of penetration of the indenter from the sample surface to its inside and then unloading once the peak load value is reached. A Load-depth curve results from which all the requisite mechanical properties can be calculated using the Oliver-Pharr approach [13-14]. The second approach involves sustaining the load for a prolonged time before unloading. The first mode of approach was used in the present work. The samples can be mounted onto the movable x-y platform and the region of choice can be selected using an optical microscope attached to the indenter system. The entire grid area is chosen and required number of indents can be selected within the grid area for indentation. Typical area of such a grid is 0.5 mm x 0.5 mm. The number of indents to be made in each such grid area can be specified. Several such grid areas can be selected and the mechanical properties calculated from each of the indentation point can be averaged to obtain the average properties for the entire sample. A schematic diagram of the nanoindenter showing its various components involved in its working is given in figure 2.9. A test run is conducted before the actual indentation measurements are done wherein the indenter approaches the sample surface and touches it without actually making any indent. Requisite information about the surface is collected and then actual measurements are made based on it. A linear motor drives the indenter tip towards and away from the sample surface.
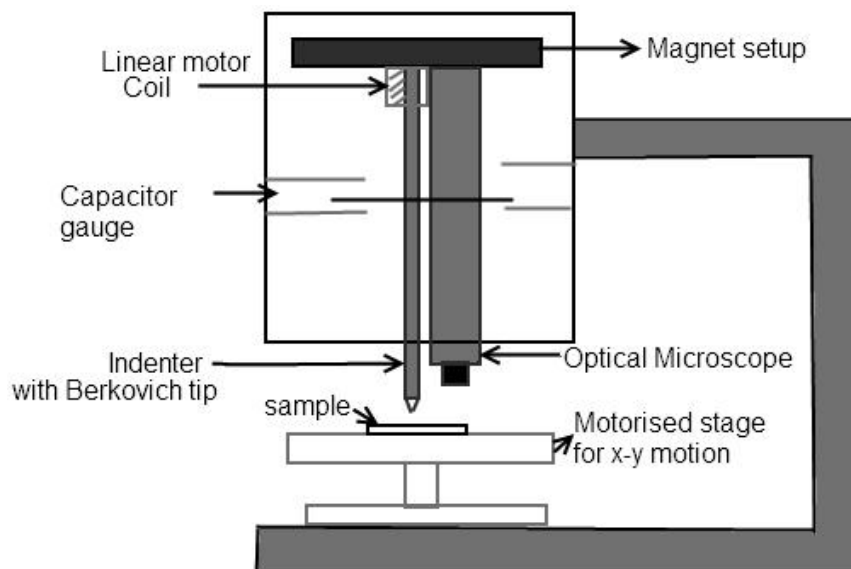
Figure 2.9 A schematic diagram of the nanoindenter showing its various components

The sample position can be adjusted with respect to the optical microscope or the indenter using the x-y motorized stage motion. The approach to calculating the mechanical properties depends on several parameters including the geometry of the tip. The entire sequence of indentation can be programmed using a computer. The resolution of the nanoindenter for measuring the depth in nanometers and force in micronewtons is what makes it an important tool to study the bulk mechanical properties of materials.

2.5 Study of microstructure using Field Emission- Scanning Electron Microscopy (FESEM)

The imaging of microstructures in a scanning electron microscope is done using the information collected by electrons that are used to raster scan the surface of a sample. The interaction of electrons with atoms present in the sample result in collection of information about the surface topography of the sample and composition of various elements present in it. A scanning electron microscope can produce several types of images depending on the kind of signals used to collect information which include secondary electrons, back-scattered electrons, characteristic x-rays, light, conduction and transmission electrons [15]. The images in the thesis were recorded using signals from reflected light (In-lens mode) and the secondary electrons imaging mode. The EDAX setup (Oxford instruments make) with the FESEM uses characteristic x-ray signals. Figure 2.10 below shows the picture of the FESEM (*Zeiss make –model Ultra55*) used in the present work. The SEM operating in the secondary electron (SEI) imaging mode produces images of the sample surface topography. The narrow size of the electron beam used for scanning results in a large depth of field thereby producing images that have a three dimensional appearance revealing the surface structure of the samples. The electrons reflected after undergoing elastic scattering

from the sample are utilized to construct back-scattered electron (BSE) images. The signal due to the back-scattered electrons can also provide information about the elements present in the sample as its intensity depends on the atomic number (Z) of the atoms that cause the back-scattering of the electrons.

Figure 2.10 The picture of Field Emission Scanning Electron Microscope (FESEM) used in the present work

The characteristic x-rays are emitted when electrons in atoms undergo transitions within the shells. This occurs when the incident electron beam interacts with an electron in an inner shell and its removal results in another electron from an outer shell to fill its place in the inner shell. This results in release of energy as x-ray photons. Depending on the

energy of the emitted x-ray photons, the composition and abundance of elements present in the sample can be estimated.

The electron beam from the electron gun is focused using a series of condenser lenses before it reaches deflector coils where scanning signals are generated depending on the deflection. The deflection is achieved using a combination of electric and magnetic fields. An objective lens is used to focus the beam to a spot on the sample. Separate detectors are used for back-scattered electrons and secondary electrons. The magnification in SEM does not depend on the power of the objective lens. It depends on the ratio of the dimensions of the raster on the sample to its dimensions on the display. Higher magnifications result from reduction in size of the raster on the specimen keeping the display size fixed. Conducting surfaces which are ground are required for proper imaging to avoid charge accumulation the sample surface due to interaction with the electrons from the beam. Gold or several other metals or alloys are coated to image surface of non-conducting materials. In an FESEM, field-emission probe is used as an attachment to get better information about the geometry of the surface under investigation. In conventional SEM, ion milling of the sample surface occurs in vacuum thereby resulting in images of poor quality and reduced accuracy. By using field emission probes, electrons are emitted

as soon as a voltage is applied across it resulting in generation of secondary electrons from the sample surface subjected to ion-milling. These secondary electrons produce quality images of the surface. Thus, a FESEM produces images of superior quality compared to the conventional scanning electron microscope.

2.6 Levitation and Suspension force measurements using a homemade force measurement setup

The levitation and suspension force measurements of bulk superconductors reveal as aspect of the quality of these samples and their suitability for practical applications [16]. The stability of these materials in applications can also be ascertained by carrying out the relaxation measurements on levitation force in these materials. The relaxation of levitation force is an aspect of relaxation of magnetization in these systems. Hence, it is interesting to study these properties using an appropriately designed set-up. This technique is one-of-a-kind of measurement technique as the entire bulk sample is used for characterization and it is a non-destructive technique. The same samples used for these measurements could further be used for other characterization studies. The figure 2.11 below shows the levitation of a $SmCo_5$ permanent magnet over an YBCO superconductor and the

homemade levitation force measuring setup used by us in the present work.

Figure 2.11 Levitation of a permanent magnet over an YBCO superconductor and the homemade setup used to measure the levitation and suspension forces

The instrument consists of a movable x-y platform onto which the sample is positioned on an electronic balance. The superconductor is kept in a small cryocontainer to which liquid nitrogen is continuously supplied. The sample container can be moved up and down along the z-axis on a rail and a depth gauge measures the gap distance between the superconductor and the magnet. The closest approach distance between the two is around 3.5 mm. The position of the magnet on the pan can be adjusted with respect to the superconductor so that the z-axis of both coincides with each other. This can be done as a part of the initial

adjustments by cooling the superconductor and bringing it to the closest approach distance and obtaining maximum force value by adjusting the x-y position of the magnet with respect to the superconductor. The force values are computed using the change in weight of the permanent magnet as the superconductor approaches or recedes away from it. The field profile of the permanent magnet along the z-axis is recorded separately so as to convert the gap distances between the superconductor and the magnet into corresponding applied magnetic field value at the surface of the superconductor due to the permanent magnet. The conversion of the gap distance into corresponding applied magnetic field is an approximate but a very convenient approach to study the magnetic behavior of the superconductors using such measurements without affecting the physics of the problem. A full hysteresis loop of levitation force as a function of magnetic field can be obtained by gradually approaching the magnet and receding after reaching the closest point of approach. The approach and the recession segments make the complete hysteresis loop cycle. The suspension curves can be obtained by field-cooling the sample in the presence of the magnet at the closest gap distance and then moving the superconductor away from the magnet. The relaxation measurements are carried out in the hysteresis cycle following the same procedure while waiting at each

gap distance for 120 seconds. The force values are noted at each 30 second interval up to a total of 120 seconds [17].

The magnetization of the permanent magnet by the superconductor was measured using the same setup by attaching a hall probe to the surface of the superconductor while noting down both the levitation force values as well as the magnetization at the surface of the magnet. The entire hysteresis loop of both the levitation force of the superconductor and the M-H loop of the magnet was thus recorded [18].

2.7 Temperature dependence of ac susceptibility

The temperature dependence of ac susceptibility of the samples was measured using a homemade ac susceptometer operating in the temperature range 77 K to 120 K. The picture of the homemade susceptometer setup is shown in the figure 2.12 below. In ac susceptibility measurements, the ac dynamics of the magnetic moments in the sample is studied by applying a small ac driving field [19]. The time-dependence of the magnetic moments causes a corresponding variation in the field associated with the moments inducing a current in the pick-up coils. The frequency band for detection is chosen to match with the fundamental frequency of the applied field and the detection circuitry is tuned accordingly.

Figure 2.12 The picture shows the homemade susceptometer setup and the coilset measuring the temperature dependence of ac susceptibility of the samples

A block diagram of the ac susceptibility measurement setup is shown in figure 2.13. The magnetization in the sample resulting from an applied field H = H$_0$ Cosωt, where ω = 2$\pi\nu$ is given by

$$M = H_0(\chi^{'} cos\omega t + \chi^{''} sin\omega t) \qquad \textbf{(2.1)}$$

Here χ' and χ'' represent real and imaginary components of the complex quantity fundamental ac susceptibility.

The principle on which this measurement technique depends is Faraday's law

$$\nabla \times \boldsymbol{E} = -\frac{\partial \boldsymbol{B}}{\partial t} \qquad \textbf{(2.2)}$$
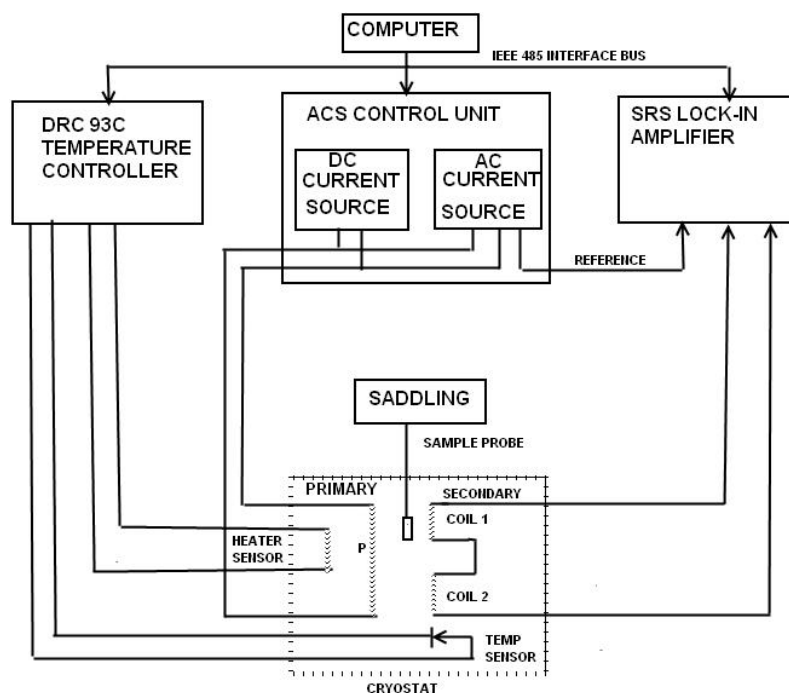
Figure 2.13 Block diagram of ac susceptibility measurement setup

The measurement circuit consists of a coil assembly with one primary coil into which a pair coaxially connected secondary coils in series are placed. The secondary coil pair is identical in all respects and connected in opposition so as to cancel the voltages induced due to the applied ac field provided to the primary coil by a constant current source.

The magnetic field due to a current 'I' in a solenoidal coil of length L_P with N_P turns is given by

$$H_{rms} = \frac{4\pi N_p I_{rms}}{10\, L_p} \qquad\qquad \textbf{(2.3)}$$

Where I_{rms} and H_{rms} are the root-mean square values for the applied current and induced magnet respectively and the applied field $H_{ac} = \sqrt{2}$ H_{rms}. It is expected that the voltage drop across the secondary coils is zero in the absence of the sample in one of them since they are connected in opposition. But, in practice, there is a drop across the coil pair and it is temperature dependent. Hence, in the presence of the sample, the necessary background subtraction is done to eliminate this voltage. Extraneous phase shifts caused due to various sources in the circuit need to be corrected by shifting the phase of the references so as to get $\chi'' = 0$ well above and well below the transition temperature T_c of the material. The dual phase lock-in amplifier senses a signal in its input when an induced voltage due to the sample is generated in the circuit. Accordingly, the lock-in amplifier gives out signals in the form of two dc voltages, say $\mathfrak{C}_r$ and $\mathfrak{C}_i$ corresponding to the real and imaginary parts of the magnetization M in the sample. The dc voltages correspond to the in-phase and out-of-phase components of the magnetization with respect to the reference signal which in turn is in-phase with the applied field, H_{ac}.

The real and imaginary components of the complex susceptibility are obtained from the measured dc voltages $\mathcal{C}_r$ and $\mathcal{C}_i$ using the formulae given below.

$$\chi_r = \frac{\mathcal{C}_r}{\alpha \omega A N \mu_0 H_m (1-D)} \qquad (2.4)$$

$$\chi_i = \frac{\mathcal{C}_i}{\alpha \omega A N \mu_0 H_m (1-D)} \qquad (2.5)$$

Here N is the number of turns in the secondary coils, H_m is the amplitude of the applied field H_{ac}, A is the area of cross-section of the sample, D is the demagnetization factor and α is the filling factor [8]. From the above equations 2.4 and 2.5, absolute values of real and imaginary parts of ac susceptibility can be computed using the formulae given by Murphy et al. [19] as

$$\chi' = \frac{\chi_r - D(\chi_r^2 + \chi_i^2)}{(1 - \chi_r D)^2 + D^2 \chi_i^2} \qquad (2.6)$$

$$\chi'' = \frac{\chi_i}{(1 - \chi_r D)^2 + D^2 \chi_i^2} \qquad (2.7)$$

Thus, the real and imaginary parts of the complex ac susceptibility are computed from the measured $\mathcal{C}_r$ and $\mathcal{C}_i$ voltage values.

2.8 Magnetization loops using Physical Property Measurement System

Study of magnetization behavior as a function of applied dc magnetic field is very important method of characterization of superconductors as it helps us to estimate the current carrying capability of the materials [20-22]. M-H loops are recorded typically using a vibrating sample magnetometer. M-H isotherms can be recorded as the applied field is increased from zero field value to a positive maximum and negative maximum value, then back to positive maximum value in a cycle. In high T_c materials, direct measurement of critical current density is a rather tedious process because of the capability of these materials to carry large currents. The direct transport measurements involve a lot of practical problems such as lack of current sources capable of providing such large currents, difficulty in making suitable contacts etc. Bean's model provides a framework for calculation of critical current density based on magnetization measurements. The relevance and correlation of magnetic critical current density to the transport critical current density has not been yet fully understood. We shall discuss the Bean's model and calculation of critical current density using the model for high T_c superconductors.

2.8.1 Bean's model and calculation of critical current density

Charles P Bean proposed a critical state model to estimate the critical current density in type-II superconductors by assuming that the supercurrents flow with a density equal to critical current density J_c in the critical state and this critical current density is independent of the local internal field [23-24]. The model also assumes a stable flux vortex array and hence no flux creep occurs in the material and the lower critical field of the specimen is zero. In the critical state, the same critical current flows everywhere in the specimen. The process of magnetization of a thin slab of thickness 2t is shown in figure 2.145with the applied field parallel to the slab surface.
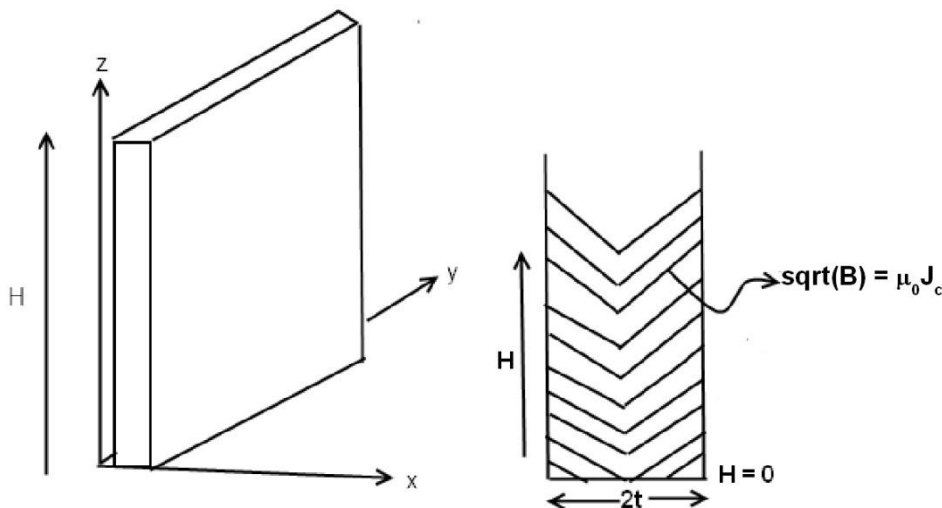
Figure 2.14 Process of magnetization of a thin superconductor slab as per Bean's model

The Maxwell's equation $\sqrt{B} = \mu_0 J_c$ signifies the linear dependence of the field within the specimen on its thickness if the material is in critical state. Here, J_c is the critical current density in Acm^{-2}, B is the magnetic induction in Tesla and μ_0 is the absolute permeability in Hm^{-1}. The local internal field inside the superconductor is given by

$$H_i = \frac{B}{\mu_0} \qquad (2.8)$$

where B is the macroscopic local flux density. The local magnetization is given by

$$M_i = H_i - H \qquad (2.9)$$

Here H is the applied field. The total magnetization hence would be the average of M_i across the sample.

Magnetization for two regimes of applied field can be considered namely

$\qquad$ 1) $0 < H < H^*$ $\qquad$ and $\qquad$ 2) $H > H^*$

Here H^* is the applied magnetic field at which the internal reaches the centre of the sample.

If the slab is of infinite dimensions, then the initial magnetization in the two field regimes can be written as

$$M(H) = -H + \frac{H^2}{2 J_c t} \qquad \text{for } 0 < H < H^* \qquad \textbf{(2.10)}$$

$$M(H) = -\frac{J_c t}{2} \qquad \text{for } H > H^* \qquad \textbf{(2.11)}$$

The magnetization for the reverse curve for maximum field $-H_m$ is given by

when $H_m - 2H^* < H < H_m$

$$M(H) = -\frac{J_c t}{2} + H_m - H - \frac{(H_m - H)^2}{4 J_c t}, \qquad \textbf{(2.12)}$$

for $-H_m - H < H_m - 2H^*$

$$M(H) = \frac{J_c t}{2}, \qquad \textbf{(2.13)}$$

When $H_m > 2H^*$,

$$M(H^+) - M(H^-) = J_c t \qquad \textbf{(2.14)}$$

Thus the critical current density J_c of the sample can be determined from the width of the M-H hysteresis loop at a given magnetic field.

For orthorhombic specimen geometry, similar relations can be derived and the J_c can be arrived at as

$$M(H^+) - M(H^-) = J_c b(1 - \frac{b}{3a}) \qquad \textbf{(2.15)}$$

Where *a* and *b* are the dimensions of the specimen along the directions perpendicular to the applied field.

2.8.2 Calculation of J_c from M-H loops recorded using PPMS

The magnetization in the superconducting sample as a function of applied magnetic field was recorded as M-H loops using the Physical Property Measurement System (Quantum Design – PPMS) at different temperatures between 20 K and 89 K in applied magnetic fields up to 9T. The *c*-axis of the specimen was restricted to less than 5 mm whereas for *a* and *b* axis it was 2 mm. Figure 2.15 shows the picture of the PPMS used in the present work. The PPMS with VSM measures the magnetic moments of the sample based on the vibrating sample magnetometer device. The sample kept at the axial center of a pick-up coil is made to vibrate at known frequency in the presence of applied magnetic field from a superconducting solenoid coil magnet. The changes in magnetic field due to induced moments in the sample are detected as voltage signals by the pick-up coil. These voltages are re-calibrated as moments.

Thus M-H loops are recorded for a given sample. From the M-H loops, using Bean's model formula, the J_c can be calculated as [25]

$$J_c = 20 \; \frac{\Delta M}{d} \; A \; cm^{-2} \qquad\qquad (2.16)$$

Figure 2.15 Picture of the PPMS (Quantum Design make) used in the present work with a VSM head mounted as attachment

where 'd' depends on the specimen dimensions given by

$$d = b\left(1 - \frac{b}{3a}\right); a > b \qquad \text{(2.17)}$$

'a' and 'b' being the dimensions of the sample in directions perpendicular to the applied field direction.

In eqn. 2.16, $\Delta M = M^+ - M^-$ (in units of emu/cc) is the difference in magnetization values for the increasing and decreasing field values corresponding to the I and V quadrant field sweeps.

References

[1] K. Jeong, D. Y. Kim, Y. K. Park, K. W. Lee, and J. C. Park, *Physica C* **185-189**, 2393 - 2394 (1991).

[2] K. Iida, N. H. Babu, Y. Shi, and D. A. Cardwell, *Supercond. Sci. Technol*. **18, 1**421–1427 (2005).

[3] H. Fang, Y. X. Zhou, K. Ravi-Chandar and K. Salama, *Supercond. Sci. Technol.* **17**, 269-273 (2004).

[4] A. Manthiram and J. B. Goodenough, *Nature* **329**, 908 (1987).

[5] D. Bahadur, A. Banerjee, A. Das, K. P. Gupta, T. Mathews, A. Mitra, M. Tiwari, and A. K. Majumdar, *Rev. Sol. Stat. Sci.* **2**, 77 (1988).

[6] C. Leblond, I. Monot, D. Bourgault, and G. Desgardin, *Supercond. Sci. Technol.* **12**, 405 (1999).

[7] E. S. Reddy and T. Rajasekharan, *J. Mater. Res.* **13** (9), 2472 (1998).

[8] A. Sanchez and D.-X. Chen, *Magnetic susceptibility of superconductors and other spin systems,* edited by R. A. Hein, T. L. Francavilla, D. H. Liebenberg, Plenum, NY 251-259 (1991).

[9] P. Benzi, E. Bottizzo, and N. Rizzi, *J. Cryst. Growth* **269**, 635-629 (2004).

[10] Ch. Zhang, A. Kulpa, and A. C. D. Chaklader, *Physica C* **252**, 67-78 (1995).

[11] C. Kittel, *Introduction to Solid State Physics - 7th Ed.*, John-Wiley & Sons, Singapore (1995).

[12] J. J. Roa, X. G. Capdevila, M. Martínez, F. Espiell, and M. Segarra, *Nanotechnology* **18**, 385701 (2007).

[13] W. C. Oliver and G. M. Pharr, *J. Mater. Res*. **7** (6), 1564 (1992).

[14] W. C. Oliver and G. M. Pharr, *J. Mater. Res*. **19** (1), 3 (2004).

[15] A. von Manfred, *Zeit. für Physik* **109** (9–10), 553–572 (1939).

[16] F. C. Moon, *Superconducting Levitation: Applications to Bearing & Magnetic Transportation*, John-Wiley & Sons, (1994).

[17] R. Parthasarathy, M. M. Lakshmi, and V. Seshubai, *Physica C* **471** (13-14), 395-399 (2011).

[18] R. Parthasarathy, M. M. Lakshmi, and V. Seshubai, *Proceedings of the 56th DAE Solid State Physics Symposium 2011. AIP Conference Proceedings, 1447, 899-900 (2012).*

[19] S. D. Murphy, K. Renouard, R. Crittenden, and S. M. Bhagat, *Solid State Commun.* **69**, 367 (1989).

[20] K. V. Bhagwat and P. Chaddah, *Pramana-J. Phys.* **33** (4), 521-540 (1989).

[21] P. Chaddah, K. V. Bhagwat, and G. Ravikumar, *Physica C* **159**, 570-576 (1989).

[22] A. Sanchez and C. Navau, *Supercond. Sci. Technol.* **14**, 444–447 (2001).

[23] C. P. Bean, *Phys. Rev. Lett.* **8**, 250 (1962).

[24] C. P. Bean, *Rev. Mod. Phys.* **36**, 31 (1964).

[25] D. X. Chen and R. B. Goldfarb, *J. Appl. Phys.* **66**, 2489 (1989).

This page is left blank intentionally.

CHAPTER 3

FABRICATION OF YBCO/Ag COMPOSITE SUPERCONDUCTORS BY INFILTRATION GROWTH PROCESSING TECHNIQUE – ROLE OF SILVER ADDITION

3.1 Introduction

The Infiltration Growth Processing (IGP) technique has been one of the most preferred methods for fabrication of bulk YBCO superconductors and YBCO/Ag superconductor composites [1-10]. The IGP technique offers several advantages, over the other techniques, such as improved control over size, shape and distribution of the non-superconducting Y-211 precipitates in the superconducting Y-123 matrix [11], reduction in density of macroscopic defects such as pores, voids and cracks [12], reduction in shrinkage and retention of the shape of the final product (near-net shape) [13] which makes these samples nearly applications-ready etc.

The phase diagram of YBCO system reveals the presence of several phases around the peritectic transformation regime. The peritectic reaction leading to the formation of YBCO phase is

$$2\ Y_1Ba_2Cu_3O_{7-\delta} \rightleftharpoons Y_2Ba_1Cu_1O_5 + Ba_3Cu_5O_8$$

In addition to the phases indicated in the above reaction, possibility of formation of other phases cannot be ruled out [14]. Thus the preparation and extraction of single phase YBCO requires precise heat treatment schedules. The Y-211 phase is a non-superconducting phase which, when leftover after the peritectic reaction as precipitates in the superconducting matrix, could create pinning centers of the size on the order of the correlation length of the system thereby being useful in arresting the magnetic flux motion in the material.

The IGP technique involves infiltration of the liquid phases present in the source pellet, after decomposition, into a target pellet of Y-211 phase. The peritectic reaction involving Y-123 and Y-211 is dependent on several process parameters such as composition of the precursor powders, compaction pressure and their sintering temperatures, heat treatment schedules used during processing and any additives used. For example, it has been reported that silver, added as an additive, has a very significant role in modifying the peritectic transformation temperatures in the YBCO system [15]. The properties of bulk end-products thus prepared depend on several other parameters such as the compaction pressure used for making pellets [9], the addition of

additives such as Ag to the precursor powders and the quantum of addition [16-19], etc. Hence, it is essential to optimize several of the processing parameters in order to obtain bulk superconductors of superior electrical and magnetic properties. The following sections of the chapter explain the preparation of the precursor powders using citrate synthesis route and the several processing steps leading to fabrication of bulk YBCO/Ag superconductors used for the present study.

3.2 Preparation of precursor powders of Y-123 and Y-211

The Y-123 and Y-211 precursor powders used in making the pellets have been prepared following the citrate synthesis route [20-21]. The technique involved dissolving stoichiometric proportions of starting chemicals in concentrated nitric acid to form nitrate mixtures. Highly pure powders of Yttrium Oxide (Y_2O_3) , Barium Carbonate ($BaCO_3$) and Copper (II) Oxide (CuO) (Merck make, 99.9 % pure) were dissolved in appropriate amounts of conc. Nitric acid after weighing out the chemicals as per the composition using a high-precision chemical balance (*Mettler make – model AE 340*). The chemicals were mixed using a magnetic stirrer with a hot plate to ensure continuous, homogeneous mixing and sustained reaction. Citric acid and ethylene glycol were

added to the mixture for cheleation and pH of the resulting solution was adjusted to 8. The solution was heated to around 250 C on the hot plate for around 3 hours for combustion reaction to take place. The fine powders from the combustion reaction were sintered at 900° C for Y-123 and 950° C for Y-211 for 24 hour duration. The sintered powders were finely ground using an agate mortar and a pestle.

The bulk samples in pellet forms were pressed using a hydraulic press capable of reaching up to 540 MPa pressures. In the present work, two different compaction pressures, viz., 460 MPa and 540 MPa, were used for making YBCO/Ag composites with 2 wt %, 4 wt % and 10 wt % metallic silver added to the precursor Y-123 powders which acted as a liquid source for the peritectic reaction. The metallic silver powder was separately ground in a clean agate mortar in ethanol medium to avoid oxidation of silver. The mixture of Y-213 and metallic Ag powders were mixed and ground thoroughly before pelletization. The resulting pellet will henceforth be referred to as liquid source pellet which is a mixture of Y-123 and metallic Ag powder. The non-superconducting Y-211 phase powders were pressed into green compacts using same compaction pressures without any additives. The Y-211 green compacts would henceforth be denoted as target pellets during the IG processing and end products or the respective samples after processing.

3.3 Metallic Ag addition to the liquid source pellet

Metallic Ag powder in different amounts were added to the liquid source pellet to make 2 wt %, 4 wt % and 6 wt % samples at two different compaction pressures of 460 MPa and 540 MPa. The samples made with 460 MPa using 2 wt %, 4 wt % and 10 wt % Ag are coded as Y460-2, Y460-4 and Y460-10 and the samples compacted at 540 MPa are coded as Y540-2, Y540-4 and Y540-10 for 2 wt %, 4 wt % and 10 wt % Ag addition respectively. The weight proportion of Ag addition was taken with respect to the weight of the liquid source powder (Y-123). The Ag powders thus weighed were ground into finer particles using a clean agate mortar in ethanol medium. The Ag powders were mixed with 16 g of Y-123 powders in each case to obtain the liquid source pellets for both the 460 MPa and 540 MPa compaction pressure series samples. The main focus of the thesis shall be on 540 MPa compacted series, denoted Y540 series, with Ag variation. The Y460 series, in which the samples were compacted with a lower compaction pressure of 460 MPa, was made with an intention of studying the effects of variation of compaction pressure on the YBCO/Ag system [22-23].

3.4 Compaction of precursor powders into pellets using Hydraulic press

The precursor pellets were pressed using a hydraulic press as mentioned earlier. Separate dies were used to press the (Y-123 + Ag) and Y-211 powders to obtain the liquid source and target pellets respectively. A constant pressure was sustained for 15 minutes on each of the source and target pellets for both 460 MPa and 540 MPa pressure series samples.

3.4.1 Y_2O_3, YSZ and Al_2O_3 pellets for supporting the samples

The powders of Yttria (Y_2O_3), Yttria Stabilized Zirconia (YSZ) and Alumina (Al_2O_3) were used to press the support pellets. The support pellets serve different purposes. The Yttria pellet reduces the probability of contamination of the target Y-211 pellet. The Alumina pellet supports the liquid outflow during melting. The YSZ pellet acts as a buffer between the Yttria and Alumina pellets. The pellets are stacked one over the other on alumina powder kept in an alumina crucible. The sample processing configuration is shown in fig. 3.1.

3.5 Infiltration Growth Processing of YBCO/Ag composites

The Infiltration Growth Processing (IGP) technique involves infiltration of liquid phases, which form after decomposition of Y-123, into the target pellet made of Y-211 precursor powders. This follows from the peritectic reaction given in Eqn. 3.1. The present work involves fabrication of YBCO/Ag composite superconductors using the IGP technique with liquid source on top to achieve infiltration by force of gravity. Here, we have an additional component in silver which is mixed to the liquid source powders. So, the physical mixture of metallic Ag to the liquid source pellets modifies the process parameters such as melting point, viscosity, density etc., of the liquid phase [15]. The optimization of the heat treatment schedule of this system, hence, involves consideration of the above parameters as well. Metallic Ag mixed to the liquid source pellets is expected to melt along with the liquid phases and infiltrate into the target pellet. The sample processing configuration of IGP technique used in the present study and the heat treatment schedule employed are shown in figure 3.1 below.
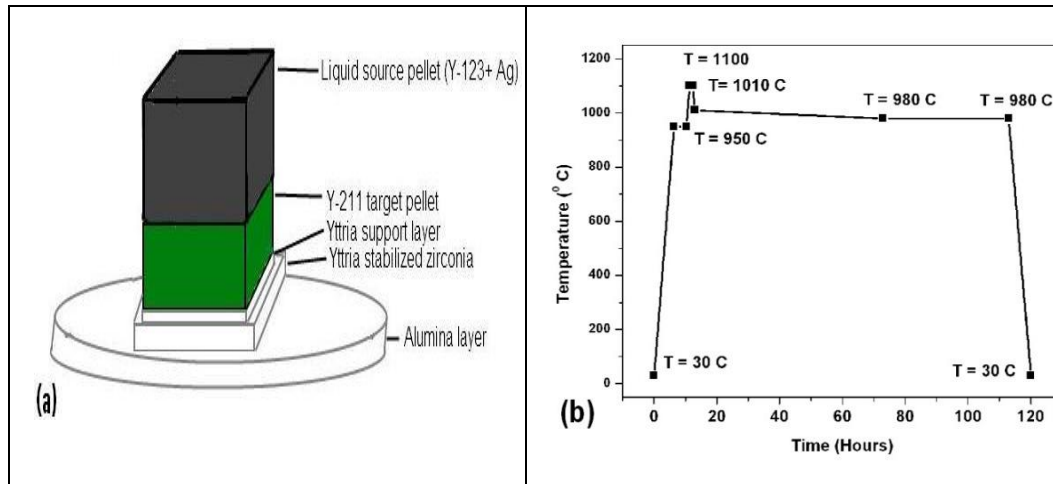
Figure 3.1 The IGP sample processing configuration and the heat treatment schedule

The samples heat treated as per the schedule depicted in figure 1 (b) were oxygenated at 450° C for 120 hours after separating out the target pellets alone.

3.6 Specimen preparation for various measurements

The as-made bulk samples were used for levitation and suspension force measurements. The same target pellets were used for various measurements after cutting out portions from them using a diamond precision saw (*Buehler make – model Isomet 1000*). The rotation speed of the blade was kept at 100 rpm to ensure smooth grinding of the specimens. A thin slice of the *ab*-plane was cut and a strip from it was used to study the temperature dependence of resistivity. Another

portion of the same plane was used for microstructural studies. The specimens for microstructural studies were embedded into Bakelite mounts by hot-pressing technique. The samples thus mounted were polished down to 0.25 μm using diamond paste as the polishing medium using a polishing machine (*Buehler Grinder-Polisher Beta with Vector LC powerhead*). For ac $\chi(T)$ and dc magnetization measurements, a parallelepiped sample with its long axis parallel to the *c*-axis of the sample was used. The nano-indentation studies were carried out using a nano-indenter (*Hysitron Tribodent*) on the same specimens used for microstructural studies. The structural characterization of the samples was done by X-ray diffraction technique using a *Bruker D90 advance* x-ray diffraction system. Small specimens taken from different regions of the bulk samples were powdered and used for the XRD measurements.

3.7 Structural dependence of YBCO/Ag composite on silver content

The X-ray diffraction studies were carried out on the YBCO/Ag samples to probe the role of Ag addition on the structure of the composite material. The Y540 series containing 2 wt %, 4 wt % and 10 wt % samples were used for this study. Typically specimens from four different regions of the bulk samples were collected and powdered for this study in order to obtain the average effect of silver addition on the

structural properties. The x-ray diffraction pattern of the three samples Y540-2, Y540-4 and Y540-10 is shown in figure 2 below.

Figure 3.2 The x-ray diffraction pattern for the three samples in the Y540 series with varying Ag content clearly reveals gradual shifts in prominent peaks and suppression of a few other peaks. The lattice parameters and cell volume were found to show gradual increase with Ag addition indicating some amount of substitution of Ag atoms in Cu sites in the YBCO lattice.

The X-ray diffraction patterns of the three samples reveal a gradual shift in 2θ values as Ag content is increased from 2 wt % in Y540-2 sample to

4 wt % in Y540-4 to 10 wt % in Y540-10 sample. The relative intensities of some of the peaks appear to be suppressed while certain other peak intensities increase in prominence. The peak indexing and lattice parameter calculations were carried out using *powderx* X-ray analysis software employing *cellref* algorithm.

The structural analysis revealed systematic variation in lattice parameters with variation in silver content as shown in figure 3 below.
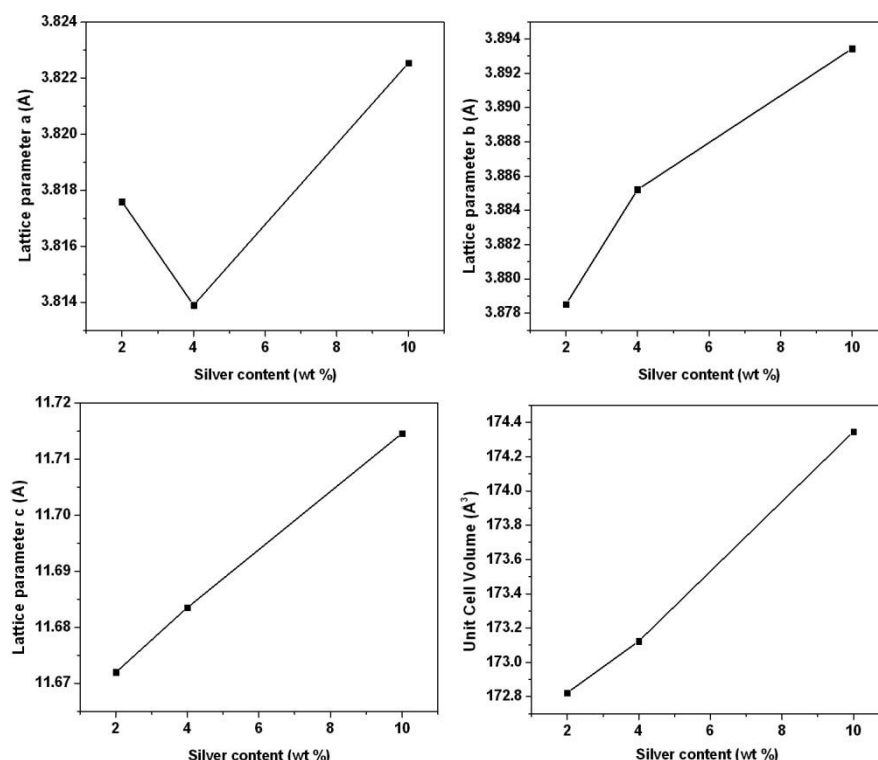

Figure 3.3 Lattice parameters and cell volume variation with Ag content in Y540 series indicating partial substitution of Ag atoms in Cu sites in Y-123 lattice

From the figure 3.3, it is clear that Ag used in making the composites by physical mixing to the liquid source powders does not entirely remain as a physical component in the end product. In other words, the metallic Ag added to the composite does not remain entirely non-reactive. Part of the silver that is added substitutes for Cu in the Y-123 unit cell [24]. This is a significant observation considering the fact that doping of Ag in Cu sites is unintended in the fabrication of YBCO/Ag composites by IGP. This could have crucial impact on the overall properties of the composite system as will be seen in the following sections. As a consequence of this substitution of Ag in Cu sites, the lattice parameters 'b' and 'c' of the orthorhombic unit cell vary by a small amount [25]. The lattice parameter 'a' on the other hand decreases for Ag content variation between 2 wt % and 4 wt % and then increases when the Ag content is increased to 10 wt %. This shows that the additional silver beyond 4 wt % possibly leads to substitution of Ag in the Cu(1) site also. But, the unit cell volume is found to increase with increasing Ag content [26-27]. This is an interesting result considering the fact that the orthorhombic lattice parameter 'a' and 'b' also vary in our data which confirms our presumption that apart from the Cu(2) site, Ag is possibly substituting for copper in Cu(1) site as well at higher values of Ag addition. The Cu(1) site correspond to the Cu(1)O chains in the YBCO lattice which act as charge reservoirs transferring charge during

conduction to the conducting Cu(2)O planes. Any substitution of Ag in Cu sites hence drastically modifies the superconducting properties of the material. Depending on the site occupancies and the amount of substitution, the properties have been affected by Ag addition, particularly beyond 4 wt %. There appears to be concentration quenching of silver beyond this value that drastically affects the superconducting properties as will be discussed in the following sections.

3.8 Effect of silver on the mechanical properties of YBCO/Ag superconductor composites

Systematic mechanical properties characterization was carried out on the Y540 series samples to probe the role of Ag on mechanical properties [28]. We have carried out detailed nanoindentation measurements on the YBCO/Ag composites by varying the Ag content starting from 2wt % up to 10 wt % in the present work to assess the effect of compositing metallic Ag on the mechanical properties of the composites. A nanoindentation system (*Hysitron make –model Tribodent*) has been used in this work. The Load-Depth curves were obtained at several regions for each of the samples by applying a maximum load of 5000 µN. The mechanical properties such as stiffness, hardness and the reduced

moduli of the samples have been calculated from the resultant load-displacement curves.

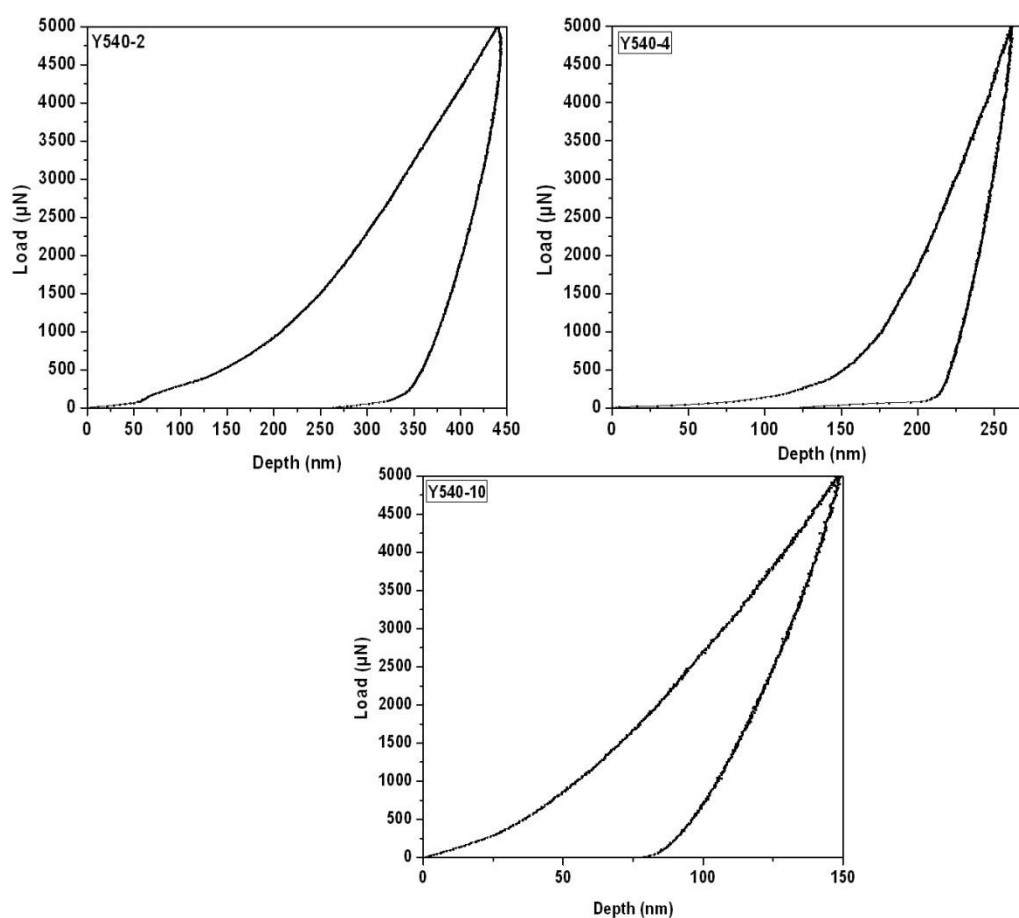The typical Load-depth curves obtained for the three samples are shown in the figure 4 below.

Figure 3.4 Typical representative Load-Depth curves for the samples Y540-2, Y540-4 and Y540-10 recorded using the nanoindenter.

The stiffness S, of the samples were calculated by calculating the slope of the unloading curve at the maximum load using the formula, following the method proposed by Oliver and Pharr [29-30]

$$S = \frac{P_{max}}{h_{max}}$$

where P_{max} is the maximum load applied and h_{max} is the maximum depth at the maximum load.

The contact penetration depth of the sample has been calculated using the relation

$$h_c = h_{max} - \varepsilon \frac{P_{max}}{S}$$

Here the term ε is a constant depending on the geometry of the tip and has been taken to be equal to 0.75 for the Berkovich indenter tip that has been used in the measurements [28]. For a perfect Berkovich indenter, the projected contact area can be taken to be

$$A(h_c) = 24.56 \, h_c^2$$

The nanohardness of the specimen is calculated using the following formula

$$H = \frac{P_{max}}{A(h_c)}$$

The reduced elastic modulus can be expressed in terms of the stiffness S and A(h_c) as

$$E_r = \frac{1}{\beta} \frac{\sqrt{\pi}}{2} \frac{S}{\sqrt{A(h_c)}}$$

The Young's moduli of the samples were calculated from these curves using the *Oliver-Pharr* approach according to the following equation

$$\frac{1}{E_r} = \frac{1 - v^2}{E} + \frac{1 - v_i^2}{E_i}$$

where v and E are the Poisson's ratio and Young's modulus of the sample whereas those with subscript i are the same properties of the indenter. The Young's modulus thus calculated is found to improve significantly with metallic silver addition to the YBCO composite.

The table 3.1 below gives average stiffness, hardness, reduced elastic modulus and Young's modulus for the three samples in the Y540 series with 2, 4 and 10 wt % Ag addition to the composite.

Sample Name	Silver content Wt %	Avg. Stiffness, S (N/m)	Avg. Hardness, H (GPa)	Avg. Reduced Elastic Modulus, E_r (GPa)	Avg. Young's Modulus, E (GPa)
Y540-2	2 wt %	90476.48	1.29	40.39	38.12
Y540-4	4 wt %	174275.87	7.04	152.75	165.02
Y540-10	10 wt %	116684.31	15.01	176.74	190.25

Table 3.1 The variation of mechanical properties such as stiffness, hardness, reduced elastic modulus and Young's modulus with varying silver content is tabulated showing remarkable improvement in the values of these properties with Ag addition.

Thus, it is obvious that the mechanical properties show marked improvement with increasing quantities of metallic Ag addition to the liquid source pellet except stiffness which is highest for the 4 wt % Ag added sample. The effect of silver addition on the superconducting properties of the samples is discussed in the subsequent sections.

3.9 Effect of Ag addition on the Microstructural properties of YBCO/Ag system

Field Emission – Scanning Electron Microscopy (FESEM) was utilized to study the effects of metallic Ag addition to the sample microstructure of

YBCO/Ag composites in the Y540 series with Ag content variation as 2 wt %, 4 wt % and 10 wt % in three samples. As mentioned in the section 3.4.1, the *ab*-plane of the samples was sliced and hot-mounted on Bakelite mounts. The mounted samples were polished starting with emery polishing paper of grade 800 down to 1200 in steps of 200. The next stage of polishing was done using Diamond paste of particle sizes 2 µm, 1 µm, 0.5µm and 0.25 µm successively on a polishing cloth. The polishing was carried out using a polishing machine (*Buehler Beta Grinder-Polisher*). The polishing speed was kept to a minimum at 30 rpm of the rotor and the holding pressure on the mounts during polishing was kept to a minimum to avoid any damage to the sample due to pressure. Kerosene was used as the lubricant during polishing.

The microstructures of the samples Y540-2, Y540-4, Y-540-10 are revealed in the FESEM images recorded using a Field Emission – Scanning Electron Microscope (FE-SEM) (*Carl Zeiss make -model Ultra 55*) in the figure 3.5 below.
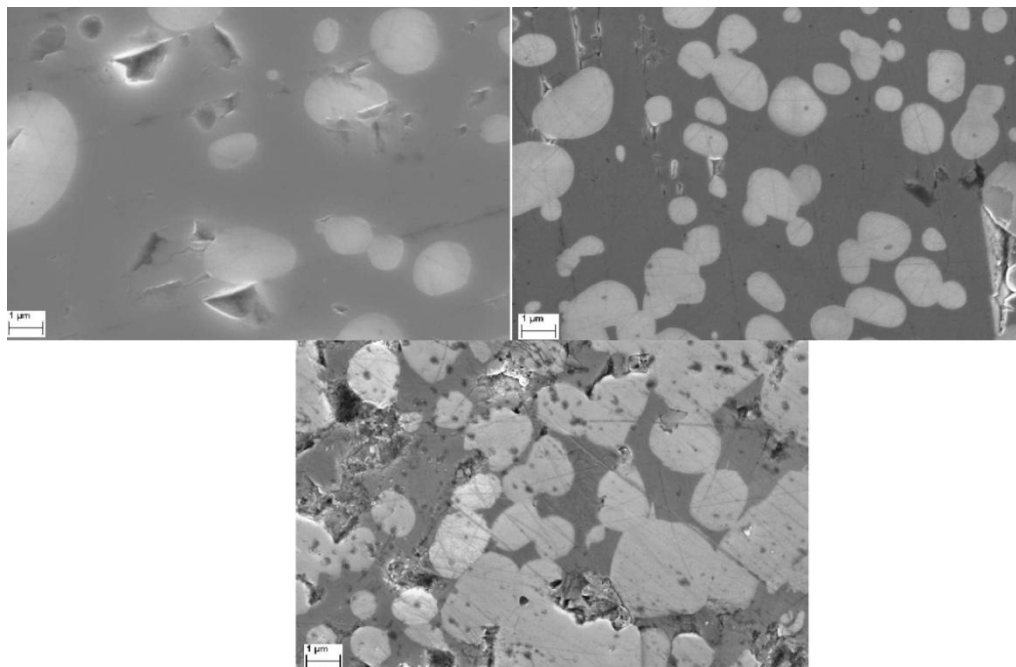
Figure 3.5 The microstructure of the three samples in the Y540 series with varying Ag content as seen through high magnification Field Emission - Scanning Electron Microscope images. Gradual changes in Y-211 size, shape and distribution with varying Ag contents indicates an indirect role for silver in modifying the sample microstructure.

3.9.1 Silver substitution in Cu sites in YBCO unit cell – EDAX analysis

We have discussed in section 3.7 that our x-ray diffraction studies on the Y540 series of samples with 2, 4 and 10 wt % Ag addition revealed the possibility of Ag getting substituted for Cu in YBCO lattice. In order to verify this possibility and probe this problem further, we carried out
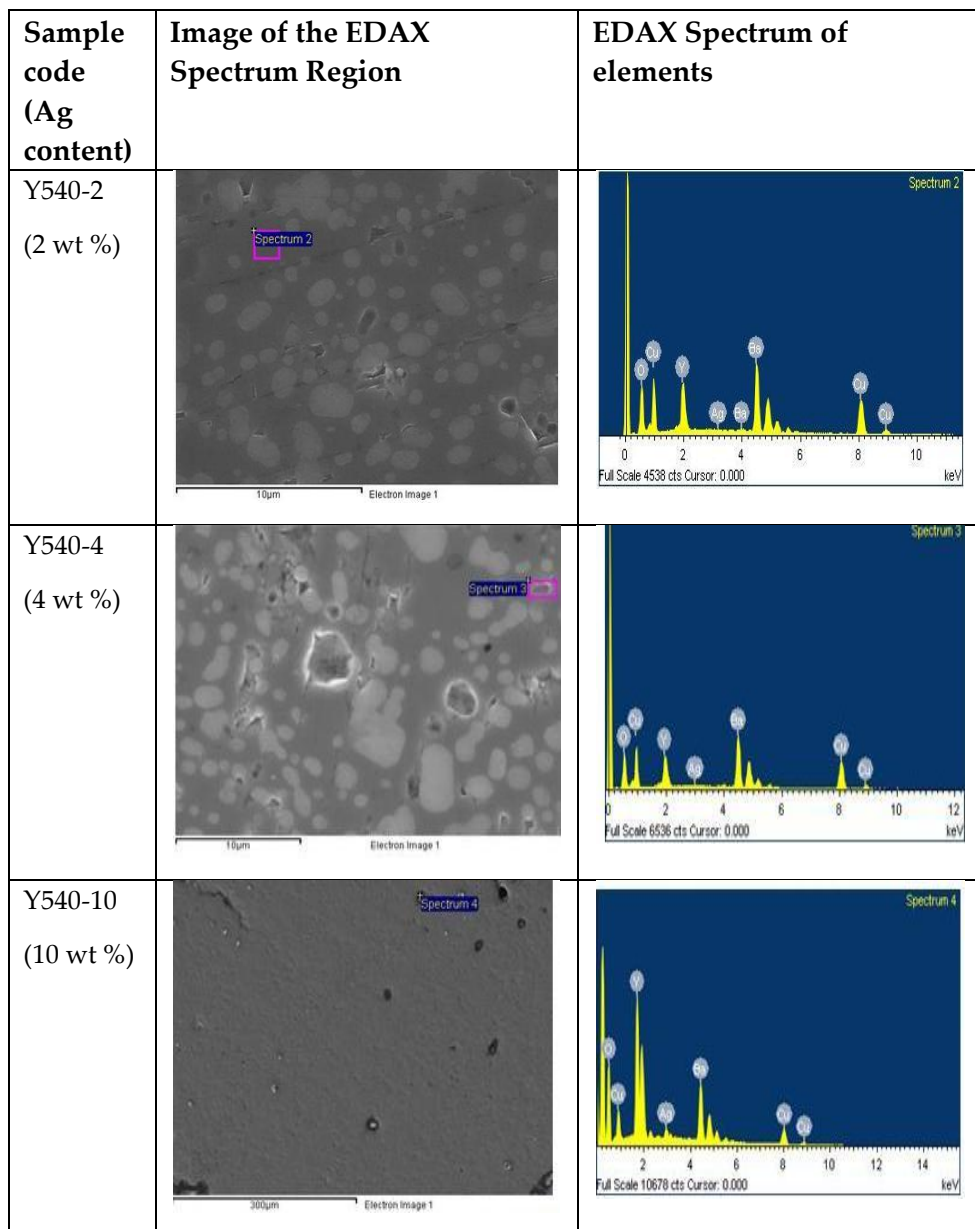
Sample code (Ag content)	Image of the EDAX Spectrum Region	EDAX Spectrum of elements
Y540-2 (2 wt %)		
Y540-4 (4 wt %)		
Y540-10 (10 wt %)		

Figure 3.6 EDAX images and spectra of Y540 series samples with varying Ag content showing the presence of Ag in the Y-123 matrix indicating possible substitution of Ag for Cu in YBCO lattice.

extensive EDAX measurements and analysis of the samples. We found that among the three samples in the Y540 series the presence of Ag in the Y-123 matrix was detected for Y540-4 and Y540-10 samples whereas we could not detect any significant Ag presence in the matrix for Y540-2 sample. We have presented below the overall results of the study.

Our analysis shows that the amount of Ag in different regions of matrix varies and there are Ag-free regions in the matrix as well, implying that the Ag substitution for Cu in YBCO lattice leading to the $Y_1Ba_2(Cu_{1-x}Ag_x)_3O_{7-\delta}$ composition was inhomogeneous. The Ag substitution for Cu hence is partial and occurs only in certain regions of the sample. The following table provides an overall quantitative perspective of Ag substitution.

Sl. No	Sample Code	Amount of Ag addition	No. of regions with Ag presence in EDAX out of 10 sample regions	Avg. amount of Ag detected in wt %
1	Y540-2	2 wt %	1	0.30 %
2	Y540-4	4 wt %	3	0.65 %
3	Y540-10	10 wt %	7	7.22 %

Table 3.2 The amount of Ag present in the Y-123 matrix through EDAX analysis is tabulated for a sample of 10 regions scanned.

From the above EDAX images and spectra, we observe that the amount of Ag in Y-123 matrix was below detectable limits for the Y540-2 sample whereas we could detect silver's presence in the matrix for the other two samples namely Y540-4 and Y540-10 with 4 wt % and 10 wt % Ag addition respectively, strongly indicating Ag substitution for Cu sites in YBCO unit cell.

3.9.2 The importance of Y-211 size, shape and distribution in Y-123 matrix

The ability to pin the vortices in the mixed state is an important property of high T_c superconductors which make them capable of carrying large currents in high magnetic fields. Hence, it is imperative to obtain a microstructure that supports the conduction of current by arresting the vortices [2,9,13]. The Y-211 particles are an important constituent of the YBCO system where their size, shape and distribution are crucial parameters that decide the quality of the sample. The finer the Y-211 particles the better their ability to create pinning centers at the Y-123/Y-211 interfaces that can arrest flux motion. The Y-211 surface area contribution according to their size is, hence, an important issue. But it seems, from our results, that the Y-211 particle size refinement

alone cannot achieve high J_c's or the sustainment of zero-field J_c's to high fields as will be discussed in section 3.10.

3.9.3 The distribution of silver precipitates in the Y-123 matrix – Concentration quenching effect

We have observed a systematic variation of silver distribution across the superconducting matrix and in the superconducting matrix with variation in silver content. In other words, the distribution of silver across the superconducting bulk of the sample is not uniform throughout the sample and the distribution is different from Y540-2 sample to Y540-10 sample across the series. The figure below shows the typical microstructure recorded using the FESEM in secondary electron imaging mode.
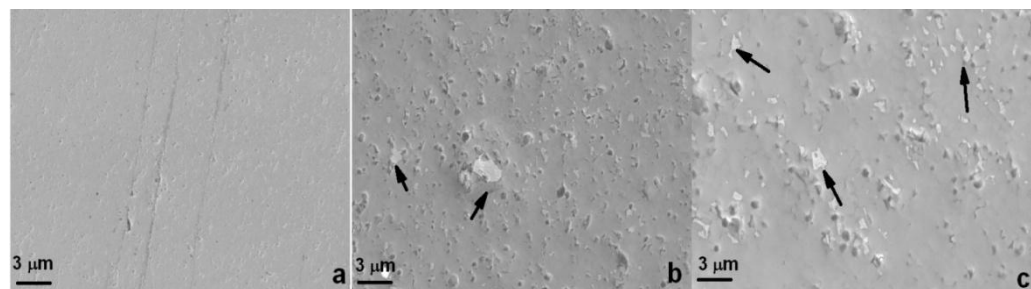

Figure 3.7 The distribution of silver as precipitates in the Y-123 matrix is shown here for the three samples in Y540 series with 2 wt %, 4 wt % and 10 wt % respectively. The agglomeration and appearance of Ag as precipitates starts beyond 2 wt % of Ag addition as Y540-2 sample does not appear to have any agglomeration.

It is interesting to note, here again, that part of the silver added while making the composite gets into the lattice and substitutes for Cu. The Ag substitution for Cu in lattice alters the composition to $Y_1Ba_2(Cu_{1-x}Ag_x)_3O_{7-\delta}$ at least in certain regions of the superconducting matrix. This substitution, though, has a threshold limit beyond which concentration quenching occurs [24, 26, 27]. The concentration quenching effect causes the additional silver to precipitate out in the matrix which can be seen in the FESEM images. In the Y540 series , from the fig. 6, we can see that the concentration quenching of Ag occurs somewhere between 2 wt % and 4 wt % silver addition as we do not see any silver precipitates in Y540-2 sample whereas in the Y540-4 we see some precipitation of Ag particles. In the Y540-10 sample where Ag addition was 10 wt %, the precipitation of Ag is more pronounced. The concentration quenching effect also plays a major role in modifying the superconducting properties of the material as we shall observe in later sections.

3.10 Magnetic and Superconducting properties of YBCO/Ag composites fabricated by IGP

3.10.1 Temperature dependence of ac susceptibility of YBCO/Ag composite superconductors

AC susceptibility as a function of temperature $\chi(T)$ was carried out on the samples using a home-made AC susceptometer to

study the ac magnetization dynamics of the samples. The set-up consists of a coil-set cum sample holder with a Pt resistor-based temperature sensor, a temperature controller (*Lakeshore DRC 93C*) and a Lock-in Amplifier (*Stanford Research Systems SR830 DSP*). Longitudinal sections parallel to the c-axis of the sample were cut for each of these measurements.
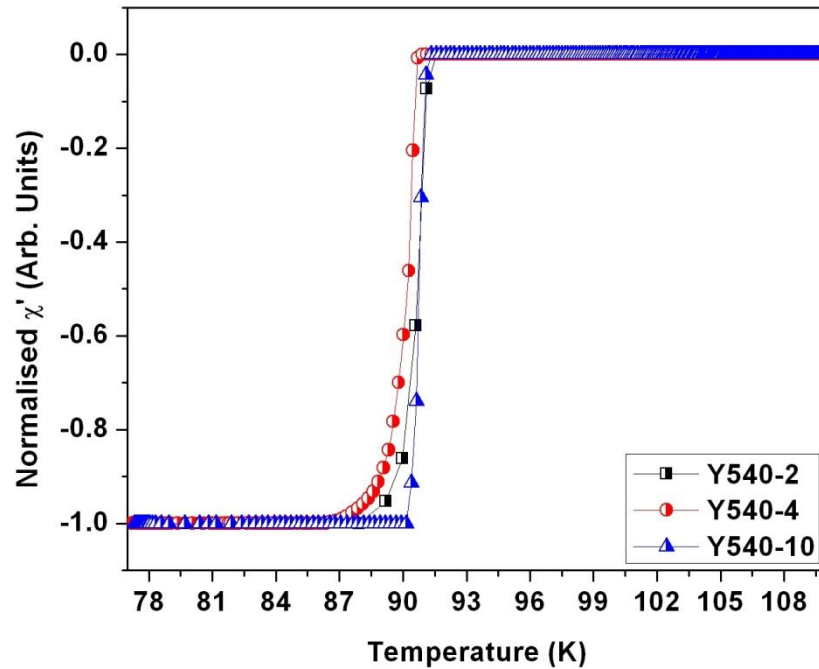

Figure 3.8 The real part of AC susceptibility as a function of temperature for the three samples A, B and C revealing variations in transition temperatures and transition widths with varying silver content. The improvement in T_c and ΔT_c for sample with maximum silver content of 10 wt % is clearly seen.

The sample is mounted in such a way so that the c-axis of the sample is parallel to the applied ac field from the primary coil. The sample is at the centre of one of the two secondary coils. The coil-set containing the primary and the two secondary coils are arranged coaxially with the secondary coils in series to one another. The sample temperature was gradually varied from 77 K to 100 K. The plots of AC χ' (real part) as a function of temperature for the three samples are shown in figure 7. The temperature variation of the real part of ac susceptibility revealed only minor variations in the transition temperature of the samples with silver addition with a maximum T_c of around 90.86 K for the 10 wt % Ag added sample Y540-10 [31].

Sample Code	Silver content wt %	Transition temperature T_c (K)	Transition width ΔT_c (K)
Y540-2	2 wt %	90.6 K	1.5 K
Y540-4	4 wt %	90.5 K	1.77 K
Y540-10	10 wt %	90.9 K	0.6 K

Table 3.3 The variation of transition temperature and width of transition of the three samples as a function of silver content is presented in the table. The variation in T_c across the three samples is minimal.

The transition width for this sample was very narrow and it is around 0.6 K compared to broader transition widths recorded for the other two samples, namely 1.5 K and 1.77 K for Y540-4 and Y-540-10 samples respectively. The table 2 shows the T_c's and ΔT_c's of the three samples with 2, 4 and 10 wt % Ag addition. It can be seen from the $\chi(T)$ behavior that the transition temperatures and widths of transition has an overall improvement with Ag addition across the series, though between 2 and 4 %, there is no perceptible improvement. The improvement in T_c and ΔT_c with Ag addition can be attributed to an improved inter-grain coupling and hence a larger unperturbed area for the supercurrent loop which shows up as a marginal improvement in T_c. Though this might appear contradictory to our belief that Ag substitution for Cu sites in Y-123 lattice should cause the secondary phases to broaden the transition width, we observe that concentration quenching occurring beyond 2 wt % silver addition could not result in any additional increase in secondary phase volume as far as Ag substituted phase composition is concerned. The secondary phase composition $Y_1Ba_2(Cu_{1-x}Ag_x)_3O_{7-\delta}$ has a saturation value [24] for x beyond which any further addition of Ag causes it to only appear as precipitates in the matrix rather than to cause any further substitution of Ag for Cu sites. The additional silver also improved the mechanical properties of the system thereby indirectly helping in marginal improvement in T_c and the transition width.

3.10.2 Magnetization loops and critical current density of the YBCO/Ag superconductor

Magnetization measurements carried out on the samples to record M-H loops, using a Physical Property Measurement System (*Quantum Design*), revealed peak effect around the 2T region for samples Y540-2 and Y540-4 which contain low amounts of silver, namely 2 wt % and 4 wt % Ag. This peak is more pronounced for the Y540-4 sample which has 4 wt % Ag and surprisingly this peak vanishes for the Y540-10 containing 10 wt % Ag.
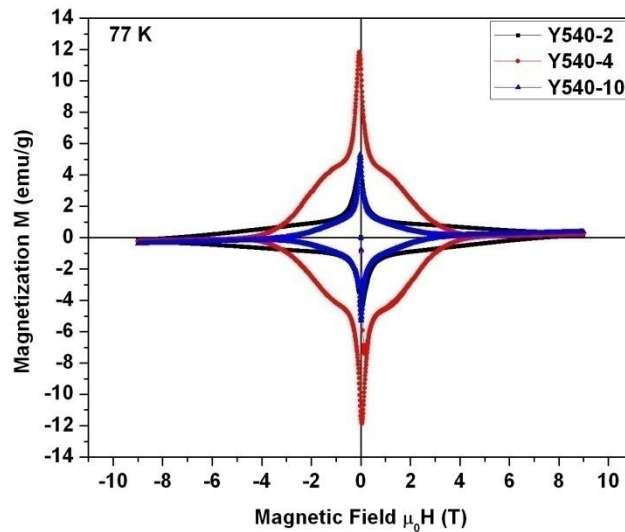
Figure 3.9 M-H loops for the three samples in Y540 series with Ag varying content recorded using a Physical Property Measurement System (QD-PPMS) is shown in the figure.

This can be explained in terms of concentration quenching of silver that occurs gradually beyond 2 wt % silver addition [32]. The magnetization loops as a function of applied magnetic field for the three samples at 77 K is shown below.
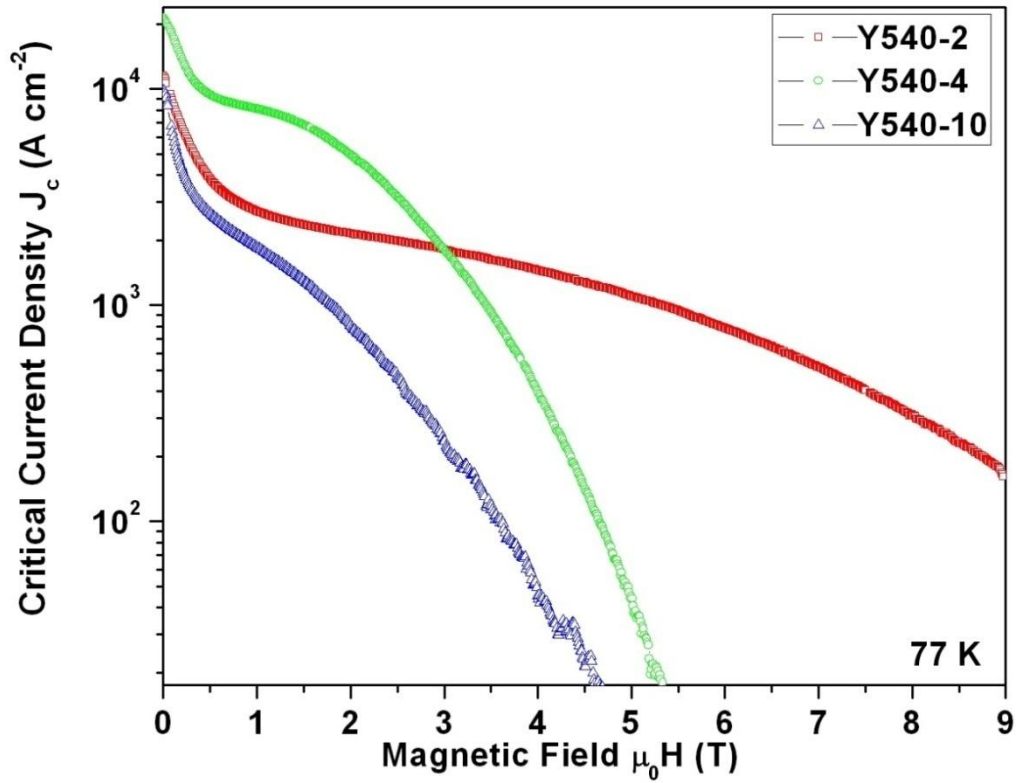

Figure 3.10 The plot of critical current density J_c of the three samples Y540-2, Y540-4, Y540-10 with varying silver content of 2, 4 and 10 wt % respectively as a function of applied magnetic field calculated from M-H loops recorded at 77 K shows a significant reduction in dependence of J_c on H for the sample Y540-2.

The critical current density J_c for all the three samples has been calculated from the M-H loops using Bean's model formula [33-34],

$$J_c = 20 \; \frac{\Delta M}{d} \; A \; cm^{-2}$$

where ΔM is the change in magnetization (in emu/cc units) between the forward and reverse field sweep arms of the M-H loop cycle and 'd' is a geometrical factor involving sample dimensions used for the measurement [35]. The applied field is parallel to the c-axis of the sample and the parallelepiped specimens used for the measurements were approximated to be cylinders for the validity of Bean's model. The magnetic field dependence of the critical current density $J_c(H)$ calculated using the Bean's model formula for the three samples in the Y540 series is shown in fig. 3.10. The critical current density J_c of the sample Y540-2 shows significant reduction on its dependence on applied field even up to fields as high as 9 T. The peak effect exhibited by this sample is around 4.5 T magnetic field whereas the peak effect for the sample Y540-4 with 4 wt % Ag is around the 1.5 T field regime which could be due to oxygen deficiencies [36]. The current carrying properties of the three samples vary drastically probably due to the direct role played by silver partially substituting in the Cu sites, thereby causing a lattice mismatch with the cells where Cu has not been substituted by Ag and also mainly due to the indirect role played by silver in modifying the sample

microstructure vis-à-vis Y-211 particles size, distribution etc as revealed from a deeper analysis of the sample microstructure which we proceed to explain in the next section. The relatively limited performance of the sample Y540-10 having 10 wt% silver content can also be attributed to other effects taking over as concentration quenching of silver occurs beyond 2 wt % and the resultant precipitation of agglomerated silver particles observed to be more prominent in this sample which also possibly playing a role.

Sl. No	Sample Code	Silver content wt %	$J_c(H=0)$ at 77 K (kA.cm^{-2})	Peak Effect Field value $H_P(T)$
1	Y540-2	2 wt%	11.55 kA.cm^{-2}	4.5 T
2	Y540-4	4 wt%	21.33 kA.cm^{-2}	1.5 T
3	Y540-10	10 wt%	9.90 kA.cm^{-2}	1.5 T

Table 3.4 The self-field critical current density and peak effect field values for the three samples are shown in the table revealing a reasonably high $J_c(H=0)$ and high H_P for Y540-2 sample.

It can be observed from the general $J_c(H)$ behavior that the sustainment of J_c up to higher fields seen for the sample Y540-2 is not observed for the other two samples where the fall in J_c beyond 3 T is probably linked

to the Ag concentration quenching and subsequent precipitation in the Y-123 matrix for samples Y540-4 and Y540-10.The table 3.4 shows the self-field current values at 77 K and the peak field values (H_P) for the three samples. The peak fields were taken from the point where change of slope occurs in the $J_c(H)$ curve. The Y540-2 sample has a superior $J_c(H)$ performance compared to the other two samples and it also has a reasonably high self-field J_c value. The Y540-4 sample, on the other hand, has the maximum self-field $J_c(H=0)$ value among the three samples. The microstructural origin of the $J_c(H)$ performance of the three samples with Ag content variation is traced and discussed in the section 3.11.

3.10.3. Pinning behavior and Irreversibility fields of YBCO/Ag samples

The pinning behavior in these samples was studied by calculating the pinning force of the samples from the $J_c(H)$ curves. From the figure 10 below, we can see that the best pinning performance is also exhibited by Y540-2 sample with 2 wt % Ag where the normalized pinning force has its maximum shifted towards higher magnetic field whereas in samples Y540-4 and Y540-10, it is around 1.5 T magnetic field. Another interesting aspect of sample Y540-2 is the broad nature of the pinning force curve compared to the other samples indicating superior

performance of this sample over a wide range of applied magnetic fields. The irreversibility fields H_{irr}, of the samples as function of temperature has been calculated from the critical current density data taken at different temperatures between 77 K and 92 K.
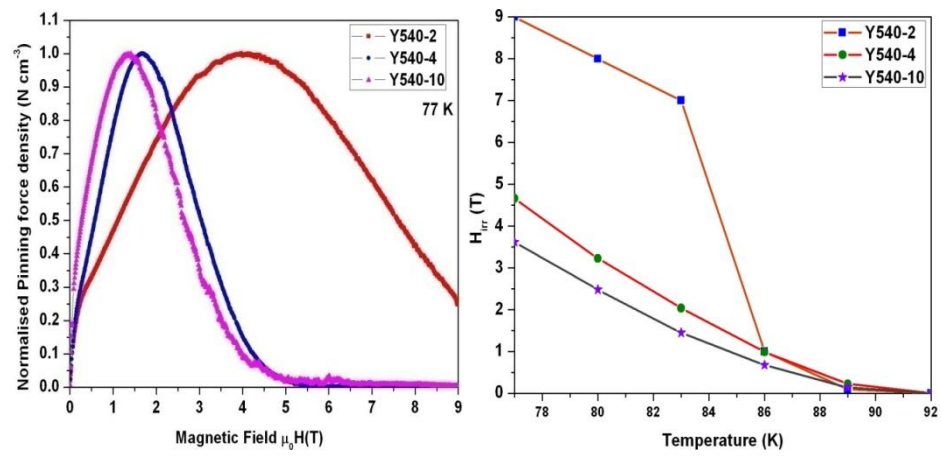

Figure 3.11 (a) The normalized pinning force as a function of magnetic field at 77 K for the three samples and (b) the irreversibility field H_{irr} as a function of temperatures between 77 K and 92 K for the samples showing the better performance of sample Y540-2 on both the counts.

The irreversibility field is taken to be the field at which the current falls to 100 Acm^{-2} in the $J_c(H)$ curve. The irreversibility field of sample Y540-2 at 77 K is greater than 9 T and it is above 7 T even at a temperature of 83 K. The superior performance of sample Y540-2 is analyzed and reasoned out using the microstructural features observed in these samples in the following section.

3.11 Microstructural origin for high current density and superior $J_c(H)$ behavior
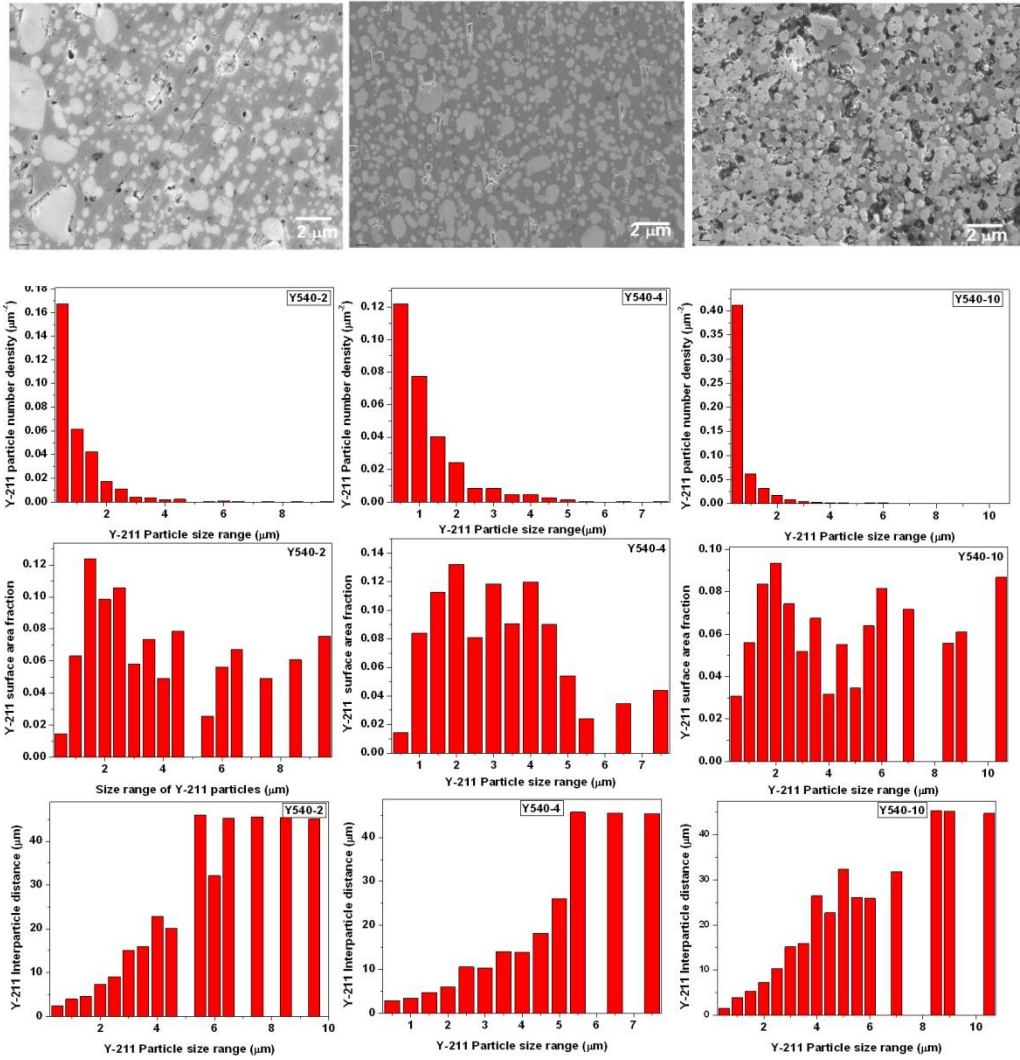
Figure 3.12 The microstructure of the three samples with varying Ag content and the corresponding histograms for Y-211 particle number density, Y-211 surface are contribution to the total area and the Y-211 interparticle distance as a function of Y-211 particle size.

The addition of silver, obviously, is observed to alter and affect the magnetic and superconducting properties of the samples to different extents depending on the silver content as seen from the data in the previous section. Here, the role of silver is found to be two-fold:

1) a direct role wherein Ag substitutes for Cu sites in the Y-123 lattice thereby possibly causing lattice mismatch effects, low-field pinning behavior, transition width broadening etc.,.

2) an indirect role wherein Ag shows concentration quenching effect beyond 2 wt % addition thereby appearing as precipitates in the Y-123 matrix which while causing an improvement in the mechanical

Sl. No	Sample Code	Silver content %	Y-211 Avg. Number Density $(\mu m)^{-1}$	Y-211 volume fraction %	Y-211 Avg. Particle size (μm)	Y-211 Avg. Inter-particle distance (μm)	Porosity (%)
1	Y540-2	2 wt %	0.315	41.54	0.842	4.31922	1.50 %
2	Y540-4	4 wt %	0.296	42.29	0.936	4.55072	1.54 %
3	Y540-10	10 wt %	1.196	45.93	0.515	2.92969	4.50 %

Table 3.5 The table shows the effect of Ag addition on the sample microstructure with respect to Y-211 phase particles and macroscopic defects structure in terms of porosity in the system.

properties also affects the superconducting properties considerably by modifying the microstructure of the non-superconducting secondary

phase Y-211 particles to exhibit variation in size, shape, distribution etc which are very crucial aspects for superior performance of the samples. From the histograms, we can observe that the Y-211 particle size, shape and distribution are hugely impacted by Ag addition. For the Y540-10 sample, the particle sizes are refined significantly, but this has not been positively transformed into a superior $J_c(H)$ performance in this sample. The table 3.4 below gives a complete picture of the microstructure with respect to Y-211 phase and porosity in these samples. It can be observed that all the above parameters play a combined role which is crucial in determining the $J_c(H)$ behavior of the samples. The Y-211 volume fraction shows a linear increase with increasing Ag content whereas the Y-211 particle size increases by a small amount between 2 wt % and 4 wt % Ag addition and then decreases considerably for the 10 wt % Ag added sample. The Y-211 interparticle distance also decreases with Ag addition after an initial increase. The porosity, a measure of macroscopic pores and voids in the system, increases with increase in Ag addition which is not expected. This may be attributed to the overall effect Ag addition has on the system in terms of modifying the microstructure with respect to Y-211 phase particles. Thus, though porosity is expected to improve with increased Ag addition, it does not improve mainly due to the modified Y-211 microstructure in terms of Y-211 volume fraction, size, number density and interparticle distance.

From figure 3.10, we observe that while the J_c(H=0) is maximum for the Y540-4 sample, the overall J_c(H) performance is superior for the Y540-2 sample. The higher J_c(H=0) value observed for the Y540-4 sample can be explained in terms of the parameters discussed above such as Y-211 size, number density, volume fraction and porosity being close to optimum values, all favoring a superior self-field current density J_c(0). The J_c(H) of this sample Y540-4 reaches lower values beyond 5 T though its J_c(0) is the highest. The origin of this fall in J_c can be attributed to the kind of pinning behavior exhibited by this sample. The pinning is strong around 1.5 T for this sample and typically the peak effect in this field regime (1.5 T to 2 T) has been known to be due to oxygen deficiency or interfacial defects in the material. The pinning occurring at around 1.5 T is not strong enough in this sample to retain the J_c to higher values. The sustainment of J_c up to higher fields requires another crucial parameter which we discuss in the next subsection where we discuss the possible cause of sustainment of J_c up to higher magnetic field values of the order of 9 T as observed in Y540-2 sample.

3.11.1 Origin of twins and twinning leading to sustainment of J_c to higher fields

In order to trace the microstructural origin of sustained J_c up to higher magnetic fields, i.e., significant reduction in magnetic field dependence of critical current density $J_c(H)$ [37], we recorded FESEM images at higher resolution for the three samples.
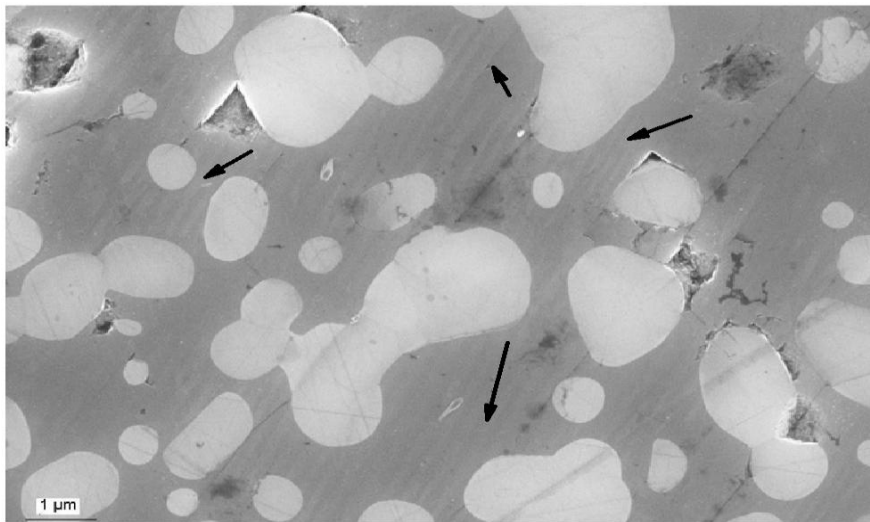
Figure 3.13 High magnification FESEM image of the Y540-2 sample shows presence of twins in the Y-123 matrix. The extensive twinning present in the sample is indicated here by arrows. It can be observed that the twin width is of the order of 20 nm and individual twinned regions extend to a few microns.

Our higher magnification FESEM images of Y540-2 sample revealed significant presence of twins distributed throughout the Y-123 matrix in

this sample. The figure 12 below reveals the presence of twins in region of the Y540-2 sample. Twins have been known to form as a result of the stresses caused in the material owing to the structural changes that occur in the material [38]. In the YBCO system, the material undergoes a transition from tetragonal to orthorhombic state as it is oxygenated and it has been observed that this gives rise to the possibility of twins in the material. The formation of twins can hence be directly linked to mainly the Y-211 inter-particle distance as too small a distance can affect twin formation [39-40]. This is equivalent to having an appropriate Y-211 particle number density in the material as the inter-particle distance is linked to the number density of Y-211 particles as follows.

If 'n' is the number of Y-211 particles per unit area as observed for the two-dimensional FESEM images, i.e., the areal number density of Y-211 particles,

$$n_{211} = \frac{number\ of\ Y - 211\ particles\ in\ a\ given\ area}{observed\ crossectional\ area}$$

then, the number of Y-211 particles per unit length N_{211} is given by

$$N_{211} = n_{211}^{1/2} = \frac{number\ of\ Y - 211\ particles}{unit\ length\ of\ the\ sample}$$

Therefore the average inter-particle distance (IPD) between the Y-211 particles is calculated as

$$IPD_{211} = (1 - V_{211})/N_{211}$$

where V_{211} is the phase volume fraction of the Y-211 phase particles which is equal to the area fraction of Y-211 particles as estimated from the micrographs [41-42]. Recently, it has been understood through Scanning SQUID microscopy that the vortices avoid getting pinned at the twin boundaries [43]. Twin boundaries act as strong barriers for vortex motion which leads to enhancement of critical current density subsequent to an enhancement in superfluid density on twin boundaries in the high T_c superconductor $Ba(Fe_{1-x}Co_x)_2As_2$.
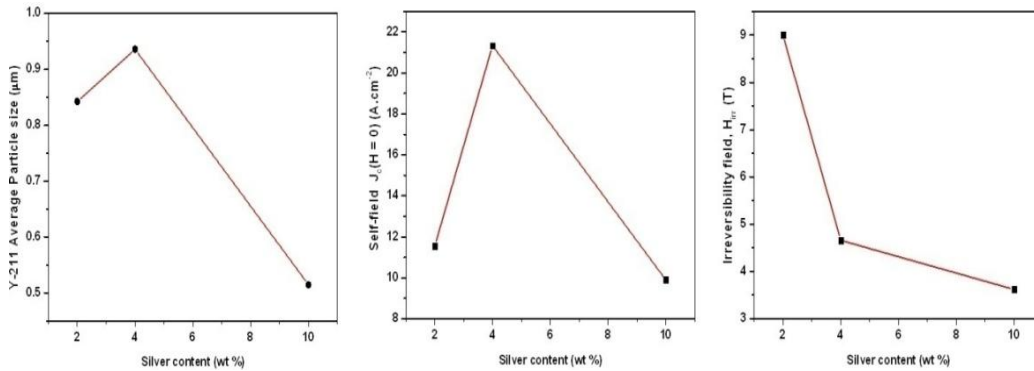
Figure 3.14 The variation of average particle size of the Y-211 particles, Jc(0) and irreversibility field H_{irr} as a function of Ag content in Y540 series of samples is shown indicating that while $J_c(0)$ follows Y-211 particle size which in turn is a function of Ag content H_{irr} depends on other parameters as well such as twinning etc.

A similar mechanism may explain the enhancement of J_c and its sustainment up to high fields in the sample Y540-2 in the present work

as twins have been observed by us only in this sample through our FESEM images. The occurrence of twins in this material has pushed the pinning to higher fields around 4.5 T and hence the $J_c(H)$ behavior of this sample is improved and decent values of J_c's are observed even up to 9 T field. Apart from the requirement of existence of twins, we observe that it is very important to have an appropriate microstructure such as distribution of Y-211 particles, their size, shape and the inter-particle distance between them as a possible criterion for having substantial twinning in the material. A combination of all these factors determines the current carrying behavior of this material. Thus from the microstructural analysis, we find that the metallic Ag added to make the YBCO/Ag composites has a silver concentration quenching beyond 2 wt% Ag addition. The Ag added has a dual role – a direct role where some amount of Ag substitutes for Cu in YBCO lattice thereby modifies the properties significantly and -- an indirect role where it modifies the microstructural properties of the secondary Y-211 phase thereby affecting the superconducting properties. We have found that optimum Ag addition is below 4 wt % in terms of both $J_c(0)$ value and overall $J_c(H)$ behavior as for the 10 wt % Ag addition, there is a substantial deterioration in superconducting properties. We have also traced the microstructural origin of high self-field critical current density and sustainment of critical current density to high magnetic fields.

3.12 Effect of compaction pressure on the properties of YBCO/Ag superconducting composites

We have carried out a study and analysis to establish the effect of compaction pressure on the properties of YBCO/Ag composite superconductors as pressure has a very significant role in modifying the properties of bulk samples prepared by IGP [44]. In the preceding sections, we had discussed on the role of metallic silver addition on the properties of YBCO/Ag samples of Y540 series where the number 540 following Y signifies the compaction pressure applied to the Y-211 target pellet used for infiltration of liquid phases. In order to study the effect of pressure, we prepared series of YBCO/Ag samples coded Y460 with varying silver content. The samples in this series have been labeled as Y460-2, Y460-4 and Y460-10 with 2 wt %, 4 wt % and 10 wt % metallic Ag addition respectively. We have zeroed in on these two values for compaction pressure since from an earlier study carried out in our group we have found that the optimum compaction pressure for Y-123/Y-211 system by IGP is around 460 MPa and 540 MPa [43]. In the following subsections we proceed to discuss various properties of Y460 series samples in comparison with Y540 series.

We focus our attention mainly on variation of microstructural and superconducting properties with compaction pressure between Y460 and Y540 series of samples.

3.12.1 Effect of compaction pressure on the microstructural features of YBCO/Ag samples

In the previous sections, we have discussed the effect of Ag addition on the microstructural and superconducting properties of YBCO/Ag superconductors by varying the Ag content in the samples for a given compaction pressure. In this section, we devote our attention to studying the microstructural changes between the samples prepared by applying two different compaction pressures while varying the Ag content across a pressure series. In this manner, we would be able to study the effect of compaction pressure on the microstructural and superconducting properties of YBCO/Ag composite superconductors. We focus on the microstructural features in the present subsection.

A comparison of the left and right column of histograms, representing samples compacted with 460 MPa and 540 MPa respectively, reveals significant size refinement of Y-211 particles with increased pressure across all values of Ag addition along the series.

Silver content wt %	Y460 series – 460 MPa pressure compacted samples	Y540 series- 540 MPa pressure compacted samples
2 wt %		
4 wt %		
10wt %		
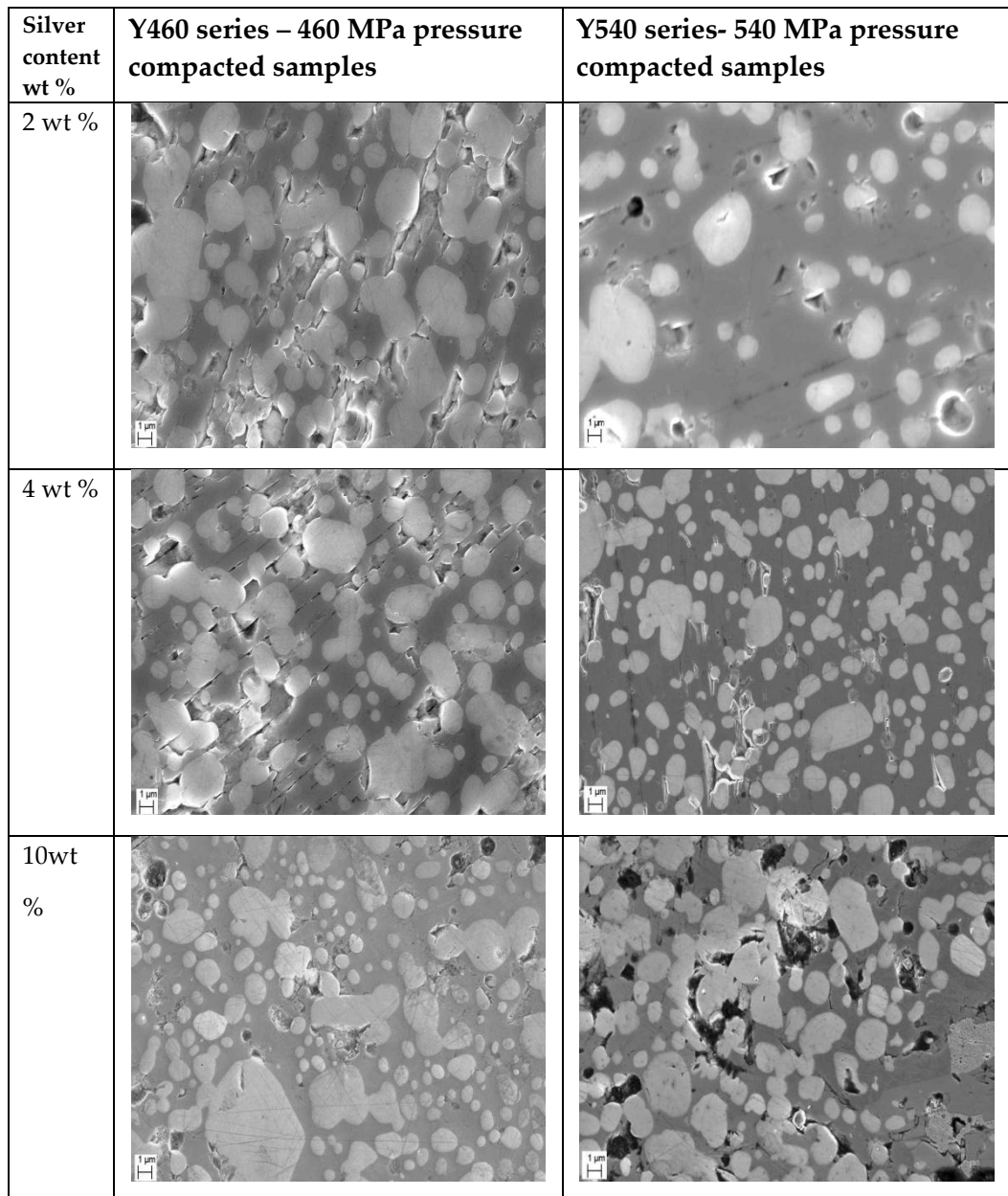
Figure 3.15 The FESEM images of the YBCO/Ag samples compacted with different pressures showing significant microstructural variations of features with compaction pressure across varying silver contents.

Silver content wt %	Y460 series – 460 MPa pressure compacted samples	Y540 series- 540 MPa pressure compacted samples
2 wt%		
4 wt%		
10wt%		
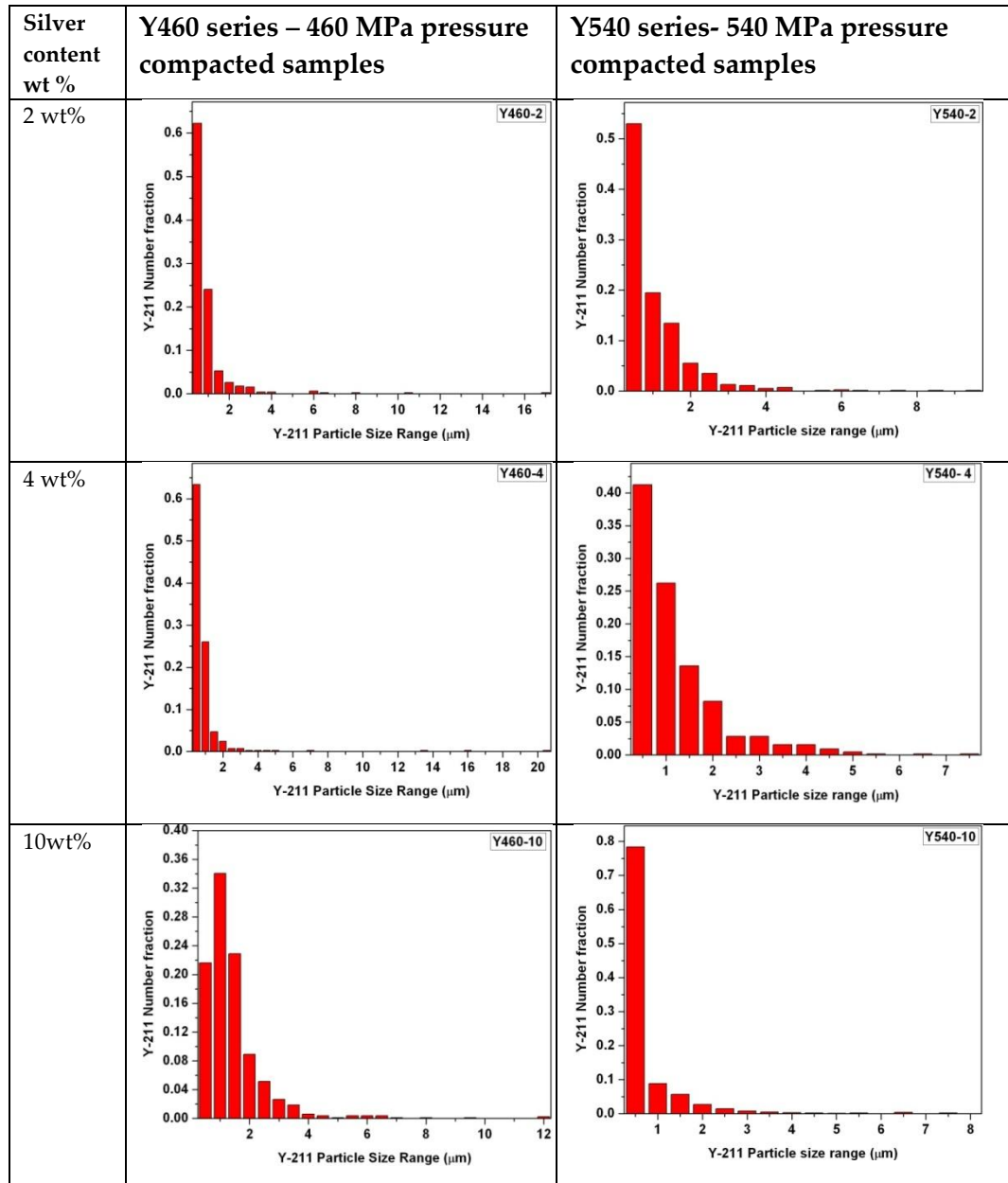
Figure 3.16 Histograms of number fraction of Y-211 according to the particle size ranges of the YBCO/Ag samples compacted under different pressures.

From the microstructure, important parameters such as Y-211 number density, Y-211 volume fraction and Y-211 interparticle distance have been calculated and a comparison of these parameters between the two series of samples can be made from the plots given below.
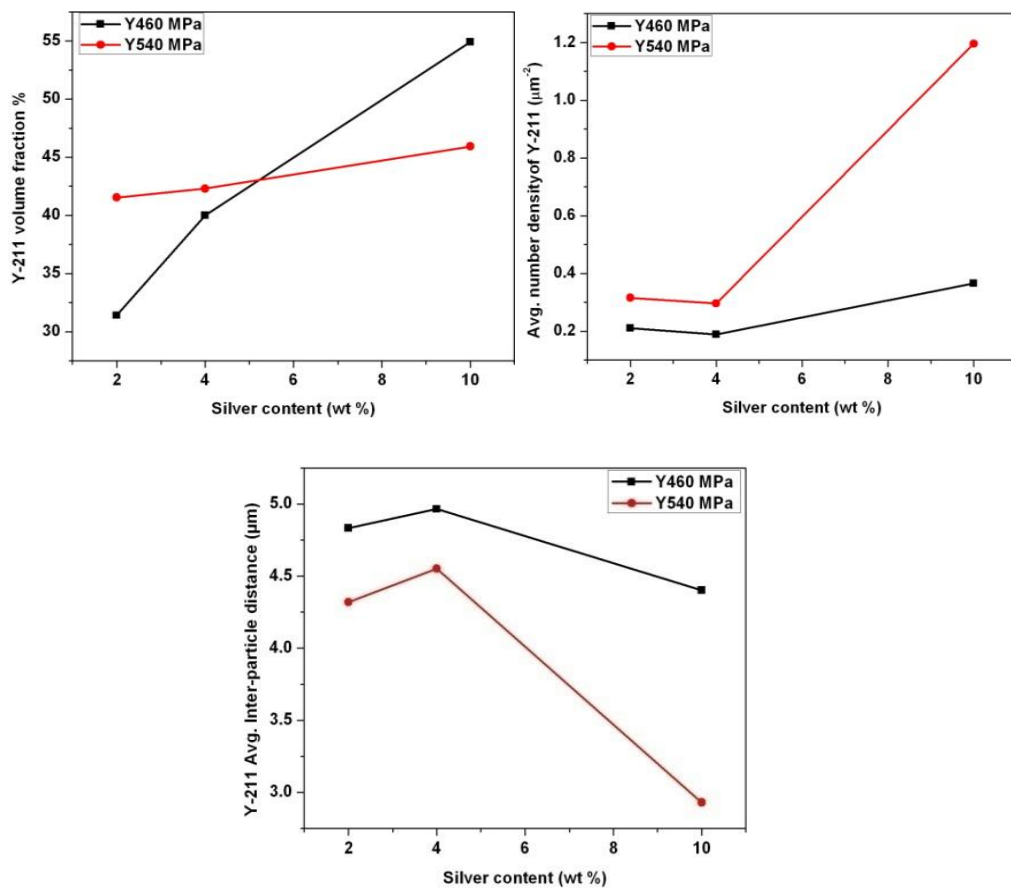
Figure 3.17 The variation of Y-211 number density, volume fraction and interparticle distance between the two series of samples compacted under different pressures.

The above figure illustrates the importance of microstructural features to attain better superconducting performance of the samples. The Y540 series has a rapid increase of Y-211 number density with increasing Ag content whereas it is slower for the Y460 series implying a higher defect density for the samples in Y540 series. The Y-211 volume fraction for the Y540 series has a gradual increase with increasing Ag content and rapid fall in Y-211 interparticle distance compared to the Y460 MPa series. All these factors contribute to the superconducting performance of the samples. It can be seen from the histograms that the samples in Y540 series have no Y-211 particles of size greater than 10 μm whereas Y460 series samples have some larger Y-211 particles also.

The histograms show that the size refinement of Y-211 particles aided by the higher compaction pressure leads to an improvement in superconducting properties of the Y540 series samples as discussed in the following subsections.

3.12.2 Effect of compaction pressure on temperature dependence of ac susceptibility

The effect of compaction pressure on the $\chi(T)$ behavior of the Y460 series can be compared with the Y540 series for each value of Ag wt %

addition. The figure below shows the variation between the two series across different Ag content.
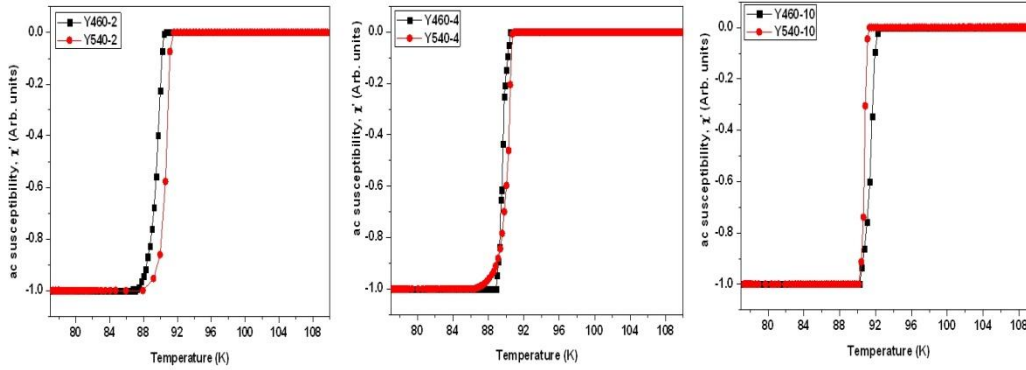
Figure 3.18 The effect of compaction pressure on the ac susceptibility as a function of temperature between Y460 and Y540 pressure series samples across varying Ag content

From the fig. 3.18, it can be seen that the samples compacted at a higher pressure of 540 MPa have a higher T_c compared to the samples compacted at 460 MPa, but this effect of pressure is gradually swamped by Ag addition. For a high silver addition of 10 wt %, we can see that the sample compacted at lower pressure of 460 MPa has a slightly better T_c. The transition widths ΔT_c's however have no systematic dependence on compaction pressures.

3.12.3 Effect of compaction pressure on $J_c(H)$ and $F_P(H)$ behavior

The Y460 series samples compacted with a pressure of 460 MPa showed similar consistency in behavior as far as Ag addition is concerned. The plots below show the effect of compaction pressure on the $J_c(H)$ and $F_P(H)$ behavior of these samples in comparison with the Y540 series of samples across varying silver content.
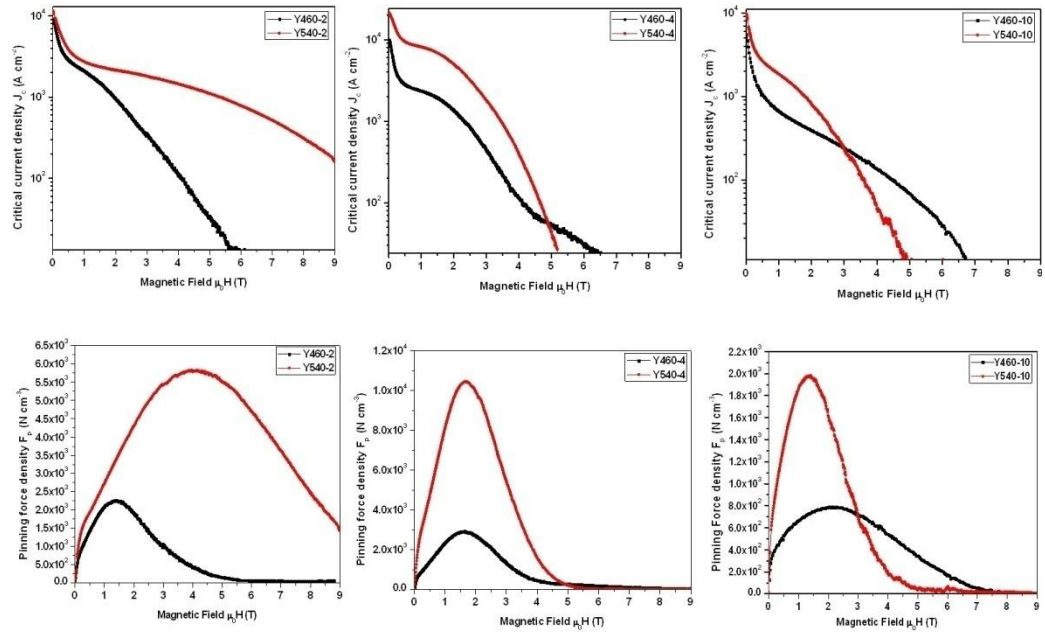
Figure 3.19 The $J_c(H)$ (top) and $F_P(H)$ (bottom) behavior of the YBCO/Ag composite samples and their variation with pressure across varying silver content.

From the above figure, we can observe the variation of critical current density, $J_c(H)$ and Pinning force density, $F_P(H)$ between two different

compaction pressure series samples, namely, Y460 – compacted with 460 MPa and Y540- compacted with 540 MPa. For a given amount of silver addition, we can see that, generally the higher compaction pressure of 540 MPa provides samples with superior $J_c(H)$ and $F_P(H)$ behavior. But, the situation becomes complex for higher Ag addition. Particularly for the 10 wt % Ag addition, the effect of silver addition starts to swamp the effect of compaction pressure which can be seen as gradual changes in $J_c(H)$ and $F_P(H)$ behavior across increasing Ag addition.

3.12.4 Effect of compaction pressure on $H_{irr}(T)$ behavior

The irreversibility fields $H_{irr}(T)$ as a function of temperature is also found to be higher for the samples compacted with 540 MPa compaction pressure compared to samples of 460 MPa pressure as shown in figure 3.16 below across varying silver content. From figure 3.16, which shows the effect of compaction pressure on the irreversibility fields $H_{irr}(T)$ across varying Ag content between Y460 and Y540 series, it can be observed that the higher compaction pressure of Y540 has a better H_{irr} fields generally. But the advantage provided by the higher pressure gradually subsides as Ag content is increased. For the 10 wt % Ag added samples Y460-10 and Y540-10, the difference in $H_{irr}(T)$ behavior is not very significant with compaction pressure.
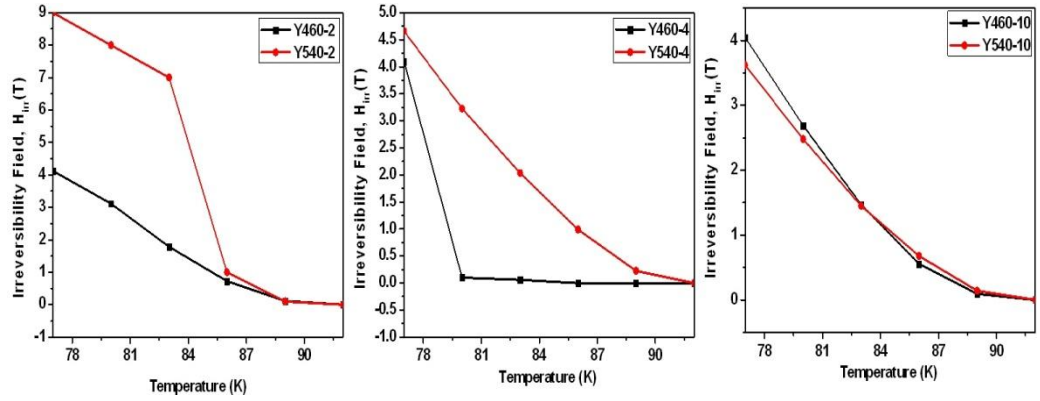
Figure 3.20 The effect of compaction pressure on the Irreversibility fields of the sample as a function of temperature across varying silver content is shown between Y460 and Y540 series samples

Hence, from the $\chi(T)$ $J_c(H)$, $F_p(H)$ and $H_{irr}(T)$ behaviors, we observe that the twin effects of Ag addition and compaction pressure on YBCO/Ag superconducting composites are have been studied. Based on the above analyses, one can conclude that, generally, increased Ag addition tends to swamp the effect of compaction pressure on the samples and that for superior performance, the optimum Ag content depends on compaction pressure as well and vice-versa. These two parameters namely, Ag content and compaction pressure seem to be functions of one another and that as we increase the compaction pressure lower amount of Ag addition seems to offer similar performance in terms of superconducting properties.

References

[1] K. Jeong, D. Y. Kim, Y. K. Park, K. W. Lee, and J. C. Park, *Physica C* **185-189**, 2393 - 2394 (1991).

[2] E. S. Reddy and T. Rajasekharan, *Supercond. Sci. Technol.* **11**, 523 (1998).

[3] K. Iida, N. H. Babu, Y. Shi, and D. A. Cardwell, *Supercond. Sci. Technol.* **18**, 1421 (2005).

[4] P. Diko, V. Antal, M. Kaňuchová, M. Jirsa, and K. Jurek, *Physica C* **470,** 155–158 (2010).

[5] N. H. Babu, Y.-H. Shi, A. R. Dennis, S. K. Pathak, and D. A. Cardwell, *IEEE Trans. Appl. Supercond.* **21** (3), 2698-2701 (2011).

[6] G.-Z. Li, W.-M. Yang, X.-F. Cheng, J. Fan, and X.-D. Guo, *J. Mater Sci.* **44,** 6423–6426 (2009).

[7] R. Cloots, T. Koutzarova, J.–P. Mathieu, and M. Ausloos, *Supercond. Sci. Technol.* **18**, R9–R23 (2005).

[8] J.-P. Mathieu, T. Koutzarova, A. Rulmont, J.-F. Fagnard, Ph. Laurent, B. Mattivi, Ph. Vanderbemden, M. Ausloos, and R. Cloots, *Supercond.Sci. Technol.* **18**, S136 (2005).

[9] N. D. Kumar, T. Rajasekharan, and V. Seshubai, *Supercond. Sci. Technol.* **24**, 085005 (2011).

[10] H. Fang, K. Ravi-Chandar, *Physica C* **340**, 261-268 (2000).

[11] E. S. Reddy, N. H. Babu, Y. Shi, D. A. Cardwell, and G. J. Schmitz, *Supercond. Sci. Technol.* **18**, S15 (2005).

[12] S. Umakoshi, Y. Ikeda, A. Wongsatanawarid, C.-J. Kim, and M. Murakami, *Physica C* **471**, 843–845 (2011).

[13] E. S. Reddy and T. Rajasekharan, *J. Mater. Res.* **13** (9), 2472-2475 (1998).

[14] J. Šesták, *Pure & Appl . Chem.* **64** (1), 125-136 (1992.).

[15] U. Wiesner, G. Krabbes, M. Ueltzen, C. Magerkurth, J. Plewa, and H. Altenburg, *Physica C* **294**, 17–22 (1998).

[16] Y. Zhao, C. H. Cheng, and J. S. Wang, *Supercond. Sci. Technol.* **18**, S43 (2005).

[17] J. W. Kell, B. C. Harrison, T. J. Haugan, C. V. Varanasi, M. Rane, and F. Ramos, *Appl. Phys. Lett.* **89** (1), 012503 – 012503-3 (2006).

[18] V. Antal, M. Kaňuchová, M Šefčiková, J. Kováč, P. Diko, M. Eisterer, N Hörhager, M. Zehetmayer, H. W. Weber, and X. Chaud, *Supercond. Sci. Technol.* **22**, 105001 (2009).

[19] P. Diko, V. Antal, M. Kaňuchová, M. Šefčiková, and J. Kováč, *J. Phys.: Conf. Ser.* **153**, 012009 (2009).

[20] A. Manthiram and J. B. Goodenough, *Nature* **329**, 908 (1987).

[21] D. Bahadur, A. Banerjee, A. Das, K. P. Gupta, T. Mathews, A. Mitra, M. Tiwari, and A. K. Majumdar, *Rev. Sol. Stat. Sci.* **2**, 77 (1988).

[22] P. Muné, E. Govea-Alcaide, R. F. Jardim, *Physica C* **384**, 491–500 (2003).

[23] C. Vipulanandan and S. Salib, *J. Mater. Sci*. **30**, 763-769 (1995).

[24] Ch. Zhang, A. Kulpa, A. C. D. Chaklader, *Physica C* **252**, 67-78 (1995).

[25] B. R. Weinberger, L. Lynds, D. M. Potrepka, D. B. Snow, C. T. Burila, H. E. Eaton Jr., R. Cipolli, Z. Tan, and J. I. Budnick, *Physica C* 161, 91 (1989).

[26] D. Cahen, Z. Moisi, and M. Schwartz, Mater. Res. Bull. **22** (11), 1581-1588 (1987).

[27] P. Diko, V. Antal, M. Kaňuchová, M. Jirsa, and K. Jurek, *Physica C* **470** (2), 155-158 (2010).

[28] J. J. Roa, X. G. Capdevila, M. Martínez, F. Espiell, and M. Segarra, *Nanotechnology* **18**, 385701 (2007).

[29] W. C. Oliver and G. M. Pharr, *J. Mater. Res*. **7** (6), 1564 (1992).

[30] W. C. Oliver and G. M. Pharr, *J. Mater. Res.* **19** (1), 3 (2004).

[31] D. Behera, N. C. Mishra, and K. Patnaik, *J. Supercond.* **10** (1), 27 (1997).

[32] A. K. Pradhan, B. K. Roula, V. V. Raoa, and V. R. Kalvey, Cryogenics **33** (9), 910-913 (1993).

[33] C. P. Bean, *Phys. Rev. Lett.* **8**, 250 (1962).

[34] C. P. Bean, *Rev. Mod. Phys.* **36**, 31 (1964).

[35] D. X. Chen and R. B. Goldfarb, *J. Appl. Phys.* **66**, 2489 (1989).

[36] H. Küpfer, Th. Wolf, C. Lessing, A. A. Zhukov, X. Lançon, R. Meier-Hirmer, W. Schauer, and H. Wühl, *Phys. Rev.* B **58**, 2886-2894 (1998).

[37] N. D. Kumar, T. Rajasekharan, R. C. Gundakaram and V. Seshubai, *IEEE Trans. Appl. Supercond.* **21** (6), 2612-2620 (2011).

[38] Z. Tingjie, W. Keguang, Z. Hian, and W. Shunqlan, *Supercond. Sci. Technol*. **2**, 118-121 (1989).

[39] S. K. Chen, L. Zhou, K. G. Wang, X. Z. Wu, P. X. Zhang, Y. Feng, *Physica C* **377** (4), 571–577 (2002).

[40] L. Wu, S. V. Solovyov, H. J. Wiesmann, D. O. Welch, and M. Suenaga, *Supercond. Sci. Technol.* **16**, 1127–1133 (2003).

[41] L. Mei and S.-W. Chan, *J. Appl. Phys*. **98**, 033908 (2005).

[42] P. Diko and D. Šuster, *J. Appl. Phys.* **105**, 063503 (2009).

[43] B. Kalisky, J. R. Kirtley, J. G. Analytis, J.-H. Chu, I. R. Fisher, K. A. Moler, *Phys. Rev. B* **83**, 064511 (2011).

[44] N. Devendra Kumar, *PhD Thesis*, Univ. of Hyderabad, India (2011).

CHAPTER 4

LEVITATION AND SUSPENSION FORCES OF YBCO/Ag SUPERCONDUCTORS, SAMPLE GEOMETRY DEPENDENCE OF THESE FORCES, RELAXATION BEHAVIOR OF LEVITATION AND SUSPENSION FORCES

4.1 Introduction

The ability of a superconducting material to lift and suspend permanent magnets in air without contact defines the phenomenon of superconducting levitation and suspension respectively. Levitation of a magnetic object occurs when a magnet is hoisted over a superconductor cooled to temperatures below its transition temperature, T_c. Levitation by the superconductor results from its ability to diamagnetically shield itself from any external magnetic field change [1-13]. As the field due to the permanent or electromagnet tries to penetrate the superconductor, the superconductor generates shielding currents which are circular currents at the surface of the material, which in turn, produce moments that oppose the applied magnetic field. In effect, levitation is a clear-cut signature of Meissner effect [14]. Perfect conductors with zero resistance

cannot exhibit Meissner effect. A perfect way to assess the pure diamagnetism of superconductors is to Field-cool the material and to observe the levitation of the magnet above the superconductor due to flux expulsion. But, in practical conditions, the high T_c superconductors may not exhibit this kind of levitation due to several factors such as the magnitude of the applied field, the weight of the magnet, the nature of flux pinning in the superconductor etc [15-18]. Thus, the levitation experiments with high T_c superconductors involve Zero-field cooling (ZFC) the material and then placing the permanent magnet on top to observe the phenomenon of levitation. The suspension effect, on the other hand, is realized as the superconducting material is field-cooled (FC) by a magnet placed over it. The field, in this case, has already penetrated into the material and on cooling, the flux gets trapped inside. The trapped flux results in the phenomenon of suspension as we try to remove the magnet from the superconductor. The suspension force, thus, is mainly an attractive force whereas the levitation force is repulsive in nature. The quantification of levitation and suspension is achieved by quantifying the forces exhibited by the superconductor on the magnet during the occurrence of these phenomena.

Some of the applications of bulk superconductors include their use as trapped field magnets, as contactless bearings in flywheels and energy

storage devices, in maglev (such as SCMaglev) systems etc. The measurement of levitation and suspension force of the bulk superconducting samples hence forms an important part of characterization of superconductors in order to assess their suitability for applications.

4.2 Measurement of Levitation and Suspension force of YBCO/Ag superconductors

The measurement of levitation and suspension forces involved using a home-made setup consisting of an electronic balance mounted on a movable X-Y platform as described in chapter 2. The samples used in the study include the two series of YBCO/Ag samples discussed in the previous chapter viz., Y540 and Y460 series. The schematic diagram of the homemade levitation and suspension force measuring set-up is shown in figure 4.1. The set-up consists of a digital depth gauge attached to a vertical column supporting the sample in a cryocontainer made of glass. The depth gauge measures the distance between the superconductor and the permanent magnet during the force measurements. A continuous supply of liquid nitrogen into the cryo-container, to cool the superconductor, is ensured. The X-Y position of the magnet with respect to the sample is adjusted initially by bringing

sample closer to the magnet and adjusting the x-y position of the magnet to obtain maximum force value. This ensures alignment of the center of the magnet and that of the sample along a single, common z-axis.
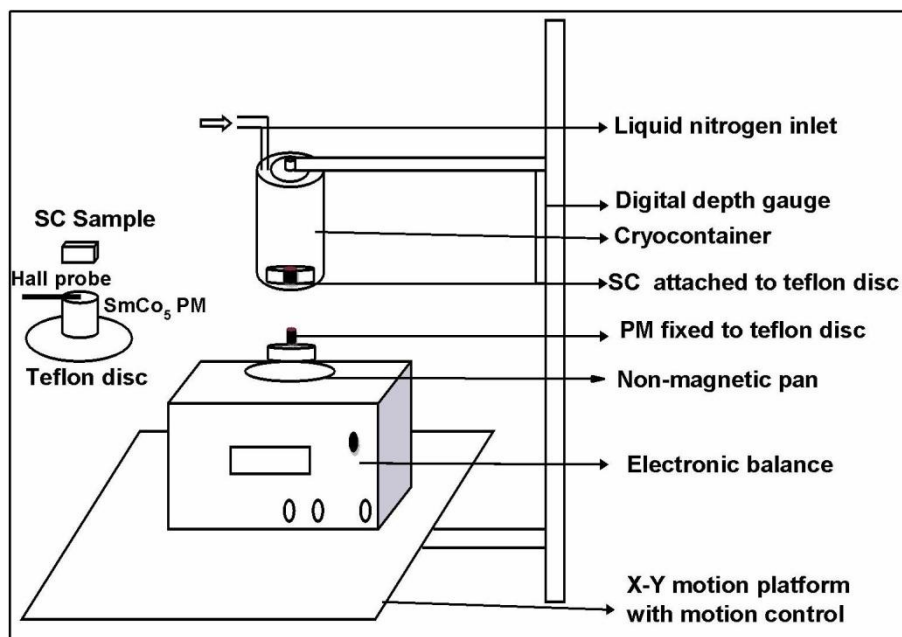
Figure 4.1 Schematic of the homemade set-up used to measure levitation and suspension force

In a separate experiment, the field profile of the permanent magnet is measured using a Hall probe to obtain the variation of field offered by the magnet along its z-axis. The result of this experiment is plotted in figure 4.2 below. The field profile of the permanent magnet was measured in order to convert the gap distance between the superconductor and the permanent magnet in the levitation force

measurement experiment into corresponding applied field values due to the permanent magnet on the surface of the superconductor.
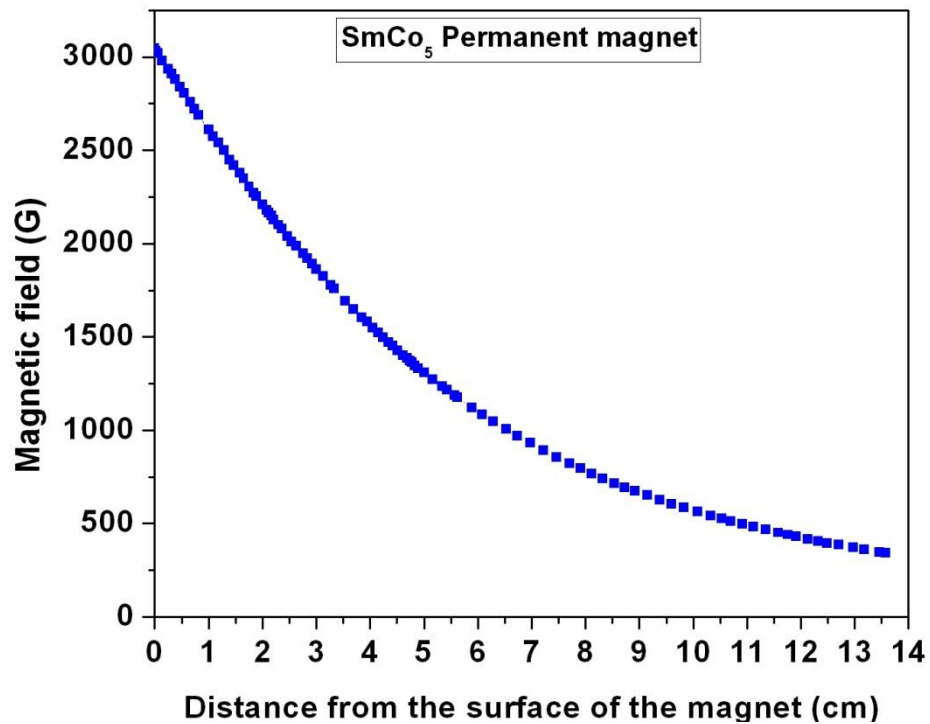
Figure 4.2 Field profile of the permanent magnet along the z-axis from the top
surface

From this conversion, we could plot the levitation or suspension force as a function of the applied field due to the permanent magnet. An essential approximation of this approach is the assumption that the superconductor experiences a uniform magnetic field due to the permanent magnet along its thickness (z-axis length) thereby assuming the field at the surface of the superconductor due to the permanent

magnet as the field on the entire bulk of the superconductor. Assumption of homogeneity and uniformity of applied magnetic field on the superconductor simplifies the problem while allowing us to concentrate on the quantification of levitation and suspension forces.

The levitation force of the samples was measured by cooling the sample, below its superconducting transition temperature, to around 77 K and slowly bringing the sample closer in steps towards the permanent magnet kept on the weighing pan. The change in weight of the magnet due to the levitation force offered by superconductor is taken to be the levitation force. This way we approach the magnet in steps while measuring the change in weight at each step till we reach the closest distance of approach. The closest distance of approach is limited mainly by the thickness of the wall of the cryocontainer. At this point, the superconductor is again taken away from the magnet in steps, while continuing to measure the force, till it reaches the starting point. The force curve for the approach and for the recession of the superconductor does not retrace the path due to the irreversibility of the type-II superconductors. The entire cycle of approach and recession produces a hysteresis loop. The levitation hysteresis loops as a function of gap distance between the superconductor and the permanent magnet for the samples in Y460 and Y540 series is shown in figure 4.3.
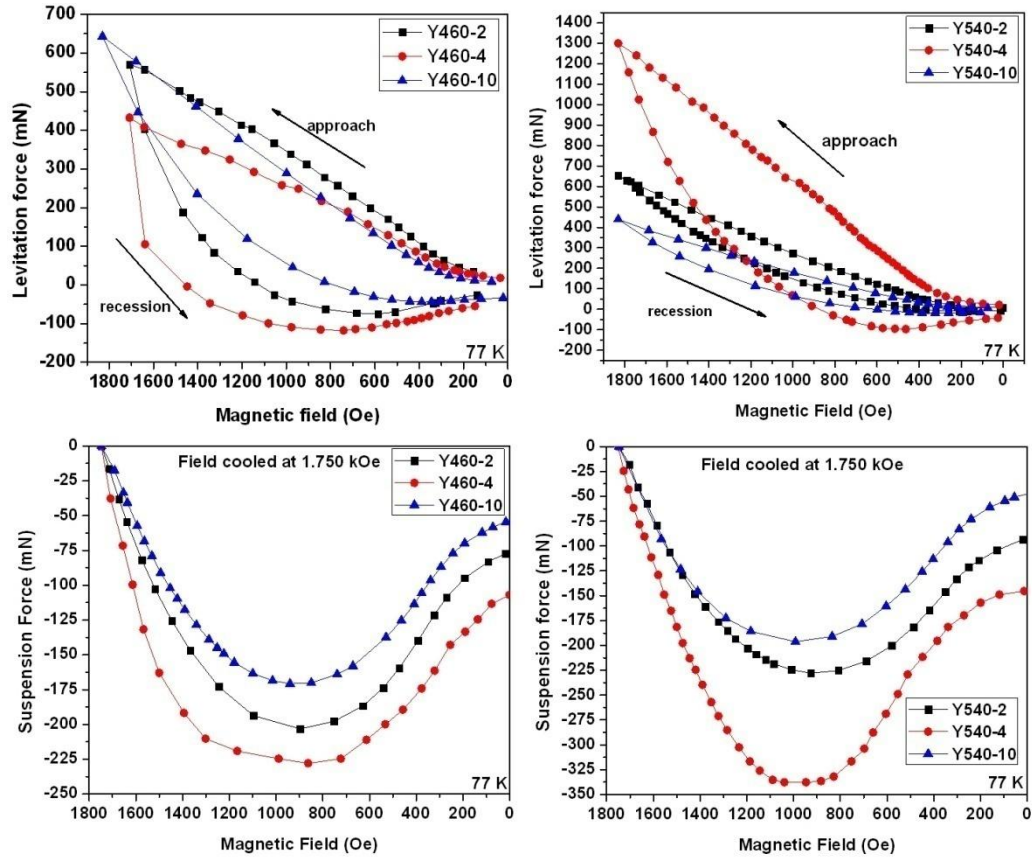
Figure 4.3 Levitation hysteresis loops and suspension curves for Y460-Ag and
Y540-Ag samples as a function of field at the surface of the
superconductor

The samples in the Y460 series, compacted with 460 MPa pressure, are
Y460-2, Y460-4 and Y460-10 with 2 wt %, 4 wt % and 10 wt % Ag
addition respectively. Similarly samples in the Y540 series, compacted
with 540 MPa pressure, are Y540-2, Y540-4 and Y540-10 with 2 wt %, 4
wt% and 10 wt % Ag respectively. The samples used for the above

measurements were parallelepiped in shape with face area 1.6 cm x 1.6m and thickness of 0.8 cm. The samples differed in weight from 11 g to 12 g. The permanent magnet used in the measurements was a $SmCo_5$ magnet weighing 20.36 g, of cylindrical shape with diameter 1.6 cm and height 1.25 cm.

The levitation hysteresis loop, in fact, consists of two segments namely the approach segment and the recession segment where the superconductor approaches the magnet and recedes form the magnet respectively. In our experiment, the maximum field at the surface of the magnet was measured to be 3045 Oe. But, in practice, it is impossible to go too close to get this kind of field value as the wall of the cryo-container holding the sample has a thickness of around 2.5 mm. The maximum field obtainable at the sample surface hence reduces to, approximately, 1850 Oe. As the superconductor approaches the magnet, the field at the surface of the sample increases from 0 Oe to the maximum field value, at the closest distance of approach. Hence, during the approach segment the superconductor is taken from completely Meissner state to vortex state, since the Hc_1 values for these materials typically are around 400-600 Oe at 77 K as seen in our magnetization measurements to record M-H loops discussed in chapter 3. So, one can safely assume that the sample goes to mixed state during the approach

segment. During the recession from the closest point of approach, the force curve shows hysteretic behavior and at a particular distance the levitation force becomes attractive and takes negative values as the magnet is lifted from the pan and there is a corresponding weight reduction of the magnet to negative values. The curve takes a dip over a field regime before reaching the baseline of the force (Y=0 axis) where the superconductor has receded far enough to exert any more force on the magnet. The dip in the shape of the curve is a consequence of the field penetration in the mixed state and the associated flux pinning by the superconductor [19]. The difference in force values at each field between the approach segment and the recession segment is a function of the flux pinning the details of which we shall discuss in the following sections. This completes one cycle of levitation hysteresis loop.

The two plots in the top row of fig 4.3 represent the levitation curves of three samples in each of the two series namely Y460-Ag and Y540-Ag with 2 wt %, 4 wt % and 10 wt % Ag addition. The two samples in Y460 and Y540 series were compacted with 460 MPa and 540 Mpa pressures respectively. It can be seen from the top row of plots that the levitation force loop area is maximum for the samples containing 4 wt % Ag in both the Y460-Ag and Y540-Ag series. A simpler way of quantifying this would be to measure the gap in the levitation force hysteresis loop at a

given applied field. We refer to this gap as levitation force gap ΔF, which is the difference in levitation force values between the approach and the recession segments at a given magnetic field value. The maximum gap, ΔF_{PL} occurs at a magnetic field value, say H_{PL} for peak levitation field. The quantity ΔF_{PL} is a measure of sample quality and its flux pinning capability. Samples with higher ΔF_{PL} values are supposed to carry larger critical current density values. We discuss a simple correlation between the levitation force and the critical current density values in section 4.5. Thus, based on the levitation force hysteresis loops one can observe that 4 wt % Ag addition turns out to be the optimum level. We also obtained the highest $J_c(0)$ values for the 4 wt % Ag added samples from our magnetic J_c measurements.

The suspension curves, shown in the bottom row of figure 4.3 for the two series of samples Y460 and Y540, are obtained under Field cooled conditions (FC) where the superconductor is cooled in the presence of the magnetic field of the permanent magnet. We used a field of 1.75 kOe to field-cool the samples in this study. The effect of varying the initial applied is discussed later in this section. Here, similar to the case of levitation force hysteresis loops, the suspension curves also show maximum force values corresponding to 4 wt % Ag added samples in both the Y460-Ag and Y540-Ag series. The maximum suspension force

occurs at a particular field value, which we denote as H_{PS} indicating peak suspension field, also shifts towards lower field values as the peak suspension force F_{PS} increases. The suspension force is a measure of flux pinning in the samples. For application of bulk superconductors as trapped field magnets, it is important that very high pinning and flux trapping capabilities are attained. The table 4.1 below gives the values of ΔF_{PL}, H_{PL}, F_{PS} and H_{PS} for the six samples in Y460-Ag and Y540-Ag series.

Sample Code	Peak levitation force gap, ΔF_{PL} (mN)	Peak levitation force gap field, H_{PL} (Oe)	Peak suspension force, F_{PS} (mN)	Peak suspension force field, H_{PS} (Oe)
Y460-2	388.5	1200	-203.2	896.5
Y460-4	391.4	1300	-227.9	862.0
Y460-10	238.4	1150	-170.7	940.6
Y540-2	128.0	1100	-227.9	926.2
Y540-4	570.2	1200	-337.7	992.9
Y540-10	115.9	1150	-196.3	992.3

Table 4.1 The peak levitation force gap value and the peak suspension force value along with the corresponding magnetic field values are tabulated. The field used for the field-cooling can be varied by varying the gap distance between the superconductor and the magnet as shown in figure 4.4 below.

The first row of the fig. 4.4 represents the suspension curves for the three samples in the Y460 MPa series with different Ag content viz., 2 wt %, 4 wt % and 10 wt % Ag. Each plot contains three curves corresponding to three different initial applied fields for field-cooling the samples. The three initial applied fields for field-cooling were 1.75 kOe, 1.5 kOe and 1 kOe.
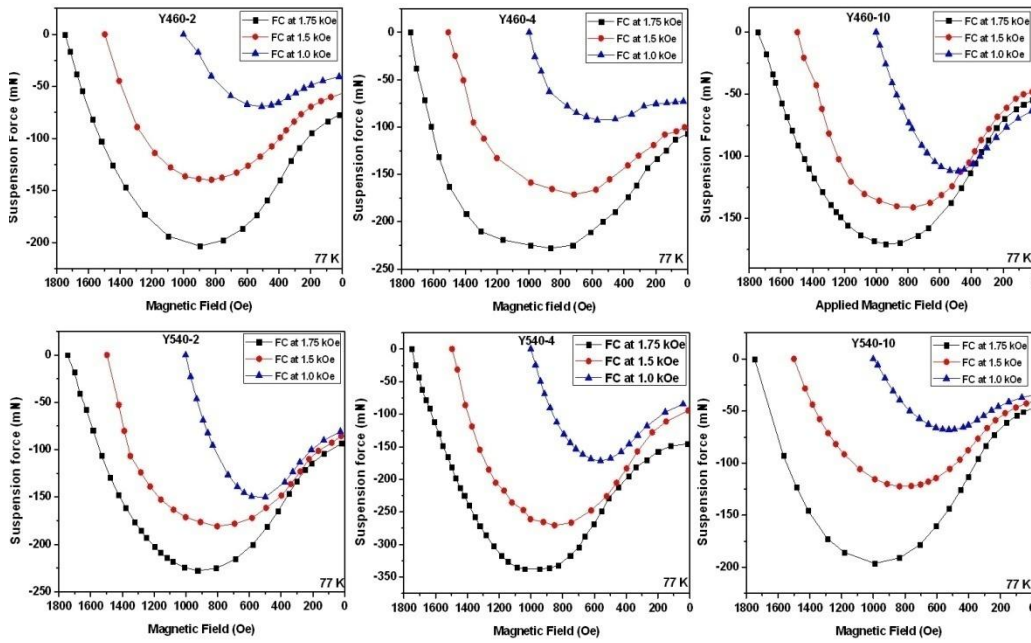
Figure 4.4 The suspension curves for the samples obtained by applying different magnetic fields to field-cool the sample

The bottom row represents similar data for the Y540-Ag series.

The field at which maximum pinning occurs, H_{PS}, assumes lower field values as the initial field applied for field-cooling is decreased. The suspension force is a measure of flux trapping in the sample as the

initial field applied is trapped as the sample is cooled below its T_c. The table 4.2 below gives the FPS and HPS values for all the six samples at three different initial applied field values as mentioned above.

Sample Code	Initial applied field (for FC) H = 1.75 kOe		Initial applied field (for FC) H = 1.50 kOe		Initial applied field (for FC) H = 1.00 kOe	
	F_{PS} (mN)	H_{PS} (Oe)	F_{PS} (mN)	H_{PS} (Oe)	F_{PS} (mN)	H_{PS} (Oe)
Y460-2	-203.2	896.5	-139.8	823.8	-69.4	507.6
Y460-4	-227.9	862.0	-171.5	714.7	-92.6	568.7
Y460-10	-170.7	940.6	-141.2	767.0	-111.9	483.2
Y540-2	-227.9	926.2	-180.9	803.0	-150.1	500
Y540-4	-337.7	992.9	-270.6	850.6	-157.6	430.5
Y540-10	-196.3	992.3	-122.4	834.9	-68.0	524.2

Table 4.2 The values of peak suspension force and the corresponding magnetic field value for different initial applied fields is tabulated for the samples in Y460 and Y540 series.

From the table, we can observe that the maximum peak suspension force F_{PS} decreases with decreasing initial applied fields for each of the sample. Generally, the maximum suspension force values have been observed for the 4 wt % Ag added samples namely Y460-4 and Y540-4 for each of the initial applied fields. The peak suspension force fields H_{PS}

though do not show any systematic behavior. Thus, the maximum pinning occurs at different field values depending on several other factors apart from the initial applied field for field-cooling. So, a combination of other factors might be involved in determining the fields H_{PS} at which the maximum suspension force values F_{PS} are achieved.

4.3 Correlation of the peak levitation force loop gap to the self-field critical current density

We observe that the peak levitation force loop gap follows a trend for different silver contents across the samples in a given series. This trend is maintained in both the series namely Y460-Ag and Y540-Ag. We have found that the samples containing 4 wt % Ag in both the series, viz., Y460-4 and Y540-4 have the best peak levitation force loop gap ΔF_{PL} and peak suspension force F_{PS} values when compared with 2 wt % and 10 wt % Ag added samples in their respective series. It is worthwhile to recall here that from our critical current density values reported in chapter 3, we found that the self-field critical current density values followed a similar trend across a given series with 4 wt % Ag added samples having the highest values of $J_c(0)$. Hence, it is natural to probe this aspect for any possible correlation between the two parameters namely the

peak levitation force gap ΔF_{PL} and the self-field critical current density $J_c(0)$ of the samples.

In both the magnetization measurements and the levitation force measurements, we take the samples through a cycle of magnetic field sweep. Hysteresis effects are seen, hence, in both these measurements. In the M-H loop measurements, the loop width or the change in magnetization values $\Delta M = (M_+ - M_-)$ between the 1st quadrant and the 5th quadrant (+H and –M during the second cycle of the M-H loop) is a measure of the critical current density of the samples. Typically, the maximum value of critical current density occurs at the zero applied field value. Similarly, in the levitation force measurements, the force gap of the hysteresis loop is a measure of the magnetization of the sample. The approach segment of the force curve corresponds to the virgin magnetization curve. In the M-H loops, as the field increases from 0 to higher values through H_{c1}, the sample undergoes a phase transition from complete a Meissner state to a mixed state. The contribution to moments below H_{c1} is purely from the shielding currents whereas in the mixed state, additional vortex currents contribute enormously to the magnetization of the material. The total current is hence a combination of the shielding currents and the vortex loop currents and this is reflected in the width of the difference in the magnetization loop,

namely ΔM. In a similar way, the width of the levitation hysteresis loop is a measure of the magnetization of the material and hence its critical current density.

$$\text{Thus,} \quad J_c \ \propto \ \Delta M$$

$$\Delta F_{PL} \ \propto \ \Delta M$$

$$\text{And hence,} \quad \Delta F_{PL} \ \propto \ J_c(0)$$
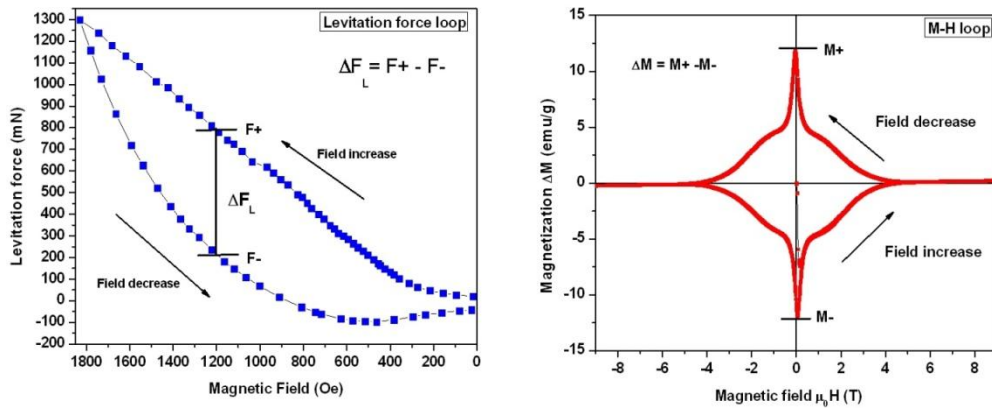
Figure 4.5 A comparison of the levitation force hysteresis and the M-H loop hysteresis both being the measure of magnetization in the material and hence proportional to the self-field critical current density

Also, the peak levitation force loop gap, ΔF$_{PL}$ appears to be proportional to the pinning force density, F$_P$ of the samples as discussed later in this section.

$$\text{That is,} \quad \Delta F_{PL} \ \propto \ F_p$$

This analogy between the two measurements is depicted in the figure 4.5 above.

Thus, the levitation force gap is an indication of the quality of the sample with respect to its superconducting properties. A direct one-to-one correspondence between the two measurements, though, cannot be established as several other factors come into play. The sample geometry is a major issue in these two measurements. In the M-H loop measurements, a small parallelepiped sample with its long axis parallel to the applied field axis is used. The magnetization is carried out with the sample completely immersed in a uniform applied magnetic field. The different regions of the sample are not subjected to any field gradients. The levitation force measurements on the other hand involve subjecting the sample to a non-uniform field. The entire sample in this measurement is subjected to considerable field gradients. Hence, the behavior of the sample as a function of field in these two measurements is not the same. Thus the $\Delta F_L(H)$ and the $J_c(H)$ behavior of the sample could be entirely different from each other. The figures 4.5 and 4.6 below represent the $\Delta F_L(H)$ plots of the samples in the two series Y460-Ag and Y540-Ag. The $\Delta F_L(H)$ curves were derived from the corresponding levitation force curves. From the figures 4.5, 4.6 and 4.7, we observe that the levitation force loop gaps vary across the samples in each of the two

series and the corresponding ΔF_L curves have their peaks at different field values.
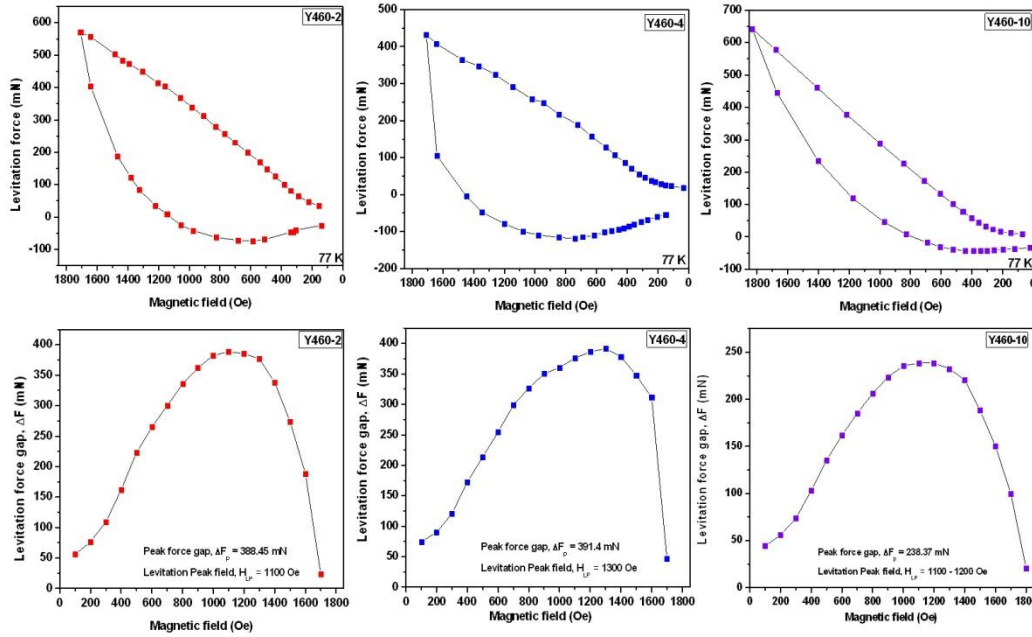
Figure 4.6 The levitation force loops for the three samples in Y460-Ag series with different Ag content and the corresponding levitation force gap curves are shown.

The peak values ΔF_{PL} for the samples also vary with varying Ag content across each series of samples. It is interesting to note that ΔF_L curves as a function of field resemble the pinning force density curves as a function of field as observed in chapter 3. The figure 4.8 compares the two kinds of plots for all the samples in the two series. Thus we can observe the similarities in the behavior of levitation force loop gap, ΔF_L

and maximum pinning force density, F_{pmax} as a function of applied magnetic field in the respective cases.
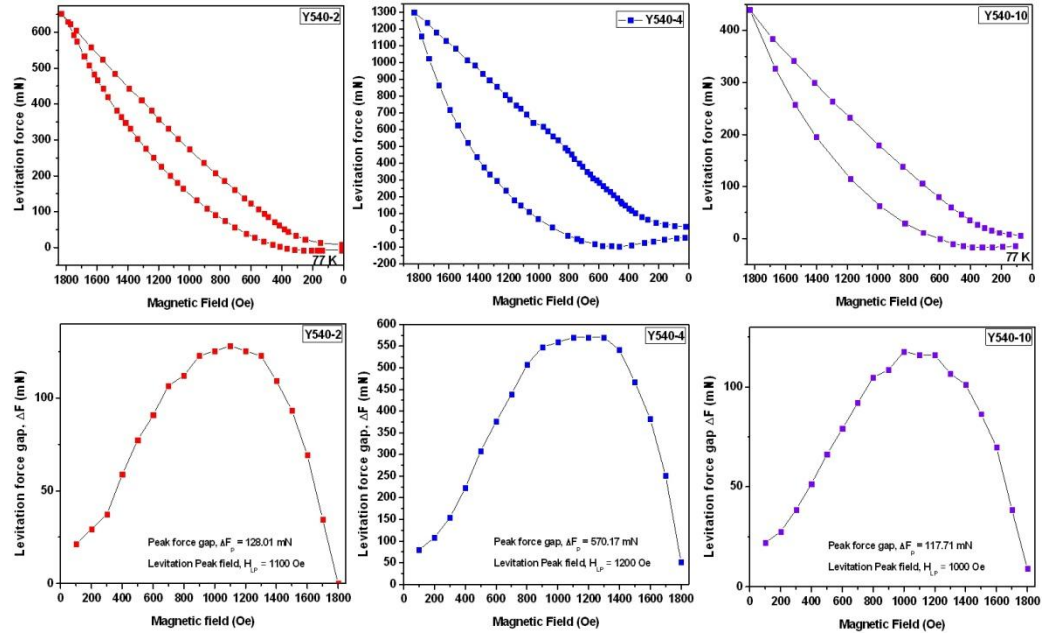
Figure 4.7 The levitation force loops for the three samples in Y540-Ag series with different Ag content and the corresponding levitation force gap curves are shown.

The domination of the corresponding 4 wt % samples in each case is clearly brought out from this analysis. Thus, the levitation force loop gap, ΔF_L is obviously an indicator of the sample quality as this parameter follows the same trend as do the self-field critical current density $J_c(0)$ and maximum pinning force density F_{pmax} of the sample. The table 4.3 below lists out the peak levitation loop gap ΔF_{PL} values, the

self-field critical current density values $J_c(0)$ and the pinning force density F_{pmax} values.
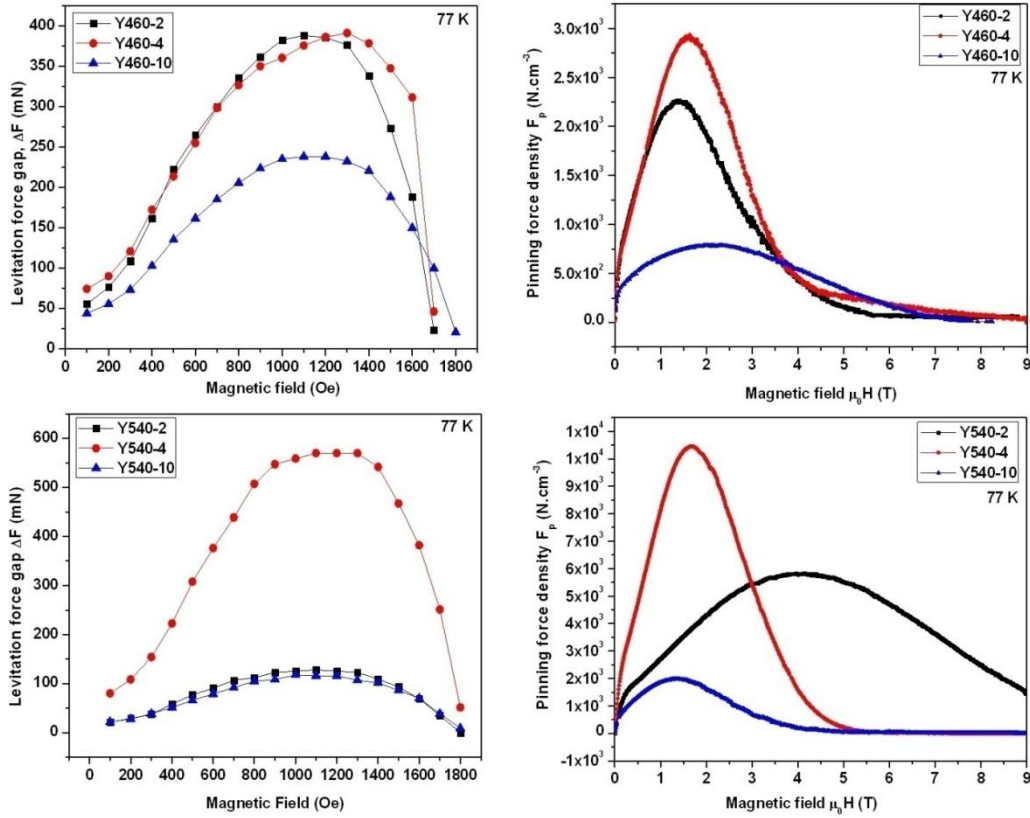
Figure 4.8 The plots of levitation force gap as a function of field is compared with the plots of pinning force density as a function of field for the samples in Y460-Ag and Y540-Ag series.

The levitation force hysteresis loop measurements hence are an effective way to assess the quality of the samples.

Sample Code	Peak levitation force gap, ΔF_{PL} (mN)	Self-field critical current density, $J_c(0)$ kA.cm^{-2}	Maximum Pinning force density, F_{pmax} (x 10^3)(N.cm^{-3})
Y460-2	388.5	9.16	2.3
Y460-4	391.4	10.01	2.9
Y460-10	238.4	5.52	0.79
Y540-2	128.0	11.5	5.8
Y540-4	570.2	21.3	10.4
Y540-10	115.9	9.9	2.0

Table 4.3 The peak levitation force gap value ΔF_{PL}, the self-field critical current density and the maximum pinning force density values for the samples in Y460-Ag and Y540-Ag series are shown.

The peak levitation force gap ΔF_{PL} seems to be the parameter that is directly proportional to the self-field critical current density and the pinning force density of the samples.

4.4 Dependence of levitation and suspension forces on the sample size and geometry

The levitation and the suspension forces are bulk physical properties that are dependent on the sample size, geometry and the properties of

the magnet. The size and geometry of the sample as well as those of the magnet decide the kind of field of interaction between the two objects [20]. The shape and uniformity of the field depends on the geometry of both these objects. Hence it would be interesting to probe the dependence of the levitation force of the samples on the sample size and geometry keeping the aspects of the permanent magnet constant. The variation of the levitation hysteresis force curves as a function of sample size or geometry is studied in this section.

For this study, two samples from the Y460-Ag series were chosen for measurements. The two samples were Y460-2 and Y460-4 with 2 wt % and 4 wt % Ag addition respectively. The generalizations for the sample geometry dependence of the levitation force could be drawn based on these two samples. The specimens from the samples were prepared by cutting the bulk samples using a diamond saw (*Buehler make - model Isomet1000*) as per the requirement. The shapes used for this study were restricted to regular shapes for simplicity. Initially, the full sample was used for the study. Then, a thin slab was sliced from the bulk sample. The levitation force measurements were carried out on both the pieces, that is the sample with reduced thickness and the thin slab that was cut from it. Then, the area of the thickness-reduced sample was reduced by slicing another piece along the b-axis of the sample. Thus, four

specimens were prepared for the study. The steps involved in making the specimens and the specimen details are illustrated in the schematic diagram in figure 4.9 below.
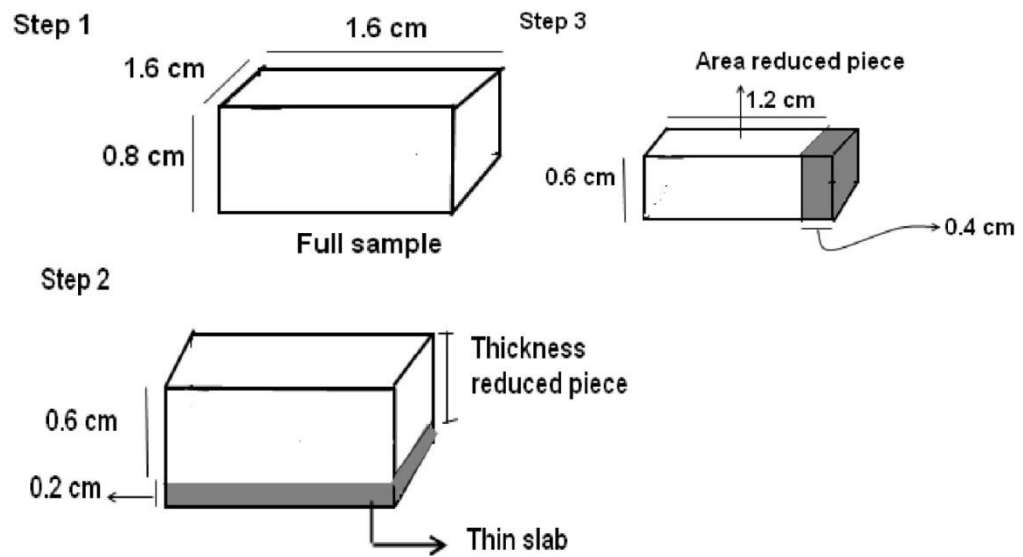
Figure 4.9 The diagram illustrates schematically the steps involved in preparing the specimens used for the study of levitation force on sample geometry

The table 4.4 below gives the specifications of the samples used in this study. The figure 4.10 below presents the levitation force hysteresis loops for the four specimens of each of the two samples and the corresponding curves of levitation force loop gap F_L. The levitation force measurements were carried out on all the four specimens for each of the two samples namely Y460-2 and Y460-4 respectively.

Sl. No	Specimen from the Y460-2 and Y460-4 samples	Typical Sample dimensions
1	Full sample Specimen	a = 1.6 cm, b = 1.6 cm c = 0.8 cm
2	Thickness reduced Specimen	a = 1.6 cm, a = 1.6 cm c = 0.6 cm
3	Area reduced Specimen	a = 1.6 cm, b = 1.2 cm c = 0.6 cm
4	Thin slab Specimen	a = 1.6 cm, b = 1.6 cm c = 0.2 cm

Table 4.4 The details of specimens and their dimensions along *a, b* and *c*-axes, used for the study of dependence of levitation force on the sample size and geometry.

Full hysteresis loops were obtained in each case to study the force values as well as the peak levitation force loop gap values for each of the specimens.
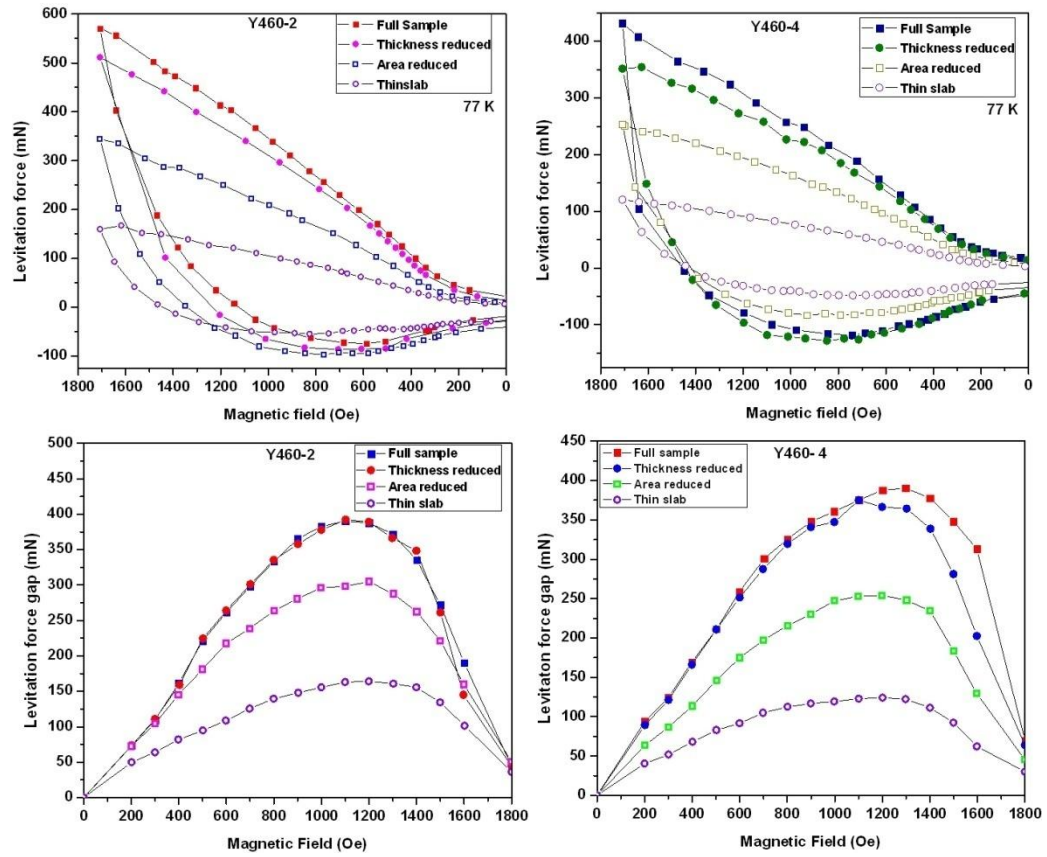
Figure 4.10 The top row in the figure gives the levitation force hysteresis loops corresponding to four specimens with different size and geometry, of the two samples Y460-2 and Y460-4. The bottom row presents the corresponding levitation force loop gap F_L curves as a function of field.

It can be observed from the curves in the top row of fig. 4.10, that the levitation force and the loop gap shows drastic reduction for a small change in area whereas the reduction in values is not as much for the same amount of reduction in sample thickness.

Sample Code	Specimen	Percentage reduction in specimen area	Percentage reduction in specimen thickness	Percentage reduction in maximum levitation force, F_m	Percentage reduction in peak levitation force gap, ΔF_{PL}
Y460-2	Full sample	NIL	NIL	NIL	NIL
	Thickness reduced	NIL	25 %	10.4 %	NIL
	Area reduced	25 %	75 %	32.7 %	22.3 %
	Thin slab	NIL	75 %	72.1 %	58.0
Y460-4	Full sample	NIL	NIL	NIL	NIL
	Thickness reduced	NIL	25 %	18.7 %	3.9 %
	Area reduced	25 %	75 %	27.8 %	32.2 %
	Thin slab	NIL	75 %	72.1 %	68.2 %

Table 4.5 The percentage reduction in maximum levitation force values F_m and peak levitation force loop gap values ΔF_{PL} for specimens of different size and geometries of the Y460-2 and Y460-4 samples is tabulated.

The reduction in dimensions in both the case was 25 %. So, it can be concluded that the dependence of levitation force on the sample area is stronger compared to the dependence of the force on the thickness. This can be attributed to the saturation effect of levitation force as a function of sample thickness as reported [21-22]. The dependence on sample area is stronger as it has no saturation effect and the force increases with increase in sample area linearly. The thin slab, on the other hand, has the same area as the full sample but 25 % of its thickness but the reductions in the loop gap values are only around 42 % implying a better preservation of the original levitation force loop gap value in spite of a significant reduction in thickness. The table 4.5 gives details of the forces and the change in the force values as a function of the sample size and geometry.

From the table 4.5 above, we observe that taking the full sample as reference, the reduction in maximum levitation force F_m for thickness reduction of 25 % is 10.4 % and 18.7 % in Y460-2 and Y460-4 samples respectively whereas the corresponding values for area reduction are 32.7 % and 27.8 % with respect to the thickness reduced sample. Thus, area reduction by the same percentage results in drastic reduction of maximum levitation force. The peak levitation force loop gap ΔF_{PL} values show almost no reduction for thickness reduction by 25 %

whereas for area reduction by 25 %, the peak force gap reduces by 22.3 % and 32.2 % for the two samples Y460-2 and Y460-4 respectively. It is interesting to note that, the thin slabs, which have a 75 % reduction in thickness in comparison with the full samples, retain more than 28 % of the maximum levitation force of the full sample and nearly 60 % of the peak force loop gap since the area for the thin slab was the same as for the full sample, thus showing the importance of dependence of the force on the surface area exposed to the magnetic field.

4.5 Time relaxation behavior of levitation and suspension force – Near-oscillatory relaxation – Bistable equilibrium of current structure Superconductor – PM interaction

The levitation force measurements, as we have discussed, are important from the point of view of bulk applications of the superconductors such as maglev systems, frictionless bearings, flywheel energy storage devices and as trapped field magnetic sources [1,8,13,15]. In this context, it would be interesting to ascertain the stability of these superconductors under applied magnetic field for such applications, as it is a very crucial issue for their reliability. It is well known that flux creep in superconductors, particularly high T_c materials, is a major problem that restricts their use in several applications. A lot of research has gone into studying the flux creep problem and ways to arrest the flux creep by

introducing pinning centers into the material. But still, the problem of flux creep has not been completely solved. The flux creep problem, where flux bundles move and cause dissipation in the material and thereby making it inefficient, is severe at higher magnetic fields as the driving force, which is Lorentz force, is more at high magnetic fields. Much of the research on arresting the flux motion has focused on improving the magnetic field dependence of the critical current density of the superconductors. In this context, it is interesting to know the origin of magnetic relaxation in superconductors. The magnetic relaxation in superconductors occurs as a result of motion of the flux bundles. The magnetic relaxation is a result of change in magnetization in the material as a function of time [23-24]. Several factors such as temperature, magnetic field, material structure etc are responsible for flux creep in these materials. Hence the study of magnetic relaxation in these materials is important from both the science and the applications points of view.

In this section, we focus our attention to studying the time-relaxation of levitation force in the material as studying the relaxation of levitation force is equivalent to studying the magnetic relaxation. This is so because all the magnetization studies involve using specific portions of the bulk samples for measurements. It is well known that the bulk

samples suffer from homogeneity problems and hence the properties vary drastically across the sample. It is not possible to characterize the whole of the bulk samples using magnetization measurements. The studies on relaxation of levitation force, on the other hand, enables use of the entire bulk sample for characterization. It not only allows one to study the magnetic relaxation in an indirect way but also helps us to study the relaxation of levitation force which is important for the utility of these materials for levitation based applications. While the flux creep problems focus on the motion of flux bundles under changing applied magnetic fields, the relaxation studies focus on the motion of flux bundles under constant magnetic fields. The time variation of magnetization M(t) is captured beautifully through such studies [25-27]. Our aim to study the relaxation of levitation force in these samples is to better understand the physics of magnetic relaxation in the YBCO/Ag materials.

For the present study, we chose one of the samples in the Y460-Ag series discussed in the previous chapter namely Y460-2. This sample has been assumed to represent the whole class of YBCO/Ag composite superconductor samples as the problem addressed is at the fundamental level. We discuss the details of the measurements and the results in the next subsection.

4.5.1 Time relaxation measurements of levitation force in YBCO/Ag sample

In the present study, we used the homemade levitation force measuring set-up discussed in the previous sections. A stop-watch was used to record time. The experiment consists of measuring the levitation force at regular intervals of 30 seconds until a total observation time of 120 seconds at each gap distance between the superconductor and the magnet. The variation in gap distances cause variations in the applied field at the surface of the superconductor. This way, at each applied field, we wait for 120 seconds to record levitation force values at intervals of 30 seconds before moving on to the next field value. Thus the entire hysteresis loop is completed as before and we get a set of 5 such hysteresis loops for 0 s, 30 s, 60 s, 90 s and 120 s. The figure 4.11 below depicts the levitation hysteresis loops obtained for the two samples and the relaxation of the levitation force. From the figure 4.11, we can see that the loops recorded at different times starting from 0 s to 120 s at 30 s intervals do not fall on one another. The relaxation at different applied magnetic field values has been plotted as a function of time till 120 s for each of the field during the entire levitation hysteresis loop consisting of the approach and the recession segments.
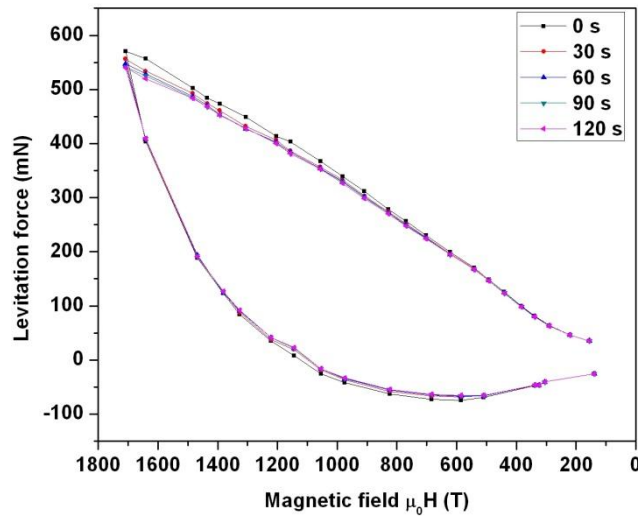
Figure 4.11 Hysteresis loops recorded at 30 second intervals from 0 s to 120 s, by measuring the relaxation of the levitation force.

Figure 4.12 below shows the relaxation of levitation force at some of the applied field values for the approach and the recession segments.
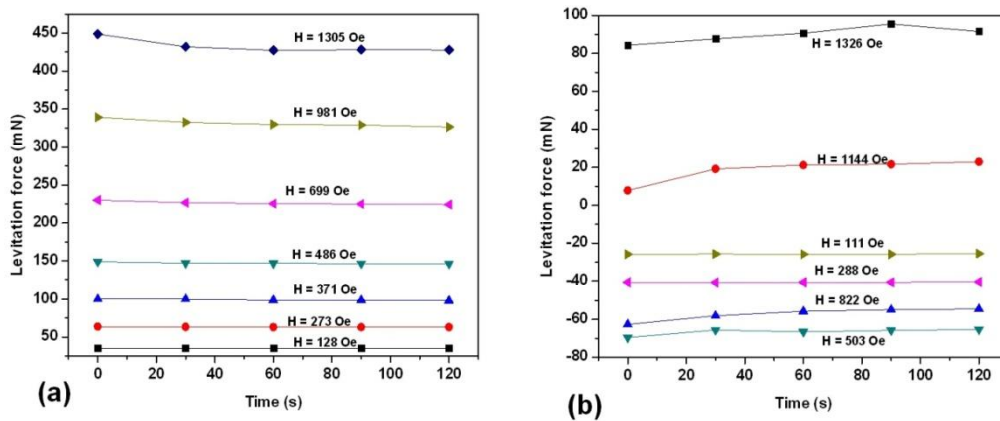
Figure 4.12 The levitation force as function of time at different applied fields for the (a) approach segment and (b) the recession segment of the levitation hysteresis loop.

There is relaxation of the levitation force with time. It is interesting to know how much relaxation is actually there and whether the relaxation is equal at each of these 30 s intervals or not. The figure 4.13 below plots the relaxation for 0-30 s, 0-60 s, 0-90 s and 0-120 s intervals by calculating the change in levitation force during these time intervals.
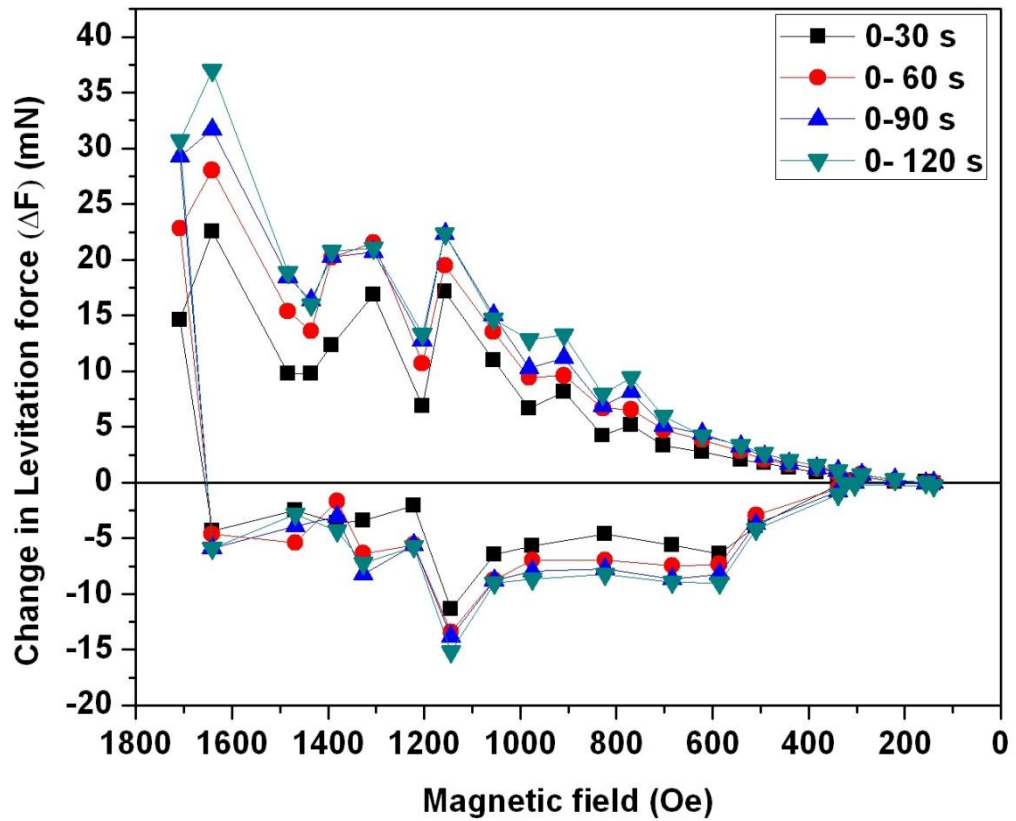
Figure 4.13 The change in levitation force as relaxation occurs in time from 0 s to 120 s. The changes in relaxation at intervals of 0-30 s, 0-60 s, 0-90 s and 0-120 s have been plotted together.

From the above plots, we can see that there is a significant relaxation even in the first 30 s and stepping up to 120 s. It is interesting to note that the relaxation amplitude increases at larger applied magnetic field values. It is even more interesting to note that there is no monotonous increase or decrease in relaxation as a function of field. For successively increasing field values, the change in relaxation is oscillatory or near-oscillatory [28]. And the change in relaxation undergoes an up-down-up-down sequence as a function of increasing field. Now, in figure 4.14 we have plotted the relaxation or the change in levitation force at each of the 30 s intervals separately to understand how fast or slow the relaxation is at each of these time intervals. This would also give an indication of the time period during which maximum relaxation occurs as we can observe from fig. 4.14. The figure 4.14 represents the change in levitation force or relaxation of levitation force at each of the 30 s intervals starting from 0 s to 120 s.

It can be seen that the relaxation is maximum during the first 30 seconds and then decreases at subsequent intervals gradually. Here the time period of the intervals have been kept constant to observe these effects. It is amusing to note that the near-oscillatory behavior is retained individually in each of these 30 s interval.
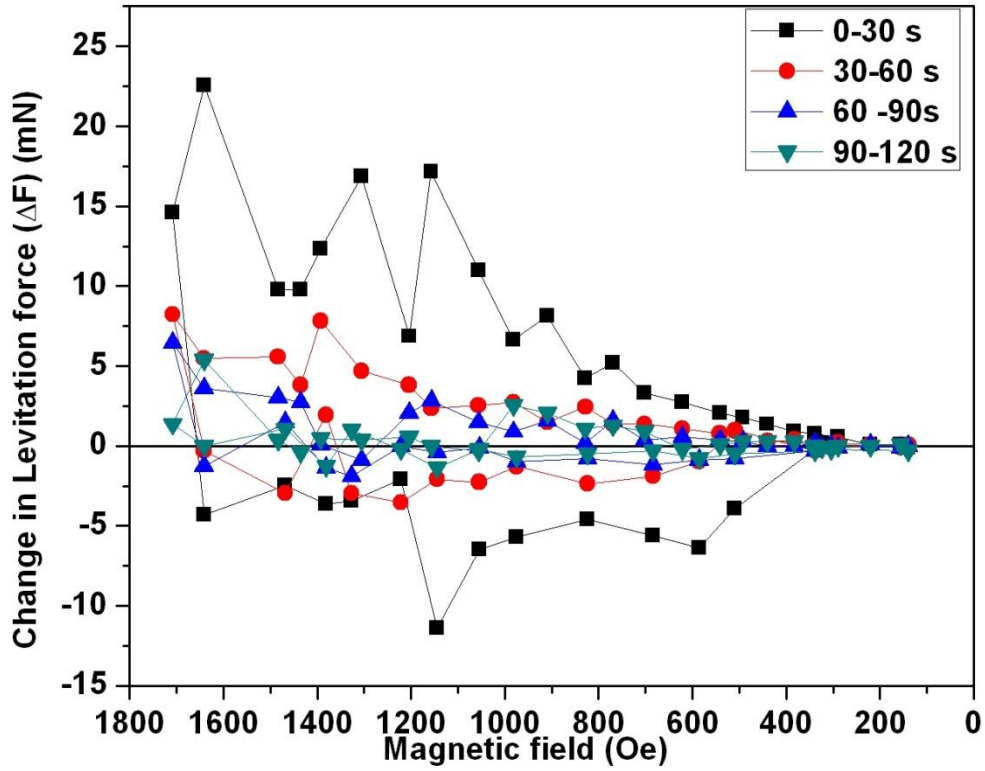
Figure 4.14 The change in levitation force at each of the 30 s intervals between 0 and 120 seconds. The oscillating trend of the change in levitation force is observed and maximum relaxation occurs during the first 30 s.

The rate of relaxation for the system is obtained by calculating ($\Delta F/\Delta T$) where ΔF is the change in levitation force or relaxation of levitation force in an interval of 30 seconds. The figure 4.15 shows the rates of relaxation corresponding to the plots in figures 4.13 and 4.14. So, one can conclude that there is consistency in the behavior in all or any of the time intervals.
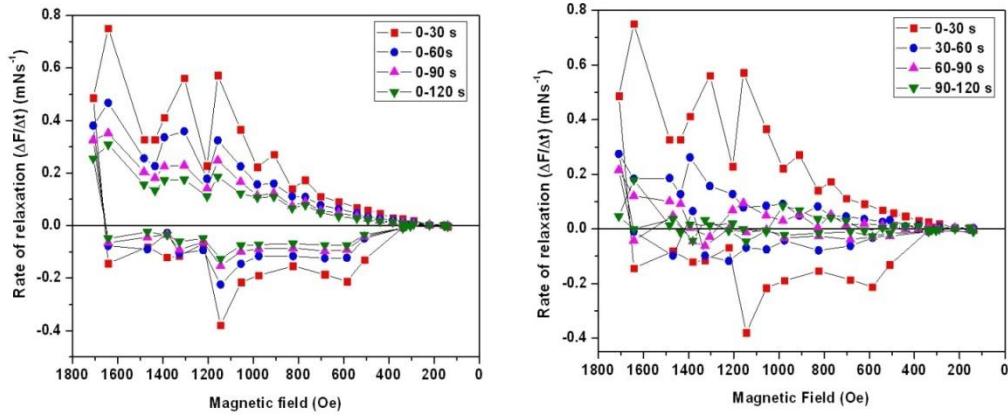
Figure 4.15 The relaxation rates of levitation force for various intervals between 0-120 s have been plotted as a function of applied field.

The near-oscillatory relaxation of levitation force is intrinsic to the system. The average amplitude of this relaxation gradually increases with the applied field. But the relaxation is near-oscillatory as a function of the applied field. This indicates that the relaxation is generally more as the applied field is increased but it does not monotonously increase with the applied field but varies in an oscillatory manner.

In the remaining part of this section we proceed to discuss a possible model proposed by us explaining the observed near-oscillatory relaxation behavior of the levitation force. It is well known that the magnetic relaxation in high T_c superconducting materials occurs as a logarithmic function of time.

The normalized relaxation rate S can be described by

$$S \equiv -\frac{dM/d(lnt)}{M_0}$$

This kind of magnetic relaxation behavior reflects as the relaxation of levitation force as well.

Thus, the rate of relaxation of levitation force is

$$S \equiv -\frac{dF/d(lnt)}{F_0} = \frac{K_B T}{U}$$

where S is the normalized rate of relaxation of levitation force and F is the levitation force, F_0 is the initial levitation force at time t = 0. Here the relaxation rate is shown to be a function of pinning energy barrier U indicating the fact that stronger the pinning slower is the relaxation. Thus by studying the relaxation of levitation force one can study the physics of flux motion and the associated vortex dynamics. The nature of pinning can also be clearly brought out from these measurements.

It can be observed that the well reported logarithmic relaxation is not strictly adhered to here in our measurements. This is quite clear from the fig. 4.12 that the relaxation behavior is different at different applied fields and the magnitudes show a near-oscillatory behavior. Our observation times were for only 120 s because we did not notice any significant relaxation of levitation force beyond these time scales.

Now, it is important to understand the observed near-oscillatory behavior through a model. The relaxation, as we have explained earlier, arises as a result of vortex motion or flux creep in these materials. But, observable flux creep of this kind requires a driving force either in the form of temperature or magnetic field. The material that we deal here is a system having strong pinning behavior. This makes it all the more interesting as we do not expect any oscillation in the relaxation rates for a fixed time period. The only driving force that we should consider is the magnetic field, but in this case, the magnetic field is varied quasi-statically as we stop for 120 s at each applied field value to observe relaxation. The up-down-up-down sequence of relaxation rate seems intriguing.

The observed near-oscillatory relaxation behavior can be explained as follows. As the magnetic field is slowly varied, the vortex structure associated with the material changes. At each successive step of increasing magnetic field more and more vortices are generated. This assumption is valid since we observe oscillatory relaxation only at higher magnetic field values implying the fact that we are in the mixed state having taken the material to fields above its H_{c1}. The Bean's model provides some of the clues to understanding the observed behavior. We would base our model on the Bean's model.

Anderson-Kim Model suggests that the azimuthal component of current density in the plane of the material, J_θ is dependent on the vortex density gradient caused by pinning in the material as

$$J_\theta = \frac{1}{\mu_r} \frac{\partial B_z}{\partial r} (r)$$

Where J_θ is the azimuthal component of the current density and r is the radial vector. This component of current density changes sign from positive to negative depending on whether the quantity $\partial B_z / \partial r$ is positive or negative as the critical current density J_c remains constant throughout the volume of the superconductor as per Bean's model.

That is, $J_\theta = J_c$ if $\frac{\partial B_z}{\partial r} < 0$ and

$$J_\theta = -J_c \ if \ \frac{\partial B_z}{\partial r} > 0$$

Hence J_θ changes sign from positive to negative as vortex density gradient changes sign.

Also, the continuity equation for the density of flux lines demands that,

$$\frac{\partial B_z}{\partial t} = -\frac{1}{r} \frac{\partial (ru\, B_z)}{\partial r}$$

where u is the flux creep velocity in the material.

The gradient of B_z causes a change in J_c. To keep the J_c constant as per Bean's model, currents of opposite polarities are generated and the current structure in the material changes from being uni-polar to bi-polar or multi-polar [28].

We propose that a systematic change in relaxation rate in a near oscillatory manner could be due to switching over of the current structure from uni-polar to bi-polar or multi-polar one. This shift from one type of current structure to another type occurs as the magnetization varies in the system. As the magnetic field varies, re-magnetization of the material occurs resulting in a modified flux structure causing a shift from uni-polar to bi-polar current structure as shown in fig. 4.16. This is to say that the system has bistable equilibrium [28]. During one state the system has a flux structure corresponding to rapid relaxation in magnetization and during the other state the flux structure corresponds and leads to suppressed relaxation. The observed up-down-up-down near-oscillatory relaxation behavior of levitation force is well explained by our model [28]. It has been reported that the magnetization of a permanent magnet can be altered in the presence of a superconductor due to reversal of polarities [29-30].It is also possible that the ferromagnet is counter-magnetized in the presence of a superconductor which in turn induces additional currents in the

superconductors which circulate in a direction opposite to the original currents [28].
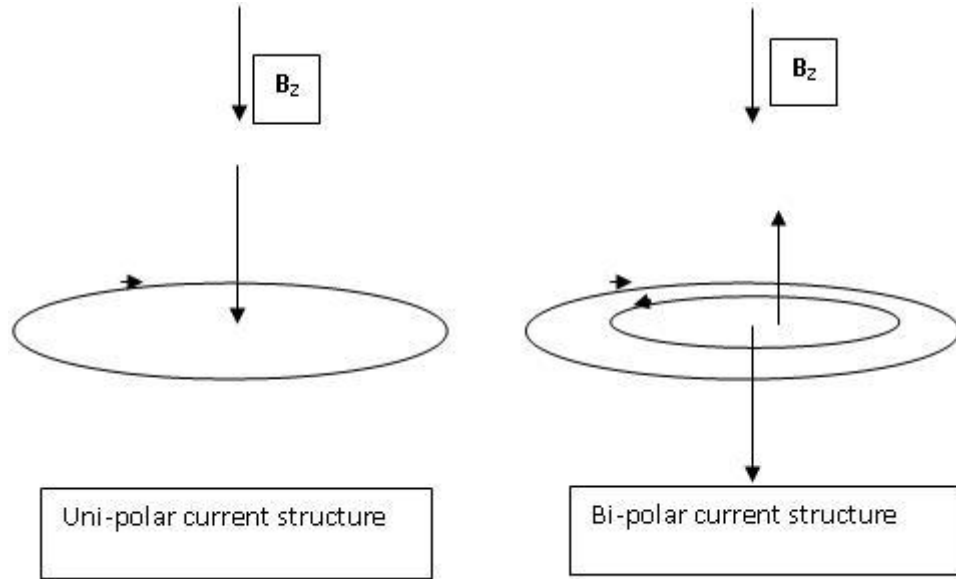
Figure 4.16 A schematic diagram of the unipolar and the proposed bipolar current structure.

The change in magnetization of the permanent magnet in the presence of the superconductor has been verified by our experiment and discussed below in the next section.

This kind of a behavior gives rise to a switch-type polarity change in the material thereby resulting in a near oscillatory behavior of levitation force relaxation rate. Also, it has been reported that the relaxation is suppressed in the presence of a transverse ac magnetic field [31]. In the

present work, as the magnet approaches the sample the magnetization increases and hence the reverse magnetization of the PM in the presence of the superconductor also increases. So, there is a competition between the magnetization and the reverse magnetization which is suppression of the original magnetization, resulting in a near-oscillatory behavior. This, we feel, convincingly explains the observed alternate high and low decay rates of levitation force with applied magnetic field.

4.6 Counter-magnetization of the permanent magnet by the superconductor

There have been reports suggesting about the possibility of the magnetization of a permanent magnet getting altered in the presence of a superconductor [29-33]. We wanted to verify these reports since we observed a near-oscillatory relaxation behavior in superconductors and the permanent magnet being a part of the system. The superconductor-magnet interactions are an interesting topic of study. We measured the magnetization and its relaxation at the surface of the $SmCo_5$ permanent magnet as the superconductor approaches the magnet surface using a Hall probe fixed to the surface of the permanent magnet as shown in the inset of Figure 4.1. Simultaneously, we recorded the levitation force of the superconductor and its relaxation as well. This experiment was performed for the full levitation hysteresis loop run. The magnetization

loop obtained in this experiment resembles the typical M-H loop of a ferromagnet as shown in Fig. 4.17. To our best knowledge, this was the first time that a permanent magnet has been magnetized and its M-H loop obtained and reported, using a superconductor. The above curve is the typical first quadrant hysteresis curve of a ferromagnet, here obtained by using a bulk superconductor as a magnet to counter-magnetize the permanent magnet itself.
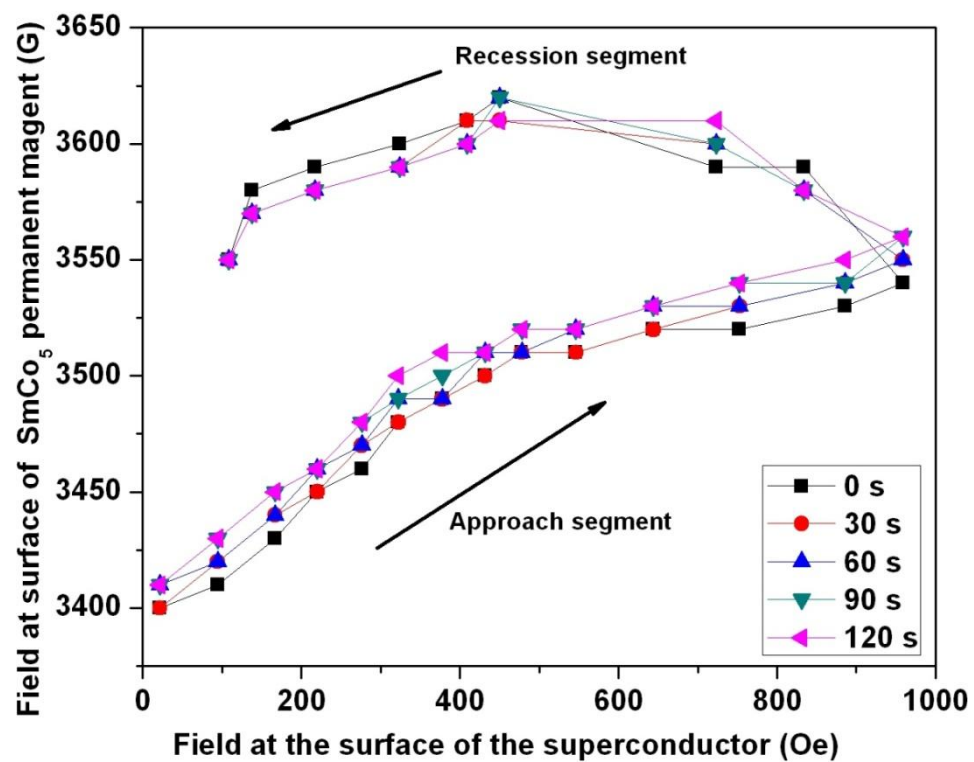
Figure 4.17 The M-H curve of the SmCo5 permanent magnet counter-magnetized by the YBCO/Ag superconductor and the relaxation of magnetization of the permanent magnet

The magnetic field at the centre of the permanent magnet surface was 3380 G in the absence of the superconductor. As the superconductor is cooled below its T_c and made to approach the $SmCo_5$ permanent magnet, the magnetization of the permanent magnet changes in the presence of the superconductor and when the superconductor is withdrawn after approaching the closest possible distance in our set up, the magnetization of the permanent magnet reverts hysteretically. The magnetization at the surface of the permanent magnet changes from an initial value of 3380 G when the superconductor is sufficiently away from the permanent magnet to a maximum value of 3620 G during the reverse curve of the hysteresis loop. Thus, we clearly see a rise in the magnetization of the permanent magnet in the presence of the superconductor which acts as a corroboration to our bistable equilibrium theory.

We also observed relaxation of the magnetization of the permanent magnet that was counter-magnetized by the superconductor after the superconductor is removed from the vicinity of the magnet [28,34].
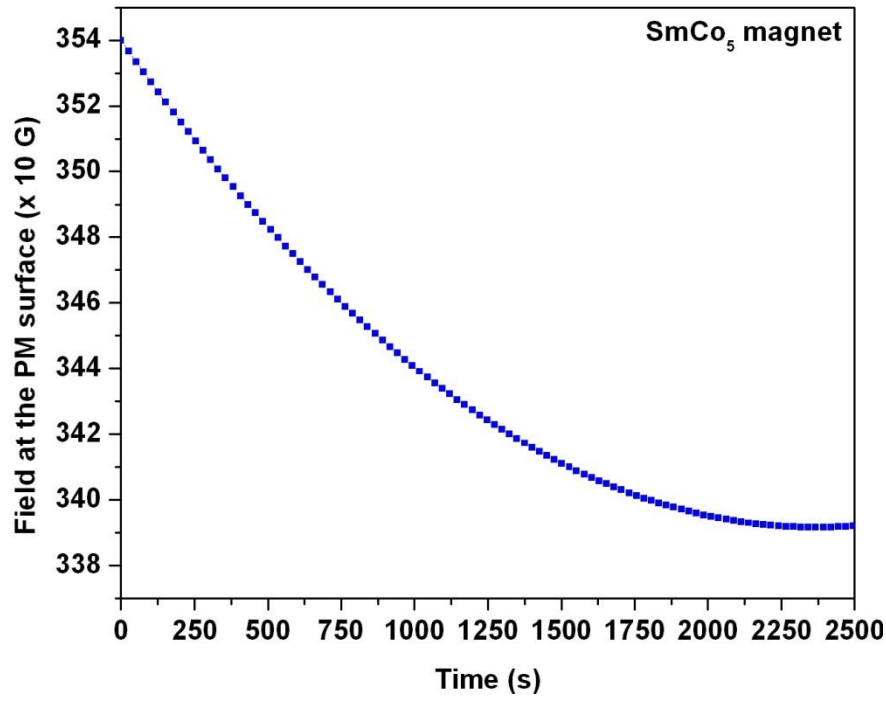
Figure 4.18 The relaxation of magnetization of the permanent SmCo₅ magnet that was counter-magnetized by the YBCO/Ag superconductor

The typical magnetization relaxation of the permanent magnet counter-magnetized by the bulk YBCO/Ag superconductor is shown in figure 4.18 above. We find from the above fig. 4.18 that it takes around 2500 seconds for the permanent magnet to relax its magnetization value to the original value after being magnetized by the bulk YBCO/Ag superconductor.

References

[1] F. C. Moon, *Superconducting Levitation: Applications to Bearing & Magnetic Transportation*, John-Wiley & Sons, (1994).

[2] E. H. Brandt, *Science* **243**, 349-355 (1989).

[3] M. J. Qin, G. Li, H. K. Liu, S. X. Dou, and E. H. Brandt, *Phys. Rev. B* **66**, 024516 (2002).

[4] E. H. Brandt, *Appl. Phys. Lett*. **53**, 1554 (1988).

[5] M. Becker, M. R. Koblischka, and U. Hartmann, *Phys. Edn*. **45** (1), 42 (2010).

[6] F. Hellman, E. M. Gyorgy, D. W. Johnson, H. M. O' Bryan, and R. C. Sherwood, *J. App. Phys*. **63** (2), 447 (1988).

[7] N. D. Valle, A. Sanchez, E. Pardo, C. Navau, and D.-X. Chen, *App. Phys. Lett*. **91**, 112507 (2007).

[8] L. Schultz, O. de Haas, P. Verges, C. Beyer, S. Röhlig, H. Olsen, L. Kühn, D. Berger, U. Noteboom, and U. Funk, *IEEE Trans. Appl. Supercond*. **15** (2), 2301-2305 (2005).

[9] A. Sanchez and C. Navau, *Phys. Rev. B* **64**, 214506 (2001).

[10] A. Sanchez and C. Navau, *Phys. Rev. B* **64**, 214507 (2001).

[11] W. Yang, M. Qiu, Y. Liu, Z. Wen, Y. Duan, and X. Chen, *Supercond. Sci. Technol.* **20**, 281 (2007).

[12] A. Sanchez and C. Navau, *Physica C* **268** (1-2) 46-52 (1996).

[13] J. R. Hull , *Supercond. Sci. Technol.* **13**, R1 (2000).

[14] W. Meissner and R. Ochsenfeld, *Naturwiss.* **21**, 787 (1933).

[15] F. C. Moon, M. M. Yanoviak, and R. Ware, *Appl. Phys. Lett*. **52** (18), 1534 (1988).

[16] X.-Y. Zhang, J. Zhou, Y.-H. Zhou, and X.-W. Liang, *Supercond. Sci.Technol*. **22**, 025006 (2009).

[17] Y. Lu, Y. Qin, Q. Dang, and J. Wang, *Physica C* **470** (22), 1994–1997 (2010).

[18] Y.-H. Zhou, X.-Y. Zhang, and J. Zhou, *J. Appl. Phys*. **103**, 123901 (2008).

[19] E. H. Brandt, *Am. J. Phys*. **58**, 43 (1990).

[20] J. Lugo and V. Sosa, *Physica C* **324**, 9-14 (1999).

[21] I. A. Rudnev and Y. S. Ermolaev, *J. Phys.: Conf. Series* **43**, 983-986 (2006).

[22] S. Kütük, S. Bolat, K. Öztürk, S. Akbulut, and O. Çakır, *J. Supercond. Novel Mag.* **24** (1-2), 475-479 (2011).

[23] Y. Yeshurun, A. P. Malozemoff, and A. Shaulov, *Rev. Mod. Phys*. **68** (3), 911-949 (1996).

[24] L. Fruchter, A. P. Malozemoff, I. A. Campbell, J. Sanchez, M. Konczykowski, R. Griessen, and F. Holtzberg, *Phys. Rev. B* **43** (10) 8709 (1991).

[25] A. B. Riise, T. H. Johansen, H. Bratsberg, and Z. J. Yang, *Appl. Phys. Lett*. **60** (18), 2294-2296 (1992).

[26] T. Suzuki, E. Ito, T. Sakai, S. Koga, M. Murakami, K. Nagashima, Y. Miyazaki, H. Seino, N. Sakai, I. Hirabayashi, and K. Sawa, *IEEE Trans. Appl. Supercond.* **17** (2), 3020 (2007).

[27] Y. S. Tseng, C. H. Chiang, W. C. Chan, *Physica C* **411** (1-2), 32-34 (2004).

[28] R. Parthasarathy, M. M. Lakshmi, and V. Seshubai, *Physica C* **471** (13-14), 395-399 (2011).

[29] B.M. Smolyak, G.V. Ermakov, *Tech. Phys. Lett.* **36**, 461 (2010).

[30] B.M. Smolyak, G.V. Ermakov, *Physica C* **470**, 218 (2010).

[31] B.M. Smolyak, G.N. Perel'shtein, G.V. Ermakov, *Tech. Phys. Lett.* **27**, 674 (2001).

[32] B.M. Smolyak, G.N. Perel'shtein, G.V. Ermakov, *Cryogenics* **42**, 635 (2002).

[33] L. M. Fisher, A. V. Kalinov, I. F. Voloshin, V. A. Yampol'skii, *Phys. Rev. B* **71**, 140503 (2005).

[34] R. Parthasarathy, M. M. Lakshmi, and V. Seshubai, *Proceedings of the 56th DAE Solid State Physics Symposium 2011. AIP Conference Proceedings, **1447**, 899-900 (2012).*

CHAPTER 5

RAPID INFILTRATION GROWTH PROCESSING TECHNIQUE FOR FABRICATION OF YBCO AND YBCO/Ag SUPERCONDUCTING COMPOSITES

5.1 Introduction

In this chapter, we discuss a rapid processing technique, which is based on the well-known Bridgman-Stockbarger technique used in single crystal growth studies, for fabrication of large, bulk YBCO and YBCO/Ag superconducting composites, called the Rapid Infiltration Growth Processing technique, RIGP for short. This technique is a derivative of some of the zone-melting and directional solidification techniques widely used to grow bulk samples of REBCO superconductors [1-16]. The conventional IGP technique [17-25], discussed in the chapter 3, used for fabrication of bulk REBCO samples including YBCO and YBCO/Ag composites, involves infiltrating liquid phases into a target pellet after decomposition of the liquid phases from a source pellet. The essential criterion, as far as the heat treatment of the samples during processing is concerned, is to have a high uniformity of temperature in the hot-zone of the furnace. The growth of the sample in the IGP technique, from the melt, after peritectic reaction, is achieved by

slow-cooling of the sample after the melting stage. The entire cycle of processing in the IGP technique takes around 120 hours of heat treatment. Any texturing in the sample during growth is achieved by random thermal gradients associated with any heat treatment processes. The RIGP technique discussed in this chapter involves slow motion of the sample through furnace utilizing the temperature gradients available across the length of the furnace. The RIGP technique, to an extent, allows for directional solidification and hence better texturing as the sample is slowly moved out of the hot-zone of the furnace. The aim of the RIGP technique is to reduce the duration of processing to less than 30 hours compared to the 120 hours required for the IGP technique. The following sections in this chapter discuss the RIGP technique in detail, the characteristics of the YBCO and YBCO/Ag samples processed by this technique and a comparison of the magnetic, microstructural and superconducting properties of the samples with those of the IGP samples made by longer heat treatment schedules. The chapter concludes with a discussion on the merits and demerits of the RIGP technique and possible scope for improvement and adaptability of the technique to other systems.

5.2 Rapid Infiltration Growth Processing Technique

The Rapid Infiltration Growth Processing (RIGP) technique has been developed based on the conventional Infiltration Growth Processing technique, by combining the aspect of directional solidification of Bridgeman technique with it. The preparation of YBCO samples by this technique involves preparing the requisite precursor powders by citrate chemical synthesis route, sintering of the powders, pelletizing the powders and processing of the pellets arranged using the same configuration as in the IGP technique described in chapter 3. The essential and crucial difference of the RIGP technique lies in the sample processing conditions and configuration of the furnace which is described below.

The RIGP technique employs a vertical tubular furnace for sample processing. A schematic diagram of the furnace and the sample mount is shown in figure 5.1. The furnace set-up consists of a vertical tubular furnace with a temperature controller, a DC motor, a pulley and a sample mounting cage. The motion of the sample through the tubular furnace in a vertical direction is achieved by attaching the sample mounting cage to the pulley which is driven by the DC motor. The speed of motion of the sample cage is kept constant at 0.25 cm.hr^{-1}.
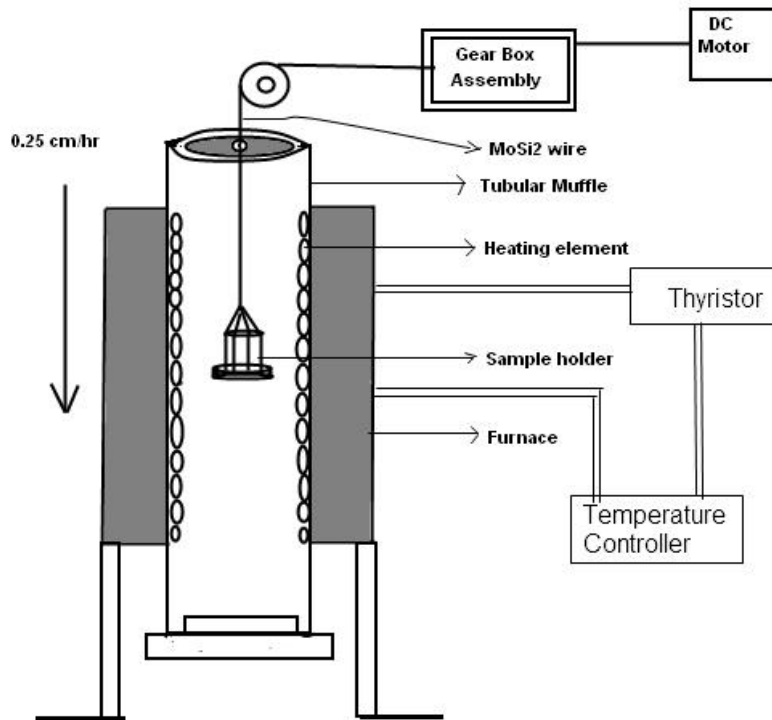
Figure 5.1 The diagram shows a schematic representation of the furnace configuration used for the RIGP sample processing technique

The speed mentioned here is the measured speed of motion of the actual sample mounting cage, in the presence of the sample, through the tubular furnace muffle. The actual speed is less than the calculated speed of 0.4 cmhr^{-1} owing to practical issues such as roles played by the friction in the pulley, weight of the cage etc. The relatively uniform hot-zone of the furnace was found to extend to about 6 cm centered at 31st cm from the top of the muffle. The sample cage attached to a pulley through a wire is suspended initially at the starting point of the hot-zone which is down at 28.5 cm from the top of the muffle. The heat

treatment schedule employed in the present work is shown in the figure 5.2 below.
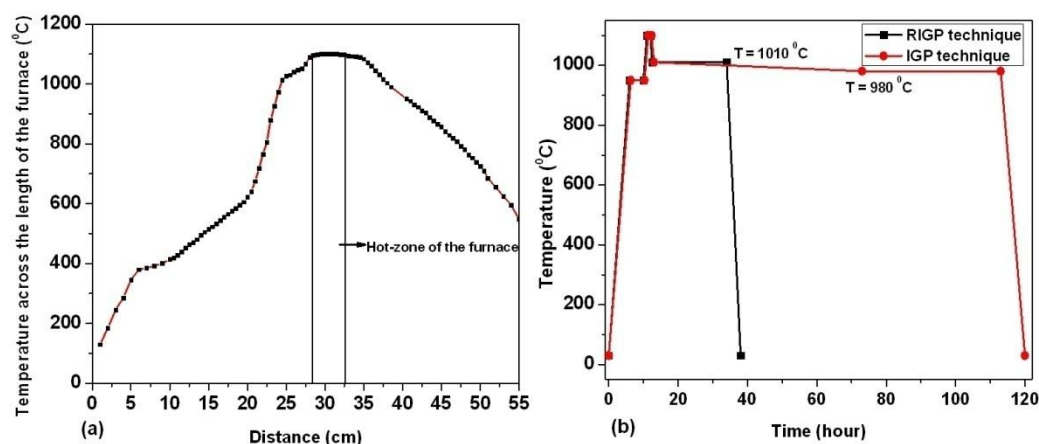
Figure 5.2 (a) Temperature profile of the furnace and **(b)** comparison of the heat treatment schedules used for the IGP and the RIGP technique.

The sample traverses the hot-zone of 4 cm length approximately in about 17 hours with a dwell of 1 hour exactly at the peak of the hot-zone as shown in figure 5.3 (b). The sample is allowed in its motion for another 7 hours in order for slow-cooling and solidification to occur. The entire processing takes around 40 hours to complete including the temperature ramping time initially. Thus, the RIGP technique takes roughly one-third of the time taken by the conventional IGP route for processing of samples. The RIGP technique, hence, ensures rapid processing of samples in shorter time durations which is critical for technological fabrication of bulk superconductors for practical applications.

5.3 Preparation of Y-123/Y-211 superconductor composites by RIGP

In this section, we explain the fabrication of bulk samples of Y-123/Y-211 and YBCO/Ag composite superconductors by the Rapid Infiltration Growth Processing technique. The precursor powders were prepared using the citrate chemical synthesis route as explained in the chapter 3 [26-27]. The Y-123 powders were sintered at 900 C for 24 hours and Y-211 powders were sintered at 950 C for 12 hours. Two samples with different compaction pressures, viz., 460 MPa and 540 MPa were processed using the RIGP technique. The two values of pressure were chosen from the previous knowledge about the optimum compaction pressure being around this regime for samples processed by conventional IGP technique [28]. The two samples are labeled as YRIGP460 and YRIGP540 for 460 MPa and 540 MPa pressure respectively. For comparison of results of RIGP technique with IGP technique, another set of samples with same compaction pressures were prepared by conventional IGP technique. These two samples are labeled as Y460 and Y540 for 460 MPa and 540 MPa compaction pressures respectively. The figure 5.3 (a) below illustrates the heat-treatment program schedule of the furnace of the RIGP technique and the corresponding sample motion (centre of the sample) thorough the furnace.
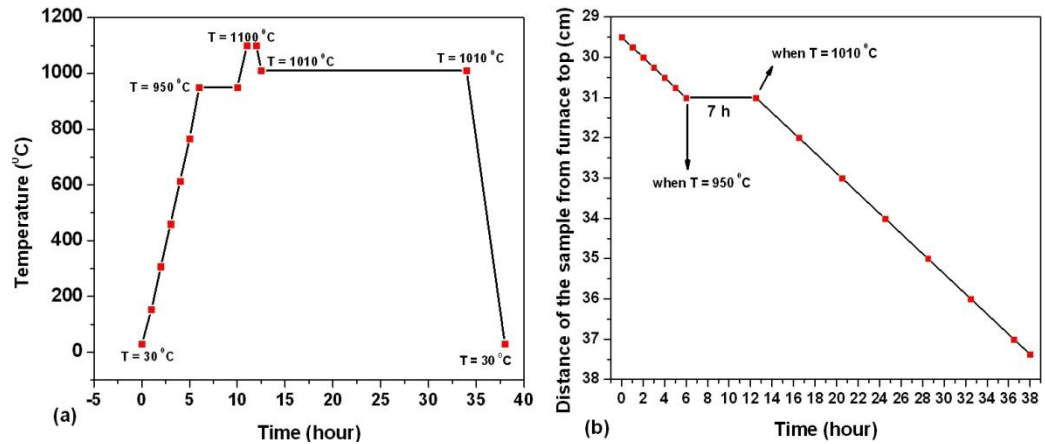
Figure 5.3 (a) The programmed temperature schedule for the furnace used for RIGP technique **(b)** The motion of the sample through the furnace as a function of time in RIGP technique.

The RIGP technique involves initially positioning the sample directly at the hot-zone of the furnace till the melting and the infiltration of the liquid phases occurs. Subsequently, the sample is allowed to move through the uniform hot-zone resulting in directional solidification of the sample governed by its motion and the thermal gradients across the length of the furnace muffle. Figure 5.3 (b) illustrates the motion of the sample through the hot-zone of the furnace and beyond during the processing of the sample by RIGP technique. The following sections discuss the properties of the RIGP samples in comparison with the IGP samples.

5. 4 Temperature dependence of ac susceptibility of RIGP samples

The temperature dependence of real part of ac susceptibility of the samples was measured using a home-made set-up in the temperature range between 77 K and 110 K. The data of RIGP samples is compared with the corresponding IGP samples compacted with same pressure.
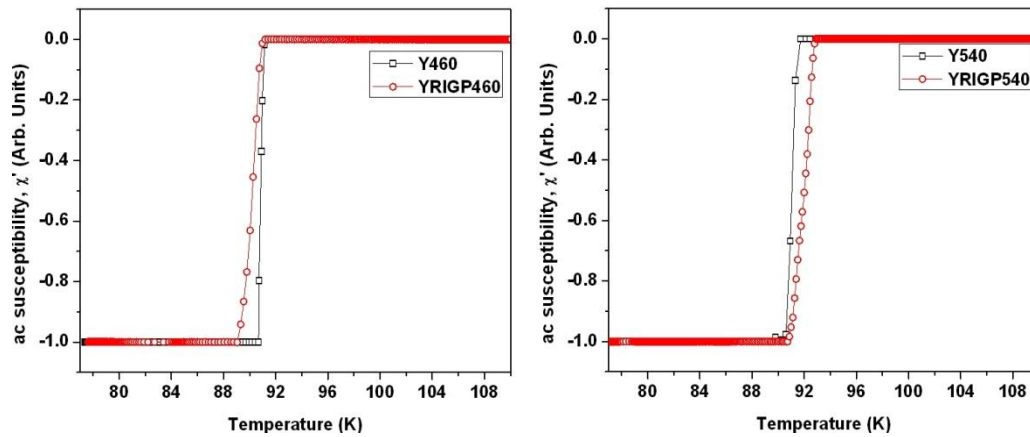
Figure 5.4 The temperature dependence of the real part of ac susceptibility of the RIGP and IGP samples are plotted together for two different compaction pressures of 460 MPa and 540 MPa

The plots of temperature dependence of ac susceptibility reveal the transition temperatures and transition widths of the RIGP samples in comparison with the IGP samples. The table below gives the values of T_c's and ΔT_c's of RIGP samples in comparison with corresponding IGP samples.

S. No	Sample Code	Processing Method	Compaction pressure (MPa)	Transition temperature, T_c (K)	Transition width, ΔT_c (K)
1	YRIGP-460	RIGP	460 MPa	90.3 K	1.43 K
2	Y460	IGP	460 MPa	90.8 K	0.44 K
3	YRIGP-540	RIGP	540 MPa	92.3 K	1.46 K
4	Y540	IGP	540 MPa	90.9 K	0.73 K

Table 5.1 The transition temperature and transition width of the RIGP and IGP samples compacted at two different pressures are tabulated for comparison

It can be seen that the T_c's do not vary significantly between the samples processed by the two techniques but the transition widths for the RIGP samples are slightly broader indicating a possible presence of secondary phases with different T_c's. The formation of secondary phases in RIGP samples may be explained in terms of the reduced processing time. The conventional IGP involves the reaction of the liquid phases decomposed from the source pellet with the Y-211 secondary phase in the target pellet. This reaction occurs when the samples are slow-cooled after melting. In RIGP technique, this duration is significantly reduced and

hence it is possible for a small amount of secondary phases with off-stoichiometric composition to be present in the samples. The secondary phases may not exactly conform to the desired Y-123 composition and hence possibly have a lower transition temperature.

5.5 Magnetic field dependence of critical current density of RIGP samples

The M-H loops of the two RIGP samples, viz., YRIGP460 MPa and YRIGP540 MPa were recorded using the Physical Property Measurement System (QD-PPMS) at 77 K up to 9 T magnetic field. The critical current density of the samples were calculated using the Bean's critical state model formula [29-31],

$$J_c = 20\frac{\Delta M}{d} \ A.cm^{-2}$$

where ΔM (in units of emu/cc) is the difference in magnetization between the first and fifth quadrants of the M-H loop and 'd' (in units of cm) is a geometrical factor involving specimen dimensions. The J_c(H) behavior of the RIGP samples at 77 K is plotted with the IGP samples at respective compaction pressures for comparison in figure 5.5 below.
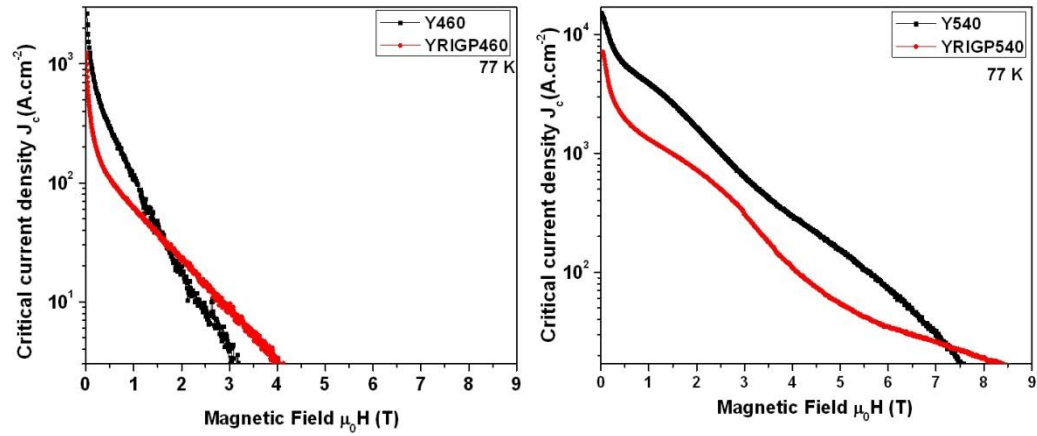
Figure 5.5 The critical current density of the RIGP samples compacted at 460 MPa and 540 MPa pressures are compared with the IGP samples.

The critical current density of the RIGP samples as a function of the applied magnetic field at 77 K is shown in figure 5.5 along with the J_c curves of the IGP samples compacted with the corresponding pressures for comparison. The RIGP samples have lower self-field critical current densities $J_c(0)$ compared to the IGP samples. But the performance of the RIGP samples is found to improve at higher field values. In fact, it can be observed that the YRIGP460 sample performs better than the corresponding IGP sample beyond 2 T magnetic field. The table below quantitatively elucidates the $J_c(H)$ behavior of the RIGP samples in comparison with the IGP samples.

Sl. No	Sample Code	Processing Method	Compaction pressure (MPa)	Self-field critical current density $J_c(0)$ at 77 K (kA.cm^{-2})	Irreversibility field, H_{irr} (T)
1	YRIGP-460	RIGP	460 MPa	1.22 kA.cm^{-2}	0.57 T
2	Y460	IGP	460 MPa	2.66 kA.cm^{-2}	1.08 T
3	YRIGP-540	RIGP	540 MPa	7.14 kA.cm^{-2}	4.11 T
4	Y540	IGP	540 MPa	15.19 kA.cm^{-2}	5.61 T

Table 5.2 The self-field critical current density and irreversibility field values of RIGP and IGP samples made with 460 MPa and 540 MPa compaction pressures are tabulated.

The pinning behavior of the RIGP samples can be studied by computing the pinning force density of the samples as a function of applied magnetic field using the equation $F_p = J_c \times H$. The pinning force curves for both the RIGP and IGP samples made at two compaction pressure values are shown in figure 5.6 below.
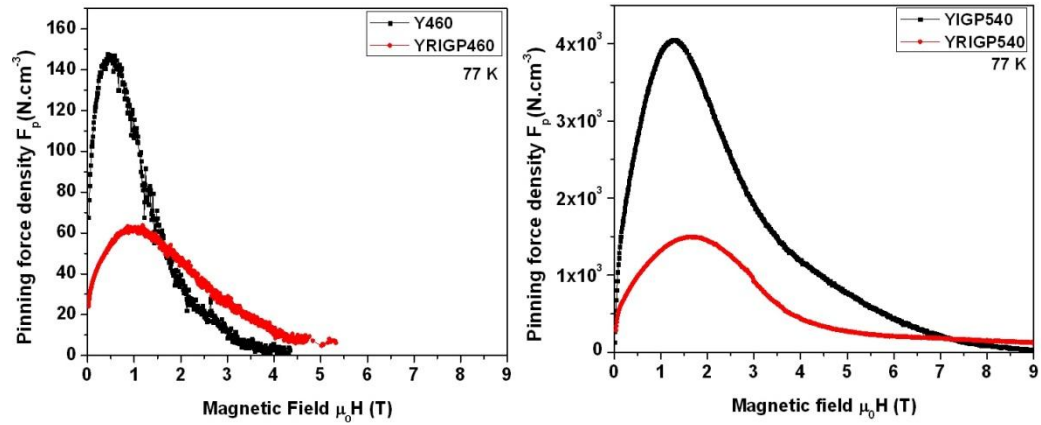
Figure 5.6   Pinning force density as a function of applied magnetic field is plotted for the RIGP samples along with similar curves for IGP samples for 460 MPa and 540 MPa compacted samples at 77 K.

The pinning force density curves reveal interesting aspects about the pinning behavior of the RIGP samples in comparison with the IGP samples. The RIGP samples are seen to have lower pinning force density values whereas the peak value of the pinning force density occurs at slightly higher fields. The pinning force density of the RIGP samples vanishes at higher fields compared to that of IGP samples. This shows that the flux pinning behavior of the samples prepared by the two techniques are different. The implication of higher values of peak field for the pinning force density is that the pinning mechanisms are not the same in the two samples and that the nature of the pinning centers is different and they are effective in different field regimes. In the next section, we attempt to find the microstructural causes for the Jc(H) behavior of the RIGP and IGP samples.

5.6 Microstructural aspects of YBCO samples prepared by RIGP technique

The microstructure imaging of well-polished samples made by RIGP and IGP technique were carried out using Field Emission – Scanning Electron Microscope (FE-SEM). From the recorded images, it can be observed that the microstructures of RIGP samples were remarkably different from those of IGP samples. The microstructural images were further analyzed for determination of the size and distribution of the secondary phase Y-211 particles. Figure 5.7 presents the sample microstructures and the corresponding histograms of the RIGP samples in comparison with the IGP samples.

YRIGP460	Y460
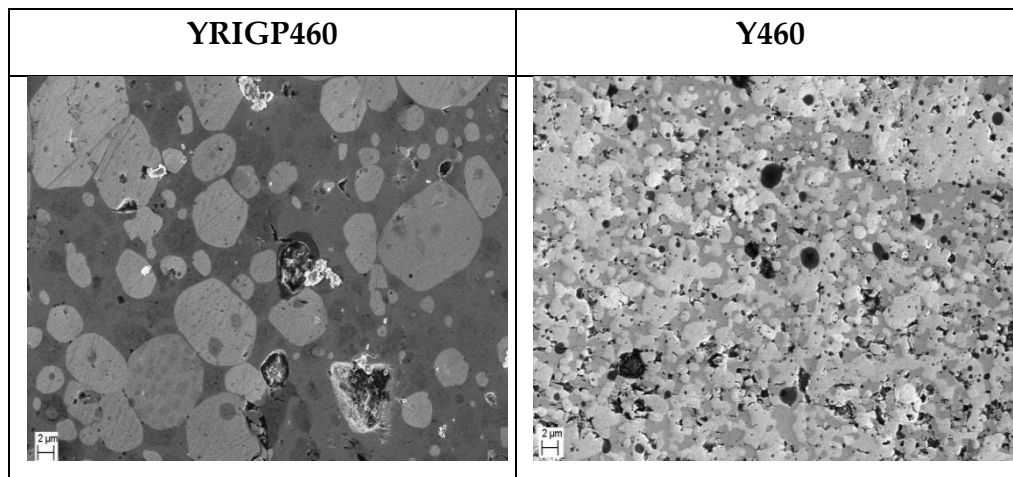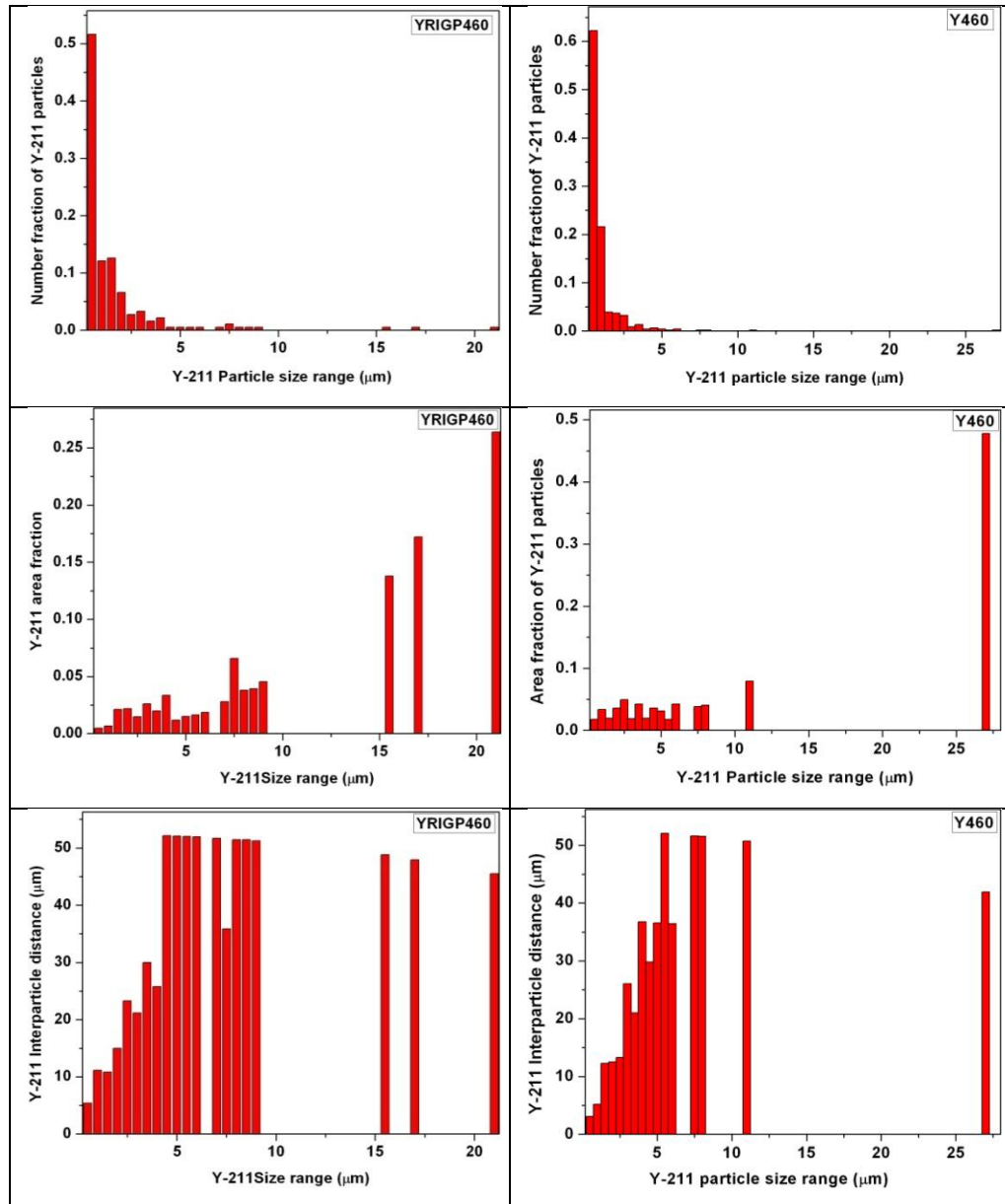
Figure 5.7 The microstructure images from FESEM and the corresponding histograms for Y-211 number fraction, Y-211 surface area contribution and Y-211 inter-particle distance as a function of Y-211 particle size for RIGP and IGP samples made with 460 MPa compaction pressure in comparison.
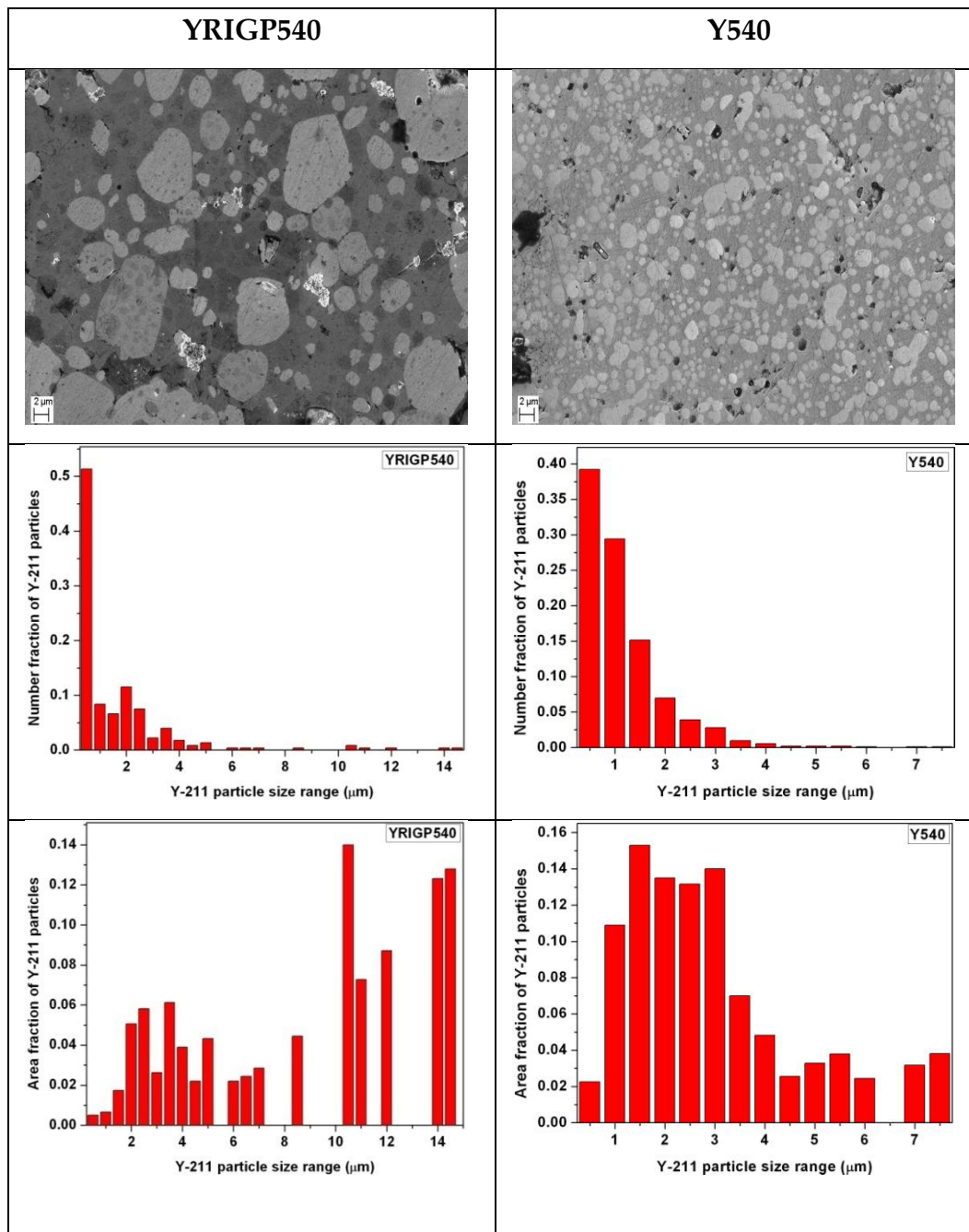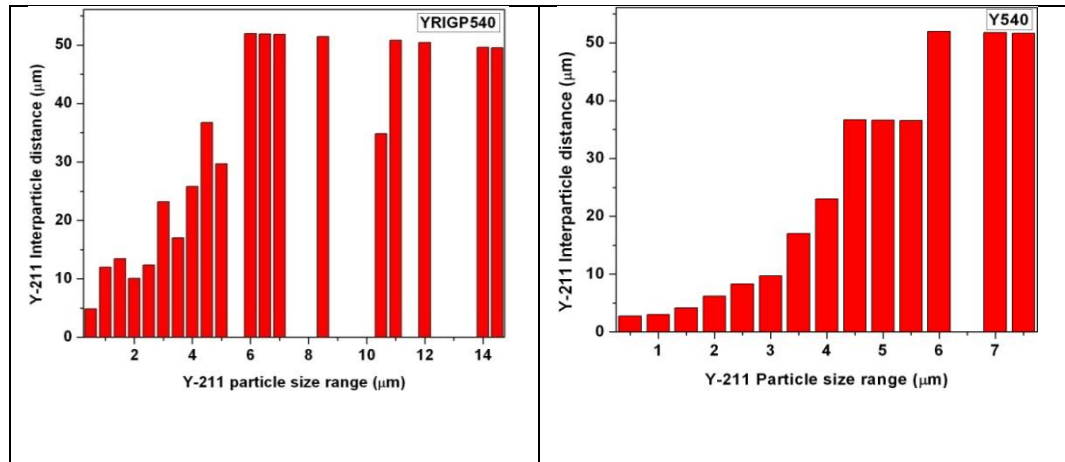
Figure 5.8 The microstructure images from FESEM and the corresponding histograms for Y-211 number fraction, Y-211 surface area contribution and Y-211 inter-particle distance as a function of Y-211 particle size for RIGP and IGP samples made with 540 MPa compaction pressure in comparison.

The microstructure of the RIGP and IGP samples generally indicate the presence of larger Y-211 particles in samples made by RIGP technique compared to the samples made by IGP technique. The critical current density of the RIGP samples is not as high as that of the IGP samples as seen in the previous section. This indicates that fine- size refinement of Y-211 particles is necessary for obtaining higher J_c values. Even within the IGP samples, YIGP540 sample has better J_c values compared to YIGP460 sample owing mainly to better microstructural features. The highest critical current values and better $J_c(H)$ behavior of the YIGP540 sample can be explained by the parameters obtained from the analysis

of the microstructure and the histograms. The Y-211 particle size-wise contribution to the total Y-211 surface area is more evenly distributed across all sizes for the Y540 sample, particularly in the smaller size ranges. The histogram pertaining to the Y-211 interparticle distance, computed as discussed in chapter 3, suggests that there is a gradual increase in interparticle distance as the Y-211 particle size increases implying that the smaller particles are closer and the larger particles are farther apart from each other. This is a crucial factor leading to superior performance of this sample compared to the other samples where the interparticle distance is not so distributed across Y-211 particle size ranges. A favorable combination of all these parameters leads to a higher self-field critical current density and better $J_c(H)$ behavior of the Y540 sample. The RIGP samples on the other hand begin to show better $J_c(H)$ behavior at higher magnetic fields in both the Y460 and Y540 pressure sets compared to the IGP counter-parts. This would indicate additional pinning contributing to enhancement of J_c at higher fields. The contribution from possible secondary phases, with composition slightly different from the stoichiometric composition, left out during the reaction in RIGP samples cannot be ruled out. These secondary phases could be present in traces throughout the samples as unreacted phases, as Y-211 particle size refinement is not complete and larger Y-

211 particles are observed in the microstructure of RIGP samples as can be seen in the table below.

S. No	Sample code	Processing method	Compaction Pressure used (MPa)	Average Y-211 particle size (μm)	Average Y-211 Interparticle distance (μm)
1	YRIGP460	RIGP	460 MPa	1.42 μm	12.34 μm
2	Y460	IGP	460 MPa	0.79 μm	6.05 μm
3	YRIGP540	RIGP	540 MPa	1.43 μm	10.96 μm
4	Y540	IGP	540 MPa	0.90 μm	4.34 μm

Table 5.3 The average Y-211 particle size and Y-211 interparticle distance for the RIGP samples in comparison with the IGP samples compacted at two different pressure values.

From the table, we can see that the Y-211 particle sizes and the interparticle distances for the RIGP samples are larger when compared with those of the IGP samples clearly indicating the microstructural link to their $J_c(H)$ performance. In the next section, we discuss the effect of addition of metallic silver to YBCO to produce YBCO/Ag superconductor composites via the RIGP technique.

5.7 Effect of silver addition in YBCO/Ag composites by RIGP technique

In the previous sections, we have seen that, generally the YBCO composites fabricated by RIGP technique, though has the advantage of processing in shorter time durations, have lower critical current densities relative to those of the IGP samples. In this section, we discuss the effect of Ag addition to make YBCO/Ag composites by the RIGP technique. The aim of the present work was to study whether Ag addition would improve the performance of the samples fabricated by RIGP technique and how metallic Ag addition affects the magnetic and superconducting properties of the RIGP samples. In this section, we would discuss the results pertaining to two YBCO/Ag composite superconductor samples with 10 wt % Ag addition to the liquid source powders in the source pellet which were compacted at two different pressures namely 460 MPa and 540 MPa. The samples are labeled as YRIGP460-10 and YRIGP540-10 indicating the compaction pressure and the silver content in each of them. The two samples were fabricated using RIGP technique as described in section 5.3 with Ag addition to the liquid source powders before pelletization. In the following subsections, we discuss the properties of YBCO/Ag samples fabricated by RIGP technique.

5.7.1 Temperature dependence of ac susceptibility of YBCO/Ag samples fabricated by RIGP technique

In this subsection, we discuss the variation of real part of ac susceptibility with temperature for the YBCO/Ag samples fabricated by RIGP method. The temperature dependence of ac susceptibility of the two YBCO/Ag samples was measured using a home-made ac susceptometer. Figure 5.9 below presents the variation of real part of ac susceptibility as a function of temperature.
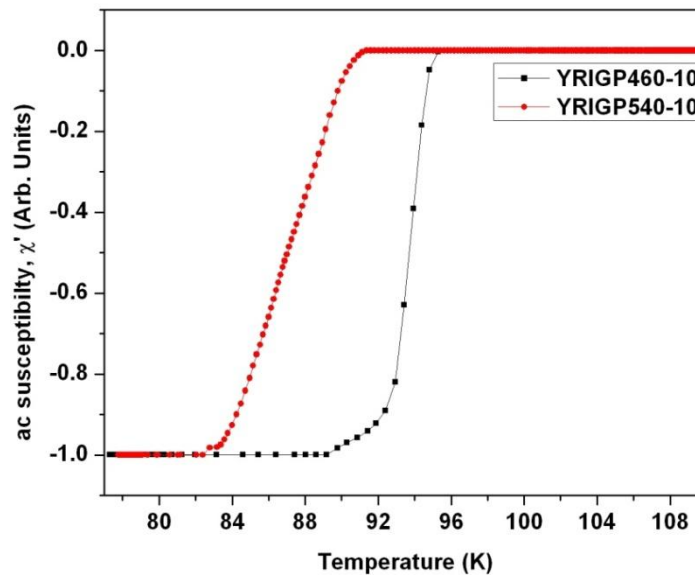
Figure 5.9 Temperature dependence of ac susceptibility of YBCO/Ag composite superconductor fabricated by the RIGP technique with two compaction pressures is shown.

Figure 5.9 reveals interesting features and effects of Ag addition in RIGP technique. The transition widths are observed to broaden due to Ag addition. This broadening is drastic for the sample compacted with 540 MPa pressure while its T_c also shifts to lower values. For the 460 MPa compacted sample YRIGP460-10, the transition broadens without much shift in the T_c value. The shift in T_c and the broadening of the transition could be due to several factors arising out of silver addition. In the YBCO/Ag samples prepared by conventional IGP technique as discussed in chapter 3, the transition width broadening or shifting of T_c to lower values was not observed. But, in RIGP samples, Ag addition has such deteriorating effects probably related to the possible incomplete reactions resulting from the rapid processing of the samples. Further, agglomerated silver and silver substituting for Cu in the YBCO lattice both play significant role in modifying the properties. We would discuss the magnetic field dependence of critical current density and microstructural features in the following subsections.

5.7.2 Critical current density of YBCO/Ag samples fabricated by RIGP technique

The critical current density of the YBCO/Ag samples fabricated by RIGP technique has been calculated from the M-H loops recorded at 77 K. The

effect of Ag addition to the samples in RIGP technique has been brought out in these measurements. The $J_c(H)$ behavior of the two YBCO/Ag samples viz., YRIGP460-10 and YRIGP540-10 is shown in figure 5.10 (a).
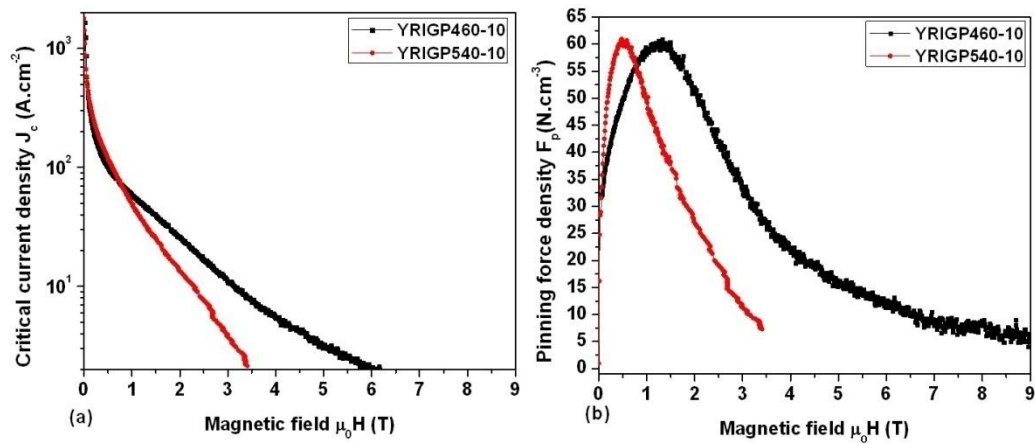
Figure 5.10 (a) Magnetic field dependence of critical current density of YBCO/Ag composite superconductors made through RIGP technique, calculated from M-H loops recorded at 77 K. **(b)** The pinning force density as a function of field for the two samples at 77 K is shown.

From the $J_c(H)$ curves for the two samples, we can see that silver addition has generally affected the critical current density values. Among the two samples, we can see that YRIGP540-10 which was compacted with higher pressure has faster deterioration of J_c compared to that of YRIGP460-10 compacted at 460 MPa pressure, though both the samples has same amount of Ag addition of 10 wt %. The pinning force density also is better for the 460 MPa compacted sample in terms of the

peak field being higher as shown in fig. 5.10 (b). The self-field critical current density $J_c(0)$ of the two samples, however, are of the same order. The table 5.4 gives the $J_c(0)$ and irreversibility field H_{irr} values of the two samples.

Sample Code	Preparation technique	Compaction pressure applied (MPa)	Amount of Ag added (wt %)	Self-field Critical current density kA.cm^{-2}	Irreversibility field H_{irr} (T)
YRIGP460-10	RIGP	460 MPa	10 wt %	1.64 kA.cm^{-2}	0.51 T
YRIGP540-10	RIGP	540 MPa	10 wt %	1.79 kA.cm^{-2}	0.6 T

Table 5.4 The self-field critical current density and the irreversibility field H_{irr} of the two YBCO/Ag samples, compacted with 460 MPa and 540 MPa pressure with 10 wt % Ag, at 77 K

It can be inferred from the values in the table that both the self-field J_c and the irreversibility fields of YBCO/Ag samples fabricated by RIGP technique are low. The microstructural aspects could throw more light on the reasons for observed $J_c(H)$ of the YBCO/Ag samples made through RIGP technique as discussed in the next subsection.

5.7.3 Microstructural aspects of the YBCO/Ag samples fabricated by RIGP technique

The microstructure of the YBCO/Ag composite superconductor samples were recorded using Field Emission Scanning Electron Microscope (FE-SEM). The effect of Ag addition on the microstructure, particularly with regard to the secondary phase Y-211 particles has been brought out in study. The figure 5.11 below gives the microstructure images and the corresponding histograms depicting Y-211 particle number fraction, Y-211 surface area contribution and Y-211 interparticle distance as a function of particle size.

YRIGP460-10	YRIGP540-10
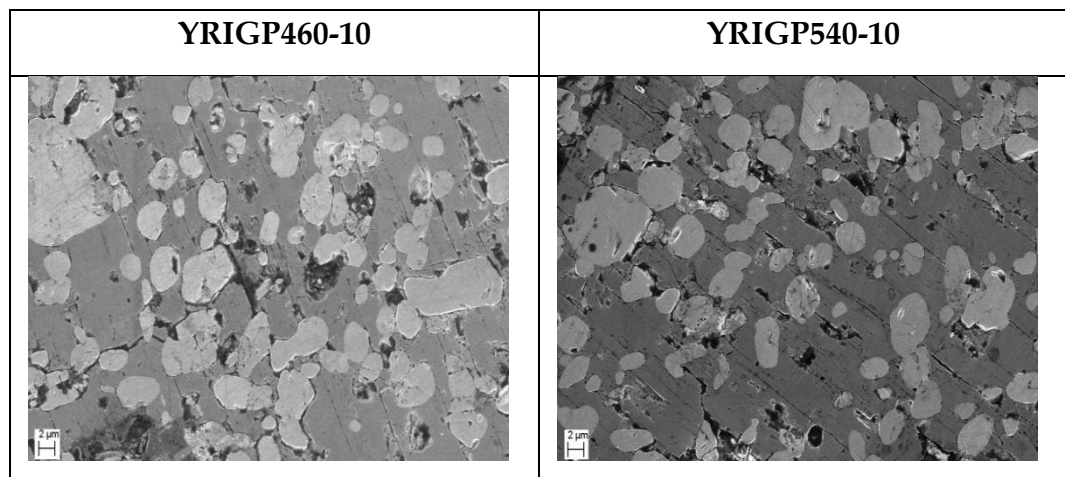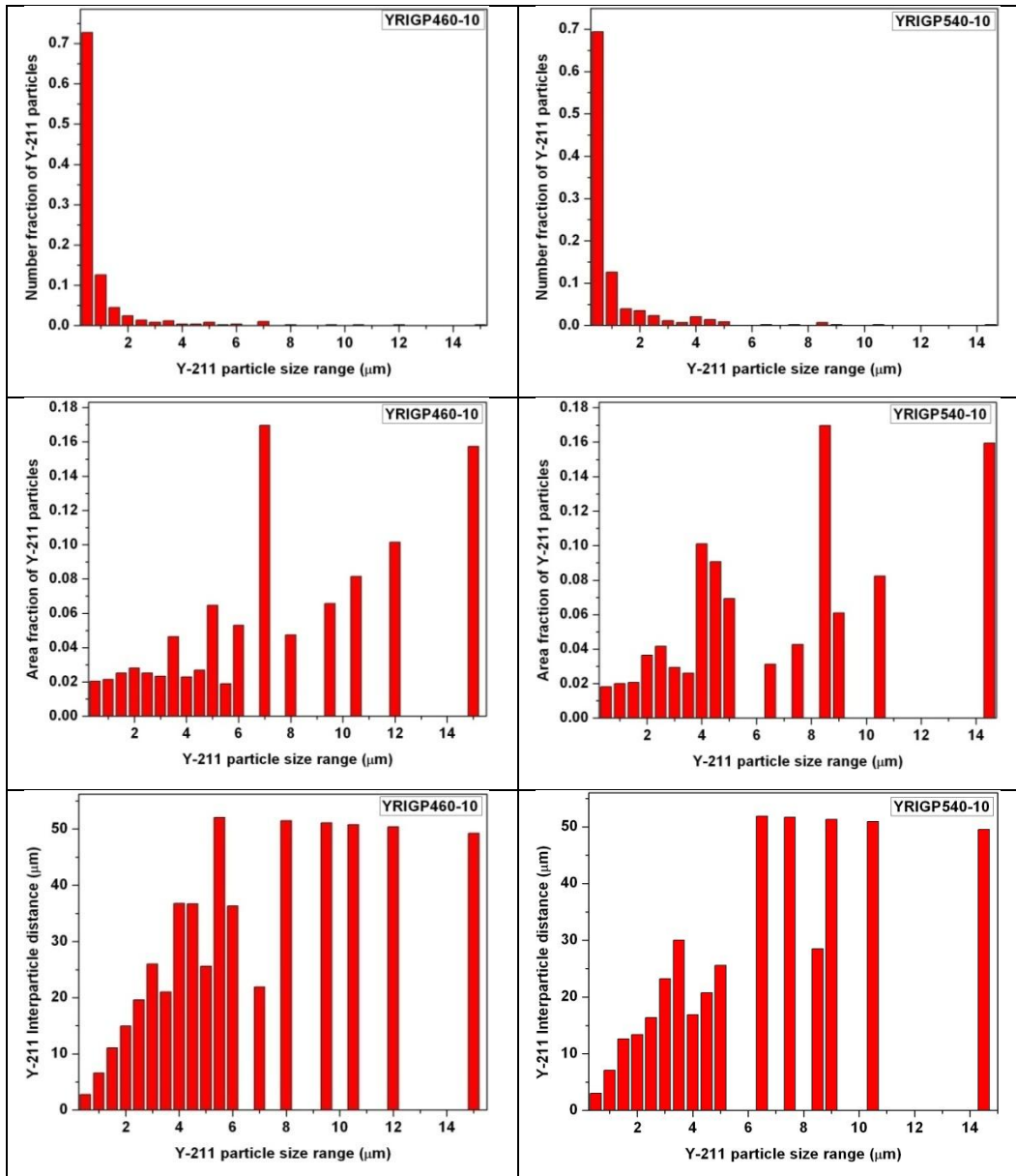
Figure 5.11 The FESEM microstructure of the YBCO/Ag samples made through RIGP technique compacted under pressures of 460 MPa and 540 MPa is shown. The histograms depict variation of Y-211 particle number fraction, surface area contribution and interparticle distance as a function of particle size.

From the microstructural analysis and the histograms depicted above, it is clear that in terms of microstructure there is not much difference between the two samples compacted at different pressures. The self-field $J_c(0)$ values and the irreversibility field values H_{irr} of the two samples were also found to be nearly the same. The histograms corresponding to size-wise surface area contribution of Y-211 particles indicate a large contribution to the Y-211 surface area from the larger sized Y-211 particles. This is an important factor because of which the critical current densities and irreversibility fields possibly are not very high in this case whereas one can compare the corresponding histograms of the IG processed sample Y540-4 from fig. 3.12 having superior current carrying properties whose histograms show a peak distribution of Y-211 surface contribution mainly at lower Y-211 particle sizes. Similarly, the histograms corresponding to the Y-211 interparticle distance indicate a trend where the larger Y-211 particles beyond 6μm size all are almost similar distances away from each other. This can be contrasted with the histograms of YBCO samples seen in the previous section where the histograms corresponding to the interparticle distance linearly stepped up to 7 μm with Y-211 particle size increase leading to better J_c and H_{irr} values. These are, it can be concluded, very crucial parameters determining the quality and the performance of the samples.

Further, it is important to establish the role of silver added to the system in modifying the microstructural properties both directly and indirectly as discussed in chapter 3. We have seen in chapter 3 that Ag added to the system in YBCO/Ag composite samples fabricated through the IGP technique plays a direct role by substituting for the Cu sites in the YBCO lattice and an indirect role by modifying the Y-211 size, shape and distribution, thereby impacting the performance of the samples. We also observed Ag agglomeration due to concentration quenching effect beyond 2 wt % Ag addition. In RIGP samples, we expected addition of 10 wt % Ag to help the system since the processing time is reduced considerably. In RIGP technique, the time for infiltration and the subsequent reactions leading to growth is also reduced [32]. We find that adding 10 wt % Ag in RIGP samples has not improved the performance of the samples. The role of silver added in RIGP technique can be better understood by microstructural observations of silver distribution in the Y-123 matrix from the FESEM images recorded in the secondary electron imaging mode as seen in figure 5.12 below.

YRIGP460-10	YRIGP540-10
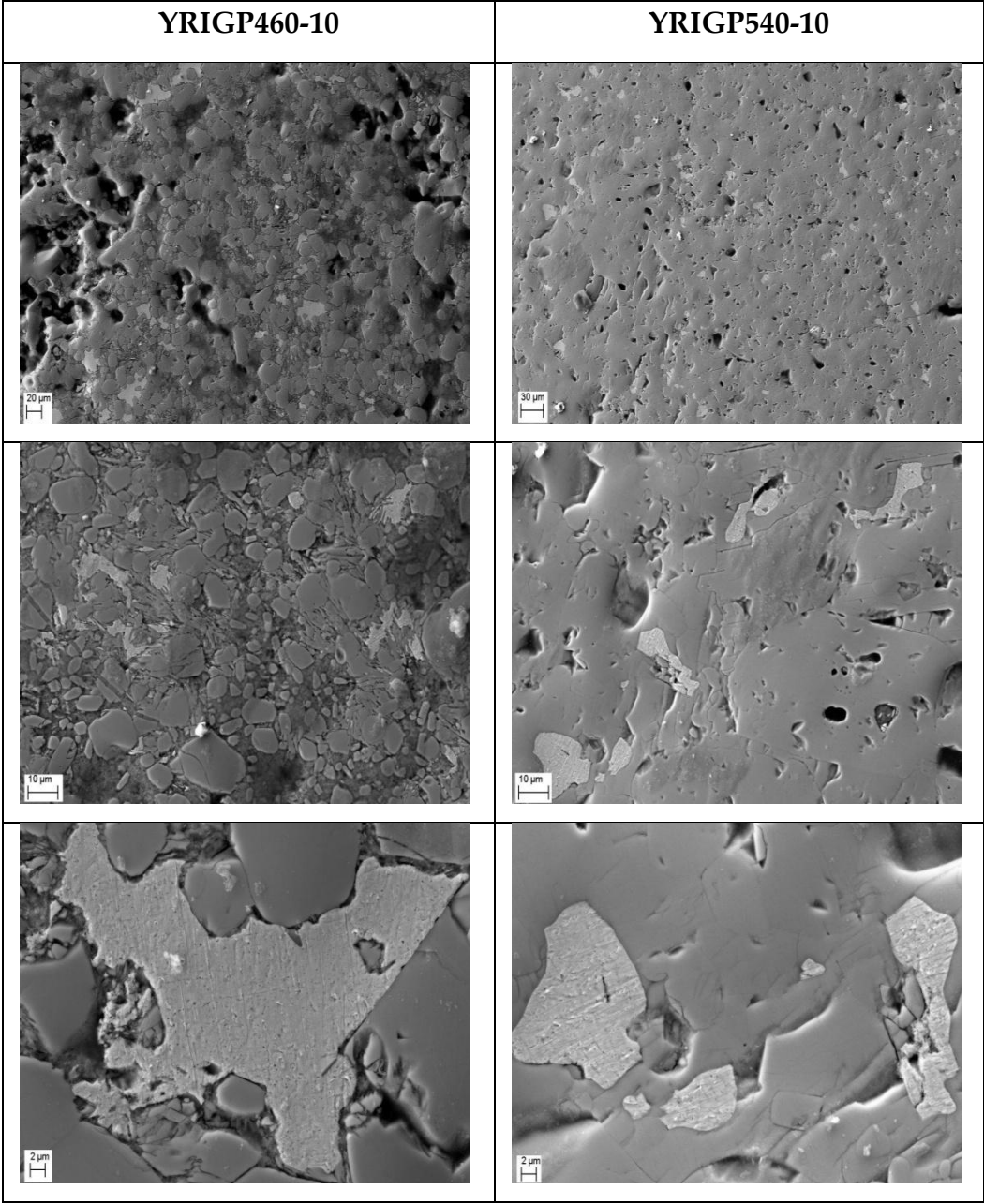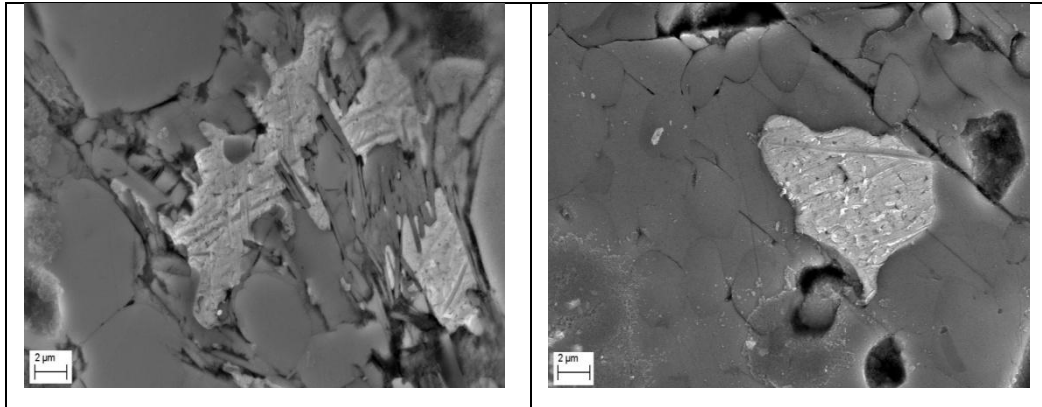
Figure 5.12 The FESEM images of the YBCO/Ag samples made through RIGP technique with 10 wt % silver compacted under different pressures, in secondary electron imaging mode.

The secondary electron images from the FESEM in Figure 5.12 above indicating distribution of agglomerates of silver particles indicate a large amount of the added silver widely distributed as throughout the sample across several regions. The effect of Ag on the microstructure with respect to the Y-211 phase particles has already been discussed. The agglomeration of silver as huge chunks throughout the sample also would have a significant impact on the performance of the sample [32]. One direct consequence is substantial reduction in superconducting volume of the sample apart from its role in modifying the microstructure. At this scale, it is possible that Ag can obstruct supercurrent structure in the material thereby impacting its performance. The reason for huge agglomeration of silver particles in

RIGP technique compared to the IGP technique possibly has to do with the reduced processing time. The excess silver has remained in the sample in RIGP technique whereas in the IGP technique, due to prolonged heating, some amount of the silver was observed to have more uniformly distributed into smaller precipitates throughout the sample. Thus we see there is a significant effect of processing conditions on the microstructure of YBCO/Ag samples in the RIGP technique.

References

[1] M. Murakami, M. Morita, K. Doi, and K. Miyamoto, *Jpn. J. Appl. Phys.* **28**, 1189-1194 (1989).

[2] G. Krabbes, P. Schätzle, W. Bieger, U. Wiesner, G. Stöver, M. Wu, T. Strasser, A. Köhler, D. Litzkendorf, K. Fischer, and P. Görnert, *Physica C* **244** (1-2), 145–152 (1995).

[3] F. S. Liu, H. L. Mou, K. G. Wang, T. J. Zhang, X. Z. Wu, and L. Zhou, *Mod. Phys. Lett. B* **5** (3), 195-200 (1991).

[4] P. McGinn, W. Chen, N. Zhu, M. Lanagan, and U. Balachandran, *Appl. Phys. Lett.* **57**, 1455 (1990).

[5] V. Selvamanickam, A. Goyal, and D. M. Kroeger, *J. Elec. Mater.* **23** (11) 1169-1173 (1994).

[6] F. Sandiumenge, S. Pińol, and X. Obradors, *Phys. Rev. B* **50**, 7032-7045 (1994).

[7] K. Salama, V. Selvamanickam, L. Gao, and K. Sun, *Appl. Phys. Lett*. **54**, 2352 (1989).

[8] A. Goyal, K. B. Alexander, D. M. Kroeger, P. D. Funkenbusch, S. J. Burns, *Physica C* **210** (1-2), 197–212 (1993).

[9] Y. Li, G. C. Hadjipanayis, *Appl Phys. Lett*. **53** (5), 412 (1988).

[10] J. Kase, J. Shimoyama, E. Yanagisawa, S. Kondoh, T. Matsubara, T. Morimoto, and M. Suzuki, *Jpn. J. Appl. Phys*. **29**, L277-L279 (1990).

[11] L. Durand, F. Kircher, P. Régnier, D. Chateigner, N. Pellerin, F. J. Gotor, P. Simon, and P. Odier, *Supercond. Sci. Technol*. **8**, 214-218 (1995).

[12] G. C. Hadjipanayis and Y. P. Li, *J. Appl. Phys*. **64** (10), 5913 (1988).

[13] M. Boffa, A. Di Trolio, S. Pace, M. Polichetti, and A. Vecchione, *Czech. J. Phys*. **46** S3 (1996).

[14] R. Y. B. Martinez, S. Pinol, F. Sandiumenge, N. Vilalta, M. Carrera, V. Gomis, X. Obradors, *IEEE Trans. Appl. Supercond*. **7** (2), 1743-1746 (1997).

[15] N. Hirano and S. Nagoya, *IEEE Trans. Appl. Supercond*. **5** (2), 1564-1567 (1995).

[16] M. Boffa, M. Boutet, A. di Trolio, S. Pace, N. Sparvieri, A. M. Testa, A. Vecchione, *Physica C* **282–287** (2), 487-488 (1997).

[17] I. K. Jeong, D. Y. Kim, Y. K. Park, K. W. Lee, and J. C. Park, *Physica C* **185-189**, 2393- 2394 (1991).

[18] E. S. Reddy and T. Rajasekharan, *Supercond. Sci. Technol.* **11**, 523(1998).

[19] K. Iida, N. H. Babu, Y. Shi, and D. A. Cardwell, *Supercond. Sci. Technol.* **18**, 1421 (2005).

[20] P. Diko, V. Antal, M. Kaňuchová, M. Jirsa, and K. Jurek, *Physica C* **470,** 155–158 (2010).

[21] N. H. Babu, Y.-H. Shi, A. R. Dennis, S. K. Pathak, and D. A. Cardwell, *IEEE Trans.Appl. Supercond*. **21** (3), 2698-2701 (2011).

[22] G.-Z. Li, W.-M. Yang, X.-F. Cheng, J. Fan, and X.-D. Guo, *J. Mater. Sci*. **44,** 6423–6426 (2009).

[23] R. Cloots, T. Koutzarova, J.–P. Mathieu, and M. Ausloos, *Supercond. Sci. Technol*. **18**, R9–R23 (2005).

[24] J.-P. Mathieu, T. Koutzarova, A. Rulmont, J.-F. Fagnard, Ph. Laurent, B. Mattivi, Ph. Vanderbemden, M. Ausloos, and R. Cloots, *Supercond. Sci. Technol.* **18**, S136 (2005).

[25] H. Fang, K. Ravi-Chandar, *Physica C* **340**, 261-268 (2000).

[26] A. Manthiram and J. B. Goodenough, *Nature* **329**, 908 (1987).

[27] D. Bahadur, A. Banerjee, A. Das, K. P. Gupta, T. Mathews, A. Mitra, M. Tiwari, and A. K. Majumdar, *Rev. Sol. Stat. Sci.* **2**, 77 (1988).

[28] N. Devendra Kumar, *PhD Thesis*, Univ. of Hyderabad, India (2011).

[29] C. P. Bean, *Phys. Rev. Lett.* **8**, 250 (1962).

[30] C. P. Bean, *Rev. Mod. Phys.* **36**, 31 (1964).

[31] D. X. Chen and R. B. Goldfarb, *J. Appl. Phys.* **66**, 2489 (1989).

[32] U. Wiesner, G. Krabbes, M. Ueltzen, C. Magerkurth, J. Plewa, and H. Altenburg, *Physica C* **294**, 17–22 (1998).

CHAPTER 6

MAGNETIC FIELD AND TEMPERATURE DEPENDENCE OF CRITICAL CURRENT DENSITY AND PINNING FORCE DENSITY OF YBCO AND YBCO/Ag SUPERCONDUCTORS FABRICATED BY INFILTRATION GROWTH PROCESSING AND RAPID INFILTRATION GROWTH PROCESSING TECHNIQUES

6.1 Introduction

In this chapter, we discuss the temperature and magnetic field dependence of critical current density and pinning force density of YBCO and YBCO/Ag superconductors prepared by Infiltration Growth Processing and Rapid Infiltration Growth Processing techniques. We present our study of these two properties from the magnetization data of the superconductors as a function of applied magnetic field at different temperatures. We shall discuss the differences in behavior between YBCO superconductors fabricated by IGP and RIGP without any silver addition. Then, we would proceed to discuss the differences in behavior exhibited by YBCO/Ag superconductors with different amounts of Ag addition. We have calculated the critical current densities of these samples using Bean's model formula from the M-H

loops recorded over a wide temperature and field range [1-3]. The Bean's model has as one of its major assumptions the field independence of critical current density. But in the high T_c superconductors, the critical current density is strongly dependent on applied magnetic field. In spite of this major restriction, Bean's model has been widely used for calculating $J_c(H)$ of high T_c superconductors since Bean's model and many of its derivatives predict the $J_c(H)$ behavior with satisfactory levels of accuracy. The critical current density is nearly field independent for these materials at low temperatures below 50 K. The YBCO family of superconductors among other materials in their class has many advantages. The problem of flux creep in YBCO based materials has been to a certain extent overcome with process modifications, engineered pinning centers, with novel processing methodologies etc. The applications of bulk YBCO superconductors require them to carry large currents even in high magnetic fields [4]. This is a major problem which has to be confronted for their use in applications as trapped field magnets, in maglev systems, as frictionless bearings in flywheel based energy storage devices etc. The self-field critical current density has been improved by several orders in YBCO and other REBCO materials. The sustainment of the self-field J_c's to high fields has been a major challenge to direct applications. Further, the use of bulk products of YBCO demands that

these materials be mechanically stable even under very high magnetic fields, capable of getting shaped into required shapes and sizes etc. Infiltration Growth processing technique [5-8] has been able to meet to a large extent many of these requirements. The performance of these materials has improved a lot over the years. But, the achievement of sustained J_c's to higher magnetic fields has eluded the materials scientists. Reports have mentioned sustainment of self-field J_c's to reasonably large fields such as 4 T or 5 T. But, consistency has been lacking in many of these results. This lacuna has resulted because of several factors such as the difficulties in fabricating samples with reproducible properties, the lack of complete understanding of both the material science as well as the physics of these materials etc. A complete understanding of the science of these materials, particularly their magnetic behavior in large magnetic fields and varying temperatures would propel research in the materials science aspects of these materials further. This would enable one to learn more about physics as well as the materials science aspects and hence result in complete understanding of the superconductivity in high T_c materials as well as fabrication of materials suitable for practical applications. The previous chapters in this thesis presented a balanced study of both the physics and materials science aspects of YBCO based composites. The work presented in this chapter is an attempt to understand the magnetic

behavior of these materials as a function of applied magnetic field at different temperatures to understand the physics of these materials better.

6.1.1 Significance of the present study

In YBCO system and other oxide compounds belonging to the cuprate family, the supercurrent conduction is mainly confined to the CuO_2 planes whereas the $CuO_{1-\delta}$ chains act as charge reservoirs supplying carriers to the conduction planes thus playing a significant role in charge transfer [9-12]. The current conduction mechanism is governed by carrier concentration in a given sample. The variation of oxygen content δ in $Y_1Ba_2Cu_3O_{7-\delta}$ hence plays the most significant role in determining intrinsic current conduction mechanisms whereas the extrinsic flux pinning behavior is decided by the defects and other such pinning centers [13-15].

In the present system, YBCO/Ag, we discussed in chapter 3 about the substitution of Ag possibly in Cu site in YBCO unit cell. The corresponding composition would hence be $Y_1Ba_2(Cu_{1-x}Ag_x)_3O_{7-\delta}$. The fact that δ is a function of x which in turn determines the hole concentration p in the system is very significant to understanding the intrinsic current conduction mechanisms.

Thus the hole concentration p≡ p(δ) ≡ p(δ(x)) in the present system.

The overall critical current density behavior is governed by two factors [16], namely

(1) depairing critical current density which is intrinsic which depends on the phase stiffness of the superconducting order parameter

(2) extrinsic depinning of the vortices from pinning sites such as defects, twins etc.,

In such complex systems, a simple power law behavior of the reduced temperature (T/T_c) fails to adequately explain the current density dependence on magnetic field and temperature. The study of dependence of self-field critical current density on temperature provides a sufficient ground for studying the intrinsic current conduction mechanisms such as the depairing current density.

The temperature dependence of critical current density follows a power-law behavior $J_c(T) \alpha (1 - \tau)^n$ as derived from Ginzburg-Landau theory [17], where τ is the reduced temperature T/T_c and n , the power-law exponent is 3/2 for YBCO. But, the power-law behavior is valid only for temperatures close to the critical temperature T_c. At lower temperatures, for granular materials, Ambegaokar-Baratoff proposed a model based on the idea that the grains in such materials behave like coupled

Josephson junctions [18]. The corresponding expression for temperature dependence of critical current density could explain the $J_c(T)$ behavior at low temperatures. J. R. Clem et al., predicted a cross-over between the two regimes at temperatures close to T_c [19]. Based on this work, several researchers have reported the $J_c(T)$ behavior in these two regimes depending on the temperatures at which the critical current densities are studied. Different pinning mechanisms could be explained based on the slope changes observed in the log-log plots of critical current density as a function of reduced temperature [20-26].

In the present study, we observed that $J_c(H)$ behavior shows significant features only for 77 K and to an extent at 65 K. For the low temperatures, below 65 K, we do not expect any significant change in pinning mechanisms in the samples as the critical current density becomes almost field independent in this regime (65 K – 20 K). Thus, the present work aims to explain the observed critical current density and pinning force density behavior of the samples as a function of temperatures at zero-field and a few values of applied magnetic field and provides simple expressions that can be used to fit the observed data.

6.2 Magnetic field dependence of critical current density J$_c$(H) of YBCO superconductors

This section deals with discussions on our study and analysis of magnetic field dependence of J$_c$(H) over a wide temperature range between 77 K and 20 K. The applied magnetic fields were up to 9 T. The samples used in the present study are Y460 & Y540 made by IGP technique and YRIGP460 & YRIGP540 fabricated by RIGP technique. The samples were prepared using the above mentioned techniques as described in chapter 5. Here we present our detailed study of low temperature magnetization data below 77 K. We discuss the variation of J$_c$(H) as a function of applied field at different temperatures for each of the samples. Figure 6.1 below provides the J$_c$(H) curves for the four samples Y460, Y540, YRIGP460 and YRIGP540 at temperatures 77 K, 65 K, 50 K, 35 K and 20 K.
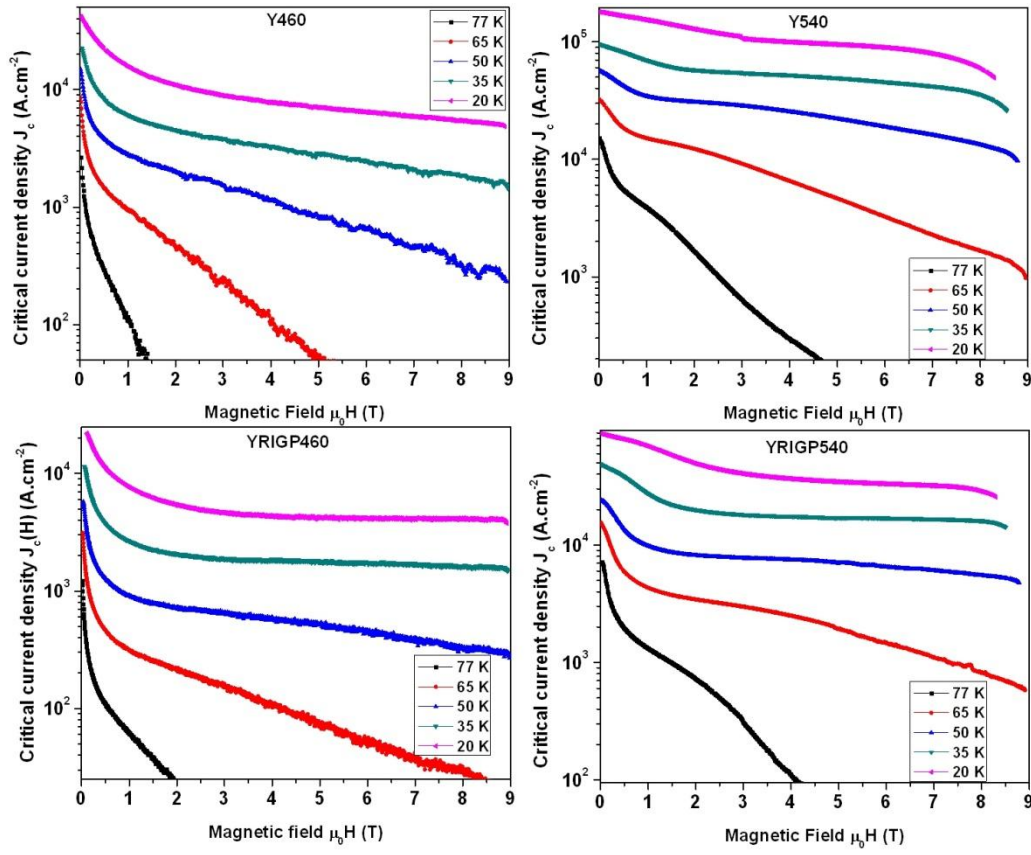
Figure 6.1 The J_c(H) curves of samples Y460 and Y540 (top row) and
YRIGP460 and YRIGP540 (bottom row) at 77 K, 65 K, 50 K, 35 K and
20 K up to magnetic field of 9 T.

The table 6.1 below gives the self-field critical current density values for

the four samples at different temperatures.

S. No	Sample Code	Self-field critical current density $J_c(0)$ (kA.cm^{-2})				
		@ 77 K	@ 65 K	@ 50 K	@ 35 K	@ 20 K
1	Y460	2.66	8.51	14.92	22.47	41.98
2	Y540	15.19	32.26	56.95	95.65	179.7
3	YRIGP460	1.22	3.13	5.77	11.45	21.96
4	YRIGP540	7.14	15.6	24.0	48.8	88.41

Table 6.1 The table displays the self-field critical current density values of the four YBCO composite samples at different temperatures.
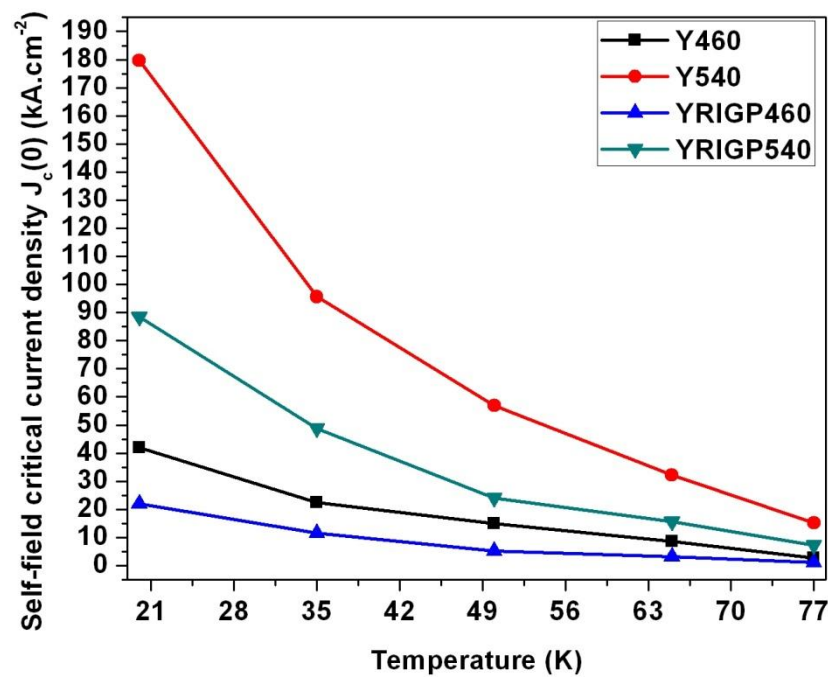
Figure 6.2 The self-field critical current density $J_c(0)$ of the four YBCO samples fabricated by IGP and RIGP techniques is plotted as a function of temperature in the range 20 K to 77 K

The $J_c(0)$ of all the samples show similar behavior though the magnitude of $J_c(0)$'s are drastically different for different samples.

The normalization of these curves individually with respect to the $J_c(0)$ value at 20 K leads to a scaling equation of the form

$$\frac{J_c(0,T)}{J_c(0,T_0)} = y_0 + A_1 \exp\left(-T/t\right) \qquad (6.1)$$
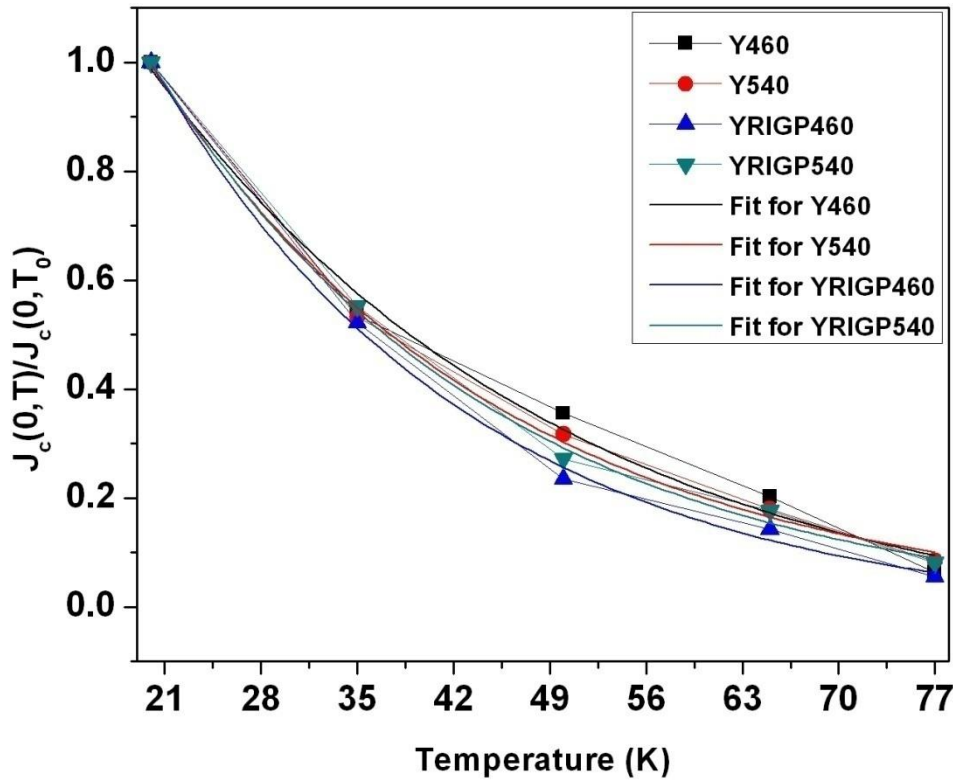
Figure 6.3 The equation 6.1 applied for each of the four samples is shown as fitted curves and the corresponding scaled data for $J_c(0,T)$ as a function of temperature.

Here $T_0 < T$ is the condition under which this equation is valid. Here $T_0 =$ 20 K and 't' is a fit paratemeter. The table below gives the fitting parameters for each of the above curves corresponding to the equation 6.1, when scaled to $J_c(0)$ at lowest available temperature. In practice, however the behavior is expected to remain the same for any lower temperature.

S. No	Sample	Y_0	A_1	t	Chi-square
1	Y460	-0.06529	2.04219	30.22354	0.98253
2	Y540	-0.00773	2.19253	25.57365	0.99619
3	YRIGP460	-0.02366	2.43515	23.0884	0.99665
4	YRIGP540	-0.01343	2.26039	24.97497	0.99605

Table 6.2 The table shows the relevant fit parameters Y0, A1 and t for the scaling equation 6.1 connecting the self-field critical current density $J_c(0,T)$ as a function of temperature scaled to $J_c(0,T_0)$ at any lower temperature.

The parameters Y_0, A_1 and t are material dependent parameters and depend on the sample under investigation. The equation 6.1 hence helps us to predict the behavior of self-field critical current density as a function of temperature given the same value for any one lower temperature such as say $T_0 = 20$ K as taken here in our calculations.

Now, we have to see if it is possible to generalize the above equation 6.1 for any other field. This would generalize and helps us to predict the $J_c(H,T)$ for any given applied magnetic field H. Figure 6.4 below shows the $J_c(T)$ behavior of the four samples Y460, Y540, YRIGP460 and YRIGP540 at four more values of magnetic fields such as 2 T, 4 T, 6 T and 8 T in the same temperature range.
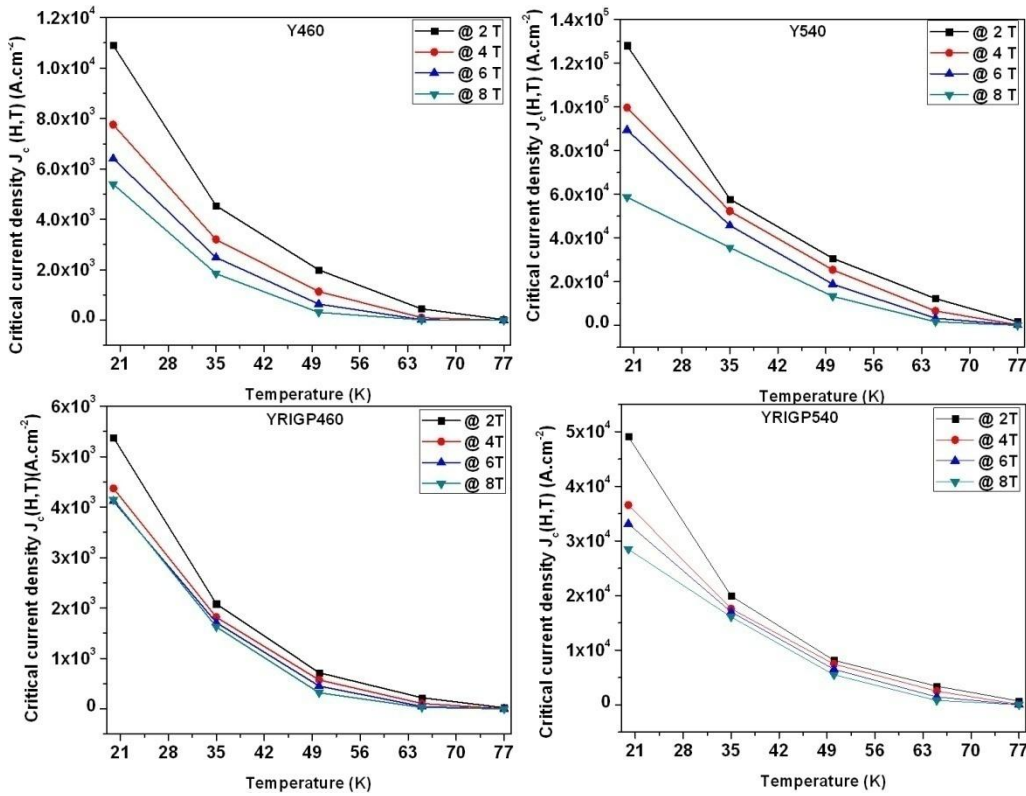
Figure 6.4 The $J_c(H,T)$ curves in the temperature range of 20 K to 77 K at 2T, 4T, 6T and 8T applied magnetic fields for the four samples Y460, Y540, YRIGP460 and YRIGP540.

From Fig. 6.4, we get a family of $J_c(H,T)$ curves for each of the four samples for a set of applied fields namely 2 T, 4 T, 6 T and 8 T. The $J_c(0)$ curves for all the samples showed similar behavior as a function of temperature but in the present case the field dependence come into picture. The equation 6.1 used to explain the $J_c(H=0, T)$ is no longer valid for the present case as any scaling equation must now incorporate the magnetic field H dependence of $J_c(H,T)$.

In order to fit the $J_c(H,T)$ curves for these four samples, we proceeded as before to fit by using the $J_c(H,20)$ for each H in the above curves to normalize the respective curves. After the normalization procedure, the curves could be fitted to Stirling's function of the form

$$\frac{J_c(H,T)}{J_c(H,T_0)} = a + b\frac{[\exp(kT)-1]}{k} \qquad (6.2)$$

Here, $T_0 = 20$ K, a, b and k are fitting parameters. The parameters b and k are sample dependent and the magnetic field dependence of $J_c(H,T)$ is contained in the fit parameter 'a'.

The dependence of parameter 'a' on the magnetic field was tested and fitted to a polynomial of the form

$$a = (a_0 + a_1H + a_2H^2 + a_3H^3 + \cdots) \qquad (6.3)$$

But the sign of the coefficients a0, a1, a2, a3 and the order of the polynomial varies from sample to sample and hence are material dependent.

The Fig. 6.5 below gives the corresponding fitting curves obtained by fitting the data shown in figure 6.4 using eqn. 6.2.
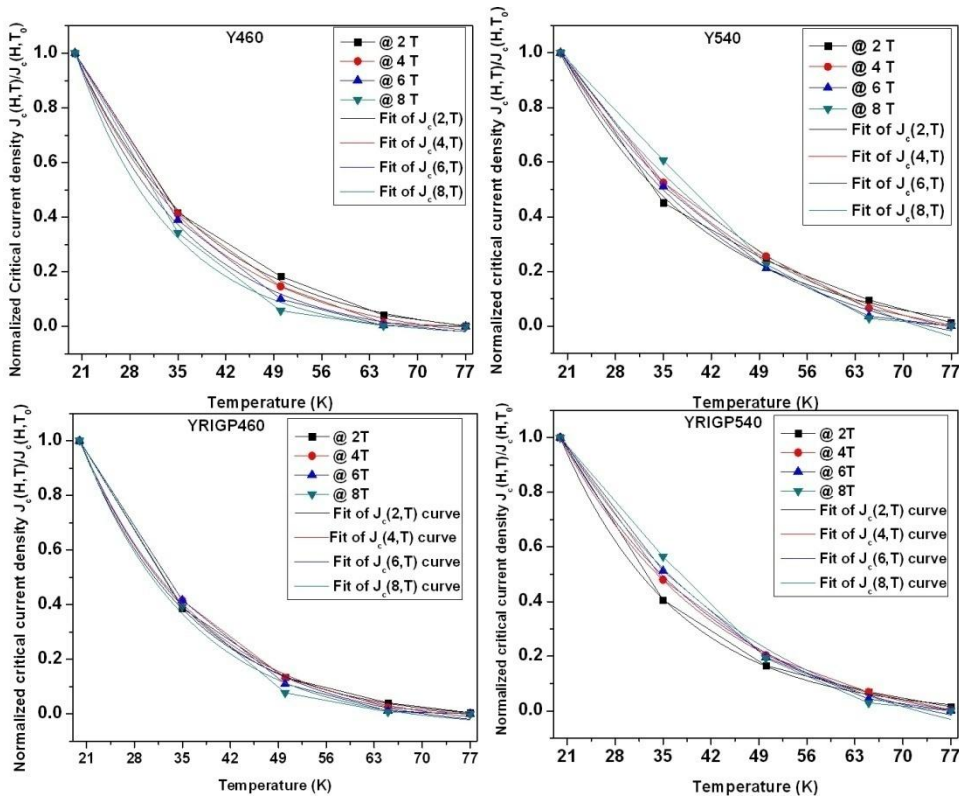
Figure 6.5 The normalized $J_c(H,T)$ curves for the four samples at different applied magnetic fields as a function of temperature is shown with corresponding fitted curves using eqn. 6.2.

The parameter k is a small negative number. The eqn. 6.2 would reduce to eqn. 6.1 if the parameter 'a' vanishes. In other words, in the absence of the field a single equation would suffice to explain both the self-field critical current density and field dependent critical function density as a function of temperature.

6.3 Pinning force density and its field and temperature dependence in YBCO samples

The magnetic field dependence of pinning force density at temperatures below 77 K for the four YBCO samples namely Y460, Y540, YRIGP460 and YRIGP540 prepared by IGP and RIGP techniques is discussed in this chapter. The pinning force density is a measure of strength of pinning in this material. Pinning centers are responsible for arresting magnetic flux bundles or vortices in the material which in turn helps to avoid dissipation and hence to improve the current carrying capability of the material. The dissipation of energy in the superconductor due to the flux motion, sometimes referred to as the flux creep depending on its magnitude, is mainly attributed to the Lorentz force acting on the flux bundles during transport of current in a perpendicular direction. In order to avoid flux motion and help sustain current without dissipation in the material, it is important to have sufficient pinning in the material.

The pinning force density is a measure of the strength of pinning. The pinning force density, F_P is calculated by using the equation,

$$F_p = J_c \; X \; H$$

Hence, the pinning force density is the product of the critical current density at a particular field and the applied field. The pinning barrier causing pinning in the material has to be overcome for flux motion to occur.

Pinning centers can be anything from defects, dislocations, grain and platelet boundaries, twin sites to Y-123/Y-211 interfaces, oxygen deficient phases or other artificial dopants. The exact mechanism of pinning has not been clearly understood considering the wide variety of entities and parameters that can act as pinning centers or cause pinning in the material.

The pinning force density is, hence, a measure of the current carrying capability of the material. One of the essential conditions for pinning has been identified as the size of the pinning center to be of the same order as the coherence length of the material at a given temperature. The dominant pinning in a material occurs at specific field and temperature regimes depending on the type of pinning or pinning centers and when the appropriate conditions for pinning are satisfied. In YBCO based

systems, several such pinning regimes have been identified and the corresponding sizes of the pinning centers responsible for pinning have been found [27-31]. We present below the magnetic field dependence of pinning force density $F_P(H)$ at several temperatures, at and below 77 K, for the four samples Y460, Y540, YRIGP460 and YRIGP540 in figure 6.6.
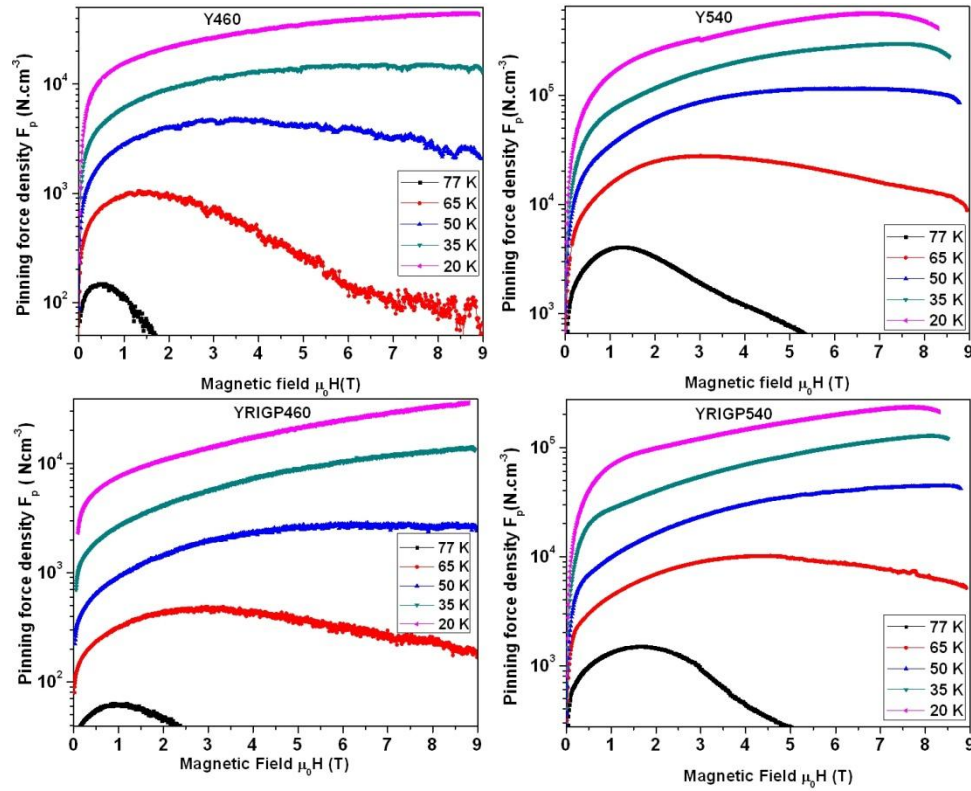
Figure 6.6 The pinning force density as a function of applied magnetic field is plotted for various temperatures between 77 K and 20 K for the four samples Y460, Y540, YRIGP460 and YRIGP540.

From the above curves, one can observe that the samples compacted at 540 MPa pressure in both the IGP as well as the RIGP method have better pinning performance. The peak value of the pinning force density curve, the corresponding magnetic field and the field range over which pinning occurs are the crucial parameters that describe the pinning strength of the material. The features are nearly similar for all the samples below 65 K. But, the features are different particularly at 77 K and 65 K from sample to sample. The fields used were up to 9 T and hence for lower temperatures the curves do not bend back to touch the abscissa. Such open $F_P(H)$ curves are common for low temperatures. In such cases, it is obvious that the pinning force densities do not fall to zero for fields even as high as 9 T.

S. No	Sample code	Peak pinning force density F_{pmax} (N.cm^{-3})	
		@ 77 K	@ 65 K
1	Y460	147.8 @ 0.44 T	1048.1 @ 1.35 T
2	Y540	4052.0 @ 1.29 T	27567.3 @ 3.03 T
3	YRIGP460	63.3 @ 0.87 T	466 @ 2.45 T
4	YRIGP540	1498.4 @ 1.63 T	10132.6 @ 4.56 T

Table 6.3 The table shows the peak pinning force density values and the corresponding magnetic fields for the four samples at 77 K and 65 K.

The table 6.3 presents the peak pinning force density value at 77 K and 65 K for all the four samples for comparison.

To study the temperature dependence of the pinning force density, we plotted the pinning force density as a function of temperature at selected field values 2 T, 4 T, 6 T and 8 T. The figure 6.7 below gives the F_P (T) family of curves for the four samples.
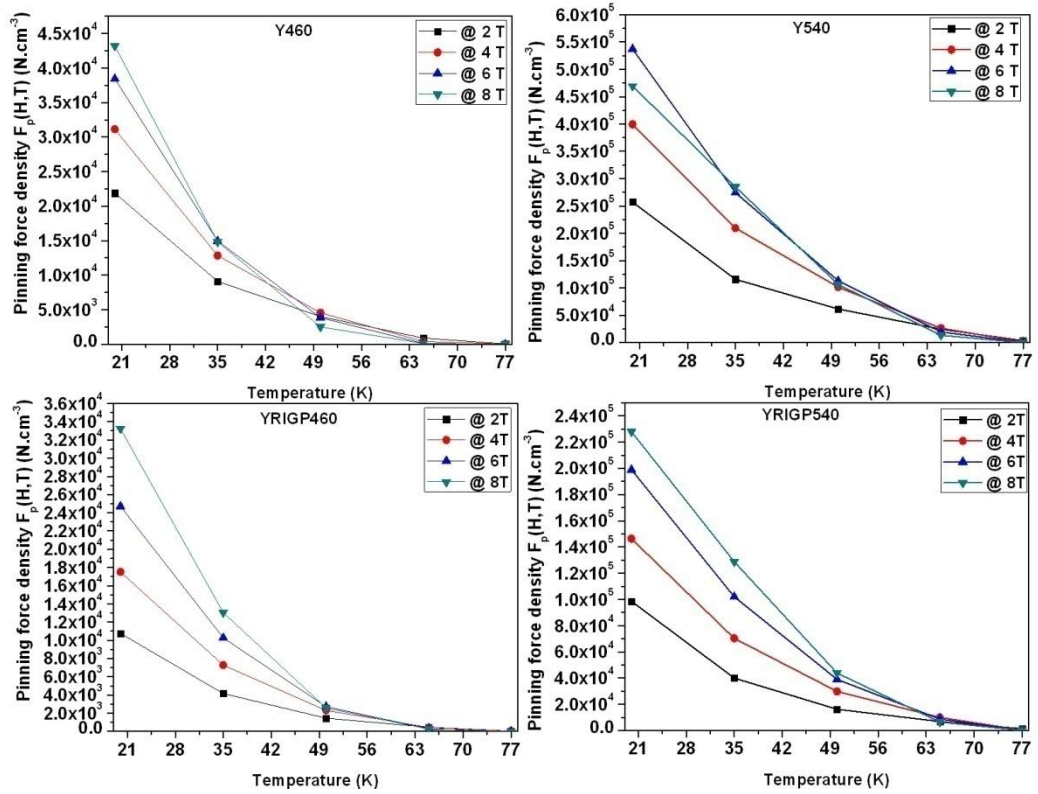
Figure 6.7 The variation of pinning force density F_P(H,T) as a function of temperature at different applied magnetic fields for the four samples Y460, Y540, YRIGP460 and YRIGP540.

The fig. 6.7 shows the variation of pinning force density as a function of temperature in the range 77 K to 20 K at applied fields of 2 T, 4 T, 6 T and 8 T. The relative performance of the four samples can be assessed based on the above plots. Figure 6.8 below shows the corresponding fitted curves. Normalization was done in each case by taking the $F_P(H,20)$ value, i.e., the pinning force density at 20 K corresponding to each of the applied field H values. The family of curves merges on normalization and allows for generalization of the behavior. The fitted curves are shown in figure 6.8 below.

The curves shown in the fig. 6.8 were fitted using the Stirling's function similar to the one used earlier to fit the $J_c(H,T)$ behavior. The corresponding equation for the $F_P(H,T)$ can be written as

$$\frac{F_p(H,T)}{F_p(H,T_0)} = c + d\frac{[\exp(lT)-1]}{l} \qquad (6.4)$$

Here, T_0 = 20 K and the parameters c, d and l are fitting parameters that are dependent on the particular sample. The field dependence is contained in the parameter 'c' and the form of c as a function of H depends on the sample and it varies from sample to sample.
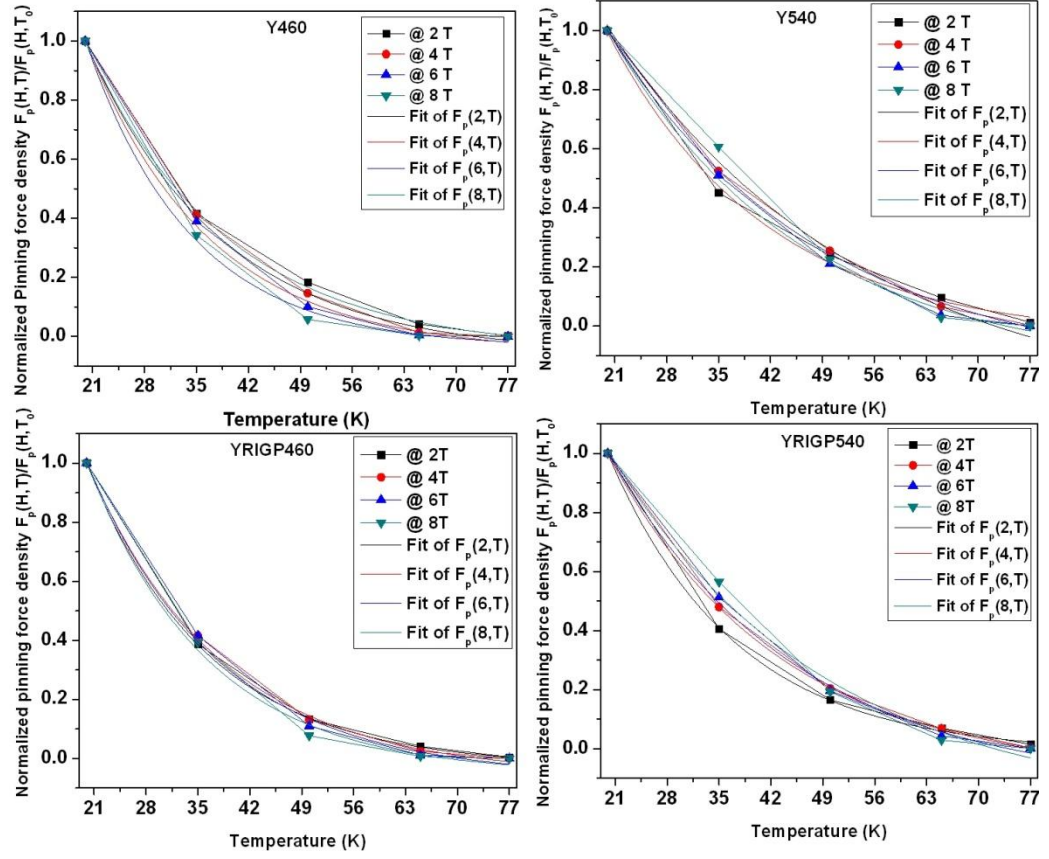
Figure 6.8 The $F_P(H,T)$ curves shown in figure 6.6 were normalized using the Fp(H,T) data at 20 K for each applied magnetic field value. The normalized curves could be fitted to a function and generalized.

Hence, the fit parameter $c \equiv c(H)$ and generally it is observed to be a polynomial in H.

6.4 Magnetic field dependence of critical current density $J_c(H)$ of YBCO/Ag superconductors

In this section, we shall analyze the magnetic field dependence of critical current density of three YBCO/Ag composite samples namely Y540-2, Y540-4 and Y540-10 prepared by IGP as discussed in chapter 3. The three samples were compacted under 540 MPa pressure and they contain 2 wt %, 4 wt % and 10 wt % Ag addition. The magnetization data for the samples were recorded using QD-PPMS in the temperature range of 20 K to 77 K in the field range of 0-9 T. The figure 6.9 below presents the $J_c(H)$ behavior of these three samples.

The samples were composited with different amounts of Ag and all were compacted with 540 MPa pressure under identical processing conditions. The families of curves bring out the effect of silver addition of the J_c dependence on the applied magnetic fields. The self-field critical current density was highest for the 4 wt % Ag added sample followed by 2 wt % sample and then 10 wt % sample at 77 K. But the sustainment of J_c to decent values at higher fields occurs only in 2 wt % sample though its self-field J_c is not as high as that of the 4 wt % sample.
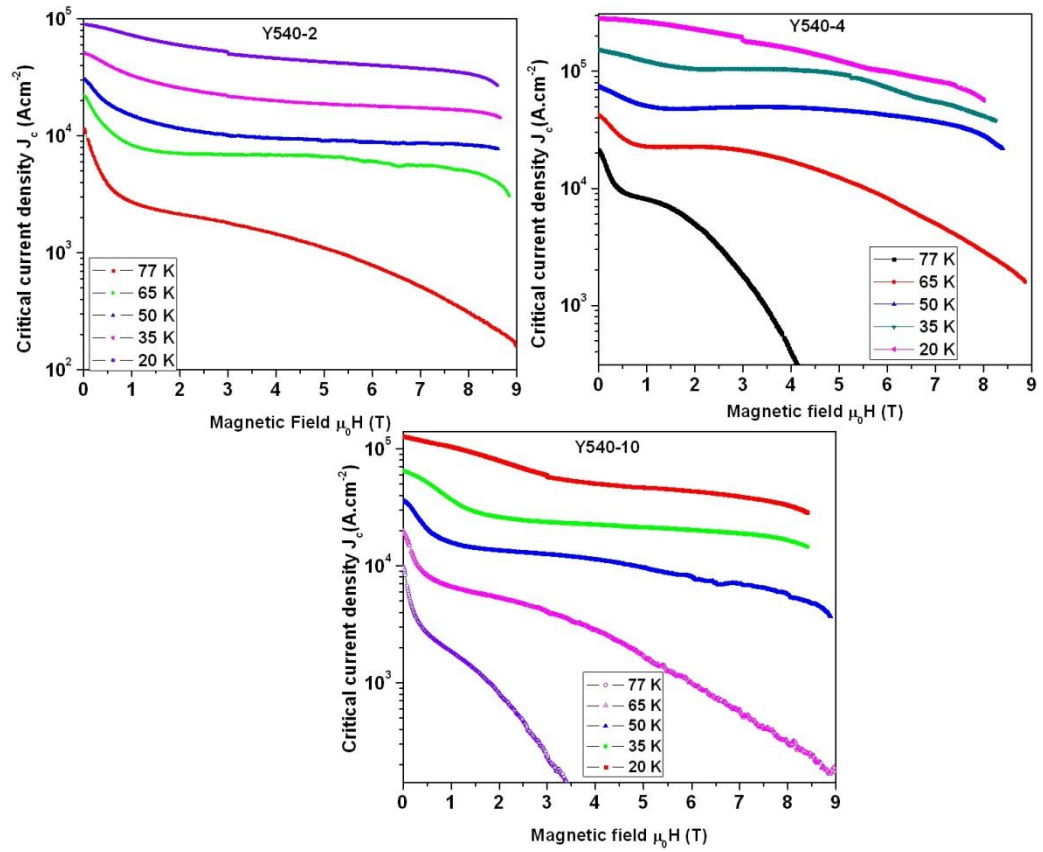
Figure 6.9 The behavior of critical current density as a function of applied magnetic field is shown in the temperature range between 77 K and 20 K for the three samples in the 540 MPa series with varying Ag content.

For lower temperatures, the 2 wt % sample shows consistency in field dependency though the field dependency improves for all the three samples below 65 K. A comparison of self-field critical current density

as a function of temperature for the three samples is shown in figure 6.10 below.
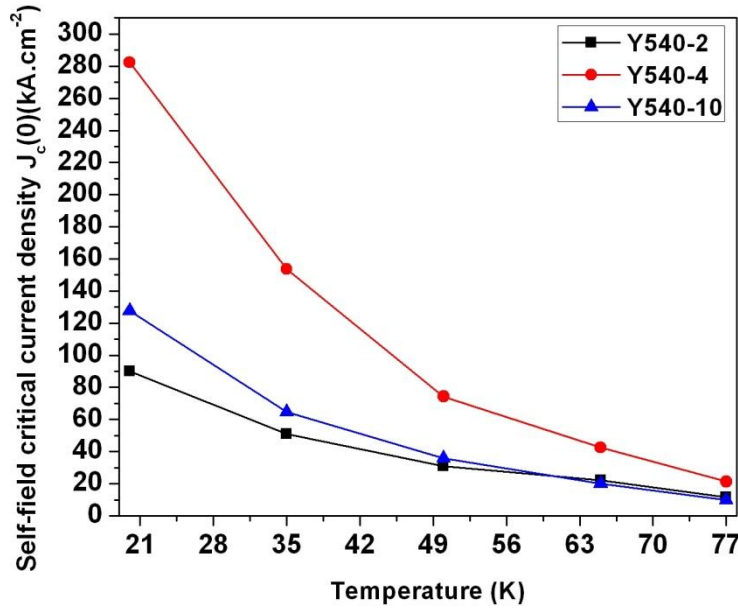
Figure 6.10 The self-field critical current density as a function of temperature of the three samples in the Y540 series with varying Ag contents is shown.

From the figure 6.10, we can see that the $J_c(T)$ behavior of the samples in the absence of applied field is similar with 4 wt % Ag added sample showing superior performance. Between the 2 wt % and 10 wt % samples, the 2 wt % sample shows a better performance only at 65 K and 77 K whereas the 10 wt % sample shows better $J_c(0,T)$ at lower temperatures below 65 K. This shows that the 10 wt % sample acquires

additional flux pinning which is active below 65 K and this pinning makes the self-field J_c better at lower temperatures.

The critical current density as a function of temperature for the three samples at higher fields namely 2 T, 4 T, 6 T and 8 T is plotted in figure 6.11.

It can be seen from the figure 6.11 presented below that the behavior of critical current density as a function of temperature is nearly the same for the three samples at different applied field values. The $J_c(T)$ curves corresponding to 2 T and 4 T fields for the Y540-4 sample shows some interesting features. The curves almost merge in the temperature range between 35 K and 50 K though the applied fields are different.
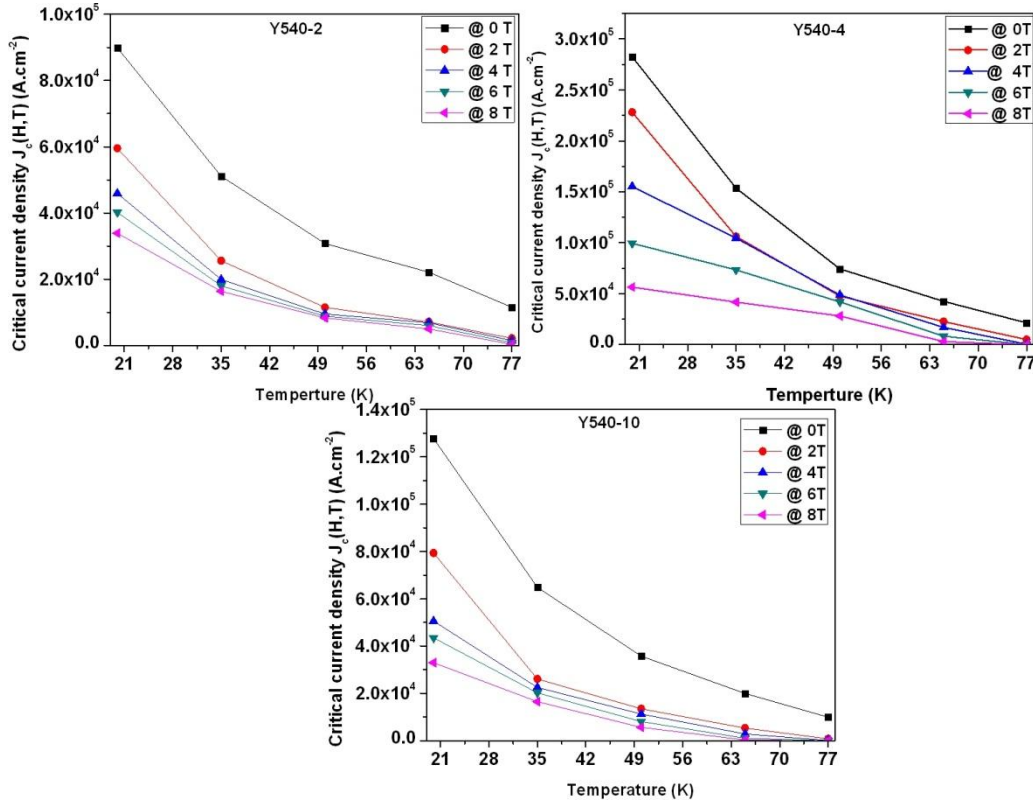
Figure 6.11 The temperature dependence of critical current density of the three samples in Y540 series with varying Ag contents at 0 T, 2 T, 4 T and 6T is shown.

The curves shown in figure 6.11 above for the three samples could be fitted to exponentials similar to the one shown in eqn. 6.2 after due normalization by the critical current density values at 20 K for each of the applied field values as shown in figure 6.12 below.
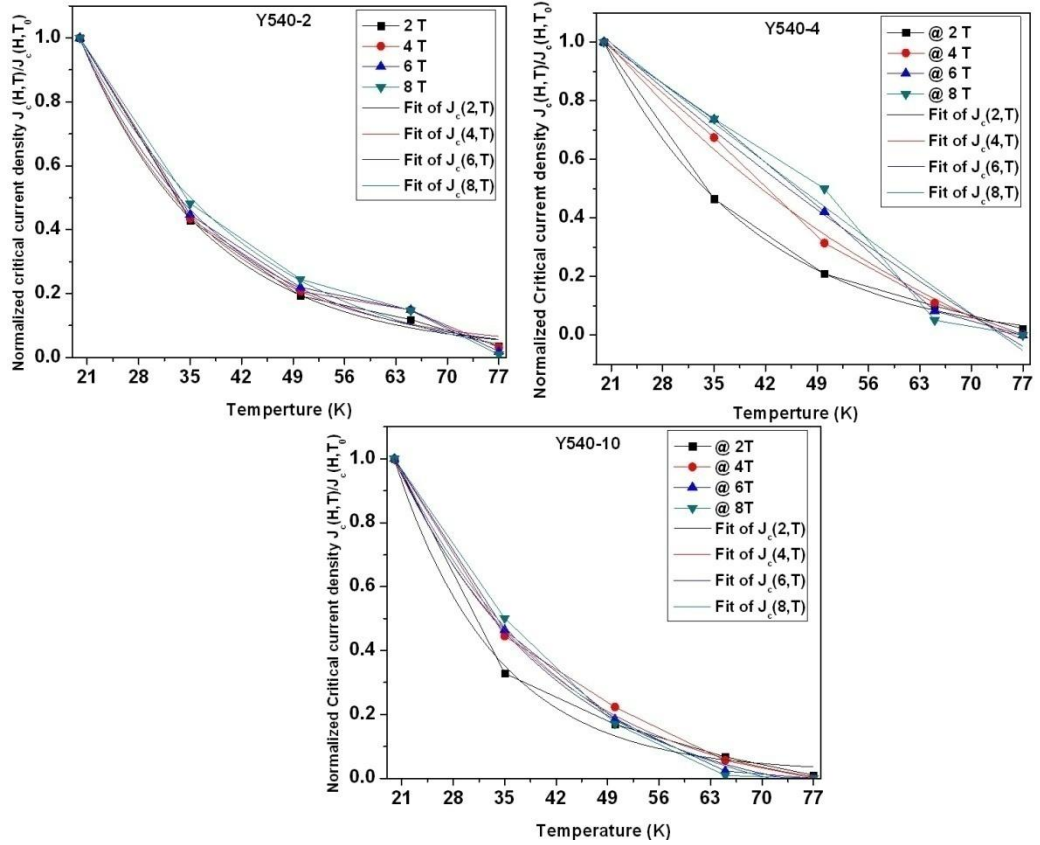
Figure 6.12 The plot of normalized critical current density values as a function of temperature at different applied magnetic fields for the three samples with corresponding fitted curves is shown.

From the figure 6.12, it can be seen that the normalization of the $J_c(T)$ by the values of J_c at 20 K for respective applied fields results in the merger of the curves for the sample Y540-2 whereas for the Y540-4 and Y540-10 the curves do not exactly merge. That is, as the silver content increases in the samples from 2 wt %, the $J_c(T)$ behavior varies and becomes more sample specific and hence the effect of applied field can be clearly seen

for higher fields in 4 wt % and 10 wt % samples. The general equation governing the behavior of the normalized critical current densities as a function of temperature for the three samples can be written as

$$\frac{J_c(H,T)}{J_c(H,T_0)} = a + b\frac{[\exp(kT)-1]}{k} \qquad (6.5)$$

Sample	Applied Fields	Parameter 'a'	Parameter 'b'	Parameter 'k'
Y540-2	2	3.08491	-0.17484	-0.051
	4	2.99515	-0.16594	-0.5589
	6	2.7712	-0.14196	-0.0513
	8	2.40253	-0.10471	-0.04273
Y540-4	2	2.66107	-0.12921	-0.04793
	4	1.70985	-0.04152	-0.01811
	6	1.50207	-0.0259	-0.00703
	8	1.42155	-0.02066	-0.00202
Y540-10	2	4.12911	-0.29526	-0.07185
	4	2.6086	-0.12333	-0.04601
	6	2.6311	-0.12102	-0.04545
	8	2.50666	-0.1108	-0.04197

Table 6.4 The values of the fit parameters for each of the field values for all the three samples are tabulated.

A closer look at the fit parameters reveals to us more about the J_c (T) behavior. From the fit parameters given in table 6.4, we see that all the three parameters namely a, b and k in the equation 6.5 are field dependent. But, significantly, only the parameter 'a' shows some consistent behavior with applied magnetic field values. The dependence of parameter 'a' on magnetic field H could again be fitted to an exponential of the form

$$a(H) = a_0 + A_1 \exp\left(-\frac{H}{t_1}\right) \qquad (6.6)$$

where the parameter A_1 is negative for the YIGP540-2 sample whereas it turns out to be positive for the other two samples in the series. This is interesting considering the fact that concentration quenching of Ag occurs in the system beyond 2 wt % Ag addition.

6.5 Pinning force density and its field and temperature dependence in YBCO/Ag samples

The pinning force density of the three samples was calculated from the J_c(H) data corresponding to temperatures between 77 K and 20 K. The peak field value of pinning force density at 77 K and 65 K were very high for the 2 wt % Ag added sample whereas the magnitudes of peak force density was highest for the 4 wt % Ag added sample as seen from

fig. 6.13. The former corresponds to better irreversibility fields shown by the 2 wt % Ag added sample while the latter relates to better self-field J_c's shown by the 4 wt % sample.
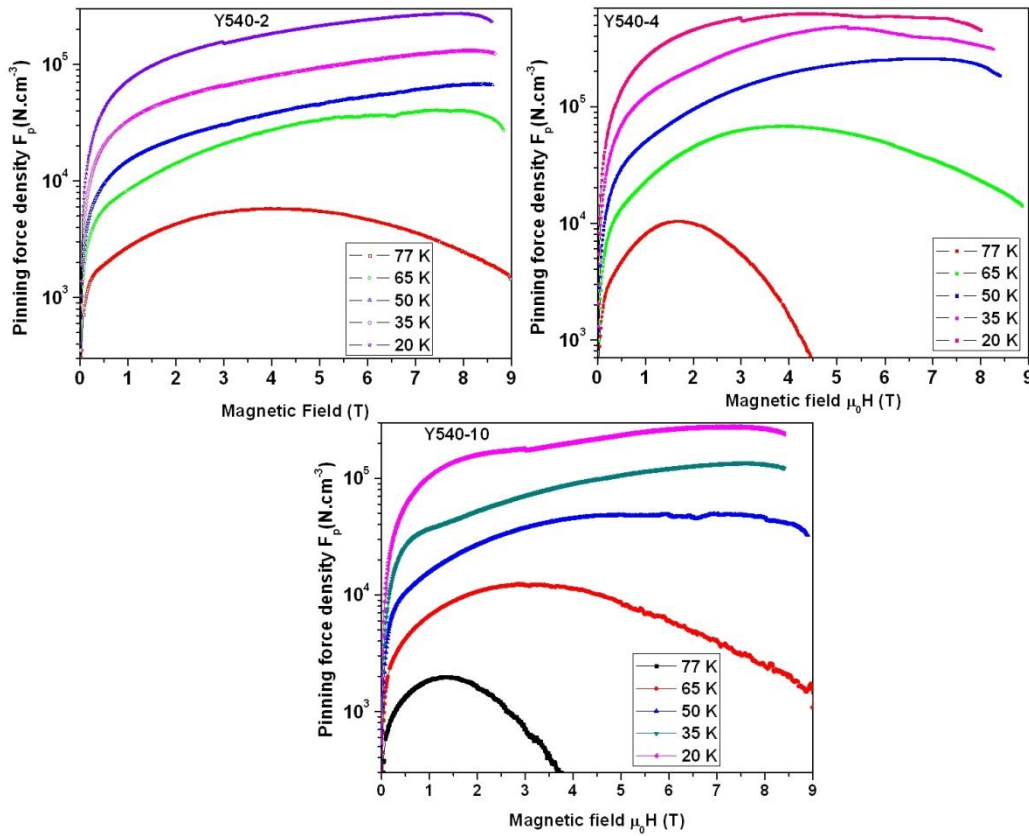
Figure 6.13 The pinning force density as a function of applied magnetic field at different temperatures down to 20 K from 77 K for the three samples in Y540 MPa series with different Ag content is shown.

The temperature dependence of the pinning force density of the three samples as a function of temperature at different applied fields is plotted in figure 6.14 below.
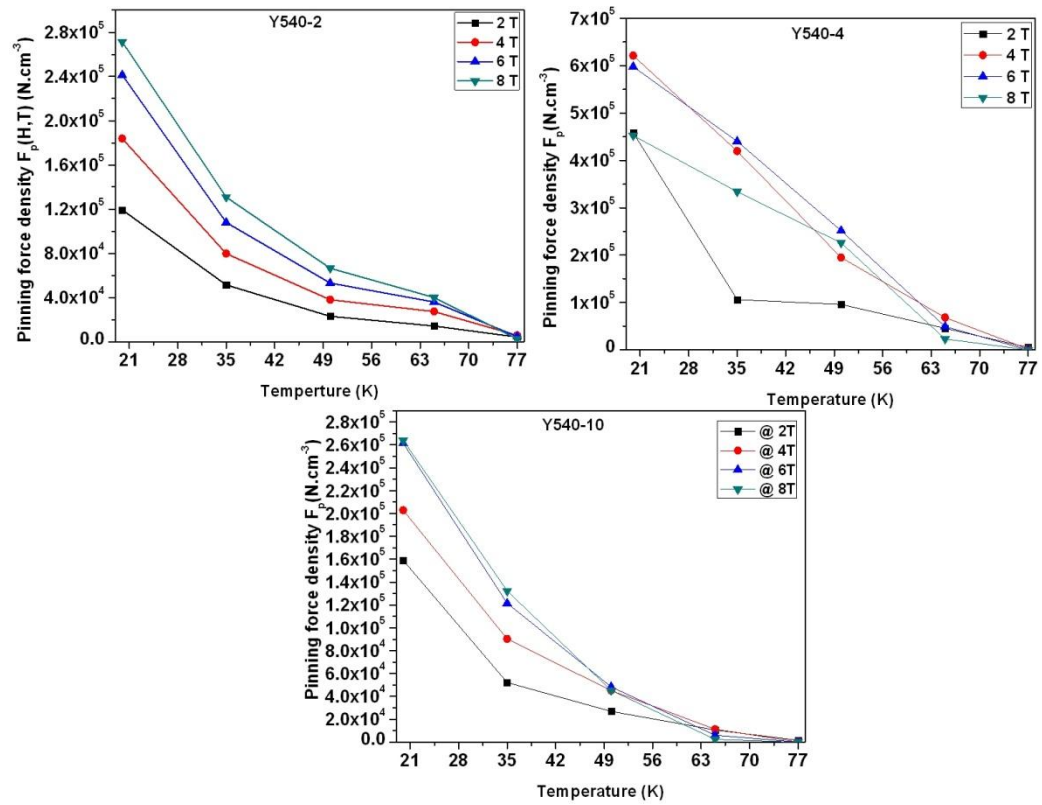
Figure 6.14 The pinning force density of the three samples in Y540 series with varying silver contents as a function of temperature at different magnetic fields is shown.

The temperature dependence of pinning force density of the samples presents certain interesting features. Though the general behavior seems to be alike for the three samples, the 4 wt % Ag added sample has

additional features in the curves. At a given temperature, the pinning force density is higher for higher applied magnetic fields. But for the 4 wt % Ag added sample, this trend is not followed. The prominent peak effect observed in this sample at 77 K seems to be sustained even at lower temperatures, the features of which could be seen even in the $F_P(H)$ curves. The deviation in behavior is observed to be due to non-linearity in pinning behavior in this sample with respect to applied fields and temperatures. The normalized pinning force density curves are shown in fig. 6.15 below.

The normalized pinning force curves replicate the interesting features observed in the absolute curves. A similar kind of deviant behavior is shown by the Y540-4 sample whereas the curves for the other samples merge. The curves could be fitted to an equation of the kind

$$\frac{F_p(H,T)}{F_p(H,T_0)} = c + d\,\frac{[\exp(lT) - 1]}{l} \qquad\qquad (6.7)$$

where the field dependency is contained in parameter 'c'. The parameters 'd' and 'l' are sample specific. The dependency of the parameter 'c' on magnetic field could again be fitted to an exponential of the kind shown in eq. 6.6. The parameter A_1 corresponding to the 2 wt % sample is negative and it is positive for the other two samples.
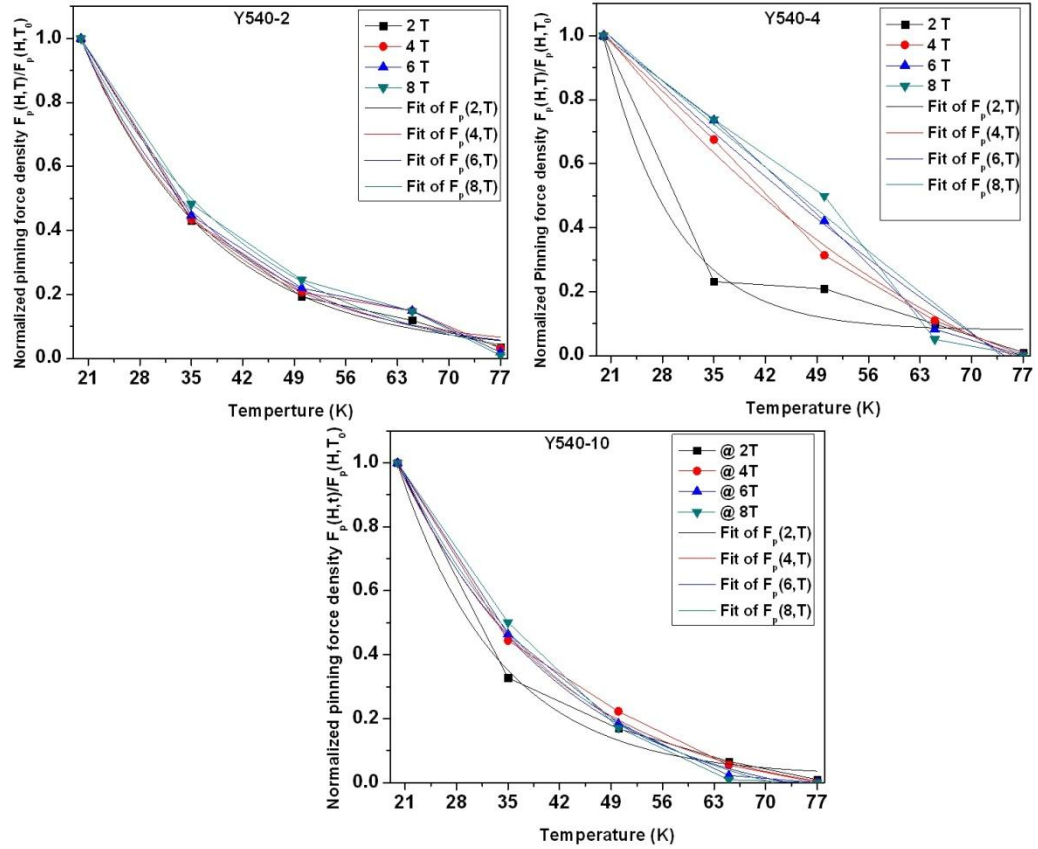
Figure 6.15 Normalized pinning force density as a function of temperature for
the three samples in Y540 series with varying Ag content is
shown.

It is surprising to note that the fit values of parameter 'a' and 'c' in
equations 6.5 and 6.7 are exactly the same for the two samples namely
Y540-2 and Y540-10 indicating a common link connected to the field
dependence of the two parameters. But the values are not equal for the
Y540-4 sample. This could imply that close to the threshold value of Ag
addition, additional contribution to pinning occurs which are subtle but

important and the pinning behavior becomes different due to these effects.

References

[1] C. P. Bean, *Phys. Rev. Lett.* **8**, 250 (1962).

[2] C. P. Bean, *Rev. Mod. Phys.* **36**, 31 (1964).

[3] D. X. Chen and R. B. Goldfarb, *J. Appl. Phys.* **66**, 2489 (1989).

[4] D. Larbalestier, A. Gurevich, D. M. Feldmann, and A. Polyanskii, *Nature* **414**, 368 (2001).

[5] I. K. Jeong, D. Y. Kim, Y. K. Park, K. W. Lee, and J. C. Park, *Physica C* **185-189**, 2393-2394 (1991).

[6] E. S. Reddy and T. Rajasekharan, *Supercond. Sci. Technol.* **11**, 523 (1998).

[7] K. Iida, N. H. Babu, Y. Shi, and D. A. Cardwell, *Supercond. Sci. Technol.* **18**, 1421 (2005).

[8] P. Diko, V. Antal, M. Kaňuchová, M. Jirsa, and K. Jurek, *Physica C* **470,** 155–158 (2010).

[9] J. Harlbritter, *Phys. Rev. B* **48**, 9735–9746 (1993).

[10] G. Hammerl, A. Schmehl, R. R. Schulz, B. Goetz, H. Bielefeldt, C. W. Schneider, H. Hilgenkamp, J. Mannhart, *Nature* **407** (6801), 162-164 (2000).

[11] T. Haugan, P. N. Barnes, R. Wheeler, F. Meisenkothen, and M. Sumption, *Nature* **430**, 867-870 (2004).

[12] K. Segawa and Y. Ando, *Phys. Rev. B* **69**, 104521 (2004).

[13] F. M. Sauerzopf, *Phys. Rev. B* **57** (17), 10959 (1998).

[14] D. M. Feldmann, T. G. Holesinger, B. Maiorov, S. R. Foltyn, J. Y. Coulter, and I. Apodaca, *Supercond. Sci.Technol.* **23**, 095004 (2010).

[15] V. Antal, M. Kaňuchová, M Šefčiková, J. Kováč, P. Diko, M. Eisterer, N Hörhager, M. Zehetmayer, H. W. Weber, and X. Chaud, *Supercond. Sci. Technol*. **22**, 105001 (2009).

[16] G. Krabbes, G. Fuchs, W.-R. Canders, H. May, and R. Palka, *High Temperature Superconductor Bulk Materials*, Wiley-VCH, Germany (2006).

[17] V. L. Ginzburg and L. D. Landau, *Zh. Eksp. Teor. Fiz.* **20**, 1064 (1950).

[18] V. Ambegaokar and A. Baratoff, *Phys. Rev. Lett*. **10** (11), 486 (1963).

[19] J. R. Clem, B. Bumble, S. I. Raider, W. J. Gallagher, and Y. C. Shih, *Phys. Rev. B* **35** (13), 6637 (1987).

[20] M. R. H. Sarkar and S. H. Naqib, *J. Sci. Res*. **4** (2), 287-296 (2012).

[21] X. Wang and J. Z. Wu, *Phys. Rev. B* **76**, 184508 (2007).

[22] M. Ohmukai, T. Fujita, and T. Ohno, *Braz. J. Phys.* **31** (3), 511 (2001).

[23] C. Varanasi, P. J. McGinn, V. Pavate, and E. P. Kvam, *Physica C* **221**, 46-52 (1994).

[24] N. A. Bogolyubov, *Physica C* **478**, 1-4 (2012).

[25] J. Albrecht, M. Djupmyr, and S. Brück, *J. Phys.: Condens. Matter.* **19**, 216211 (2007).

[26] A. A. Gapud, R. Feenstra, D. K. Christen, J. R. Thompson, and T. G. Holesinger, *IEEE Trans. Appl. Supercond.* **15** (2), 2578 (2005).

[27] N. D. Kumar, T. Rajasekharan, R. C. Gundakaram and V. Seshubai, *IEEE Trans. Appl. Supercond.*, **21** (6), 2612-2620 (2011).

[28] Z. Tingjie, W. Keguang, Z. Hian, and W. Shunqlan, *Supercond. Sci. Technol.* **2**, 118-121 (1989).

[29] S. K. Chen, L. Zhou, K. G. Wang, X. Z. Wu, P. X. Zhang, Y. Feng, Physica C **377** (4), 571–577 (2002).

[30] L. Wu, S. V. Solovyov, H. J. Wiesmann, D. O. Welch, and M. Suenaga, *Supercond. Sci. Technol.* **16**, 1127–1133 (2003).

[31] M. D. Sumption, T. J. Haugan, P. N. Barnes, T. A. Campbell, N. A. Pierce, and C. Varanasi, *Phys. Rev. B* **77**, 094506 (2008).

CHAPTER 7

SUMMARY AND CONCLUSIONS

High temperature superconductivity has been one of the most studied areas of modern materials science over the last twenty five years since the discovery of superconductivity in Lanthanum based cuprate ceramic oxide material [1]. Following the improvement in transition temperatures to values above the boiling point of liquid nitrogen with Yttrium based cuprate compound [2], the field of high T_c superconductivity has seen tremendous growth due to the potential applications that these materials offer. Among the class of cuprate superconductors YBCO has emerged as the preferred choice due to several advantages that it offers over the others in this class such as the ease of preparation of single phase compound, the ability of the material to offer large current densities with the possibility for further improvements, the economical advantages over other REBCO compounds, the chemical stability of the material over long time periods, the suitability of the compound to several other bulk practical applications and moreover the rich physics that cuprate superconductors offer, of which YBCO is a simple but powerful model system [3] etc.

Bulk samples of YBCO superconductor have several applications such as trapped field magnets, levitation based systems, magnetic bearings in flywheel based energy storage devices, as magnets in motors and generators and other such potential applications [4]. In this regard, YBCO, being a ceramic material, can be brittle for some of these applications particularly those that involve low temperatures and high magnetic fields. At temperatures much below their transition temperature of around 92 K, these materials offer very high self-field critical current density. Such large currents at low temperatures can cause cracking in the material leading to deterioration of properties when used in practical applications. Among the several ways to improve the mechanical strength of these materials, addition of silver has been one of the favorable methods due to several advantages with using silver. Silver is known to improve the mechanical properties to a large extent without causing much effect on the superconducting properties. In fact, several instances of improvement in superconducting properties with Ag addition have also been reported [5]. In technological applications of superconductors as wires and tapes, use of silver as sheath in them allows for permeation of oxygen. Additionally, silver maintains the stability of the material over long terms of usage while being a relatively economical option as well. Thus, the choice of silver to improve mechanical properties is the most appropriate one.

The ceramic nature of these materials makes them brittle with a high defect density due to inherent macroscopic defects such as cracks, voids and pores. The addition of Ag reduces the defects to a large extent. But, the biggest problem with such polycrystalline materials is the grain boundary effects [6]. In YBCO, the current densities drastically reduce across the grain boundaries. If the grain boundary angle is beyond five degrees, drastic reduction in inter-grain current density occurs. Textured growth of grains would facilitate and improve current conduction across the grain boundaries [7]. The need to modify and improve the microstructure prompted a lot of research into the materials processing of these compounds to further improve both intra-grain as well as inter-grain current densities [8]. Several modifications to the material processing by developing new growth techniques have been carried out with a lot of improvement. Melt Growth based techniques improved the usability of these materials in practical applications in a huge way. The different versions of the Melt Growth Processing technique [9] such Quench Powder Melt Growth (QMG) [10], Melt Powder Melt Growth (MPMG) [11] etc have taken these materials to the next level. Silver addition to the melt grown samples improved the sample microstructures to a significant level. Additional texturing and improvement in grain sizes have been achieved using several seeding techniques as textured samples with large or single-grains are found to

have superior properties while being suitable for many of the bulk applications. Top Seeded Melt Growth [TSMG] has been one such widely used technique for the growth of these materials [12]. But, the seeds used to grow YBCO large grain samples ought to be stable at the high temperatures needed for the growth of this material. Appropriate seeds have been identified such as NdBCO, SmBCO or GdBCO rare-earth based compounds. Using any of these materials as seed improves grain growth, grain size and texturing in YBCO compound. But the practicability of seed usage has been an intense topic of debate for quite some time now. The reasons include the question of chemical stability of seeds at such high temperatures, the dependence of the properties of the material grown on the seed used, the dependence of homogeneity of the properties of the material on the size, shape, positioning and orientation of seed etc. The size of the grain, its texturing and direction of growth all depend on the seeding method. To confront many of the problems with seeding mentioned above, multiple seeding techniques have been tried [13], but with little success. Though seeding brings in several advantages to the growth of these materials, problems such as homogeneity of the seeded samples, restriction on the size and shape of the samples with seeds, dependence of the properties of the sample on the seed size, shape, position and orientation in the sample etc makes the seeding methods less favorable for use. More importantly, seeding is

not a compatible methodology in fabrication of wires and tapes or with process optimization for large scale applications.

The Melt Growth Processing, though offers several advantages over the conventional sintering methods, has some disadvantages that put to question the practical usability of these materials in applications. One of the major drawbacks with the MGP technique is the shrinkage of the end product after melt processing [14]. It has been reported that the overall shrinkage of the sample volume could be as high as 25 % in some cases. In addition to shrinkage, due to melting, other problems such as macroscopic defects, voids and pores form after melting during the cooling stage. Also, microstructurally, the secondary phase Y-211 particle size, shape and distribution are not uniform and not as desired in MGP samples. This makes them vulnerable to inferior performance when put to use in practical applications, especially development of bulk devices or wires.

Infiltration Growth Processing has been developed to overcome the disadvantages of the MGP technique while retaining many of its advantages [15]. IGP technique is basically a melt-growth technique where the melting and growth occurs at different places within the system due to the sample configuration during processing. Hence, samples made by IGP have substantial reduction in defect density, have

significant improvement in microstructure in terms of Y-211 size, shape and distribution and above all shape retention after processing which is a major feature of the IGP technique. The possibility of near-net shape processing of bulk ceramic samples by IGP technique makes it a very important breakthrough in processing of REBCO superconductors [16-17].

Fabrication of YBCO composites with Y-211 phase particles distributed in Y-123 matrix through IGP technique is a successful way of making bulk YBCO samples. Silver addition to the system brings in an entirely different problem as metallic Ag addition makes this system a ceramic-metal composite system. Improvements in mechanical properties with Ag addition to YBCO to make YBCO/Ag composites have been reported [18]. But, there are few reports which bring out any other role for Ag in this composite system. A few studies have focused on the effect of Ag addition on the processing conditions such as on the melting temperature and peritectic reaction temperature of YBCO system [19]. But, otherwise, a deeper study on the role of metallic Ag added to make YBCO/Ag composite has been missing.

 The aim of the present work is to study any additional and possible role that metallic Ag added to the composite has on the magnetic behavior of the composite YBCO/Ag system. Thus, silver, apart from improving the

mechanical properties, could play a significant role in modifying the properties. In this context, it is interesting to note that Ag has been also used as a dopant for Cu site in YBCO unit cell in some studies. The results have generally showed that there is an optimum level of Ag doping in Cu sites beyond which concentration quenching occurs. Any further doping of Ag in Cu sites causes deterioration in properties [20]. Thus, it is possible that Ag added to YBCO to make YBCO/Ag composite may not remain simply as a physical mixture in the Y-123 matrix and enhance its mechanical properties only. There is a definite possibility that Ag added to the system acts chemically and gets doped into Cu sites in YBCO/Ag composites though such an event is unintentional. This has wide-ranging ramifications on the properties of the system. It is interesting to study the possibility of any such substitution occurring and its effects. Further, a study of variation of several of the magnetic and superconducting properties with varying silver content and optimization of addition of Ag with respect to these properties is also important from the applications view-point.

In the present work, we have found that metallic Ag added to the liquid source powders to make YBCO/Ag composite superconductors has additional role apart from improvement in mechanical properties of the system. We have observed that Ag added to the system begins to

agglomerate beyond 2 wt % addition with respect to the liquid source powders. Silver could be seen as precipitates distributed in the Y-123 matrix for 4 wt % and 10 wt % Ag added samples from our FESEM studies. Thus, as a physical mixture also, Ag has a concentration threshold beyond which it starts to agglomerate as precipitates in the Y-123 matrix. The consequences of this include improvement in the mechanical properties and possibly, a modification of the YBCO sample microstructure with respect to the secondary Y-211 phase particles. We have also observed from our x-ray diffraction studies and EDAX studies of the YBCO/Ag samples that there is a possibility of Ag having replaced a few of the Cu atoms in the Y-123 lattice at least in some of the regions of the bulk sample. We have found, from our XRD data analysis that the lattice parameters 'b' and 'c' and the unit cell volume of the YBCO/Ag composite increase with increase in Ag content from 2 wt % to 10 wt %. The increase is proportional to the increase in weight percentage of silver. The EDAX studies have also revealed the presence of Ag in the Y-123 matrix in some of the regions. The number of such regions with presence of Y-123 in the matrix increases with increase in Ag content. We have also observed from our FESEM images that Ag significantly alters the sample microstructure. The Y-211 particle size and distribution have been found to vary with Ag addition. Significantly, the refinement of Y-211 particle size with Ag addition has

not been found to directly improve the superconducting properties of the system. Further, other microstructural features such as the Y-211 number density, surface area contribution, volume fraction and interparticle distance have all been observed to be dependent on the amount of Ag added to the system. The optimization of the amount of Ag with respect to the superconducting properties is carried out mainly based on levitation force measurements and critical current density calculations on these samples. It has been found that both the levitation force and the self-field critical current density are highest for the samples with 4 wt % Ag added to the liquid source powders made under two different compaction pressures namely 460 MPa and 540 MPa. The sustainment of critical current density to higher fields, however, has been observed in 2 wt % sample compacted at 540 MPa pressure. The presence of twinning has been observed only in this sample and hence we could attribute the sustainment of critical current densities to fields as high as 9 T to the pinning caused by the twins or the defects associated with twinning [21-23]. Overall, the samples compacted at 540 MPa have better properties compared to the samples compacted at 460 MPa. The possible cause for absence of twinning in samples with higher Ag content could be due probably to easing out of local strains during the tetragonal to orthorhombic transformation by the presence of silver.

It is interesting to note that both the levitation force, which is a bulk property where the entire sample is characterized, and the self-field critical current density where specific regions of the samples are characterized have a concurrence as far as the optimization of Ag content at 4 wt % is concerned. The optimum values for both these properties for 4 wt % Ag added samples has been observed for both the pressure series namely 460 MPa and 540 MPa.

The study of the levitation and suspension forces on these samples is important from the point of view of bulk applications of these samples. In this context, it is important to study the dependence of levitation force on the sample size and geometry. It has been found that the levitation force depends more on the area of the sample than on its thickness as observed in our study of reduction of both area and thickness by 25 % of the original value. This may be due to the fact that the levitation force saturates with sample thickness [24] whereas it has not been reported to do so with sample area.

For practical applications of bulk samples, stability of the properties such as magnetization and levitation force is an important criterion. In levitating systems, the relaxation of levitation force would be a key factor to be taken into account while employing these materials for such applications. Also, the bulk characterization of the material by studying

the relaxation of levitation force is equivalent to studying the magnetic relaxation as well. In this connection, we studied the relaxation of levitation force of the entire bulk sample and found that the rate of relaxation of levitation force do not vary monotonously with the applied field due to a permanent magnet. The relaxation rates of levitation force shows a near-oscillatory behavior. We have proposed a model for the current structure based on the possibility of its bistable equilibrium. This bistability arises from the fact that two distinct states of relaxation of levitation force occur at successive increments of applied magnetic field in our levitation force hysteresis curve measurements [25]. The faster and slower relaxation might correspond to two different current structures in the material arising from its constant interaction with the approaching magnet. We have not observed a complete arrest of relaxation of levitation force in the presence of a magnet. Rather, we observed two possible states of relaxation rate of levitation force as a function of magnetic field. The bistable equilibrium model proposed by us in the present work discussed the possibility of two states of current structure corresponding to the faster and the slower states of relaxation of levitation force. We have also studied the effects of the superconductor on the permanent magnet as it could be an important factor in applications involving a superconductor and a magnet. From the physics of it, it is interesting to study such interactions and its effect.

Significantly, we have observed for the first time the counter-magnetization of the permanent magnet in the presence of the superconductor due to the magnetic field offered by the superconductor. We have obtained a complete M-H loop of the first quadrant for the $SmCo_5$ magnet by counter-magnetizing it using the YBCO/Ag superconductor while in parallel we obtained its levitation force hysteresis loop [26]. We have simultaneously observed the relaxation of the permanent magnet and of the superconductor during this experiment as well.

We have developed a rapid processing technique named Rapid Infiltration Growth Processing (RIGP) technique based on the IGP technique and the Bridgman method used for single crystal growth for processing samples in shorted time durations compared to IGP technique. We have been able to process both YBCO and YBCO/Ag composite samples in one-fourth of the time of IG processing technique. We have studied the properties of these samples in comparison with conventional IG processed YBCO samples. We found that the properties are inferior compared to the IGP samples at lower magnetic fields but marginally improve at higher fields. We have studied the effect of pressure and found 540 MPa to be optimum for samples by RIGP as well. We have also made YBCO/Ag by RIGP technique to study the

effect of Ag addition to the composite. We have found that Ag agglomerates as large clustered precipitates and modifies the sample microstructure significantly thereby affecting the properties drastically.

Finally, we have studied the magnetization of YBCO and YBCO/Ag samples at lower temperatures down to 20 K for magnetic fields up to 9 T. We have calculated critical current density and pinning force density of the samples as a function of field up to 9 T at temperatures 77 K, 65 K, 50 K, 35 K and 20 K. We have obtained the critical current density and pinning force density as a function of temperature based on the data. We have obtained generalized equations that describe the behavior of the self-field critical current densities and critical current densities in the presence of field as a function of temperature. These generalized equations have helped us to better understand and extract the sample dependent parameters. We have carried out a similar analysis for the pinning force density of the samples. Thus, we could conclude that for YBCO and YBCO/Ag samples the general behavior of $J_c(0,T)$, $J_c(H,T)$ and $F_P(H,T)$ as a function of temperature is similar for both IGP and RIGP samples but for the sample specific parameters in the generalized equations that get modified to different extents for samples depending on their microstrucutres.

References

[1] J. G. Bednorz, and K. A. Mueller, *Zeitschrift für Physik B* **64** (2), 189–193 (1986).

[2] M. K. Wu, J. R. Ashburn, C. J. Torng, P. H. Hor, R. L. Meng, L. Gao, Z. J. Huang, Y. Q. Wang, and C. W. Chu, *Phys. Rev. Lett*. **58**, 908-910 (1987).

[3] G. Krabbes, G. Fuchs, W.-R. Canders, H. May, and R. Palka, *High Temperature Superconductor Bulk Materials*, Wiley-VCH, Germany (2006).

[4] D. Larbalestier, A. Gurevich, D. M. Feldmann, and A. Polyanskii, *Nature* **414**, 368 (2001).

[5] G. Bolaños, E. Baca, J. Osario, and P. Prieto, *Phys. Stat. Solidi.* 220 (1), 517-520 (2000).

[6] R. F. Klie, J. P. Buban, M. Varela, A. Franceschetti, C. Jooss, Y. Zhu, D. Browning, S. T. Pantelides, and S. J. Pennycook, *Nature* **435**, 475 (2005).

[7] J. G. P. Binner and I. A. H. Al-Dawery, *Supercond. Sci. Technol*. **11**, 1230 (1998).

[8] J. Jung and I. Isaac, and M. A-K. Mohamed, *Phys. Rev. B* **48**, 7526–7536 (1993).

[9] S. Jin, T. H. Tiefel, R. C. Sherwood, M. E. Davis, R. B. van Dover, G. W. Kammlott, R. A. Fastnacht, and H. D. Keith, *Appl. Phys. Lett.* **52**, 2074 (1988).

[10] M. Morita, S. Takebayashi, M. Tanaka, K. Kimura, K. Miyamoto, K. Sawano, *Advances in Superconductivity III (ISS '90)*, 733-736 (1991).

[11] M. Murakami, T. Oyama, H. Fujimoto, S. Gotoh, K. Yamaguchi, *IEEE Trans. Magnetics*, **27** (2) 1479 (1991).

[12] Y. Yamada and Y. Shiohara, *Physica C* **217** (1–2), 182-188 (1993).

[13] A. Wongsatanawarid, H. Seki, and M. Murakami, *J. Phys.: Conf. Ser.* **234**, 012047 (2010).

[14] E. S. Reddy and T. Rajasekharan, *Supercond. Sci. Technol.* **11**, 183 (1998).

[15] I. K. Jeong, D. Y. Kim, Y. K. Park, K. W. Lee, and J. C. Park, *Physica C* **185-189**, 2393-2394 (1991).

[16] N. H. Babu, M. Kambara, P. J. Smith, D. A. Cardwell, and Y. Shi, *J. Mater. Res.* **15**, 1235-1238 (2000).

[17] V. Ganesan, R. Srinivasan, S. Aswathy, K. D. Chandrasekaran, B. Srinivas, U. V. Varada Raju, G. V. Subba Rao, R. Gopalan, T. Rajasekaran, *Bull. Mater. Sci.* **7** (1), 87-93 (1994).

[18] D. Lee and K. Salama, *Jpn. J. Appl. Phys.* **29**, L2017-L2019 (1990).

[19] U. Wiesner, G. Krabbes, M. Ueltzen, C. Magerkurth, J. Plewa, and H. Altenburg, *Physica C* **294**, 17–22 (1998).

[20] Ch. Zhang, A. Kulpa, and A. C. D. Chaklader, *Physica C* **252**, 67-78 (1995).

[21] B. Kalisky, J. R. Kirtley, J. G. Analytis, J.-H. Chu, I. R. Fisher, K. A. Moler, *Phys. Rev. B* **83**, 064511 (2011).

[22] V. S. Boyko and S. -W. Chan, *Physica C* **466** (1-2), 56-60 (2007).

[23] N. D. Kumar, T. Rajasekharan, R. C. Gundakaram and V. Seshubai, *IEEE Trans. Appl. Supercond.,* **21** (6), 2612-2620 (2011).

[24] I. A. Rudnev and Y. S. Ermolaev, *J. Phys.: Conf. Series* **43**, 983-986 (2006).

[25] R. Parthasarathy, M. M. Lakshmi, and V. Seshubai, *Physica C* **471**, (13-14), 395-399 (2011).

[26] R. Parthasarathy, M. M. Lakshmi, and V. Seshubai, *Proceedings of the 56th DAE Solid State Physics Symposium 2011. AIP Conf. Proc.* **1447**, *899-900 (2012).*

FIGURE CAPTIONS

Figure 1.1 A typical resistance versus temperature plot of a superconductor showing its transition from normal state to the superconducting state. Here, the sample studied was an YBCO superconductor.

Figure 1.2 A schematic representation of Meissner effect and levitation of a $SmCo_5$ permanent magnet over an YBCO superconductor revealing an aspect of the Meissner effect.

Figure 1.3 M-H phase diagram of type-I and type-II showing Meissner and mixed states.

Figure 1.4 The structure of YBCO compound is shown here with the two different copper sites Cu(1) and Cu(2) identified.

Figure 1.5 A pseudo-binary phase diagram for the Y-Ba-Cu-O system given here shows the various phases and their corresponding temperatures.

Figure 1.6 Sample processing configuration of the conventional IGP technique

Figure 2.1 A combined picture of preparation of precursor powders during combustion stage

Figure 2.2 The picture shows the furnace used for heat treatment of the samples

Figure 2.3 Hydraulic press used in the present work and the sample pellets made are shown

Figure 2.4 Schematic diagram of the furnace used for the heat treatment of the samples

Figure 2.5 Picture of the specially designed oxygenation furnace for oxygenation of the samples

Figure 3.8 The real part of AC susceptibility as a function of temperature for the three samples A, B and C revealing variations in transition temperatures and transition widths with varying silver content. The improvement in T_c and ΔT_c for sample with maximum silver content of 10 wt % is clearly seen.

Figure 3.9 M-H loops for the three samples in Y540 series with Ag varying content recorded using a Physical Property Measurement System (QD-PPMS) is shown in the figure.

Figure 3.10 The plot of critical current density J_c of the three samples Y540-2, Y540-4, Y540-10 with varying silver content of 2, 4 and 10 wt % respectively as a function of applied magnetic field calculated from M-H loops recorded at 77 K shows a significant reduction in dependence of J_c on H for the sample Y540-2.

Figure 3.11 (a) The normalized pinning force as a function of magnetic field at 77 K for the three samples and (b) the irreversibility field H_{irr} as a function of temperatures between 77 K and 92 K for the samples showing the better performance of sample Y540-2 on both the counts.

Figure 3.12 The histograms below three micrographs reveal the corresponding Y-211 particle number density distribution, the surface area contribution of the Y-211 particles, size-wise, to the total area of the Y-211 particles and the size-wise distribution of Y-211 interparticle distance.

Figure 3.13 High magnification FESEM image of the Y540-2 sample shows presence of twins in the Y-123 matrix. The extensive twinning present in the sample is indicated here by arrows. It can be observed that the twin width is of the order of 20 nm and individual twinned regions extend to a few microns.

TABLE CAPTIONS

Table 3.1 The variation of mechanical properties such as stiffness, hardness, reduced elastic modulus and Young's modulus with varying silver content is tabulated showing remarkable improvement in the values of these properties with Ag addition.

Table 3.2 The amount of Ag present in the Y-123 matrix through EDAX analysis is tabulated for a sample of 10 regions scanned.

Table 3.3 The variation of transition temperature and width of transition of the three samples as a function of silver content is presented in the table. The variation in T_c across the three samples is minimal.

Table 3.4 The self-field critical current density and peak effect field values for the three samples are shown in the table revealing a reasonably high $J_c(H=0)$ and high H_P for Y540-2 sample.

Table 3.5 The table shows the effect of Ag addition on the sample microstructure with respect to Y-211 phase particles and macroscopic defects structure in terms of porosity in the system.

Table 4.1 The peak levitation force gap value and the peak suspension force value along with the corresponding magnetic field values are tabulated. The field used for the field-cooling can be varied by varying the gap distance between the superconductor and the magnet as shown in figure 4.4 below.

Table 4.2 The values of peak suspension force and the corresponding magnetic field value for different initial applied fields is tabulated for the samples in Y460 and Y540 series.

Table 6.4 The values of the fit parameters for each of the field values for all the three samples are tabulated.

LIST OF PUBLICATIONS

Publications in Journals

1. Near-oscillatory relaxation behavior of levitation force in infiltration and growth processed bulk YBCO/Ag superconducting composites
R. Parthasarathy, M. M. Lakshmi and V. Seshubai
Physica C **471**, 395-399 (2011).

2. Significant reduction in magnetic field dependence of critical current density of YBCO/Ag composite bulk superconductors fabricated by Infiltration and Growth processing technique
R. Parthasarathy and V. Seshubai
(To be communicated)

3. Fabrication of bulk YBCO and YBCO/Ag composites in shorter time durations via a new   process: Rapid Infiltration Growth Processing (RIGP) technique
R. Parthasarathy and V. Seshubai
(Under preparation)

4. Magnetic behavior of YBCO and YBCO/Ag composites fabricated by IG process
R. Parthasarathy and V. Seshubai
(Under preparation)

Publications in Conferences/ Proceedings

1. Levitation force measurements on Ag doped SIG processed bulk YBCO superconductor
   R. Parthasarathy, M. Maha Lakshmi, N. Devendra Kumar and V. Seshubai
   Proceedings of the 54th DAE-Solid State Physics Symposium, Page 813, December 14-18, 2009, Vadodara, Gujarat, India.

2. Optimization of Ag content in SIG processed bulk YBCO superconductors by levitationand suspension force measurements
   R. Parthasarathy, M. Maha Lakshmi, N. Devendra Kumar and V. Seshubai
   Proceedings of the 54th DAE-Solid State Physics Symposium, Page 817, December 14-18, 2009, Vadodara, Gujarat, India.

3. Strong pinning and enhanced flux trapping due to nanometer sized defects caused by submicron non-superconducting precipitates in Ag doped YBCO superconductors
   R. Parthasarathy, M. M. Lakshmi, V. Seshubai and T. Rajasekharan
   Proceedings of Indo-Singapore Joint Physics Symposium 2012 (ISJPS-2010), Page 73, February 19-21, 2010, University of Hyderabad, Hyderabad, India.

4. Centre Seeded Infiltration and Growth Process for fabrication of Large Grain Bulk YBCO/Ag Superconducting Composites
   R. Parthasarathy and V. Seshubai
   Proceedings of the 56th DAE-Solid State Physics Symposium, Page 166, December 19-23, 2011, Kattankulathur, Tamil Nadu, India.
   Published in Solid State Physics, *AIP Conf. Proc.*, **1447**, 883-884 (2012).

5. Counter-magnetization of $SmCo_5$ permanent magnet by YBCO/Ag composite bulk superconductor – A Competing Interaction picture
   R. Parthasarathy, M. M. Lakshmi, and V. Seshubai

R. PARTHASARATHY
CURRICULUM VITAE

School of Physics
University of Hyderabad
Hyderabad – 500046   Phone: +91-9492756687
India   E-mail: r.parthasarathy@gmail.com

Education

Currently Pursuing	PhD Physics (Experimental Condensed Matter Physics) (*Thesis Submitted)* University of Hyderabad, Hyderabad, India.
June 2005	MPhil Physics (Non-linear dynamics - Theoretical - BEC) Gold Medalist, University Topper Pondicherry University, Puducherry, India.
May 2004	MSc Physics Passed with Distinction – 7.92 /10 (CGPA) Pondicherry University, Puducherry, India.
May 2002	BSc Physics Passed as College Topper – 76 % Pondicherry University, Puducherry, India.

Research and Teaching Positions

Currently	CSIR - Senior Research Fellow School of Physics, University of Hyderabad.
Oct 2008 – March 2012	Meritorious Research Fellow School of Physics, University of Hyderabad.
July 2008 – December 2008	Graduate Student Teaching Assistant School of Physics, University of Hyderabad.

August 2006 –   University Research Fellowship.
September 2008

Fellowships and Awards

2012   CSIR – National Senior Research Fellowship

2008   UGC – National Meritorious Research Fellowship

2006   UGC – University Research Fellowship

2005   MPhil University Topper – Gold Medalist

2002   BSc College Topper

1997   Matriculation School Topper

Publications
Publications in Journals

1.   Near-oscillatory relaxation behavior of levitation force in infiltration
      and growth processed bulk YBCO/Ag superconducting composites
      R. Parthasarathy, M. M. Lakshmi and V. Seshubai
      Physica C **471**, 395-399 (2011).

2.   Significant reduction in magnetic field dependence of critical current
      density of YBCO/Ag composite bulk superconductors fabricated by
      Infiltration and Growth processing technique
      R. Parthasarathy and V. Seshubai
      (To be communicated)

3.   Fabrication of bulk YBCO and YBCO/Ag composites in shorter time
      durations via a new   process: Rapid Infiltration Growth Processing
      (RIGP) technique
      R. Parthasarathy and V. Seshubai
      (Under preparation)

4.   Magnetic behavior of YBCO and YBCO/Ag composites fabricated by IG process
       R. Parthasarathy and V. Seshubai
       (Under preparation)

Publications in Conferences/ Proceedings

1.   Levitation force measurements on Ag doped SIG processed bulk YBCO superconductor
       R. Parthasarathy, M. Maha Lakshmi, N. Devendra Kumar and V. Seshubai
       Proceedings of the 54th DAE-Solid State Physics Symposium, Page 813, December 14-18, 2009, Vadodara, Gujarat, India.

2.   Optimization of Ag content in SIG processed bulk YBCO superconductors by levitationand suspension force measurements
       R. Parthasarathy, M. Maha Lakshmi, N. Devendra Kumar and V. Seshubai
       Proceedings of the 54th DAE-Solid State Physics Symposium, Page 817, December 14-18, 2009, Vadodara, Gujarat, India.

3.   Strong pinning and enhanced flux trapping due to nanometer sized defects caused by submicron non-superconducting precipitates in Ag doped YBCO superconductors
       R. Parthasarathy, M. M. Lakshmi, V. Seshubai and T. Rajasekharan
       Proceedings of Indo-Singapore Joint Physics Symposium 2012 (ISJPS-2010), Page 73, February 19-21, 2010, University of Hyderabad, Hyderabad, India.

4.   Centre Seeded Infiltration and Growth Process for fabrication of Large Grain Bulk YBCO/Ag Superconducting Composites
       R. Parthasarathy and V. Seshubai
       Proceedings of the 56th DAE-Solid State Physics Symposium, Page 166, December 19-23, 2011, Kattankulathur, Tamil Nadu, India.
       Published in Solid State Physics, *AIP Conf. Proc.*, **1447**, 883-884 (2012).

5. Counter-magnetization of SmCo$_5$ permanent magnet by YBCO/Ag composite bulk superconductor – A Competing Interaction picture
R. Parthasarathy, M. M. Lakshmi, and V. Seshubai
Proceedings of the 56th DAE-Solid State Physics Symposium, Page 223, December 19-23, 2011, Kattankulathur, Tamil Nadu, India.
Published in Solid State Physics, *AIP Conf. Proc.*, **1447**, 889-900 (2012).

I hereby declare that the information provided in the CV above is true to the best of my knowledge and belief.

Place: Hyderabad

Date :   R. PARTHASARATHY.